Modular Synthesis of Templated Multicomponent Active Sites in Metal–Organic Frameworks via Cross-linking Strategies

Jackson Geary

A dissertation

submitted in partial fulfillment of the

requirements for the degree of

Doctor of Philosophy

University of Washington

2024

Reading Committee:

Dianne J. Xiao, Chair

Brandi M. Cossairt

Matthew Golder

Program Authorized to Offer Degree:

Chemistry

University of Washington

Abstract

Modular Synthesis of Templated Multicomponent Active Sites in Metal–Organic Frameworks via Cross-linking Strategies

Jackson Geary

Chair of the Supervisory Committee:

Dianne Xiao

Chemistry

Binuclear metal active sites are found throughout all subfields of catalysis, from homogeneous and heterogeneous systems to enzymes. The installation of bimetallic active sites within metal–organic framework (MOF) pores is an enticing strategy to leverage the intrinsic benefits of MOFs for catalysis – their porosity derived site isolation, rigid periodic secondary structure, and high degree of tunability. However, the actual construction of bimetallic sites is nontrivial. While a small number of bimetallic sites in MOFs have been reported, progress in this space is limited by synthetic challenges in controlling both the local coordination environments and relative metal positioning within the framework. The work herein describes progress towards the installation of precisely templated bimetallic active sites within MOF pores, and the exploration of these bimetallic sites as catalysts for oxidative catalysis.

Chapter 1 provides an overview and perspective of the current landscape for the installation of bimetallic sites within MOFs for catalysis. Particular emphasis is placed on the synthetic strategies employed, as well as the spectroscopic shortcomings in designing active sites that are explicitly bimetallic in nature.

Chapter 2 describes the development of an initial templating strategy. The strategy leverages simple protecting group chemistry (i.e. tertiary esters) to install cross-linked ligand dimers into the framework, Mg_2dotpdc (dotpdc^{4-} = 4,4″-dioxido-[1,1′:4′,1″-terphenyl]-3,3″-dicarboxylate), wherein the length of the cross-linking tether restricts the tethered struts to a single conformation (~ 7Å down the pore channel). Subsequent thermal removal of the cross-linker under microwave conditions exposes templated carboxylate pairs.

The generalizability of this templating method is a key advantage over other synthetic approaches. Chapter 3 details the expansion of the strategy first explored in Chapter 2 to other functional group pairs, specifically templated aryl and alkyl amines via tertiary carbamate cross-linkers. The ability to install templated amine pairs is particularly exciting because they are amenable to a variety of post-synthetic covalent modifications to generate diverse chelating sites for metal cations. As initial examples, the quantitative conversion of the aryl amine and alkyl amine pairs to iminopyridine (IP) and dipicolylamine (DPA) sites, respectively, is described. The iminopyridine and pyridyl amine sites can then be metalated with a variety of M(I/II) cations (M = Mn(II), Fe(II), Co(II), Ni(II), Cu(II) and Cu(I)). Detailed characterization of the metalated materials, including electron paramagnetic resonance (EPR) spectroscopy and extended X-ray absorption fine structure spectroscopy (EXAFS) are provided.

Chapter 4 details a departure from the installation of bimetallic sites to explore the structural implications of cross-linker incorporation in flexible MOFs. Incorporation of a primary

ester cross-linker into a previously unreported terphenyl expanded analogue of MIL53(Al) revealed that the otherwise highly flexible framework was stabilized in an open-pore configuration. The degree of flexibility could be further tuned by changing the concentration of ligand dimer used. While the parent framework is inactive, the cross-linked MOF is a competent Prins condensation catalyst. This work highlights the potential versatility of the templating strategy to dictate other parameters beyond installing functional groups.

Appendix A marks a return to the installation of bimetallic sites, specifically the expansion of the previously discussed post-synthetic chemistry to other N-donor ligands. Here, the modularity of the post-synthetic covalent modification is highlighted. Beyond the aforementioned IP and DPA scaffolds, di[2-(2-pyridyl)ethyl]amine, di[2-(diethylamino)ethyl]amine, alkylamine-based iminopyridine, and thiazole-2-carboxaldehyde based ligand scaffolds and their ability to bind transition metals are discussed.

An initial investigation of our Cu(II) metalated DPA and iminothiazole materials as catalysts for the oxidation of catechols and is explored in Appendix B, including a foray into statistical modeling and the use of design of experiments (DoE) to elucidate key parameters. Our results suggest that while our materials are catalytically competent, there is not a major templating effect, highlighting the importance of a metal–metal distance match between the framework active sites and the target reaction.

Appendix C provides additional context for how the strategies presented in this body of work compare to other common heterogeneous platforms: mesoporous silicas and zeolites. While both mesoporous silicas and zeolites can be post-synthetically modified, the molecular level precision and modularity of our MOF chemistry detailed in Chapters 2 and 3 cannot be replicated in those materials. As highlighted in Chapter 4, the rich landscape of MOF

architectures also provides an exciting and unique opportunity to explore structural implications such as rigidification in a way that cannot be done with amorphous materials like silica nor rigidly crystalline zeolitic materials.

Table of Contents

List of Figures

List of Tables

Acknowledgements

Graduate school is a wild journey, and not one taken alone despite how lonely it sometimes feels. My PhD experience has been shaped as much, if not more so, by the people around me as by the science itself. I'm not always one for sentimentality, but I hope to thank everyone who's impacted me throughout this journey.

First, I'd like to thank my advisor, Prof. Dianne Xiao. Dianne and I came to the University of Washington at essentially the same time. In fact, during my visit weekend in 2019, she hadn't yet officially moved, so she had taken over Prof. Mike Heineky's office for her meetings with students. I remember being excited by the ideas she proposed for the start of her research group and continued to email her throughout the summer before my first year. That fall I decided to pursue research in her lab and haven't looked back. Her passion for science, inquisitive nature, high standards, and seemingly steel-trap memory have absolutely shaped who I am as a scientist. Beyond scientific expertise, it takes a particular tenacity to build a successful research group, and I hope some of that tenacity has worn off on me over the past five years.

I want to thank Prof. Brandi Cossairt for her guidance particularly in my early days at UW. When I first committed to go to UW, her group was my first choice. Then, when I got here, I had a great time rotating in her group. We had a chat one day about my options- her group or Dianne's. She said something that has stuck with me: "Go where you can make the most impact." That helped push me to take the leap and join Dianne's lab, and so I'm forever grateful for the candid and powerful advice.

Being one of the first students in a group is a unique opportunity, because you get to not only kick off the research program, but also build the culture. It's been an awesome experience to

see the lab grow and take shape over the last five years, and I've had the pleasure of working with some really incredible scientists.

Leo, Bobby and I joined the lab together that first fall. In truth, Leo and I already started our journey together back in the spring (we ran into each other at at least one other visit weekend, whether he remembers it or not). We were really in the trenches together in the early days, especially during Covid, and I'm proud of us for pushing through that. I've always been inspired by Leo's ability to persevere and bounce back from the inevitable challenges and setbacks of research. With his desk in the lab's left office, CHB 312, and mine in the right office, CHB 318, I've often thought of us as the two pillars of the lab. I'm excited to see how the new pillars, the later students, hold up without us!

Every year has brought new students, who've shaped the dynamics of the lab for the better. In 2020, Ashe and Kathleen joined, bringing fresh life into the otherwise basically empty offices (I know Dianne was thankful Leo and I had new people to talk to!). I was excited because they fit in with my secret goal of building as queer a lab as possible. While grad school isn't necessarily a great time, Kathleen and I have had a great time the last four years commiserating and gossiping over coffee, and I'm going to miss our escapes to the café in the Henry gallery (the best spot for coffee on campus). She's also an incredibly thoughtful scientist and lab mate, and always goes out of her way to help others in the lab any way she can. I admire her patience as a mentor and friend. Ashe's quick wit, inquisitive nature, and passion for making new compounds for even just for the sake of making them earned them the moniker of 'future PI', however much they protest. But honestly, I am inspired by their love of chemistry and their exceptional synthetic skills. I'm equally inspired by the depth and breadth of their musical knowledge!

I was profoundly lucky in getting to work with Devin when he joined the lab in 2021. Technically I was his mentor, but he came in already a fully-fledged MOF chemist so I can't really take any credit for his growth! Beyond science, when I think of Devin I think of fashion, running, Real Housewives, and Rihanna. He and I (I think) set the standard for lab 'looks'. But I also think of his calm demeanor, chemical intuition, and quick wit. Phuong joined the lab at the same time, and has been my sunscreen/skincare partner ever since. The queen of desk snacks, I respect her determination and indefatigable spirit in lab. Truly, no one works harder or deserves their scientific success more.

Sophie, Doug, and Adrian joined in 2022, rounding out our current crew. Sophie constantly impresses me with how thoughtful a scientist she is, and Adrian brings a flair to lab that is hard to match. Doug's determination to do better for himself and his family, and ability to juggle being a graduate student and a parent is inspiring to me. I'm excited to see how they shape the lab in the next few years as they grow to be the senior students.

We also saw a set of incredible undergrads come through the lab during my time. Andy, who took on a huge chunk of the work to set up the lab that first summer, and later worked alongside me on major portions of my work. No one's smiled more despite a failed Suzuki coupling (and perhaps no one's had more failed Suzuki couplings, but that's a different story). But truly, I've never met a kinder soul. Jonathan, Audrey, and EJ never failed to impress me with their work ethic and positivity, nor failed to make me feel old when they mentioned their age. More recently, it's been exciting to watch Kamaya grow into a confident, independent member of the 'MOF templating' family.

The group has also had some wonderful postdocs and a research scientist whom I'm grateful to have met. Dawei Xiao helped kick off the templating project, and I'm thankful for his

help with that. Ryan Shafranek brought a lot of wisdom and an interesting perspective to the group as a polymer chemist. I admire his grit and his way of framing science and the struggles of research in a healthy way. He also deserves a shoutout as the only member of the Xiao lab with his own Slack emoji! Nate Schuster, our resident research scientist and tomato plant expert, is not only an exceptional synthetic chemist, but an extremely thoughtful and attentive mentor. I know the group is in good hands with him around.

One of the most incredible parts of grad school has been the community I've found outside of the lab. In the depths of the pandemic, I'm so thankful for Skye, who brought such a bright light to an otherwise really bleak time. She is also to blame for my addiction to Survivor and The Real Housewives franchises, coincidentally. Deciding whether that's a good thing or a bad thing is an exercise left up to the reader. Heath, Jerry, and Ian are some of the best people, and I've loved all our nights out, nights in watching Drag Race, and in general just having a little queer family here in Seattle. I'm so grateful to have met Tanner and his husband Julian, who welcomed me into their life so generously. It's rare that you meet people that you mesh so well with. I've loved all our adventures, like going to Vegas to see Erika Jayne 'for the bit', but also just getting to hang out and jabber. I'm excited for where this next chapter takes us.

I couldn't have done any of this without my family. My siblings, Ainsley and Will, who never fail to be interested in what I'm doing with my 'dust' (MOFs, which do admittedly look a lot like dust). My mom, who has always been my rock, and never fails to talk me down from a spiral. My dad, who's humor and good nature, and propensity to nerd out with me, are some of my favorite things. I love getting a random text about something like a new Scooby Doo cartoon to distract me from a failed experiment. They've always supported me in my goals, even as they've shifted throughout the years. My aunt Sandi, who is always game to talk science. I'm sorry that

Grandma didn't get to see me finish, but I'm so thankful for all her support when I was growing up and truly her whole life, and I hope she's proud. I know my Grandfather and Nana are proud, because they never fail to tell me when I call. I have such respect for their work ethic and determination, and I try to emulate it myself in my own life.

Lastly, I want to thank my partner, Colton, for going on this wild adventure with me. Grad school would've been so much grimmer to go through alone. Not only is Colton the funniest person I know, he's self-assured and confident, and he's the best dog parent I could ask for. I'm so thankful that after every hard day in lab, I could come home and unplug with someone (one of the benefits of dating someone who isn't in science is that you can't get sucked in to venting about lab work). I'm so glad we've gotten to build our little family in Seattle, explore the PNW, and create so many beautiful memories together. I'm so excited for what comes next for us, and can't wait to go through it together!

To everyone I've mentioned here, and to the many people whom I haven't, thank you from the bottom of my heart for making grad school such an impactful and rewarding chapter of my life!

Dedication

For Colton. There's no one else I'd rather go on this adventure with.

Chapter 1: Engineering Bimetallic Active Sites in Metal–Organic Frameworks: Challenges and Opportunities

1.1 Introduction

Binuclear metal active sites can be found throughout all subfields of catalysis, from homogeneous and heterogeneous systems to enzymes. The mechanisms by which two metal centers may interact synergistically are as rich and varied as the diverse bimetallic structures that have been synthesized in the laboratory and evolved in biology. For example, two redox-active metals can work together to share the redox load of demanding multi-electron transformations.[1–4] Similarly, redox-inactive metal centers can cooperatively bind and orient reaction partners, enhancing their local concentration, electrophilicity, and/or nucleophilicity.[5–7] In other cases, the second metal may have no direct interaction with the substrate(s), but serves a critical role in modulating the reactivity of its partner.[8,9] While an exhaustive discussion of the different classes of bimetallic catalysis is beyond the scope of this perspective, these selected examples underscore the diversity of bimetallic structures and catalytic mechanisms.

Even from the brief overview outlined above, it is evident that different bimetallic mechanisms require different metal identities, ligand environments, and metal–metal distances. *Thus, both structural precision and tunability are key to engineering productive bimetallic catalysts.* While these structural parameters are easily controlled in enzymes and molecular catalysts, comparable synthetic control is more difficult to achieve in a heterogeneous platform. However, while the synthetic barriers are high, the potential pay-off is also considerable. Heterogeneous supports allow researchers to explore unique catalyst design parameters, including site isolation, highly constrained geometries, pore confinement, and microenvironment effects.[10–15] As crystalline porous solids built from metal nodes connected by bridging organic linkers,

metal–organic frameworks (MOFs) maximize both structural precision and chemical tunability. From this perspective, MOFs are an ideal platform for investigating bimetallic motifs in a heterogeneous context. Indeed, many of the cooperative mechanisms observed in enzymes, molecular catalysts, and heterogeneous systems have been implemented in MOFs (**Fig. 1.1**). For example, redox-active diiron and dicopper pairs have been explored in MOFs for methane oxidation,[16–18] and diiron sites have been studied for photochemical H_2 production.[19,20] Redox-inactive pairs have also been investigated, such as Zr(IV) and Zn(II) sites for CO_2 hydrogenation to methanol.[21] Finally, bimetallic sites containing one redox-active and one redox-inactive metal have also been designed, such as the pairing of anionic $[Co(CO)_4]^-$ complexes and Lewis acidic metal nodes for epoxide and β-lactone carbonylation (**Fig. 1.1**).[22,23]

Here, we summarize the different ways researchers have approached the synthesis of bimetallic active sites in metal–organic frameworks and discuss the strengths and limitations of each method. Finally, we conclude with an outlook on the challenges and opportunities in MOF-supported bimetallic catalysis.

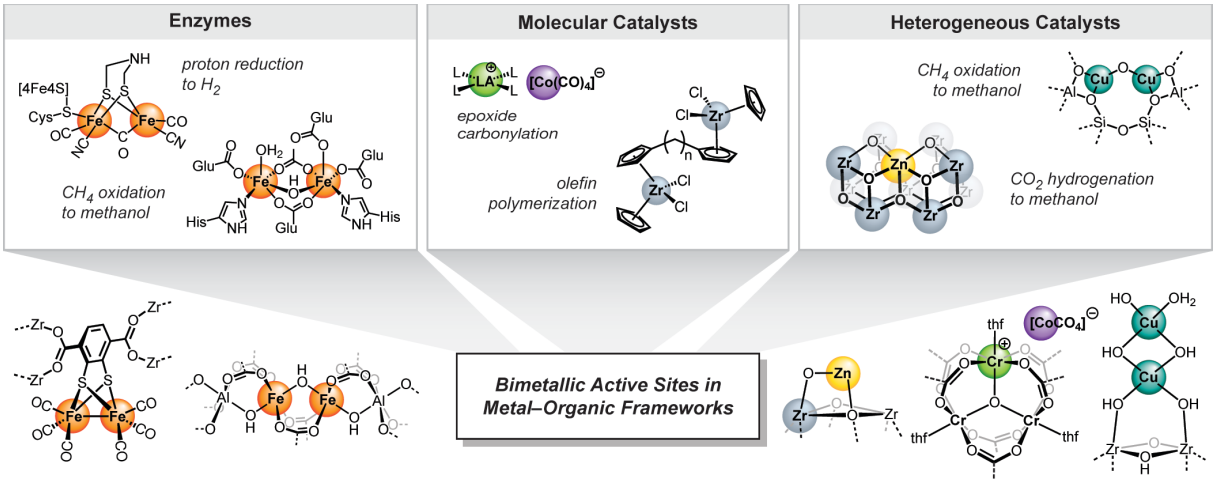

Fig. 1.1 | Overview of bimetallic active sites in biological and synthetic systems. *Top:* Selected examples of bimetallic active sites in enzymes, molecular complexes, and heterogeneous systems, redrawn from references 1–4, 5–7, 10, and 15. *Bottom:* Overview of how these bimetallic active sites have been replicated in metal–organic frameworks, redrawn from references 16–23.

1.1.1 Scope and Aims

The aim of this perspective is to introduce readers to the different ways binuclear metal active sites have been synthesized in metal–organic frameworks. Selected examples from the literature will be used to illustrate both the diversity of synthetic approaches as well as the diversity of bimetallic structures that can be obtained. While catalytic applications will be touched upon briefly within the context of each example, more comprehensive discussions on MOF catalysis can be found elsewhere,[12,24,25] including focused reviews on MOF electrocatalysis[26–28] and photocatalysis.[29–31] Furthermore, our discussion will be restricted to well-defined active sites where the two metal centers are colocalized within the same pore. Thus, we will not discuss systems where the metals are more spatially separated, such as core–shell structures,[32–36] or systems that are less molecularly defined, such as MOF-derived amorphous materials[36–39] and MOF-supported bimetallic nanoparticles.[40,41] Finally, while there are several elegant examples of using cooperative metal–metal interactions to enhance gas sorption,[42–44] the emphasis here will be on the use of bimetallic sites for reactivity and catalysis. We encourage readers interested in these areas to consult the articles and reviews cited above.

1.2 Synthetic strategies

An overview of the strategies researchers have used to achieve two proximal metal centers in MOFs is provided in **Fig. 1.2**. The different synthetic methods can be broadly divided into two categories: 1) the use of multinuclear metal nodes directly for catalysis (Section 1.2.1), and 2) surface grafting approaches, where bimetallic sites are anchored to the pore walls (Sections 1.2.2–

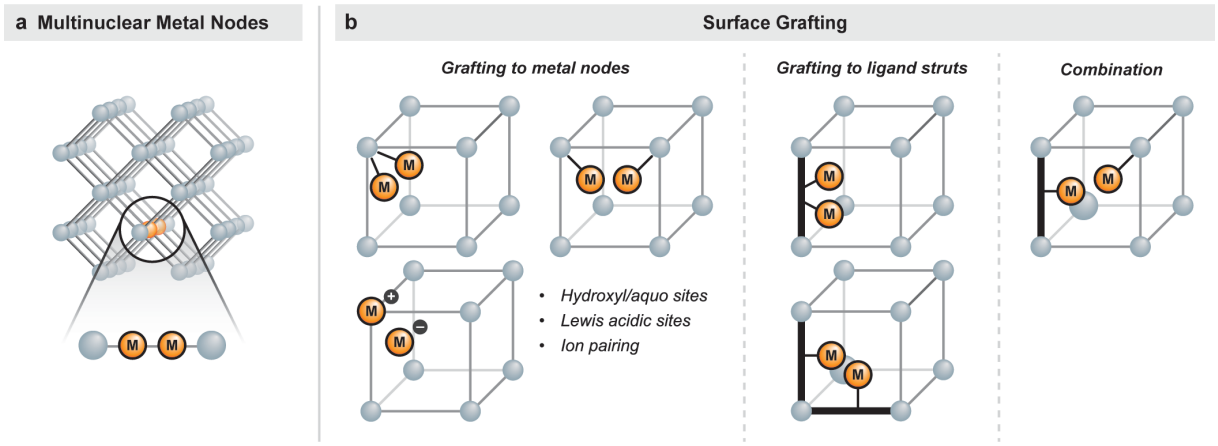

Fig. 1.2 | Overview of strategies to incorporate bimetallic active sites in metal–organic frameworks. Examples include (a) the direct use of multinuclear metal nodes and (b) surface grafting strategies: grafting to metal nodes, grafting to ligand struts, and combinatorial approaches.

1.2.4). The grafting approaches can be further subdivided according to where the metal center is attached, such as at the metal node (1.2.2), ligand strut (1.2.3), or a combination of the two (1.2.4).

1.2.1 Multinuclear metal nodes

In many metal–organic frameworks, the inorganic building blocks are not isolated monomeric metal cations, but rather multinuclear metal clusters or even infinite 1D metal–ligand chains. These clusters and chains can serve directly as binuclear or multinuclear active sites for catalysis, either in single metal or mixed-metal variants (**Figs. 1.3** and **1.4**). While this approach affords somewhat lower chemical tunability, as it is limited to the structures of existing metal nodes, the advantage of this approach lies in its relative synthetic ease. Bimetallic active sites can often be obtained directly upon MOF formation, with no additional post-synthetic modifications required.

1.2.1.1 Multinuclear clusters

Frameworks containing redox-active bi- and multinuclear cluster-based nodes have been used to facilitate challenging multi-electron processes, both stoichiometrically and catalytically (**Fig. 1.3**). For example, Powers and coworkers have studied C–H amination in $Ru_6btc_4Cl_3$ (btc^{3-} = benzene-1,3,5-tricarboxylate), a framework containing dimeric Ru_2(II/III) nodes (**Fig. 1.3a**). The axial chloride bound to each dimer was replaced with N_3^- and used to carry out the stoichiometric conversion of toluene to benzylamine.[45,46]

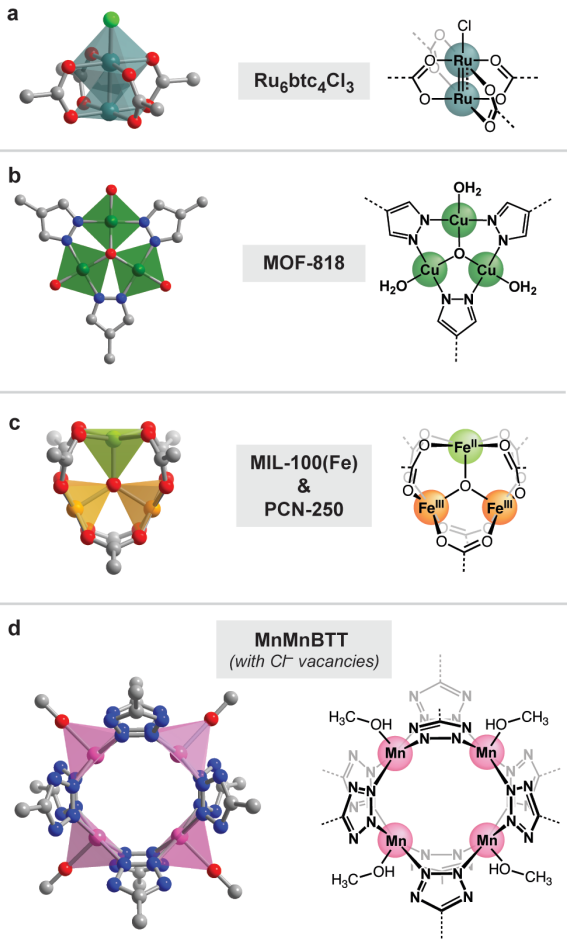

Fig. 1.3 | Multinuclear MOF nodes, including (a) diruthenium sites for C–H amination, (b) trinuclear copper clusters for aerobic catechol oxidation, (c) trinuclear iron(II)/(III) clusters for methane oxidation, and (d) tetranuclear manganese sites for reversible O_2 cleavage. Figures redrawn from references 45, 47, 49, and 51.

Redox-active trinuclear metal nodes have also been explored for oxidative reactions. One example is MOF-818, which contains trinuclear copper(II) nodes with three open coordination sites (typically bound by water or solvent) (**Fig. 1.3b**).[47] These tricopper centers have been explored as catalysts for bio-inspired catechol oxidation using O_2.[48] Similarly, the trinuclear iron nodes in MIL-100(Fe) (MIL = Materials of Institute Lavoisier) and PCN-250 (PCN = Porous Coordination Network) have been investigated for the stoichiometric oxidation of methane to methanol in the presence of N_2O. In these frameworks, the reactivity is

attributed to the one coordinatively unsaturated Fe(II) site per cluster that forms upon framework activation (**Fig. 1.3c)**.[49,50]

Finally, stoichiometric O_2 reactivity has been observed in the framework MnMnBTT (MnMnBTT = $Mn_3[(Mn_4Cl)_3BTT_8]_2$, BTT^{3-} = 1,3,5-benzenetristetrazolate), which is constructed from tetranuclear $[Mn_4Cl]^{7+}$ nodes.[51] Recently, Dincă and coworkers discovered that a portion of the bridging chlorides can be removed post-synthetically, leaving behind an unusual cavity with four inward-oriented open metal sites (**Fig. 1.3d**). By distributing the redox burden across four metals, these square-pyramidal tetramanganese clusters are able to reversibly cleave and re-form the O–O bonds in O_2, a challenging 4 e^- process.[52] This example nicely highlights how the structural rigidity of MOFs allows the formation of unusual metal arrangements and geometries that would be difficult to achieve otherwise.

1.2.1.2 1D chains

The short intermetal distances and strong metal–metal communication in frameworks constructed from infinite 1D metal–ligand chains have been leveraged to cooperatively bind molecules such as CO_2 and CO.[42,43] In addition to gas separation applications, such systems have also been investigated for cooperative reactivity. For example, Wade and coworkers synthesized $Fe(bppdi)(DMF)_{0.5}$ (H_2bppdi = 2,6-bis(1H-pyrazolyl)pyromellitic diimide), a framework containing 1D chains of coordinatively unsaturated Fe(II) centers, and showed it could be used to carry out the stoichiometric reduction of NO to N_2O (**Fig. 1.4a**).[53]

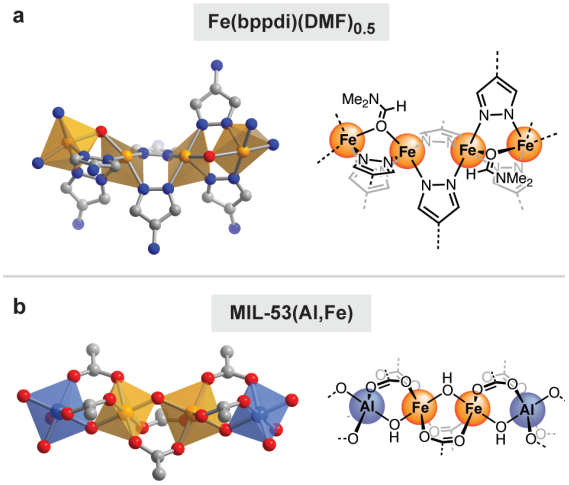

Fig. 1.4 | Frameworks containing 1D chains, including (a) $Fe(bppdi)(DMF)_{0.5}$, a framework containing coordinatively unsaturated Fe(II)-pyrazolate centers, and (b) electrochemically synthesized MIL-53(Al,Fe). Figures redrawn from references 53 and 16.

In addition to using the monometallic frameworks directly, researchers have also explored the use of mixed-metal frameworks to achieve site-isolated bimetallic species within an extended 1D chain. One example of efforts in this area is the work by Pidko, Gascon, and coworkers on the MIL-53 structure,[16] which has the formula M(OH)bdc (bdc^{2-} = 1,4-benzenedicarboxylate).[54–57] The framework is composed of infinite chains of corner-sharing M^{3+} octahedra bridged by bdc^{2-} and hydroxide ligands to generate a framework with diamond-shaped one-dimensional channels. Pidko, Gascon, and coworkers proposed that isolated monomeric and dimeric Fe(III) centers could be achieved in the electrochemically synthesized mixed-metal framework MIL-53(Al,Fe), which contains a mixture of Al(III) and Fe(III) sites (**Fig. 1.4b**).[16] The researchers showed that the mixed-metal system catalyzed the selective oxidation of methane using H_2O_2 as the oxidant, with a combined selectivity for oxygenates (MeOH, MeOOH and formic acid) of ~80%. Spectroscopic methods such as Mössbauer spectroscopy suggested the presence of both isolated, monomeric Fe(III) sites and antiferromagnetically coupled Fe(III)–Fe(III) dimers, though longer chain oligomers cannot be ruled out based on the spectroscopic evidence provided.

The distribution of monomeric, dimeric and potentially oligomeric active sites in MIL-53(Al,Fe) highlights the main shortcoming of mixed-metal frameworks: controlling active site nuclearity. While the overall metal composition is readily tuned, the spatial distribution of metal

cations is not. However, Gándara and coworkers recently showed that pre-formed molecular clusters can be used to control the relative arrangement of metals in mixed-metal MOFs.[58] As such strategies mature, they may become promising routes to achieve the selective synthesis of site-isolated bimetallic species in mixed-metal frameworks.

1.2.2 Grafting to metal nodes

The surfaces of metal nodes often feature reactive functional groups, such as Brønsted acidic hydroxyl/aquo ligands, Lewis acidic metal centers, and loosely bound counterions. The chemistry of these reactive groups can be leveraged to attach additional metal centers via covalent bonds, coordination bonds, and electrostatic interactions. While many of these procedures were originally developed in the context of grafting mononuclear metal complexes, they have since been adapted to achieve bimetallic active sites.

The majority of MOFs that have been explored for grafting at the metal node are constructed from highly oxophilic metals (e.g., Ti^{4+}, Zr^{4+}, and Hf^{4+}). The polynuclear metal oxide clusters found in these structures have both high chemical stability as well as rich surface chemistry (**Fig. 1.5**).[59] For example, these metal oxide clusters are often decorated with surface hydroxyl and aquo groups, which can be deprotonated and used to anchor additional metal cations (Section 1.2.2.1). Similarly, dangling surface monocarboxylates can be exchanged for ditopic ligands that can react with additional metal cations (Section 1.2.2.2). Finally, charged metal nodes with loosely bound counterions can be used to tether oppositely charged metal complexes through ion pairing (Section 1.2.2.3).

1.2.2.1 Anchoring to surface hydroxyl/aquo groups

The use of surface hydroxyl/aquo groups to anchor organometallic species and other metal complexes has been most extensively explored in zirconium-based frameworks. The structures of three representative zirconium frameworks, UiO-66 (UiO = University of Oslo),[60] NU-1000 (NU = Northwestern University),[61] and MOF-808,[62] are illustrated in **Fig. 1.5**. While the nodes of all three frameworks share the same hexanuclear $Zr_6(\mu_3\text{-}O)_4(\mu_3\text{-}OH)_4$ core, the clusters differ in the number of bound bridging ligands. For example, the nodes in UiO-66 are 12-connected (i.e., bound by 12 ligand struts, see **Fig. 1.5a**), to give an overall formula of $Zr_6O_4(OH)_4(bdc)_6$ (bdc^{2-} = 1,4-benzenedicarboxylate). On the other hand, the nodes of NU-1000 and MOF-808 are 8- and 6-connected, respectively. In NU-1000, the excess charge of the cluster and open coordination sites are balanced by additional hydroxide (4×) and water molecules (4×) to give an overall formula of $Zr_6O_4(OH)_8(H_2O)_4(TBAPy)_2$ ($TBAPy^{4-}$ = 4,4',4",4"'-(pyrene-1,3,6,8-tetrayl)tetrabenzoate) (**Fig. 1.5b**). In MOF-808, the remaining charge and coordination sites are balanced by six additional

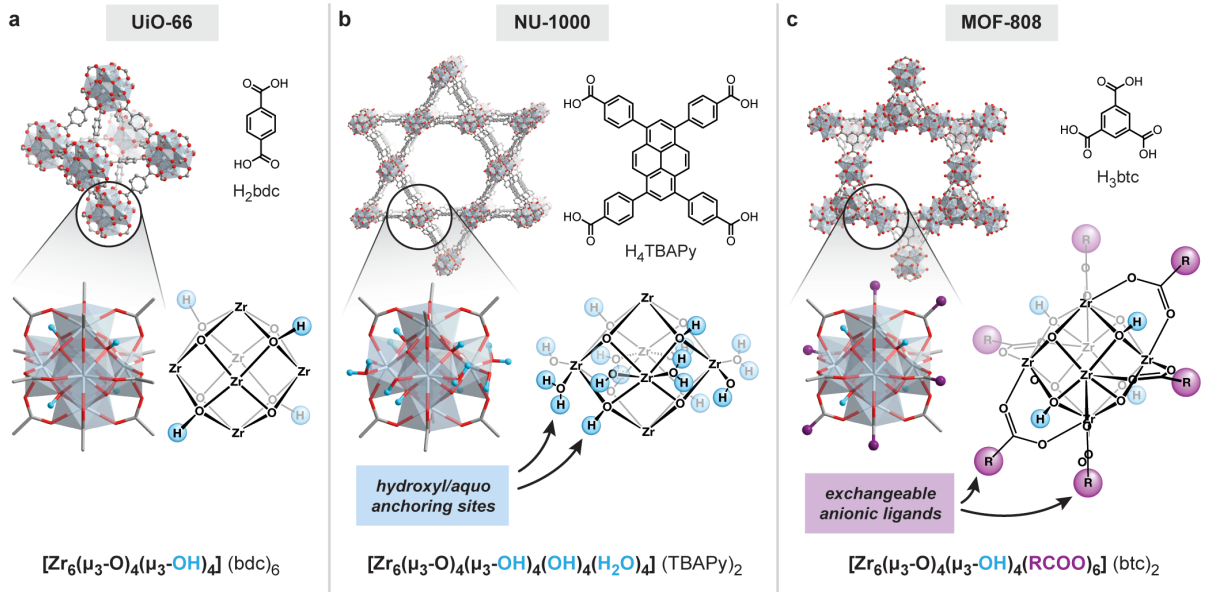

Fig. 1.5 | Overview of the hexanuclear Zr_6 nodes found in UiO-66, NU-1000, and MOF-808. Both the reactive Brønsted acidic hydroxyl/aquo groups, as well as the dangling anionic ligands attached to Lewis acidic Zr^{4+} sites, can be used as attachment points for grafting additional metals. For clarity, the bridging ligand struts are omitted in the Lewis structure depictions of the Zr_6 nodes. Figures redrawn from references 60, 61, and 62.

monoanionic ligands (e.g., a monocarboxylate $RCOO^-$, such as acetate or formate) to give the overall formula unit $Zr_6O_4(OH)_4(RCOO)_6(btc)_2$ (btc^{3-} = 1,3,5-benzenetricarboxylate) (**Fig. 1.5c**).

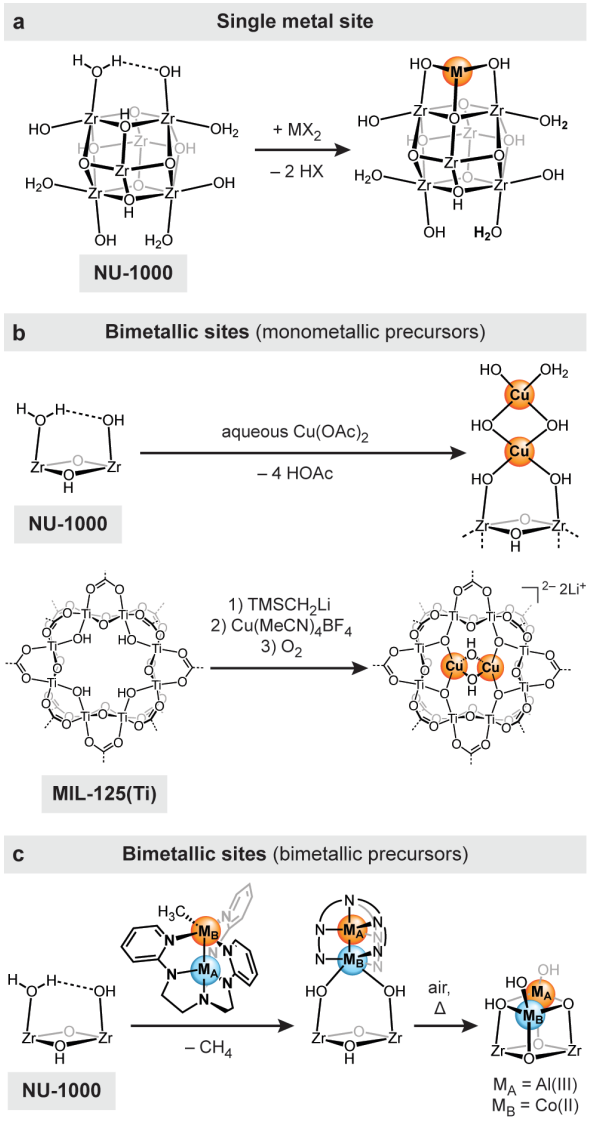

Fig. 1.6 | Grafting metal centers to the surface hydroxyl species in NU-1000 and MIL-125(Ti). In principle, this strategy can be used to install (a) monometallic sites, (b) bimetallic sites using mononuclear precursors, and (c) bimetallic sites using preformed binuclear complexes. Figures redrawn from references 61, 18, 69, and 70.

Farha, Hupp, and coworkers were among the first to recognize that these zirconium nodes could be used as grafting sites. In 2013, they reported the gas-phase metalation of NU-1000 with reactive organometallic complexes.[61] In a procedure analogous to atomic layer deposition (ALD), NU-1000 was exposed to volatile organometallic precursors such as $AlMe_3$ and $ZnEt_2$ in the gas-phase, which led to the deprotonation of the surface-bound hydroxyl/aquo ligands and subsequent metalation (**Fig. 1.6a**). The strategy, named atomic layer deposition in metal–organic frameworks (AIM), was later extended to other volatile organometallic precursors, including $InMe_3$ and metal bis(amidinate) complexes (M(II) = Ni, Co, Cu).[63–66] Conceptually similar approaches have also been developed for solution-phase metalation. For example, Lin and coworkers showed that the hydroxyl groups in UiO-68, the terphenyl-expanded analogue of UiO-66, can be deprotonated using *n*BuLi.[67] Subsequent salt metathesis with MX_2 salts (e.g.,

$CoCl_2$, $FeBr_2$) can be used to quantitatively achieve mononuclear transition metal active sites. Wang and coworkers extended this strategy to MOF-808.[21] They used $ZnEt_2$ to simultaneously deprotonate and metalate the four surface hydroxyl groups with Zn(II), creating Zn–Zr sites for CO_2 hydrogenation.[21]

A major challenge in extending this grafting approach from mononuclear sites to binuclear sites is controlling and characterizing active site nuclearity. As the metal loading increases, the speciation of active sites becomes more difficult to control and can even vary depending on the synthetic route. For example, Lercher and coworkers have studied methane oxidation in copper-metalated NU-1000 frameworks synthesized via gas-phase and solution-phase routes.[18,66] Gas-phase metalation routes led to higher Cu loadings (10 wt%),[66] whereas solution-phase metalation with copper(II) acetate generated lower Cu loadings (0.6–2.9 wt%).[18] Both samples were pretreated with O_2 at 200 °C, exposed to CH_4, and then purged with H_2O/He to desorb the products of methane oxidation. While both frameworks exhibited similar methanol yields (11.1 mmol CH_3OH per mol Cu and 9.7 mmol CH_3OH per mol Cu for the gas-phase and solution-phase metalated materials, respectively), the solution-phase material shows markedly higher selectivity for methanol over other products (70% selectivity vs. 40–60%). For the gas-phase metalated material, the authors attributed the reactivity to predominantly tricopper clusters on the basis of extended X-ray absorption fine structure (EXAFS) data and density functional theory (DFT) calculations.[66] On the other hand, for the solution-phase metalated samples, reactivity was attributed to dicopper sites (**Fig. 1.6b**).[18] However, as both materials likely contain a complex distribution of isolated copper cations in addition to dimeric and oligomeric species, more rigorous spectroscopic investigation is needed to confirm the identity of the active sites.

In principle, it is possible to limit the formation of higher nuclearity clusters by carefully designing the binding pocket. For example, the framework MIL-125(Ti) is formed from cyclic $Ti_8(\mu_2\text{-}O)_8(\mu_2\text{-}OH)_4$ clusters, and has an overall formula of $Ti_8O_8(OH)_4(bdc)_6$ (bdc^{2-} = 1,4-benzenedicarboxylate).[68] The octameric titanium cluster creates a small cavity lined by four bridging hydroxides, with opposing hydroxides slightly less than 6 Å apart (**Fig. 1.6b**). Due to these steric constraints, Lin and coworkers showed that deprotonation of the bridging hydroxides and metalation with excess $Cu(CH_3CN)_4BF_4$ leads to the installation of just two copper centers per Ti_8 cluster (**Fig. 1.6b**).[69] A short Cu–Cu distance of 2.80 Å was observed by EXAFS. Mononuclear control samples could be made by using a subcess of the copper precursor. The binuclear system exhibited substantially higher activity for the aerobic epoxidation of olefins, with a TOF of 175 h^{-1} compared to 10 h^{-1} for the mononuclear control.

Another promising approach to control active site nuclearity is to use pre-formed bimetallic precursors, a strategy that was pioneered by the Lu group (**Fig. 1.6c**).[70,71] This approach is particularly attractive for installing heterobimetallic sites. For example, cobalt-aluminum sites were installed in NU-1000 by treating it with a predefined molecular Co-Al complex, (py_3tren)-AlCoMe (py_3tren^{3-} = N,N,N-tris(2-(2pyridylamino)ethyl)amine). Further heating of the material at 300 ºC under air resulted in the loss of the py_3tren ligand and the generation of a Co-Al diamond core.[70] Both the ligated and the heat-treated materials were competent catalysts for the oxidation of benzyl alcohol to benzaldehyde in the presence of *tert*-butyl hydroperoxide (TBHP), showing 7.5-fold greater activity per Co atom relative to the monometallic control framework. Similarly, Ga-Rh–functionalized NU-1000 could be synthesized by soaking the framework in a solution of (py_3tren)GaRhX (X = Me, OPh).[71] Compared to molecular analogues and the Rh-only MOF, the

Ga/Rh-functionalized catalyst showed much higher selectivity for *E*-alkenes in the semi hydrogenation of diphenylacetylene.

1.2.2.2 Anchoring to Lewis acidic surface sites

In addition to Brønsted acidic hydroxyl sites, Lewis acidic surface sites can also be used as grafting points for post-synthetic metalation. For example, the nodes of MOF-808 contain monocarboxylates anchored to Lewis acidic Zr^{4+} metal centers (**Fig. 1.5**). These surface ligands can be exchanged with other anions, including ditopic ligands capable of binding additional metals.

Yaghi and coworkers leveraged the controlled stoichiometry of inward-facing capping ligands and the spatial constraints of the pores to install dicopper sites for the oxidation of methane to methanol (**Fig. 1.7**).[17] Metal-binding sites were introduced into MOF-808 by exchanging the monoanionic capping ligands with different imidazole-containing carboxylic acids (e.g., L-histidine, 4-imidazoleacrylic acid, and 5-benzimidazolecarboxylic acid). A series of oxygen-bridged dicopper(II) sites were then installed by metalation with copper(I) iodide under air. To probe the reactivity of these copper-functionalized frameworks with methane, the frameworks were activated at 150 °C with flowing He, then treated sequentially with 3% N_2O/He, CH_4, and 3% steam/He. After this treatment, roughly 12.5–25 mmol MeOH was generated per mol Cu, depending on the ligand used.[17] Given these yields, the speciation of copper is likely more complex than what is shown in **Fig. 1.7**, with a subpopulation of copper sites active for methane oxidation. While the authors use computational modeling to propose the active bridged copper dimers, additional spectroscopic evidence is needed to confirm the active site identity.

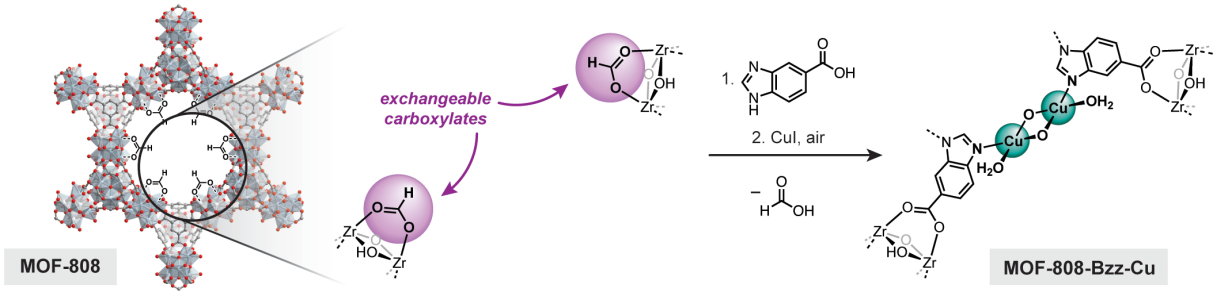

Fig. 1.7 | Grafting metal centers to Lewis-acidic surface sites in MOF-808. The exchange of anionic carboxylate ligands with imidazole-containing carboxylic acids is proposed to provide binding sites for copper(I) pairs. Figure redrawn from reference 17.

1.2.2.3 Ion pairing

Ion-exchange methods can be used to install bimetallic sites in cationic or anionic metal–organic frameworks containing weakly bound counterions. In an example of this strategy, Dincă, Román-Leshkov, and coworkers used post-synthetic anion exchange to electrostatically tether anionic $[Co(CO)_4]^-$ complexes to the cationic trinuclear chromium(III) nodes of Cr-MIL-101 (**Fig. 1.8**).[22] The strongly bound F^- anions in the as-synthesized framework were first exchanged for more labile Cl^- anions, which were then exchanged for $[Co(CO)_4]^-$. This leads to heterobimetallic active sites where anionic metal carbonyl complexes are held in proximity to strongly Lewis acidic Cr(III) centers. Like the homogeneous $[Lewis\ acid]^+[Co(CO)_4]^-$ catalysts developed by Coates and

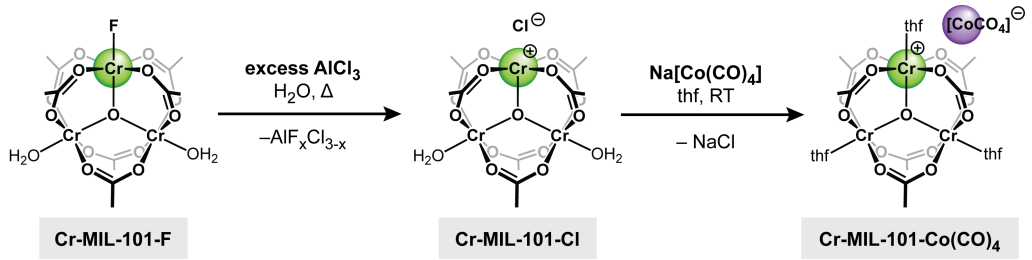

Fig. 1.8 | Overview of ion pairing strategy in Cr-MIL-101. Anchoring of $Co(CO)_4^-$ near the Lewis acidic Cr(III) sites is achieved through stepwise ion exchange to yield bimetallic Cr/Co sites for ring-expansion carbonylation of epoxides and β-Lactones. For clarity, ligands have been truncated at the terminal carboxylate unit. Figure redrawn from reference 22.

coworkers,[72,73] the $Co(CO)_4^-$-incorporated Cr-MIL-101 framework (abbreviated $Co(CO)_4 \subset$Cr-MIL-101) is a highly active catalyst for the ring-expansion carbonylation of epoxides[22] and β-Lactones.[23] We note that, relative to other tethering strategies, an advantage of the ion-pairing

approach is that it offers much greater flexibility in the relative M–M distance and coordination sphere. For example, in $Co(CO)_4$⊂Cr-MIL-101, the $Co(CO)_4^-$ complex is free to adjust its primary coordination sphere and the relative Co–Cr distance.

1.2.3 Grafting to ligand struts

In addition to grafting metal cations to the framework nodes, it is also possible to install metal chelating sites to the framework struts. One advantage of this approach is the diversity of ligand environments that can be obtained (**Fig. 1.9**). Binding sites can be pre-integrated into the ligand strut and installed during framework formation. Bipyridine,[74–76] salen,[77] porphyrin,[78–80] and di-pyrazole[81] groups have been incorporated using this route (**Fig. 1.9a**). Chelating sites can also be installed after MOF synthesis through post-synthetic ligand exchange or covalent modification strategies. Iminopyridine,[82] salicylidene,[83] aminopyridineimine,[84] and bis(2-pyridylmethyl)amine[85] groups, among others, have been introduced in this manner (**Fig. 1.9b**). These different strategies have been comprehensively summarized by Moon and coworkers in a recent review.[86]

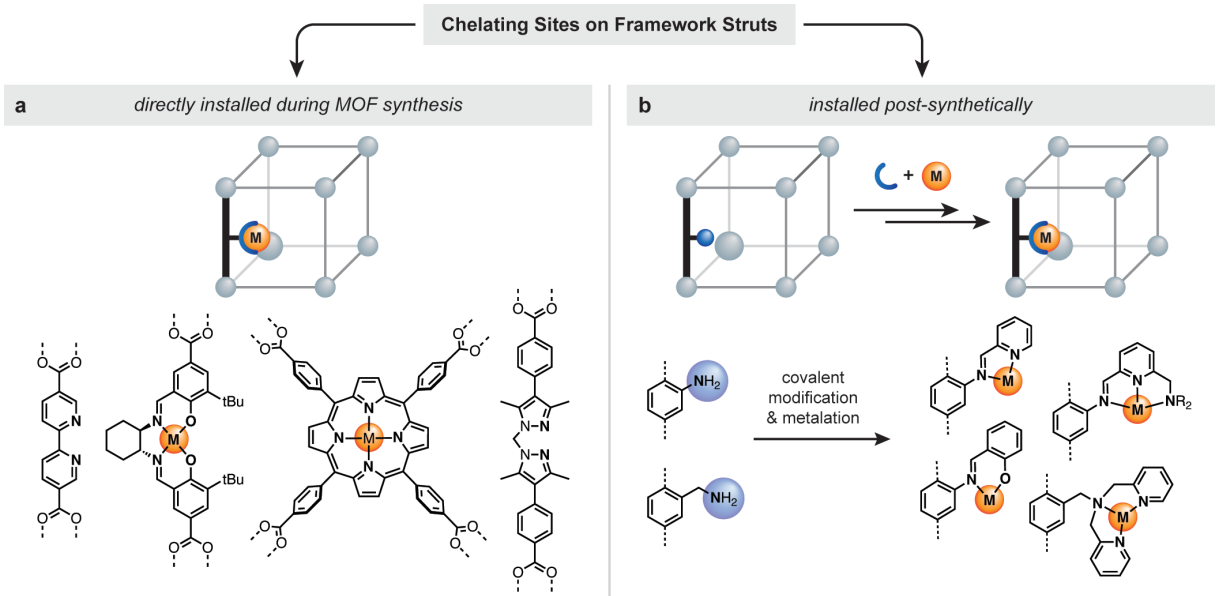

Fig. 1.9 | Overview of strategies to install metal-binding sites on ligand struts. Chelating sites can be installed either a) during synthesis, or b) after synthesis via post-synthetic modification strategies.

While the metalation of ligand struts was initially developed for mononuclear metal complexes, researchers have recently extended these methods to bimetallic active sites. As with grafting to the metal nodes, the dominant challenge is controlling active site nuclearity. At low surface coverages, mononuclear sites dominate, while at high coverages larger clusters can form. Several strategies to overcome this challenge have been reported, including the use of pre-formed clusters (Section 1.2.3.1) and exogenous bridging ligands to dimerize metals bound to neighboring struts (Section 1.2.3.2). In addition, templating approaches have been developed to selectively functionalize neighboring ligands (Section 1.2.3.3).

1.2.3.1 Anchoring pre-formed clusters

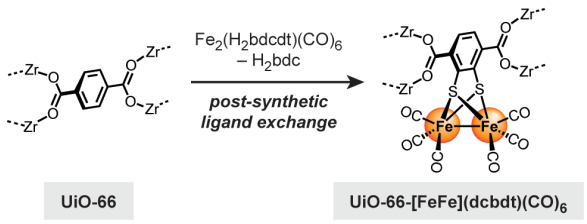

Fig. 1.10 | Overview of post-synthetic ligand exchange to install pre-formed dithiolate diiron clusters in UiO-66 for photocatalytic proton reduction. Figure redrawn from reference 19.

Using a post-synthetic ligand exchange strategy, Cohen, Ott, and coworkers were able to attach dithiolate-bound diiron clusters to the struts of UiO-66 (**Fig. 1.10**).[19] Up to 14% of the original 1,4-benzenedicarboxylate ligands could be exchanged for a diiron-functionalized strut, $[Fe_2(dcbdt)(CO)_6]^{2-}$ ($dcbdt^{2-}$ = 1,4-dicarboxylbenzene-2,3-dithiolate). One advantage of using pre-formed clusters is their structural fidelity. Extended X-ray absorption fine structure (EXAFS) spectroscopy confirmed that the local coordination environment around the iron centers in UiO-66-[FeFe](dcbdt)$(CO)_6$ is identical to molecular analogues, with a short Fe–Fe distance of ~2.4 Å. The MOF-supported diiron system, which closely resembles the active site of [FeFe] hydrogenases, catalyzes the photocatalytic reduction of protons into H_2 in the presence of $[Ru(bpy)_3]^{2+}$ as the photosensitizer and ascorbate as the electron donor. Relative to a molecular

analogue, the MOF-supported dimer showed both higher initial rates and greater overall production of H_2.

1.2.3.2 Anchoring to neighboring ligand struts

Metal–organic frameworks constructed from 1D metal–ligand chains (also called "rod-shaped" secondary building units) often display one-dimensional pore channels that are densely lined with bridging ligands.[87,88] In these frameworks, anchoring metals to neighboring struts is an appealing way to design bimetallic sites due to the short distance between adjacent ligands (~6–10 Å).

A nice example of this strategy was reported by Cui and coworkers in 2016, who synthesized a Cd-based framework with 1D channels lined with chiral vanadium-salen units (**Fig. 1.11a**).[89] The authors showed that the neighboring vanadyl sites, which are roughly 8 Å apart, work together to activate and pre-orient the substrates for the asymmetric cyanation of aldehydes. To confirm the bimetallic nature of the mechanism, an isostructural framework with alternating vanadium and copper sites was used, which showed both lower conversion (50% vs. 98%) and lower enantioselectivity (75% ee vs. 86% ee) than the all-vanadium framework.

In 2023, Lin and coworkers used this strategy to generate bimetallic sites in a bipyridyl-decorated aluminum framework, MOF-253 (also known as Al(OH)bpydc, $bpydc^{2-}$ = 2,2'-bipyridine-5,5'-dicarboxylate).[90] The framework, which is isostructural with

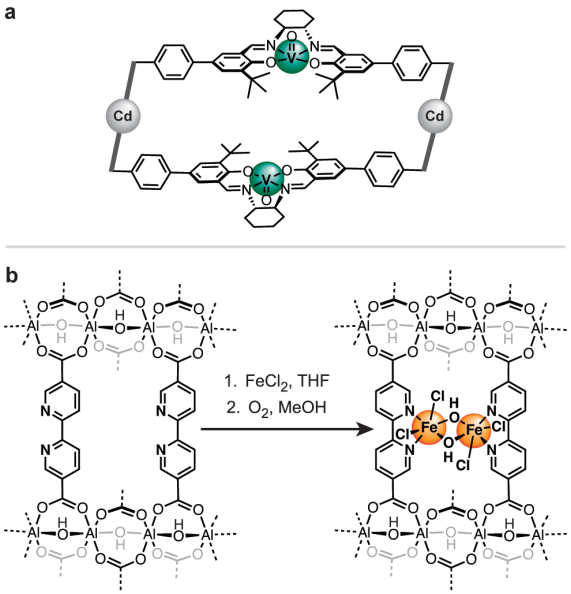

Fig. 1.11 | Neighboring ligand struts can be used to install (a) bimetallic vanadyl sites for asymmetric aldehyde cyanation and (b) Fe(III) dimers for benzylic C–H oxidation and alkene epoxidation. Figures redrawn from references 89 and 90.

MIL-53, contains rhombic, one-dimensional channels lined with 2,2'-bipyridine-functionalized struts spaced roughly 6.6 Å apart. Metalation of the bipyridine units with $FeCl_2$ followed by bubbling O_2 in MeOH resulted in the formation of dihydroxo-bridged Fe(III) dimers (**Fig. 1.11b**). The $Fe_2(\mu\text{-}OH)_2$ dimers were characterized by EXAFS, which showed a strong Fe–Fe scattering feature consistent with the expected ~3 Å distance between Fe sites. The diiron MOF was a competent catalyst for both benzylic C–H oxidation and alkene epoxidation reactions using O_2 as the oxidant and pivaldehyde as the sacrificial reductant. A mononuclear control framework was synthesized where only ~11% of the ligands are functionalized with bipyridine units. The bimetallic framework showed a 27-fold increase in activity compared to the mononuclear control, highlighting the impact of the bimetallic sites.

1.2.3.3 Templating approaches

As described in Section 1.2.3.2, neighboring ligand struts can support the formation of well-defined bimetallic sites with the addition of exogenous bridging ligands such as hydroxide (**Fig. 1.11**). However, this strategy is less effective at lower metal loadings, as it is difficult to control the relative distribution of partially metalated ligand struts. At low loadings, isolated mononuclear metal sites are predominantly formed. This can be limiting, as lower metal loadings may be desired to reduce pore clogging or prevent cross-reactivity between neighboring active sites.

To address this challenge, we recently reported a strategy to introduce closely spaced pairs of functional groups within MOF pores, irrespective of functional group loading.[91] We first showed that thermolabile tertiary ester-based cross-linkers can be used to template pairs of carboxylic acids ~7 Å apart down the pore channels of Mg_2dotpdc (dotpdc^{4-} = 4,4″-dioxido-[1,1′:4′,1″-terphenyl]-3,3″-dicarboxylate), a mesoporous framework with one-dimensional

hexagonal channels. We later developed tertiary carbamate-based cross-linkers that, upon thermolysis, reveal pairs of templated amines (**Fig. 1.12a**).[85] These amine pairs could be post-synthetically elaborated into iminopyridine and bis(2-pyridylmethyl)amine chelating sites (**Fig. 1.12b**) and metalated with a variety of first-row transition metals (M = Mn(II), Fe(II), Co(II), Ni(II), Cu(I), and Cu(II)).

Relative to the other synthetic approaches described here, templating strategies require much larger upfront synthetic investment, as a suitable labile cross-linker must first be designed and incorporated into the desired framework. However, once the templated functional groups are installed, there is the potential for rapid catalyst derivatization via well-established post-synthetic

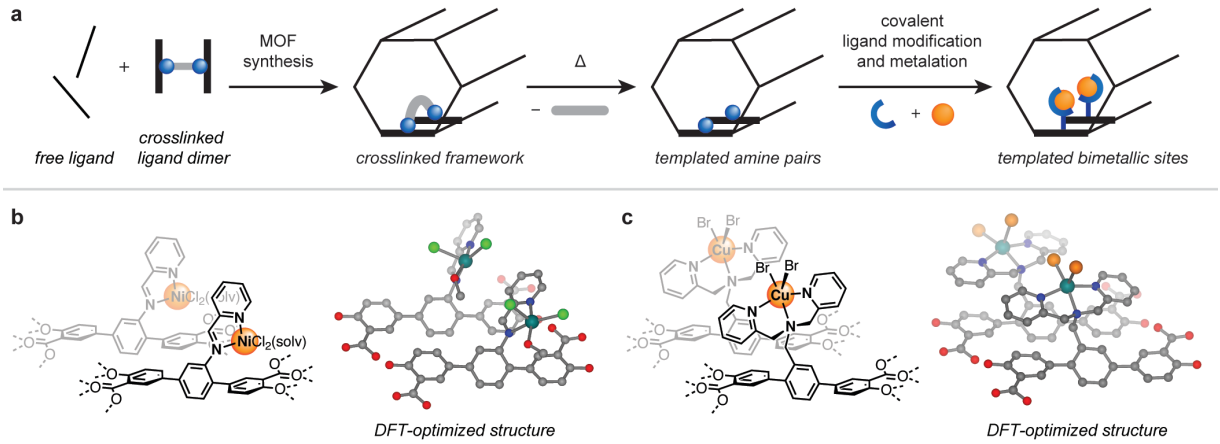

Fig. 1.12 | a) Thermolabile cross-linkers can be used to template amine pairs, which can be elaborated into bimetallic sites with tunable ligand environments, such as b) iminopyridine and c) bis(2-pyridylmethyl)amine. Figure adapted from reference 85.

modification reactions. Indeed, the main advantage of molecular templating is the structural versatility. In principle, it should be possible to independently control the pore architecture, metal identity, local ligand environment, and metal–metal distance of the templated bimetallic sites.

1.2.4 Other strategies

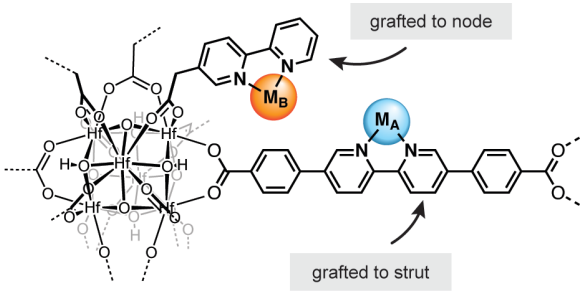

Fig. 1.13 | Multiple grafting strategies can be used in tandem. For example, Ru-based photosensitizers at the ligand struts can work cooperatively with Re or Mn cocatalysts post-synthetically grafted to the Hf cluster through carboxylate exchange. Figure redrawn from reference 92.

A combination of grafting approaches can also be used to generate bimetallic sites, such as attaching one metal to the framework nodes and the other to the struts. For example, Lin and coworkers took advantage of distinct metal node and ligand strut chemistry to functionalize hafnium-based metal–organic sheets with both Ru-based photosensitizers and Re or Mn-based cocatalysts (**Fig. 1.13**).[92] The Ru-based photosensitizer was bound to bipyridine-functionalized struts and installed directly during framework synthesis. The Re or Mn-based cocatalyst was post-synthetically grafted to the metal nodes by exchanging surface-bound trifluoroacetate groups with carboxylate-functionalized bipyridine ligands and metalating with either $Re(CO)_5Cl$ and $Mn(CO)_5Br$. Both Ru/Re and Ru/Mn systems showed good activity for the photoreduction of CO_2 to CO in the presence of sacrificial electron donors, with turnover numbers of up to 3849 and 1367 after 25 h, respectively. Greater than 70-fold increase in catalytic activity was observed in the MOF systems relative to homogeneous controls, which the authors attributed to the proximity of the Ru photosensitizer to the catalytic Re/Mn centers.

1.3 Critical assessment and future outlook

The synthesis of binuclear metal active sites in metal–organic frameworks has seen significant progress over the last decade. While barriers to controlling active site nuclearity remain, promising solutions are already emerging, including the use of pre-formed clusters,[19,58,70,71] sterically constrained binding pockets,[69] and templating approaches.[85,91] We conclude this

perspective by shifting our focus away from synthetic strategies and towards the future potential of these materials as heterogeneous catalysts. Below, we highlight unique opportunities for MOF-supported bimetallic catalysis as well as outstanding challenges.

Rigorous characterization of active site structure: The conclusive spectroscopic identification of binuclear sites remains an open challenge in MOF catalysis and is critical for advancing the field. In many of the examples highlighted in this perspective, a complex distribution of metal species is both observed spectroscopically as well as inferred by the relatively low yields of product per metal in stoichiometric reactions. While initial reports have placed greater emphasis on synthesis and reactivity, going forward more detailed spectroscopic investigations are needed to understand the initial metal speciation, identify which species are catalytically relevant, and determine how these structural distributions change over time.

Balancing active site rigidity vs. flexibility: In certain cases, active site rigidity is beneficial. Geometric constraints enforced by rigid protein superstructures and zeolite lattices can lead metal sites to adopt unusual coordination environments, generating highly reactive "entatic" states.[10,93] At the same time, greater active site flexibility can also be advantageous, as different intermediates may be stabilized by subtly different active site conformations. One advantage of metal–organic frameworks is the ability to accommodate structures at both extremes as well as the many gradations in between. For example, the rigid multinuclear metal nodes discussed in Section 1.2.1 greatly constrain the possible M–M distances and coordination environments that can be accessed during catalysis, while the electrostatically tethered ion pairs discussed in Section 1.2.2.3 offers much greater flexibility. Going forward, a challenge in catalyst design will be navigating the wealth of choices and selecting the appropriate balance of flexibility and rigidity for a given catalytic application.

Leveraging pore environment effects: Many of the reports highlighted in this perspective focus on tuning the primary coordination sphere of the two metal sites. In contrast, the interplay between the binuclear active site and its surrounding pore environment remains understudied. The enzyme-like ability of metal–organic frameworks to control and confine the surrounding three-dimensional microenvironment is a distinct yet underutilized advantage of MOF catalysts.[94–96] We note that this is a challenge and opportunity for all MOF catalysis, beyond the binuclear active sites focused on here.

Higher throughput catalyst synthesis and screening: Studies in this field generally report a single bimetallic active site design for a single target reaction. To accelerate catalyst discovery, greater throughput in catalyst synthesis and screening is needed. If the synthetic advances described in this perspective have uncovered a treasure chest of bimetallic MOF systems, then high throughput experimentation may be the key to unlock their untapped potential as catalysts.

Assessing active site stability: While significant strides in metal–organic framework stability have been made,[97,98] active sites can be degraded even if the surrounding pore structure remains intact. For example, in the absence of strongly chelating groups, surface-grafted systems may be susceptible to metal leaching. Initially well-defined systems may lose structural fidelity if metal cations become mobile under reaction conditions. In addition to identifying active site degradation mechanisms, strategies to mitigate degradation and regenerate spent catalysts are needed.

In conclusion, metal–organic frameworks provide an exciting opportunity to re-examine bio-inspired and organometallic binuclear active sites in a heterogeneous context. It is possible that greater catalytic activity, selectivity, and/or stability can be realized due to properties unique to porous scaffolds, including site isolation, entatic states, and microenvironment effects. Going

forward, coupling existing synthetic routes with greater throughput catalyst screening and more rigorous characterization may reveal new reactivity not yet observed in other heterogeneous or homogeneous platforms.

1.4 References

(1) Lubitz, W.; Ogata, H.; Rüdiger, O.; Reijerse, E. Hydrogenases. *Chem. Rev.* **2014**, *114* (8), 4081–4148. https://doi.org/10.1021/cr4005814.

(2) Elwell, C. E.; Gagnon, N. L.; Neisen, B. D.; Dhar, D.; Spaeth, A. D.; Yee, G. M.; Tolman, W. B. Copper–Oxygen Complexes Revisited: Structures, Spectroscopy, and Reactivity. *Chem. Rev.* **2017**, *117* (3), 2059–2107. https://doi.org/10.1021/acs.chemrev.6b00636.

(3) Jasniewski, A. J.; Que, L. Dioxygen Activation by Nonheme Diiron Enzymes: Diverse Dioxygen Adducts, High-Valent Intermediates, and Related Model Complexes. *Chem. Rev.* **2018**, *118* (5), 2554–2592. https://doi.org/10.1021/acs.chemrev.7b00457.

(4) Snyder, B. E. R.; Bols, M. L.; Schoonheydt, R. A.; Sels, B. F.; Solomon, E. I. Iron and Copper Active Sites in Zeolites and Their Correlation to Metalloenzymes. *Chem. Rev.* **2018**, *118* (5), 2718–2768. https://doi.org/10.1021/acs.chemrev.7b00344.

(5) Wilcox, D. E. Binuclear Metallohydrolases. *Chem. Rev.* **1996**, *96* (7), 2435–2458. https://doi.org/10.1021/cr950043b.

(6) Mitić, N.; Smith, S. J.; Neves, A.; Guddat, L. W.; Gahan, L. R.; Schenk, G. The Catalytic Mechanisms of Binuclear Metallohydrolases. *Chem. Rev.* **2006**, *106* (8), 3338–3363. https://doi.org/10.1021/cr050318f.

(7) Delferro, M.; Marks, T. J. Multinuclear Olefin Polymerization Catalysts. *Chem. Rev.* **2011**, *111* (3), 2450–2485. https://doi.org/10.1021/cr1003634.

(8) Cooper, B. G.; Napoline, J. W.; Thomas, C. M. Catalytic Applications of Early/Late Heterobimetallic Complexes. *Catalysis Reviews* **2012**, *54* (1), 1–40. https://doi.org/10.1080/01614940.2012.619931.

(9) Cammarota, R. C.; Clouston, L. J.; Lu, C. C. Leveraging Molecular Metal–Support Interactions for H2 and N2 Activation. *Coordination Chemistry Reviews* **2017**, *334*, 100–111. https://doi.org/10.1016/j.ccr.2016.06.014.

(10) Rhoda, H. M.; Heyer, A. J.; Snyder, B. E. R.; Plessers, D.; Bols, M. L.; Schoonheydt, R. A.; Sels, B. F.; Solomon, E. I. Second-Sphere Lattice Effects in Copper and Iron Zeolite Catalysis. *Chem. Rev.* **2022**, *122* (14), 12207–12243. https://doi.org/10.1021/acs.chemrev.1c00915.

(11) Li, X.; Liu, L.; Ren, X.; Gao, J.; Huang, Y.; Liu, B. Microenvironment Modulation of Single-Atom Catalysts and Their Roles in Electrochemical Energy Conversion. *Sci. Adv.* **2020**, *6* (39), eabb6833. https://doi.org/10.1126/sciadv.abb6833.

(12) Liu, J.; Goetjen, T. A.; Wang, Q.; Knapp, J. G.; Wasson, M. C.; Yang, Y.; Syed, Z. H.; Delferro, M.; Notestein, J. M.; Farha, O. K.; Hupp, J. T. MOF-Enabled Confinement and Related Effects for Chemical Catalyst Presentation and Utilization. *Chem. Soc. Rev.* **2022**, *51* (3), 1045–1097. https://doi.org/10.1039/D1CS00968K.

(13) Liu, L.; Corma, A. Bimetallic Sites for Catalysis: From Binuclear Metal Sites to Bimetallic Nanoclusters and Nanoparticles. *Chem. Rev.* **2023**, *123* (8), 4855–4933. https://doi.org/10.1021/acs.chemrev.2c00733.

(14) Kulkarni, A.; Lobo-Lapidus, R. J.; Gates, B. C. Metal Clusters on Supports: Synthesis, Structure, Reactivity, and Catalytic Properties. *Chem. Commun.* **2010**, *46* (33), 5997. https://doi.org/10.1039/c002707n.
(15) Wang, J.; Li, G.; Li, Z.; Tang, C.; Feng, Z.; An, H.; Liu, H.; Liu, T.; Li, C. A Highly Selective and Stable ZnO-ZrO2 Solid Solution Catalyst for CO2 Hydrogenation to Methanol. *Science Advances* **2017**, *3* (10), e1701290. https://doi.org/10.1126/sciadv.1701290.
(16) Osadchii, D. Y.; Olivos-Suarez, A. I.; Szécsényi, Á.; Li, G.; Nasalevich, M. A.; Dugulan, I. A.; Crespo, P. S.; Hensen, E. J. M.; Veber, S. L.; Fedin, M. V.; Sankar, G.; Pidko, E. A.; Gascon, J. Isolated Fe Sites in Metal Organic Frameworks Catalyze the Direct Conversion of Methane to Methanol. *ACS Catalysis* **2018**, *8* (6), 5542–5548. https://doi.org/10.1021/ACSCATAL.8B00505.
(17) Baek, J.; Rungtaweevoranit, B.; Pei, X.; Park, M.; Fakra, S. C.; Liu, Y.-S.; Matheu, R.; Alshmimri, S. A.; Alshehri, S.; Trickett, C. A.; Somorjai, G. A.; Yaghi, O. M. Bioinspired Metal–Organic Framework Catalysts for Selective Methane Oxidation to Methanol. *J. Am. Chem. Soc.* **2018**, *140* (51), 18208–18216. 25.
(18) Zheng, J.; Ye, J.; Ortuño, M. A.; Fulton, J. L.; Gutiérrez, O. Y.; Camaioni, D. M.; Motkuri, R. K.; Li, Z.; Webber, T. E.; Mehdi, B. L.; Browning, N. D.; Penn, R. L.; Farha, O. K.; Hupp, J. T.; Truhlar, D. G.; Cramer, C. J.; Lercher, J. A. Selective Methane Oxidation to Methanol on Cu-Oxo Dimers Stabilized by Zirconia Nodes of an NU-1000 Metal–Organic Framework. *J. Am. Chem. Soc.* **2019**, *141* (23), 9292–9304. https://doi.org/10.1021/jacs.9b02902.
(19) Pullen, S.; Fei, H.; Orthaber, A.; Cohen, S. M.; Ott, S. Enhanced Photochemical Hydrogen Production by a Molecular Diiron Catalyst Incorporated into a Metal–Organic Framework. *J. Am. Chem. Soc.* **2013**, *135* (45), 16997–17003. https://doi.org/10.1021/ja407176p.
(20) Castner, A. T.; Johnson, B. A.; Cohen, S. M.; Ott, S. Mimicking the Electron Transport Chain and Active Site of [FeFe] Hydrogenases in One Metal–Organic Framework: Factors That Influence Charge Transport. *J. Am. Chem. Soc.* **2021**, *143* (21), 7991–7999. https://doi.org/10.1021/jacs.1c01361.
(21) Zhang, J.; An, B.; Li, Z.; Cao, Y.; Dai, Y.; Wang, W.; Zeng, L.; Lin, W.; Wang, C. Neighboring Zn–Zr Sites in a Metal–Organic Framework for CO_2 Hydrogenation. *J. Am. Chem. Soc.* **2021**, *143* (23), 8829–8837. https://doi.org/10.1021/jacs.1c03283.
(22) Park, H. D.; Dincă, M.; Román-Leshkov, Y. Heterogeneous Epoxide Carbonylation by Cooperative Ion-Pair Catalysis in $Co(CO)_4^-$-Incorporated Cr-MIL-101. *ACS Cent. Sci.* **2017**, *3* (5), 444–448. https://doi.org/10.1021/acscentsci.7b00075.
(23) Park, H. D.; Dincă, M.; Román-Leshkov, Y. Continuous-Flow Production of Succinic Anhydrides via Catalytic β-Lactone Carbonylation by $Co(CO)_4 \subset$Cr-MIL-101. *J. Am. Chem. Soc.* **2018**, *140* (34), 10669–10672. https://doi.org/10.1021/jacs.8b05948.
(24) Gascon, J.; Corma, A.; Kapteijn, F.; Llabrés i Xamena, F. X. Metal Organic Framework Catalysis: *Quo Vadis* ? *ACS Catal.* **2014**, *4* (2), 361–378. https://doi.org/10.1021/cs400959k.
(25) Song, Y.; Feng, X.; Lin, W. Metal-Organic Frameworks for Catalytic Applications. In *Comprehensive Coordination Chemistry III*; Elsevier, 2021; pp 228–259. https://doi.org/10.1016/B978-0-08-102688-5.00025-8.
(26) Zheng, W.; Lee, L. Y. S. Metal–Organic Frameworks for Electrocatalysis: Catalyst or Precatalyst? *ACS Energy Lett.* **2021**, *6* (8), 2838–2843. https://doi.org/10.1021/acsenergylett.1c01350.
(27) Al-Rowaili, F. N.; Jamal, A.; Ba Shammakh, M. S.; Rana, A. A Review on Recent Advances for Electrochemical Reduction of Carbon Dioxide to Methanol Using Metal–Organic

Framework (MOF) and Non-MOF Catalysts: Challenges and Future Prospects. *ACS Sustainable Chem. Eng.* **2018**, *6* (12), 15895–15914. https://doi.org/10.1021/acssuschemeng.8b03843.
(28) Li, C.; Zhang, H.; Liu, M.; Lang, F.-F.; Pang, J.; Bu, X.-H. Recent Progress in Metal–Organic Frameworks (MOFs) for Electrocatalysis. *Ind. Chem. Mater.* **2023**, *1* (1), 9–38. https://doi.org/10.1039/D2IM00063F.
(29) Zhang, T.; Lin, W. Metal–Organic Frameworks for Artificial Photosynthesis and Photocatalysis. *Chem. Soc. Rev.* **2014**, *43* (16), 5982–5993. https://doi.org/10.1039/C4CS00103F.
(30) Wang, J.-L.; Wang, C.; Lin, W. Metal–Organic Frameworks for Light Harvesting and Photocatalysis. *ACS Catal.* **2012**, *2* (12), 2630–2640. https://doi.org/10.1021/cs3005874.
(31) Whelan, É.; Steuber, F. W.; Gunnlaugsson, T.; Schmitt, W. Tuning Photoactive Metal–Organic Frameworks for Luminescence and Photocatalytic Applications. *Coordination Chemistry Reviews* **2021**, *437*, 213757. https://doi.org/10.1016/j.ccr.2020.213757.
(32) Liu, M.; Xing, Z.; Li, Z.; Zhou, W. Recent Advances in Core–Shell Metal Organic Frame-Based Photocatalysts for Solar Energy Conversion. *Coordination Chemistry Reviews* **2021**, *446*, 214123. https://doi.org/10.1016/j.ccr.2021.214123.
(33) Dai, S.; Tissot, A.; Serre, C. Recent Progresses in Metal–Organic Frameworks Based Core–Shell Composites. *Advanced Energy Materials* **2022**, *12* (4), 2100061. https://doi.org/10.1002/aenm.202100061.
(34) Hong, D. H.; Shim, H. S.; Ha, J.; Moon, H. R. MOF-on-MOF Architectures: Applications in Separation, Catalysis, and Sensing. *Bulletin of the Korean Chemical Society* **2021**, *42* (7), 956–969. https://doi.org/10.1002/bkcs.12335.
(35) Zhao, Z.; Ding, J.; Zhu, R.; Pang, H. The Synthesis and Electrochemical Applications of Core–Shell MOFs and Their Derivatives. *J. Mater. Chem. A* **2019**, *7* (26), 15519–15540. https://doi.org/10.1039/C9TA03833G.
(36) Chen, L.; Wang, H.-F.; Li, C.; Xu, Q. Bimetallic Metal–Organic Frameworks and Their Derivatives. *Chem. Sci.* **2020**, *11* (21), 5369–5403. https://doi.org/10.1039/D0SC01432J.
(37) Konnerth, H.; Matsagar, B. M.; Chen, S. S.; Prechtl, M. H. G.; Shieh, F.-K.; Wu, K. C.-W. Metal-Organic Framework (MOF)-Derived Catalysts for Fine Chemical Production. *Coordination Chemistry Reviews* **2020**, *416*, 213319. https://doi.org/10.1016/j.ccr.2020.213319.
(38) Hao, M.; Qiu, M.; Yang, H.; Hu, B.; Wang, X. Recent Advances on Preparation and Environmental Applications of MOF-Derived Carbons in Catalysis. *Science of The Total Environment* **2021**, *760*, 143333. https://doi.org/10.1016/j.scitotenv.2020.143333.
(39) Liu, D.; Gu, W.; Zhou, L.; Wang, L.; Zhang, J.; Liu, Y.; Lei, J. Recent Advances in MOF-Derived Carbon-Based Nanomaterials for Environmental Applications in Adsorption and Catalytic Degradation. *Chemical Engineering Journal* **2022**, *427*, 131503. https://doi.org/10.1016/j.cej.2021.131503.
(40) Mukoyoshi, M.; Kitagawa, H. Nanoparticle/Metal–Organic Framework Hybrid Catalysts: Elucidating the Role of the MOF. *Chemical Communications* **2022**, *58* (77), 10757–10767. https://doi.org/10.1039/D2CC03233C.
(41) Xiang, W.; Zhang, Y.; Lin, H.; Liu, C. Nanoparticle/Metal–Organic Framework Composites for Catalytic Applications: Current Status and Perspective. *Molecules* **2017**, *22* (12), 2103. https://doi.org/10.3390/molecules22122103.

(42) McDonald, T. M.; Mason, J. A.; Kong, X.; Bloch, E. D.; Gygi, D.; Dani, A.; Crocellà, V.; Giordanino, F.; Odoh, S. O.; Drisdell, W. S.; Vlaisavljevich, B.; Dzubak, A. L.; Poloni, R.; Schnell, S. K.; Planas, N.; Lee, K.; Pascal, T.; Wan, L. F.; Prendergast, D.; Neaton, J. B.; Smit, B.; Kortright, J. B.; Gagliardi, L.; Bordiga, S.; Reimer, J. A.; Long, J. R. Cooperative Insertion of CO2 in Diamine-Appended Metal-Organic Frameworks. *Nature* **2015**, *519* (7543), 303–308. https://doi.org/10.1038/nature14327.

(43) Reed, D. A.; Keitz, B. K.; Oktawiec, J.; Mason, J. A.; Runčevski, T.; Xiao, D. J.; Darago, L. E.; Crocellà, V.; Bordiga, S.; Long, J. R. A Spin Transition Mechanism for Cooperative Adsorption in Metal–Organic Frameworks. *Nature* **2017**, *550* (7674), 96–100. https://doi.org/10.1038/nature23674.

(44) Bien, C. E.; Chen, K. K.; Chien, S.-C.; Reiner, B. R.; Lin, L.-C.; Wade, C. R.; Ho, W. S. W. Bioinspired Metal–Organic Framework for Trace CO2 Capture. *J. Am. Chem. Soc.* **2018**, *140* (40), 12662–12666. https://doi.org/10.1021/jacs.8b06109.

(45) Wang, C.-H.; Das, A.; Gao, W.-Y.; Powers, D. C. Probing Substrate Diffusion in Interstitial MOF Chemistry with Kinetic Isotope Effects. *Angew. Chem. Int. Ed.* **2018**, *57* (14), 3676–3681. https://doi.org/10.1002/anie.201713244.

(46) Wang, C.-H.; Gao, W.-Y.; Powers, D. C. Measuring and Modulating Substrate Confinement during Nitrogen-Atom Transfer in a Ru_2 -Based Metal-Organic Framework. *J. Am. Chem. Soc.* **2019**, *141* (49), 19203–19207. https://doi.org/10.1021/jacs.9b09620.

(47) Liu, Q.; Song, Y.; Ma, Y.; Zhou, Y.; Cong, H.; Wang, C.; Wu, J.; Hu, G.; O'Keeffe, M.; Deng, H. Mesoporous Cages in Chemically Robust MOFs Created by a Large Number of Vertices with Reduced Connectivity. *J. Am. Chem. Soc.* **2019**, *141* (1), 488–496. https://doi.org/10.1021/jacs.8b11230.

(48) Li, M.; Chen, J.; Wu, W.; Fang, Y.; Dong, S. Oxidase-like MOF-818 Nanozyme with High Specificity for Catalysis of Catechol Oxidation. *J. Am. Chem. Soc.* **2020**, *142* (36), 15569–15574. https://doi.org/10.1021/jacs.0c07273.

(49) Hall, J. N.; Bollini, P. Low-Temperature, Ambient Pressure Oxidation of Methane to Methanol Over Every Tri-Iron Node in a Metal–Organic Framework Material. *Chemistry – A European Journal* **2020**, *26* (70), 16639–16643. https://doi.org/10.1002/chem.202003894.

(50) Simons, M. C.; Prinslow, S. D.; Babucci, M.; Hoffman, A. S.; Hong, J.; Vitillo, J. G.; Bare, S. R.; Gates, B. C.; Lu, C. C.; Gagliardi, L.; Bhan, A. Beyond Radical Rebound: Methane Oxidation to Methanol Catalyzed by Iron Species in Metal–Organic Framework Nodes. *J. Am. Chem. Soc.* **2021**, *143* (31), 12165–12174. https://doi.org/10.1021/jacs.1c04766.

(51) Dincă, M.; Dailly, A.; Liu, Y.; Brown, C. M.; Neumann, Dan. A.; Long, J. R. Hydrogen Storage in a Microporous Metal−Organic Framework with Exposed Mn^{2+} Coordination Sites. *J. Am. Chem. Soc.* **2006**, *128* (51), 16876–16883. https://doi.org/10.1021/ja0656853.

(52) He, X.; Iliescu, A.; Yang, T.; Arguilla, M. Q.; Chen, T.; Kulik, H. J.; Dincă, M. Reversible O–O Bond Scission and O_2 Evolution at MOF-Supported Tetramanganese Clusters. *J. Am. Chem. Soc.* **2023**, *145* (30), 16872–16878. https://doi.org/10.1021/jacs.3c05374.

(53) Cai, Z.; Tao, W.; Moore, C. E.; Zhang, S.; Wade, C. R. Direct NO Reduction by a Biomimetic Iron(II) Pyrazolate MOF. *Angew Chem Int Ed* **2021**, *60* (39), 21221–21225. https://doi.org/10.1002/anie.202108095.

(54) Serre, C.; Millange, F.; Thouvenot, C.; Noguès, M.; Marsolier, G.; Louër, D.; Férey, G. Very Large Breathing Effect in the First Nanoporous Chromium(III)-Based Solids: MIL-53 or CrIII(OH)·{O2C−C6H4−CO2}·{HO2C−C6H4−CO2H}x·H2Oy. *J. Am. Chem. Soc.* **2002**, *124* (45), 13519–13526. https://doi.org/10.1021/ja0276974.

(55) Barthelet, K.; Marrot, J.; Riou, D.; Férey, G. A Breathing Hybrid Organic–Inorganic Solid with Very Large Pores and High Magnetic Characteristics. *Angewandte Chemie International Edition* **2002**, *41* (2), 281–284. https://doi.org/10.1002/1521-3773(20020118)41:2<281::AID-ANIE281>3.0.CO;2-Y.
(56) Loiseau, T.; Serre, C.; Huguenard, C.; Fink, G.; Taulelle, F.; Henry, M.; Bataille, T.; Férey, G. A Rationale for the Large Breathing of the Porous Aluminum Terephthalate (MIL-53) Upon Hydration. *Chemistry – A European Journal* **2004**, *10* (6), 1373–1382. https://doi.org/10.1002/chem.200305413.
(57) Whitfield, T. R.; Wang, X.; Liu, L.; Jacobson, A. J. Metal-Organic Frameworks Based on Iron Oxide Octahedral Chains Connected by Benzenedicarboxylate Dianions. *Solid State Sciences* **2005**, *7* (9), 1096–1103. https://doi.org/10.1016/j.solidstatesciences.2005.03.007.
(58) López-García, C.; Canossa, S.; Hadermann, J.; Gorni, G.; Oropeza, F. E.; de la Peña O'Shea, V. A.; Iglesias, M.; Angeles Monge, M.; Gutiérrez-Puebla, E.; Gándara, F. Heterometallic Molecular Complexes Act as Messenger Building Units to Encode Desired Metal-Atom Combinations to Multivariate Metal–Organic Frameworks. *J. Am. Chem. Soc.* **2022**. https://doi.org/10.1021/jacs.2c06142.
(59) Yang, D.; Babucci, M.; Casey, W. H.; Gates, B. C. The Surface Chemistry of Metal Oxide Clusters: From Metal–Organic Frameworks to Minerals. *ACS Cent. Sci.* **2020**, *6* (9), 1523–1533. https://doi.org/10.1021/acscentsci.0c00803.
(60) Cavka, J. H.; Jakobsen, S.; Olsbye, U.; Guillou, N.; Lamberti, C.; Bordiga, S.; Lillerud, K. P. A New Zirconium Inorganic Building Brick Forming Metal Organic Frameworks with Exceptional Stability. *J. Am. Chem. Soc.* **2008**, *130* (42), 13850–13851. https://doi.org/10.1021/ja8057953.
(61) Mondloch, J. E.; Bury, W.; Fairen-Jimenez, D.; Kwon, S.; DeMarco, E. J.; Weston, M. H.; Sarjeant, A. A.; Nguyen, S. T.; Stair, P. C.; Snurr, R. Q.; Farha, O. K.; Hupp, J. T. Vapor-Phase Metalation by Atomic Layer Deposition in a Metal–Organic Framework. *J. Am. Chem. Soc.* **2013**, *135* (28), 10294–10297. https://doi.org/10.1021/ja4050828.
(62) Furukawa, H.; Gándara, F.; Zhang, Y.-B.; Jiang, J.; Queen, W. L.; Hudson, M. R.; Yaghi, O. M. Water Adsorption in Porous Metal–Organic Frameworks and Related Materials. *J. Am. Chem. Soc.* **2014**, *136* (11), 4369–4381. https://doi.org/10.1021/ja500330a.
(63) Kim, I. S.; Borycz, J.; Platero-Prats, A. E.; Tussupbayev, S.; Wang, T. C.; Farha, O. K.; Hupp, J. T.; Gagliardi, L.; Chapman, K. W.; Cramer, C. J.; Martinson, A. B. F. Targeted Single-Site MOF Node Modification: Trivalent Metal Loading via Atomic Layer Deposition. *Chem. Mater.* **2015**, *27* (13), 4772–4778. https://doi.org/10.1021/acs.chemmater.5b01560.
(64) Kung, C.-W.; Mondloch, J. E.; Wang, T. C.; Bury, W.; Hoffeditz, W.; Klahr, B. M.; Klet, R. C.; Pellin, M. J.; Farha, O. K.; Hupp, J. T. Metal–Organic Framework Thin Films as Platforms for Atomic Layer Deposition of Cobalt Ions To Enable Electrocatalytic Water Oxidation. *ACS Appl. Mater. Interfaces* **2015**, *7* (51), 28223–28230. https://doi.org/10.1021/acsami.5b06901.
(65) Li, Z.; Schweitzer, N. M.; League, A. B.; Bernales, V.; Peters, A. W.; Getsoian, A. "Bean"; Wang, T. C.; Miller, J. T.; Vjunov, A.; Fulton, J. L.; Lercher, J. A.; Cramer, C. J.; Gagliardi, L.; Hupp, J. T.; Farha, O. K. Sintering-Resistant Single-Site Nickel Catalyst Supported by Metal–Organic Framework. *J. Am. Chem. Soc.* **2016**, *138* (6), 1977–1982. https://doi.org/10.1021/jacs.5b12515.
(66) Ikuno, T.; Zheng, J.; Vjunov, A.; Sanchez-Sanchez, M.; Ortuño, M. A.; Pahls, D. R.; Fulton, J. L.; Camaioni, D. M.; Li, Z.; Ray, D.; Mehdi, B. L.; Browning, N. D.; Farha, O. K.; Hupp,

J. T.; Cramer, C. J.; Gagliardi, L.; Lercher, J. A. Methane Oxidation to Methanol Catalyzed by Cu-Oxo Clusters Stabilized in NU-1000 Metal–Organic Framework. *J. Am. Chem. Soc.* **2017**, *139* (30), 10294–10301. https://doi.org/10.1021/jacs.7b02936.

(67) Manna, K.; Ji, P.; Lin, Z.; Greene, F. X.; Urban, A.; Thacker, N. C.; Lin, W. Chemoselective Single-Site Earth-Abundant Metal Catalysts at Metal–Organic Framework Nodes. *Nat Commun* **2016**, *7* (1), 12610. https://doi.org/10.1038/ncomms12610.

(68) Dan-Hardi, M.; Serre, C.; Frot, T.; Rozes, L.; Maurin, G.; Sanchez, C.; Férey, G. A New Photoactive Crystalline Highly Porous Titanium(IV) Dicarboxylate. *J. Am. Chem. Soc.* **2009**, *131* (31), 10857–10859. https://doi.org/10.1021/ja903726m.

(69) Feng, X.; Song, Y.; Chen, J. S.; Xu, Z.; Dunn, S. J.; Lin, W. Rational Construction of an Artificial Binuclear Copper Monooxygenase in a Metal–Organic Framework. *J. Am. Chem. Soc.* **2021**, *143* (2), 1107–1118. https://doi.org/10.1021/jacs.0c11920.

(70) Thompson, A. B.; Pahls, D. R.; Bernales, V.; Gallington, L. C.; Malonzo, C. D.; Webber, T.; Tereniak, S. J.; Wang, T. C.; Desai, S. P.; Li, Z.; Kim, I. S.; Gagliardi, L.; Penn, R. L.; Chapman, K. W.; Stein, A.; Farha, O. K.; Hupp, J. T.; Martinson, A. B. F.; Lu, C. C. Installing Heterobimetallic Cobalt–Aluminum Single Sites on a Metal Organic Framework Support. *Chem. Mater.* **2016**, *28* (18), 6753–6762. https://doi.org/10.1021/acs.chemmater.6b03244.

(71) Desai, S. P.; Ye, J.; Zheng, J.; Ferrandon, M. S.; Webber, T. E.; Platero-Prats, A. E.; Duan, J.; Garcia-Holley, P.; Camaioni, D. M.; Chapman, K. W.; Delferro, M.; Farha, O. K.; Fulton, J. L.; Gagliardi, L.; Lercher, J. A.; Penn, R. L.; Stein, A.; Lu, C. C. Well-Defined Rhodium–Gallium Catalytic Sites in a Metal–Organic Framework: Promoter-Controlled Selectivity in Alkyne Semihydrogenation to *E* -Alkenes. *J. Am. Chem. Soc.* **2018**, *140* (45), 15309–15318. https://doi.org/10.1021/jacs.8b08550.

(72) Getzler, Y. D. Y. L.; Mahadevan, V.; Lobkovsky, E. B.; Coates, G. W. Synthesis of β-Lactones: A Highly Active and Selective Catalyst for Epoxide Carbonylation. *J. Am. Chem. Soc.* **2002**, *124* (7), 1174–1175. https://doi.org/10.1021/ja017434u.

(73) Mahadevan, V.; Getzler, Y. D. Y. L.; Coates, G. W. [Lewis Acid]+[Co(CO)4] Complexes: A Versatile Class of Catalysts for Carbonylative Ring Expansion of Epoxides and Aziridines. *Angew. Chem. Int. Ed.* **2002**, *41* (15), 2781–2784. https://doi.org/10.1002/1521-3773(20020802)41:15<2781::AID-ANIE2781>3.0.CO;2-S.

(74) Bloch, E. D.; Britt, D.; Lee, C.; Doonan, C. J.; Uribe-Romo, F. J.; Furukawa, H.; Long, J. R.; Yaghi, O. M. Metal Insertion in a Microporous Metal−Organic Framework Lined with 2,2′-Bipyridine. *J. Am. Chem. Soc.* **2010**, *132* (41), 14382–14384. https://doi.org/10.1021/ja106935d.

(75) Wang, C.; Xie, Z.; deKrafft, K. E.; Lin, W. Doping Metal–Organic Frameworks for Water Oxidation, Carbon Dioxide Reduction, and Organic Photocatalysis. *J. Am. Chem. Soc.* **2011**, *133* (34), 13445–13454. https://doi.org/10.1021/ja203564w.

(76) Gonzalez, M. I.; Bloch, E. D.; Mason, J. A.; Teat, S. J.; Long, J. R. Single-Crystal-to-Single-Crystal Metalation of a Metal–Organic Framework: A Route toward Structurally Well-Defined Catalysts. *Inorg. Chem.* **2015**, *54* (6), 2995–3005. https://doi.org/10.1021/acs.inorgchem.5b00096.

(77) Song, F.; Wang, C.; Falkowski, J. M.; Ma, L.; Lin, W. Isoreticular Chiral Metal−Organic Frameworks for Asymmetric Alkene Epoxidation: Tuning Catalytic Activity by Controlling Framework Catenation and Varying Open Channel Sizes. *J. Am. Chem. Soc.* **2010**, *132* (43), 15390–15398. https://doi.org/10.1021/ja1069773.

(78) Feng, D.; Gu, Z.; Li, J.; Jiang, H.; Wei, Z.; Zhou, H. Zirconium-Metalloporphyrin PCN-222: Mesoporous Metal–Organic Frameworks with Ultrahigh Stability as Biomimetic Catalysts. *Angew Chem Int Ed* **2012**, *51* (41), 10307–10310. https://doi.org/10.1002/anie.201204475.
(79) Feng, D.; Chung, W.-C.; Wei, Z.; Gu, Z.-Y.; Jiang, H.-L.; Chen, Y.-P.; Darensbourg, D. J.; Zhou, H.-C. Construction of Ultrastable Porphyrin Zr Metal–Organic Frameworks through Linker Elimination. *J. Am. Chem. Soc.* **2013**, *135* (45), 17105–17110. https://doi.org/10.1021/ja408084j.
(80) Feng, D.; Gu, Z.-Y.; Chen, Y.-P.; Park, J.; Wei, Z.; Sun, Y.; Bosch, M.; Yuan, S.; Zhou, H.-C. A Highly Stable Porphyrinic Zirconium Metal–Organic Framework with **Shp-a** Topology. *J. Am. Chem. Soc.* **2014**, *136* (51), 17714–17717. https://doi.org/10.1021/ja510525s.
(81) Bloch, W. M.; Burgun, A.; Coghlan, C. J.; Lee, R.; Coote, M. L.; Doonan, C. J.; Sumby, C. J. Capturing Snapshots of Post-Synthetic Metallation Chemistry in Metal–Organic Frameworks. *Nature Chem* **2014**, *6* (10), 906–912. https://doi.org/10.1038/nchem.2045.
(82) Doonan, C. J.; Morris, W.; Furukawa, H.; Yaghi, O. M. Isoreticular Metalation of Metal−Organic Frameworks. *J. Am. Chem. Soc.* **2009**, *131* (27), 9492–9493. https://doi.org/10.1021/ja903251e.
(83) Ingleson, M. J.; Perez Barrio, J.; Guilbaud, J.-B.; Khimyak, Y. Z.; Rosseinsky, M. J. Framework Functionalisation Triggers Metal Complex Binding. *Chem. Commun.* **2008**, No. 23, 2680. https://doi.org/10.1039/b718367d.
(84) Rasero-Almansa, A. M.; Corma, A.; Iglesias, M.; Sánchez, F. One-Pot Multifunctional Catalysis with NNN-Pincer Zr-MOF: Zr Base Catalyzed Condensation with Rh-Catalyzed Hydrogenation. *ChemCatChem* **2013**, *5* (10), 3092–3100. https://doi.org/10.1002/cctc.201300371.
(85) Geary, J.; Aalto, J. P.; Xiao, D. J. *Modular Synthesis of Templated Bimetallic Sites in Metal–Organic Framework Pores*; preprint; Chemistry, 2023. https://doi.org/10.26434/chemrxiv-2023-njhwz.
(86) Jeoung, S.; Kim, S.; Kim, M.; Moon, H. R. Pore Engineering of Metal-Organic Frameworks with Coordinating Functionalities. *Coordination Chemistry Reviews* **2020**, *420*, 213377. https://doi.org/10.1016/j.ccr.2020.213377.
(87) Rosi, N. L.; Kim, J.; Eddaoudi, M.; Chen, B.; O'Keeffe, M.; Yaghi, O. M. Rod Packings and Metal−Organic Frameworks Constructed from Rod-Shaped Secondary Building Units. *J. Am. Chem. Soc.* **2005**, *127* (5), 1504–1518. https://doi.org/10.1021/ja045123o.
(88) Schoedel, A.; Li, M.; Li, D.; O'Keeffe, M.; Yaghi, O. M. Structures of Metal–Organic Frameworks with Rod Secondary Building Units. *Chem. Rev.* **2016**, *116* (19), 12466–12535. https://doi.org/10.1021/acs.chemrev.6b00346.
(89) Zhu, C.; Xia, Q.; Chen, X.; Liu, Y.; Du, X.; Cui, Y. Chiral Metal–Organic Framework as a Platform for Cooperative Catalysis in Asymmetric Cyanosilylation of Aldehydes. *ACS Catal.* **2016**, *6* (11), 7590–7596. https://doi.org/10.1021/acscatal.6b02359.
(90) Wang, Z.; Yeary, P.; Feng, X.; Lin, W. Self-Adaptive Metal–Organic Framework Assembles Di-Iron Active Sites to Mimic Monooxygenases. *J. Am. Chem. Soc.* **2023**, *145* (15), 8647–8655. https://doi.org/10.1021/jacs.3c01498.
(91) Geary, J.; Wong, A. H.; Xiao, D. J. Thermolabile Cross-Linkers for Templating Precise Multicomponent Metal–Organic Framework Pores. *J. Am. Chem. Soc.* **2021**, *143* (27), 10317–10323. https://doi.org/10.1021/jacs.1c04030.

(92) Lan, G.; Li, Z.; Veroneau, S. S.; Zhu, Y.-Y.; Xu, Z.; Wang, C.; Lin, W. Photosensitizing Metal–Organic Layers for Efficient Sunlight-Driven Carbon Dioxide Reduction. *J. Am. Chem. Soc.* **2018**, *140* (39), 12369–12373. https://doi.org/10.1021/jacs.8b08357.
(93) Vallee, B. L.; Williams, R. J. Metalloenzymes: The Entatic Nature of Their Active Sites. *Proc. Natl. Acad. Sci. U.S.A.* **1968**, *59* (2), 498–505. https://doi.org/10.1073/pnas.59.2.498.
(94) Rayder, T. M.; Bensalah, A. T.; Li, B.; Byers, J. A.; Tsung, C.-K. Engineering Second Sphere Interactions in a Host–Guest Multicomponent Catalyst System for the Hydrogenation of Carbon Dioxide to Methanol. *J. Am. Chem. Soc.* **2021**, *143* (3), 1630–1640. https://doi.org/10.1021/jacs.0c08957.
(95) Xiao, D. J.; Oktawiec, J.; Milner, P. J.; Long, J. R. Pore Environment Effects on Catalytic Cyclohexane Oxidation in Expanded Fe $_2$ (Dobdc) Analogues. *J. Am. Chem. Soc.* **2016**, *138* (43), 14371–14379. https://doi.org/10.1021/jacs.6b08417.
(96) Liu, J.; Goetjen, T. A.; Wang, Q.; Knapp, J. G.; Wasson, M. C.; Yang, Y.; Syed, Z. H.; Delferro, M.; Notestein, J. M.; Farha, O. K.; Hupp, J. T. MOF-Enabled Confinement and Related Effects for Chemical Catalyst Presentation and Utilization. *Chem. Soc. Rev.* **2022**, *51* (3), 1045–1097. https://doi.org/10.1039/D1CS00968K.
(97) Yuan, S.; Feng, L.; Wang, K.; Pang, J.; Bosch, M.; Lollar, C.; Sun, Y.; Qin, J.; Yang, X.; Zhang, P.; Wang, Q.; Zou, L.; Zhang, Y.; Zhang, L.; Fang, Y.; Li, J.; Zhou, H.-C. Stable Metal–Organic Frameworks: Design, Synthesis, and Applications. *Advanced Materials* **2018**, *30* (37), 1704303. https://doi.org/10.1002/adma.201704303.
(98) Ding, M.; Cai, X.; Jiang, H.-L. Improving MOF Stability: Approaches and Applications. *Chem. Sci.* **2019**, *10* (44), 10209–10230. https://doi.org/10.1039/C9SC03916C.

Chapter 2: Thermolabile Cross-linkers for Templating Precise Multicomponent Metal–Organic Framework Pores

2.1 Introduction

In enzymes, multiple primary and secondary coordination sphere elements work in concert to lower activation barriers and promote catalysis.[1–7] By controlling the spatial arrangement of amino acids and their corresponding side chains, enzymes can direct the self-assembly of complex metal cofactors,[8,9] promote a single reaction outcome over many competing pathways,[2,7] and enhance reaction rates by up to 10^{19}-fold.[2,10]

Crystalline porous materials such as metal–organic frameworks (MOFs) provide an exciting opportunity to explore these bioinspired design principles in the solid state.[11] In theory, many different functional groups, comparable to that of enzymes, can be simultaneously incorporated within MOF pores. In practice, however, current methods still lack the structural versatility and molecular precision needed to replicate biological active sites. Two common strategies towards mixed-ligand MOFs are briefly summarized below. The first is the multivariate approach, where two or more geometrically similar ligands are directly combined to form mixed-ligand frameworks.[12] Multivariate frameworks are distinguished by high chemical and structural diversity but low precision, as the location of functional groups is largely random.[13] On the other end of the spectrum, frameworks composed of two or more geometrically distinct ligands can be used to generate precise pores where functional group positions are crystallographically resolvable. Although creative one-pot[14–17] and sequential ligand installation strategies[18–21] have greatly expanded the scope of frameworks amenable to this strategy, this method is inherently limited to a small subset of MOF structures and ligand geometries.

A less explored but potentially more versatile route towards multicomponent metal–organic frameworks relies on molecular templating, also known as molecular imprinting (**Fig. 2.1a**). This approach has a rich history in polymer and silica-based materials.[22–24] Small molecules that interact strongly with polymer or silica precursors template the formation of pores with highly complementary surface chemistry, size, and shape. The small molecule templates feature reversible covalent or noncovalent linkages that enable postsynthetic removal. Extending such strategies from amorphous polymer or silica hosts to a crystalline porous framework could be an exceptionally powerful means of generating sophisticated, bioinspired active sites.

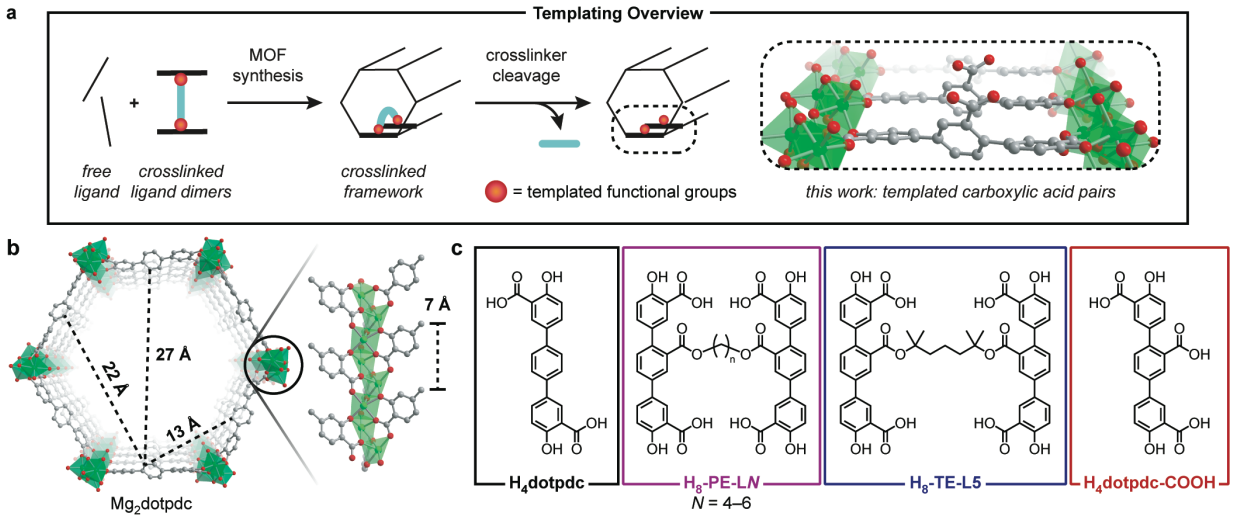

Figure 2.1. (a) Overview of the templating strategy reported in this work, which relies on the use of cleavable covalent cross-linkers to template the formation of well-defined functional group pairs. This work specifically focuses on the use of ester-based cross-linkers to template carboxylic acids. (b) Structure of Mg_2dotpdc, an expanded MOF-74 analogue, with four distinct interligand distances highlighted. (c) Structures and abbreviations of ligands and cross-linked ligand dimers used in this work.

The first demonstration of molecular imprinting in MOFs, specifically ZIF-8, was recently reported by Zhou and coworkers.[25] Pairs of imidazole ligands were tethered by imine-based cross-linkers that, upon hydrolysis, revealed templated aldehyde groups. Because the imines readily decomposed during MOF synthesis, the cross-linked ligands could only be installed via mild postsynthetic ligand exchange methods. This may limit the scope of imine-based cross-linkers, as not all frameworks undergo facile ligand exchange. Furthermore, from a catalysis viewpoint, the

small pore apertures (~3.4 Å) of ZIF-8 greatly restrict the types of active sites and substrates that can be further investigated.[26]

To address these concerns, we sought to design a more chemically stable cross-linker that not only tolerates standard MOF synthesis conditions but could also be adapted to mesoporous (2–50 nm) frameworks. Here, we report the construction of thermolabile, tertiary ester-based cross-linkers that template synthetically versatile carboxylic acid pairs. The ester linkages remain intact during framework formation but are readily thermolyzed into carboxylic acids upon microwave heating. Successful cross-linker synthesis, framework incorporation, and thermolysis is demonstrated using the mesoporous, terphenyl expanded analogues of MOF-74.[27,28] When short pentyl cross-linkers are used, modeling studies suggest that the acid pairs are installed in a single configuration down the pore channels, spaced ~7 Å apart.

2.2 Results and Discussion

2.2.1 Framework selection and general templating strategy

At the outset, an important goal of this work was to extend molecular templating strategies to a mesoporous metal–organic framework, as large pores will be critical for future reactivity studies and catalyst development. Therefore, we selected the MOF-74 archetype (also known as M_2dobdc) for our initial studies,[29] as expanded MOF-74 structures with pore diameters approaching 100 Å have been reported.[27] We have focused on the magnesium-based, terphenyl expanded analogue Mg_2dotpdc (dotpdc^{4-} = dioxidoterphenyldicarboxylate), which is highly amenable to ligand functionalization and postsynthetic chemistry.[28,30,31]

The structure of Mg_2dotpdc is illustrated in **Fig. 2.1b**. Extended, terphenylene-based organic ligands bridge rod-like metal oxide chains to form one-dimensional, hexagonal pores with a diameter of ~27 Å. Four distinct interligand distances are highlighted in **Fig. 2.1b**: the distance

across the hexagonal channel (27 Å), between adjacent hexagonal edges (13 Å) and next-nearest neighbor edges (22 Å), and finally, down the pore channels (7 Å). We hypothesized that, by controlling the length and geometry of our ligand cross-linker, we should be able to force functional group pairs to adopt one out of these four relative orientations. A short cross-linker of <10 Å, for example, should tether functional groups pairwise down the pore channels (**Fig. 2.1a**). Post-synthetic cross-linker cleavage would reveal two functional groups spaced just ~7 Å apart. This strategy would be especially powerful at low functional group concentrations, where all existing methods, such as the standard multivariate approach, would lead to randomly diluted spatial distributions.

2.2.2 Cross-linker design

Pioneering studies by the Cohen group have shown that MOFs can be synthesized from chemically cross-linked ligand dimers,[32] trimers,[33] and even polymers,[34] provided that the length and geometry of the covalent tethers are carefully selected. Although a number of cross-linked and "polyMOF" frameworks have been reported for the MOF-5 and UiO-66 families,[32–38] similar studies have not been performed for the MOF-74 structure type. Furthermore, all previous cross-linkers have employed strong amide or ether-based linkages. Cleavage and removal of these cross-linkers has not been previously demonstrated.

In an effort to develop a cleavable cross-linker design viable across a range of MOFs, we sought a structural motif that possessed both high geometric tunability and controllable chemical stability. To that end, ester-based cross-linkers were selected (**Fig. 2.1c**). Diesters are readily synthesized from carboxylic acids and diols, a number of which are commercially available. Furthermore, the chemical stability of esters is highly dependent on its structure. Primary esters are typically hydrolyzed under basic conditions, while tertiary esters are acid labile and susceptible

to thermolysis at elevated temperatures.[39–41] Postsynthetic thermolysis is particularly attractive, given the relatively high thermal stabilities of many metal–organic frameworks (T_d ~ 300 °C or above).[42]

The primary and tertiary ester-based cross-linked ligand dimers outlined in **Fig. 2.1c** were synthesized from 2,5-dibromobenzoic acid and the corresponding aliphatic diol over three steps in excellent overall yields (55–80%, see SI for synthetic details). For this study, we specifically chose short cross-linkers that can span only the smallest interligand distance (~7 Å down the pore channels, see **Fig. 2.1b**). The resulting dimers are abbreviated H_8-PE-LX and H_8-TE-LX, where PE and TE stand for primary and tertiary ester, respectively, and X refers to the number of methylene units in the alkyl chain (**Fig. 2.1c**).

2.2.3 Synthesis of cross-linked frameworks

With our ligand dimers in hand, we first tested whether the primary ester-based variants, H_8-PE-LX (X = 4, 5, and 6), could be successfully incorporated into Mg_2dotpdc. These dimers were relatively straightforward to synthesize, as both primary aliphatic diols were commercially available. We have abbreviated all cross-linked frameworks as Mg_2dotpdc-(PE/TE)-LX-R%, where R% indicates the percentage of cross-linked dotpdc^{4-} relative to the total amount of dotpdc^{4-} in the framework.

All attempts to synthesize the expanded MOF-74 structure with mixtures of H_4dotpdc and H_8-PE-L4 led to the formation of undesired phases or poorly crystalline material (**Fig. 2.S1**). From these results, we concluded that a butyl chain is too short to bridge the 7 Å distance between neighboring ligands down the pore walls.

In contrast, when the pentyl cross-linker H_8-PE-L5 was combined with H_4dotpdc and $Mg(NO_3)_2 \cdot 6H_2O$, a clean powder X-ray diffraction (PXRD) pattern matching the parent

Mg_2dotpdc framework was obtained. Rigorous washing of the cross-linked materials followed by digestion and ^{1}H NMR analysis confirmed that the amount of cross-linked dotpdc^{4-} incorporated closely matches the amount predicted based on the initial ratio of H_4dotpdc to H_8-PE-L5 (**Table 2.S1, Figs. 2.S2–2.S6**). Infrared spectroscopy of the ester cross-linked frameworks revealed the growth of a new peak at 1695 cm^{-1}, consistent with an ester carbonyl stretch (**Fig. 2.S7**). Excellent phase purity is maintained and no peak broadening is observed even at 100% cross-linker incorporation (**Fig. 2.2 and Table 2.S4**), highlighting how well the length of the pentyl unit matches the geometry of framework. Interestingly, the longer cross-linker H_8-PE-L6 was also readily accommodated in the MOF-74 structure type (**Fig. 2.S8**). However, for simplicity, the remainder of this study will focus on H_8-PE-L5, as short cross-linker lengths minimize the number of possible ligand configurations within the framework.

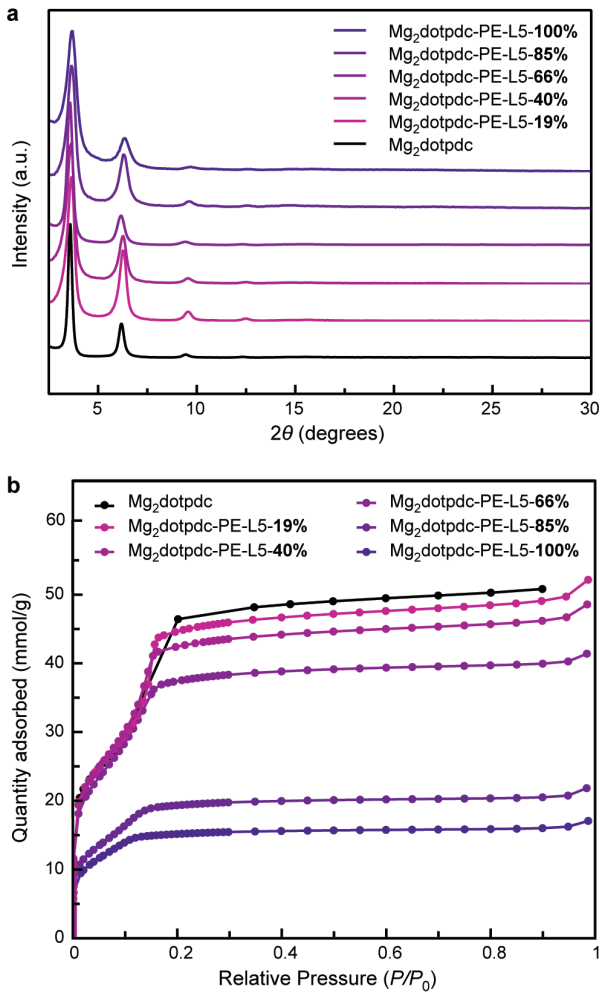

Figure 2.2. Characterization of primary ester cross-linked Mg_2dotpdc frameworks. (a) PXRD patterns and (b) surface areas of Mg_2dotpdc (16 h) and Mg_2dopdc-PE-L5-R% (R = 18–100%).

The chemically cross-linked Mg_2dotpdc frameworks are permanently porous and display high Brunauer–Emmett–Teller (BET) and Langmuir surface areas (**Fig. 2.2**, **Table 2.1**). For example, Mg_2dotpdc-PE-L5-23% displays BET and Langmuir surface areas of 2700 and 4900 m^2/g, respectively. These values are only slightly lower than the parent Mg_2dotpdc

framework (**Table 2.1**), providing strong evidence that the integrity of the framework is not compromised by cross-linker incorporation, and that no dangling or unincorporated ligands are trapped in the pores. Lower surface areas were observed at higher cross-linker concentrations, consistent with the additional mass and volume present inside the pore channels.

After identifying the pentyl unit as the minimum cross-linker length, we next investigated the structurally related tertiary ester-based dimer, H_8-TE-L5. Developing solvothermal conditions compatible with tertiary esters proved more challenging. Under the standard MOF-74 synthesis conditions (120 °C, 16 h), roughly 20% of the H_2-TE-L5 dimer decomposed to form two equivalents of monomeric ligand containing a free carboxylic acid, H_4dotpdc-COOH (**Fig. 2.S9**). Inadvertent cross-linker cleavage is likely facilitated by the mild acidity of the initial reaction mixture, the elevated temperature, and prolonged reaction time. Fortunately, shortening the synthesis to 3 h eliminated any observable cross-linker decomposition. Although these short reaction times led to slightly broadened diffraction peaks (**Fig. 2.S10**), similar surface areas were obtained for the parent Mg_2dotpdc framework synthesized at 3 and 16 h (**Table 2.1**).

Table 2.1. BET and Langmuir surface areas of Mg_2dotpdc, primary ester cross-linked Mg_2dotpdc-PE-L5-R%, and tertiary ester cross-linked Mg_2dotpdc-TE-L5-R%.

Sample	SA_{BET} (m^2/g)	$SA_{Langmuir}$ (m^2/g)
Mg_2dotpdc (16 h)[1]	2700	5120
Mg_2dotpdc (3 h)[1]	2700	4700
Mg_2dotpdc-PE-L5-19%[1]	2700	4920
Mg_2dotpdc-PE-L5-40%[1]	2740	4620
Mg_2dotpdc-PE-L5-66%[1]	2550	3970
Mg_2dotpdc-PE-L5-85%[1]	1630	2150
Mg_2dotpdc-PE-L5-100%[1]	1580	1950
Mg_2dotpdc-TE-L5-23%[2]	2290	3660
Mg_2dotpdc-TE-L5-50%[2]	2250	3300

[1]Samples were activated at 150 °C.

[2]All Mg_2dotpdc-TE-L5-R% samples were activated at RT.

Like their primary ester analogues, the cross-linked frameworks Mg_2dotpdc-TE-L5-R% (R = 23, 50%) display relatively high BET surface areas of ~2300 m^2/g (**Table 2.1**). To avoid any cross-linker thermolysis, sample activation was carried out at room temperature. As these mild conditions are not sufficient to remove solvent bound to the Mg^{2+} sites present in the framework, lower surface areas relative to the primary ester analogues were observed. With a 3 h reaction time, slightly greater amounts of cross-linked dotpdc^{4-} are incorporated than expected (e.g., 18% predicted vs 23% observed, see **Table 2.S1** and **Figs. 2.S11–2.S12**), perhaps indicating a small kinetic preference for the cross-linked ligands owing to its templated geometry and higher number of coordination sites.

2.2.4 Modeling studies

Based on simple geometric considerations, there are only two possible configurations the pentyl cross-linker can adopt within the framework, which we have illustrated in **Fig. 2.3**. In both structures, labeled "symmetric" and "offset," the cross-linker bridges adjacent ligands down the pore channels. However, they differ in the way the esters are attached to the central phenyl rings. To probe which orientation of the ligand dimer TE-L5^{8-} is energetically preferred, we first optimized the extended structure of Mg_2dotpdc using the Forcite module in Materials Studio. This structure was then truncated to two neighboring ligands and partially frozen such that only the central

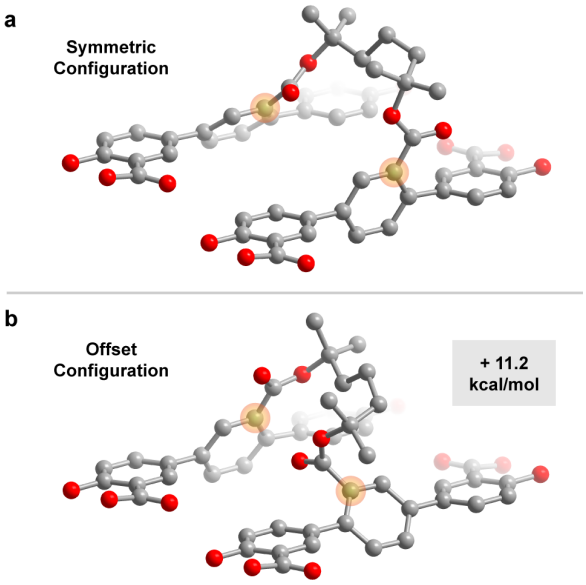

Figure 2.3. Modeling studies. Truncated structures show the two distinct configurations the cross-linker can adopt down the pore channels, labeled as (a) "symmetric" and (b) "offset." DFT calculations show that the symmetric configuration is more stable by 11.2 kcal/mol.

phenyl rings could freely move, mimicking the geometric restrictions of the MOF lattice. A bridging cross-linker was added, and the geometries of the cross-linker and central phenyl ring were optimized using density functional calculations at the B3LYP/6-311+G(d,p)//B3LYP/6-31G+(d) level of theory. These calculations suggest a strong energetic preference for the symmetric configuration by over 11 kcal/mol (**Table 2.S5**). As 1.36 kcal/mol corresponds to a 10-fold shift in equilibrium constant, we hypothesize that this configuration is the predominant structure found in the framework.

2.2.5 Cross-linker thermolysis

With the successful incorporation of cross-linked ligand dimers firmly established, we finally turned to the last step in our overall templating scheme: postsynthetic cross-linker cleavage. Tertiary esters are known to decompose at elevated temperatures into free carboxylic acids and the corresponding alkenes (**Fig. 2.4a**).[39–41] While this specific reaction has never been demonstrated in a MOF, the analogous thermolysis of tertiary carbamates is well-established,[43,44] and we anticipated that similar conditions could be used.

We adapted a procedure previously reported by Yaghi and coworkers to cleave *tert*-butyl carbamates into free amines, which employed microwave heating at 230°C for 10 minutes in a solvent mixture of 2-ethyl-1hexanol, ethylene glycol, and water.[45] We reduced the heating time and eliminated water out of an abundance of caution for the hydrolytic stability of the framework. Excitingly, using this modified procedure, we obtained nearly quantitative conversion (98–99%) of Mg_2dotpdc-TE-L5-R% to Mg_2dotpdc-(t)-COOH-R% (**Fig. 2.S13–2.S14**). Note that the (t) denotes the templated, pairwise nature of the carboxylic acids. Importantly, the amount of H_4dotpdc-COOH observed by ^{1}H NMR following rigorous DMF washes and digestion closely matches the amount of cross-linked dotpdc^{4-} present before thermolysis. This clearly demonstrates

that the cross-linked ligand dimers were fully incorporated in the framework. Any dangling ligands would have been washed away after cross-linker cleavage, leading to lower-than-expected amounts of H_4dotpdc-COOH.

While the PXRD pattern reveals no loss in crystallinity post-thermolysis (**Fig. 2.4b**), Mg_2dotpdc-(t)-COOH-49% does not display the expected increase in surface area (**Fig. 2.4c** and **Table 2.S2**). Given the known sensitivity of Mg_2dotpdc towards acidic conditions,[46] we hypothesized that the framework may be incompatible with such a high density of free carboxylic acid sites, and that higher surface areas may be observed at a lower functional group concentrations. Indeed, at lower concentrations of templated carboxylic acid (<25%), the thermolyzed framework appears pristine by both PXRD and gas sorption studies (**Fig. 2.4**). After thermolysis, dramatic increases in both the BET and Langmuir surface areas are observed for Mg_2dotpdc-(t)-COOH-23%, from 2290 to 2510 m^2/g and 3660 to 4480 m^2/g,

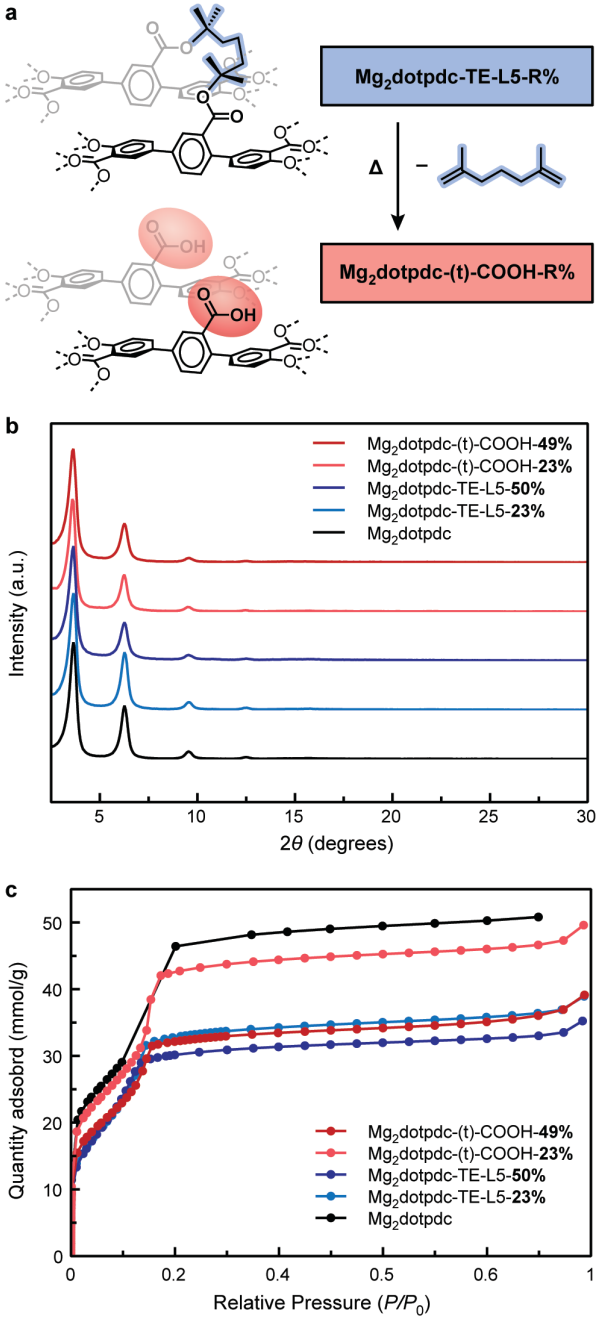

Figure 2.4. Characterization of tertiary ester cross-linked Mg_2dotpdc frameworks before and after thermolysis. (a) General thermolysis reaction scheme. (b) PXRD patterns and (c) surface areas of Mg_2dotpdc (3 h), cross-linked Mg_2dotpdc-TE-L5-R%, and thermolyzed Mg_2dotpdc-(t)-COOH-R% (R = 23–50%)

respectively (**Fig. 2.4c**). Infrared spectroscopy shows a shift in the $\nu_{C=O}$ of the ester linkage from 1705 to 1675 cm^{-1}, consistent with the conversion of the ester to a free carboxylic acid (**Fig. 2.S20**). To our knowledge, this represents the first time that a thermolabile protecting group has been used to install free carboxylic acids within MOF pores. More broadly, this work illustrates how molecular templating can serve as a new and complementary strategy for manipulating the interior surface chemistry of metal–organic frameworks.

2.3 Conclusion

We have shown that simple, thermolabile tertiary ester-based cross-linkers can be used to template carboxylic acid pairs within metal–organic frameworks. A key advantage of this strategy is how it couples structural versatility with molecular precision. By changing the cross-linker length and geometry, as well as the overall framework topology, it should be possible to precisely fine-tune the ultimate orientation and position of free carboxylic acids within the framework pores. Future studies with the carboxylate pairs will investigate whether our templated carboxylic acid pairs can mimic biological active sites, such as the diacid active site of glycosidase[47–49] or the site-isolated carboxylate-bridged diiron sites found in many metalloproteins.[50–52] Additional work expanding our templating strategy to other functional groups, such as amines, will be discussed in the next chapter.

2.4 Acknowledgements

We gratefully acknowledge University of Washington startup funds and the Donors of the American Chemical Society Petro-leum Research Fund for support of this research under PRF# 61949-DNI3. We thank the Mary Gates research scholarship for supporting A.H.W. Part of this work was conducted at the Molecular Analysis Facility, a National Nanotechnology Co-ordinated Infrastructure (NNCI) site at the University of Washington, which is supported in part by funds

from the National Science Foundation (awards NNCI-2025489, NNCI-1542101), the Molecular Engineering & Sciences Institute, and the Clean Energy Institute. In addition, the authors acknowledge the use of facilities and instrumentation sup-ported by the U.S. National Science Foundation through the UW Molecular Engineering Materials Center (MEM-C), a Materials Research Science and Engineering Center (DMR171797). This work was facilitated through the use of advanced computational, storage, and networking infrastructure provided by the Hyak supercomputer system at the University of Washington.

2.5 References

(1) Warshel, A.; Sharma, P. K.; Kato, M.; Xiang, Y.; Liu, H.; Olsson, M. H. M. Electrostatic Basis for Enzyme Catalysis. *Chem. Rev.* **2006**, *106* (8), 3210–3235. https://doi.org/10.1021/cr0503106.

(2) Frey, P. A.; Hegeman, A. D. Enzymes and Catalytic Mechanisms. In *Enzymatic reaction mechanisms*; Oxford University Press: Oxford ; New York, 2007; pp 1–68.

(3) Knowles, R. R.; Jacobsen, E. N. Attractive Noncovalent Interactions in Asymmetric Catalysis: Links between Enzymes and Small Molecule Catalysts. *Proceedings of the National Academy of Sciences* **2010**, *107* (48), 20678–20685. https://doi.org/10.1073/pnas.1006402107.

(4) Rakowski DuBois, M.; DuBois, D. L. The Roles of the First and Second Coordination Spheres in the Design of Molecular Catalysts for H_2 Production and Oxidation. *Chem. Soc. Rev.* **2009**, *38* (1), 62–72. https://doi.org/10.1039/B801197B.

(5) Shook, R. L.; Borovik, A. S. Role of the Secondary Coordination Sphere in Metal-Mediated Dioxygen Activation. *Inorg. Chem.* **2010**, *49* (8), 3646–3660. https://doi.org/10.1021/ic901550k.

(6) Zhao, M.; Wang, H.-B.; Ji, L.-N.; Mao, Z.-W. Insights into Metalloenzyme Microenvironments: Biomimetic Metal Complexes with a Functional Second Coordination Sphere. *Chem. Soc. Rev.* **2013**, *42* (21), 8360. https://doi.org/10.1039/c3cs60162e.

(7) Visser, S. P. Second-Coordination Sphere Effects on Selectivity and Specificity of Heme and Nonheme Iron Enzymes. *Chem. Eur. J.* **2020**, *26* (24), 5308–5327. https://doi.org/10.1002/chem.201905119.

(8) Dudev, T.; Lim, C. Metal Binding Affinity and Selectivity in Metalloproteins: Insights from Computational Studies. *Annu. Rev. Biophys.* **2008**, *37* (1), 97–116. https://doi.org/10.1146/annurev.biophys.37.032807.125811.

(9) Dudev, T.; Lim, C. Competition among Metal Ions for Protein Binding Sites: Determinants of Metal Ion Selectivity in Proteins. *Chem. Rev.* **2014**, *114* (1), 538–556. https://doi.org/10.1021/cr4004665.

(10) Wolfenden, R.; Snider, M. J. The Depth of Chemical Time and the Power of Enzymes as Catalysts. *Acc. Chem. Res.* **2001**, *34* (12), 938–945. https://doi.org/10.1021/ar000058i.

(11) Bour, J. R.; Wright, A. M.; He, X.; Dincă, M. Bioinspired Chemistry at MOF Secondary Building Units. *Chem. Sci.* **2020**, *11* (7), 1728–1737. https://doi.org/10.1039/C9SC06418D.

(12) Deng, H.; Doonan, C. J.; Furukawa, H.; Ferreira, R. B.; Towne, J.; Knobler, C. B.; Wang, B.; Yaghi, O. M. Multiple Functional Groups of Varying Ratios in Metal-Organic Frameworks. *Science* **2010**, *327* (5967), 846–850. https://doi.org/10.1126/science.1181761.
(13) Kong, X.; Deng, H.; Yan, F.; Kim, J.; Swisher, J. A.; Smit, B.; Yaghi, O. M.; Reimer, J. A. Mapping of Functional Groups in Metal-Organic Frameworks. *Science* **2013**, *341* (6148), 882–885. https://doi.org/10.1126/science.1238339.
(14) Koh, K.; Wong-Foy, A. G.; Matzger, A. J. A Crystalline Mesoporous Coordination Copolymer with High Microporosity. *Angewandte Chemie International Edition* **2008**, *47* (4), 677–680. https://doi.org/10.1002/anie.200705020.
(15) Furukawa, H.; Ko, N.; Go, Y. B.; Aratani, N.; Choi, S. B.; Choi, E.; Yazaydin, A. O.; Snurr, R. Q.; O'Keeffe, M.; Kim, J.; Yaghi, O. M. Ultrahigh Porosity in Metal-Organic Frameworks. *Science* **2010**, *329* (5990), 424–428. https://doi.org/10.1126/science.1192160.
(16) Koh, K.; Van Oosterhout, J. D.; Roy, S.; Wong-Foy, A. G.; Matzger, A. J. Exceptional Surface Area from Coordination Copolymers Derived from Two Linear Linkers of Differing Lengths. *Chemical Science* **2012**, *3* (8), 2429. https://doi.org/10.1039/c2sc20407j.
(17) Liu, L.; Konstas, K.; Hill, M. R.; Telfer, S. G. Programmed Pore Architectures in Modular Quaternary Metal–Organic Frameworks. *Journal of the American Chemical Society* **2013**, *135* (47), 17731–17734. https://doi.org/10.1021/ja4100244.
(18) Yuan, S.; Lu, W.; Chen, Y.-P.; Zhang, Q.; Liu, T.-F.; Feng, D.; Wang, X.; Qin, J.; Zhou, H.-C. Sequential Linker Installation: Precise Placement of Functional Groups in Multivariate Metal–Organic Frameworks. *Journal of the American Chemical Society* **2015**, *137* (9), 3177–3180. https://doi.org/10.1021/ja512762r.
(19) Yuan, S.; Chen, Y.-P.; Qin, J.-S.; Lu, W.; Zou, L.; Zhang, Q.; Wang, X.; Sun, X.; Zhou, H.-C. Linker Installation: Engineering Pore Environment with Precisely Placed Functionalities in Zirconium MOFs. *Journal of the American Chemical Society* **2016**, *138* (28), 8912–8919. https://doi.org/10.1021/jacs.6b04501.
(20) Yuan, S.; Zou, L.; Li, H.; Chen, Y.-P.; Qin, J.; Zhang, Q.; Lu, W.; Hall, M. B.; Zhou, H.-C. Flexible Zirconium Metal-Organic Frameworks as Bioinspired Switchable Catalysts. *Angew. Chem. Int. Ed.* **2016**, *55* (36), 10776–10780. https://doi.org/10.1002/anie.201604313.
(21) Bosch, M.; Yuan, S.; Rutledge, W.; Zhou, H.-C. Stepwise Synthesis of Metal–Organic Frameworks. *Acc. Chem. Res.* **2017**, *50* (4), 857–865. https://doi.org/10.1021/acs.accounts.6b00457.
(22) Margelefsky, E. L.; Zeidan, R. K.; Davis, M. E. Cooperative Catalysis by Silica-Supported Organic Functional Groups. *Chemical Society Reviews* **2008**, *37* (6), 1118. https://doi.org/10.1039/b710334b.
(23) Chen, L.; Xu, S.; Li, J. Recent Advances in Molecular Imprinting Technology: Current Status, Challenges and Highlighted Applications. *Chemical Society Reviews* **2011**, *40* (5), 2922. https://doi.org/10.1039/c0cs00084a.
(24) Lofgreen, J. E.; Ozin, G. A. Controlling Morphology and Porosity to Improve Performance of Molecularly Imprinted Sol–Gel Silica. *Chem. Soc. Rev.* **2014**, *43* (3), 911–933. https://doi.org/10.1039/C3CS60276A.
(25) Feng, L.; Wang, K.-Y.; Lv, X.-L.; Powell, J. A.; Yan, T.-H.; Willman, J.; Zhou, H.-C. Imprinted Apportionment of Functional Groups in Multivariate Metal–Organic Frameworks. *J. Am. Chem. Soc.* **2019**, *141* (37), 14524–14529. https://doi.org/10.1021/jacs.9b06917.
(26) Park, K. S.; Ni, Z.; Cote, A. P.; Choi, J. Y.; Huang, R.; Uribe-Romo, F. J.; Chae, H. K.; O'Keeffe, M.; Yaghi, O. M. Exceptional Chemical and Thermal Stability of Zeolitic

Imidazolate Frameworks. *Proceedings of the National Academy of Sciences* **2006**, *103* (27), 10186–10191. https://doi.org/10.1073/pnas.0602439103.
(27) Deng, H.; Grunder, S.; Cordova, K. E.; Valente, C.; Furukawa, H.; Hmadeh, M.; Gandara, F.; Whalley, A. C.; Liu, Z.; Asahina, S.; Kazumori, H.; O'Keeffe, M.; Terasaki, O.; Stoddart, J. F.; Yaghi, O. M. Large-Pore Apertures in a Series of Metal-Organic Frameworks. *Science* **2012**, *336* (6084), 1018–1023. https://doi.org/10.1126/science.1220131.
(28) Milner, P. J.; Martell, J. D.; Siegelman, R. L.; Gygi, D.; Weston, S. C.; Long, J. R. Overcoming Double-Step CO $_2$ Adsorption and Minimizing Water Co-Adsorption in Bulky Diamine-Appended Variants of Mg $_2$ (Dobpdc). *Chem. Sci.* **2018**, *9* (1), 160–174. https://doi.org/10.1039/C7SC04266C.
(29) Rosi, N. L.; Kim, J.; Eddaoudi, M.; Chen, B.; O'Keeffe, M.; Yaghi, O. M. Rod Packings and Metal−Organic Frameworks Constructed from Rod-Shaped Secondary Building Units. *J. Am. Chem. Soc.* **2005**, *127* (5), 1504–1518. https://doi.org/10.1021/ja045123o.
(30) Xiao, D. J.; Oktawiec, J.; Milner, P. J.; Long, J. R. Pore Environment Effects on Catalytic Cyclohexane Oxidation in Expanded Fe $_2$ (Dobdc) Analogues. *J. Am. Chem. Soc.* **2016**, *138* (43), 14371–14379. https://doi.org/10.1021/jacs.6b08417.
(31) Fracaroli, A. M.; Furukawa, H.; Suzuki, M.; Dodd, M.; Okajima, S.; Gándara, F.; Reimer, J. A.; Yaghi, O. M. Metal–Organic Frameworks with Precisely Designed Interior for Carbon Dioxide Capture in the Presence of Water. *J. Am. Chem. Soc.* **2014**, *136* (25), 8863–8866. https://doi.org/10.1021/ja503296c.
(32) Allen, C. A.; Boissonnault, J. A.; Cirera, J.; Gulland, R.; Paesani, F.; Cohen, S. M. Chemically Cross-linked Isoreticular Metal–Organic Frameworks. *Chemical Communications* **2013**, *49* (31), 3200. https://doi.org/10.1039/c3cc40635k.
(33) Allen, C. A.; Cohen, S. M. Exploration of Chemically Cross-Linked Metal–Organic Frameworks. *Inorganic Chemistry* **2014**, *53* (13), 7014–7019. https://doi.org/10.1021/ic500951b.
(34) Zhang, Z.; Nguyen, H. T. H.; Miller, S. A.; Cohen, S. M. PolyMOFs: A Class of Interconvertible Polymer-Metal-Organic-Framework Hybrid Materials. *Angewandte Chemie International Edition* **2015**, *54* (21), 6152–6157. https://doi.org/10.1002/anie.201502733.
(35) Zhang, Z.; Nguyen, H. T. H.; Miller, S. A.; Ploskonka, A. M.; DeCoste, J. B.; Cohen, S. M. Polymer–Metal–Organic Frameworks (PolyMOFs) as Water Tolerant Materials for Selective Carbon Dioxide Separations. *J. Am. Chem. Soc.* **2016**, *138* (3), 920–925. https://doi.org/10.1021/jacs.5b11034.
(36) Ayala, S.; Zhang, Z.; Cohen, S. M. Hierarchical Structure and Porosity in UiO-66 PolyMOFs. *Chem. Commun.* **2017**, *53* (21), 3058–3061. https://doi.org/10.1039/C6CC10225E.
(37) Schukraft, G. E. M.; Ayala, S.; Dick, B. L.; Cohen, S. M. Isoreticular Expansion of PolyMOFs Achieves High Surface Area Materials. *Chem. Commun.* **2017**, *53* (77), 10684–10687. https://doi.org/10.1039/C7CC04222A.
(38) MacLeod, M. J.; Johnson, J. A. Block Co-PolyMOFs: Assembly of Polymer–PolyMOF Hybrids via Iterative Exponential Growth and "Click" Chemistry. *Polym. Chem.* **2017**, *8* (31), 4488–4493. https://doi.org/10.1039/C7PY00922D.
(39) Hurd, C. D.; Blunck, F. H. The Pyrolysis of Esters. *J. Am. Chem. Soc.* **1938**, *60* (10), 2419–2425. https://doi.org/10.1021/ja01277a035.
(40) Emovon, E. U.; Maccoll, A. 56. Gas-Phase Eliminations. Part III. The Pyrolysis of Some Secondary and Tertiary Alkyl Acetates. *J. Chem. Soc.* **1962**, 335. https://doi.org/10.1039/jr9620000335.

(41) Dugas, V.; Chevalier, Y. Chemical Reactions in Dense Monolayers: In Situ Thermal Cleavage of Grafted Esters for Preparation of Solid Surfaces Functionalized with Carboxylic Acids. *Langmuir* **2011**, *27* (23), 14188–14200. https://doi.org/10.1021/la2029438.
(42) Healy, C.; Patil, K. M.; Wilson, B. H.; Hermanspahn, L.; Harvey-Reid, N. C.; Howard, B. I.; Kleinjan, C.; Kolien, J.; Payet, F.; Telfer, S. G.; Kruger, P. E.; Bennett, T. D. The Thermal Stability of Metal-Organic Frameworks. *Coordination Chemistry Reviews* **2020**, *419*, 213388. https://doi.org/10.1016/j.ccr.2020.213388.
(43) Deshpande, R. K.; Minnaar, J. L.; Telfer, S. G. Thermolabile Groups in Metal-Organic Frameworks: Suppression of Network Interpenetration, Post-Synthetic Cavity Expansion, and Protection of Reactive Functional Groups. *Angew. Chem. Int. Ed.* **2010**, *49* (27), 4598–4602. https://doi.org/10.1002/anie.200905960.
(44) Lun, D. J.; Waterhouse, G. I. N.; Telfer, S. G. A General Thermolabile Protecting Group Strategy for Organocatalytic Metal−Organic Frameworks. *J. Am. Chem. Soc.* **2011**, *133* (15), 5806–5809. https://doi.org/10.1021/ja202223d.
(45) Fracaroli, A. M.; Furukawa, H.; Suzuki, M.; Dodd, M.; Okajima, S.; Gándara, F.; Reimer, J. A.; Yaghi, O. M. Metal-Organic Frameworks with Precisely Designed Interior for Carbon Dioxide Capture in the Presence of Water. *Journal of the American Chemical Society* **2014**, *136* (25), 8863–8866. https://doi.org/10.1021/ja503296c.
(46) Wang, Z.; Bilegsaikhan, A.; Jerozal, R. T.; Pitt, T. A.; Milner, P. J. Evaluating the Robustness of Metal–Organic Frameworks for Synthetic Chemistry. *ACS Appl. Mater. Interfaces* **2021**, *13* (15), 17517–17531. https://doi.org/10.1021/acsami.1c01329.
(47) Zechel, D. L.; Withers, S. G. Glycosidase Mechanisms: Anatomy of a Finely Tuned Catalyst. *Acc. Chem. Res.* **2000**, *33* (1), 11–18. https://doi.org/10.1021/ar970172+.
(48) Rousseau, C.; Nielsen, N.; Bols, M. An Artificial Enzyme That Catalyzes Hydrolysis of Aryl Glycosides. *Tetrahedron Letters* **2004**, *45* (47), 8709–8711. https://doi.org/10.1016/j.tetlet.2004.09.134.
(49) Ortega-Caballero, F.; Rousseau, C.; Christensen, B.; Petersen, T. E.; Bols, M. Remarkable Supramolecular Catalysis of Glycoside Hydrolysis by a Cyclodextrin Cyanohydrin. *J. Am. Chem. Soc.* **2005**, *127* (10), 3238–3239. https://doi.org/10.1021/ja042678a.
(50) Tshuva, E. Y.; Lippard, S. J. Synthetic Models for Non-Heme Carboxylate-Bridged Diiron Metalloproteins: Strategies and Tactics. *Chem. Rev.* **2004**, *104* (2), 987–1012. https://doi.org/10.1021/cr020622y.
(51) Friedle, S.; Reisner, E.; Lippard, S. J. Current Challenges of Modeling Diiron Enzyme Active Sites for Dioxygen Activation by Biomimetic Synthetic Complexes. *Chem. Soc. Rev.* **2010**, *39* (8), 2768. https://doi.org/10.1039/c003079c.
(52) Jasniewski, A. J.; Que, L. Dioxygen Activation by Nonheme Diiron Enzymes: Diverse Dioxygen Adducts, High-Valent Intermediates, and Related Model Complexes. *Chem. Rev.* **2018**, *118* (5), 2554–2592. https://doi.org/10.1021/acs.chemrev.7b00457.

2.6 Supplementary Information.

1. General materials and methods.

Reagents and solvents were purchased from commercial vendors (Millipore Sigma, TCI America, Alfa Aesar, Fisher, Oakwood Chemical, Combi-Blocks) and used without purification

unless otherwise noted. Deuterated solvents ($CDCl_3$, DMSO-d_6) were purchased from Cambridge Isotope Laboratories. NMR spectra were acquired on Bruker AV300, AV301, DRX499, or AV500 instruments. ^{1}H and ^{13}C NMR spectra were referenced to residual deuterated solvent peaks. High resolution mass spectrometry data of ligands and their intermediates were collected on a Thermo Scientific LTQ Orbitrap XL instrument in positive ion mode. C, H, N combustion analysis was conducted by Atlantic Microlabs Inc.

Powder X-ray diffraction data were collected on either a Bruker D8 Discover powder X-ray diffractometer located in University of Washington's Molecular Analysis Facility, or a Bruker D2 PHASER benchtop diffractometer.

Microwave reactions were carried out using a CEM Discover SP Microwave synthesizer housed in the University of Washington Molecular Engineering Materials Center (MEM-C).

2. Ligand syntheses.

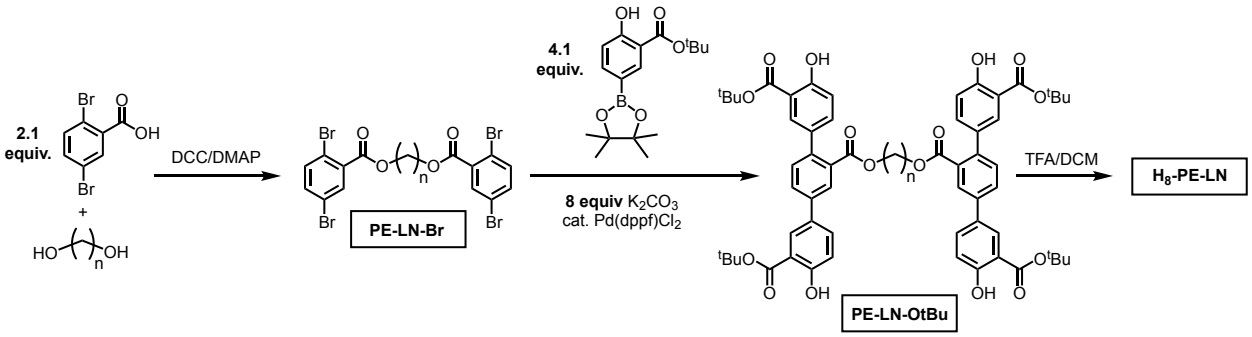

Scheme 2.S1. Overview of the synthesis of primary ester-based ligand dimers, **H_8-PE-LN** (N = 4–6).

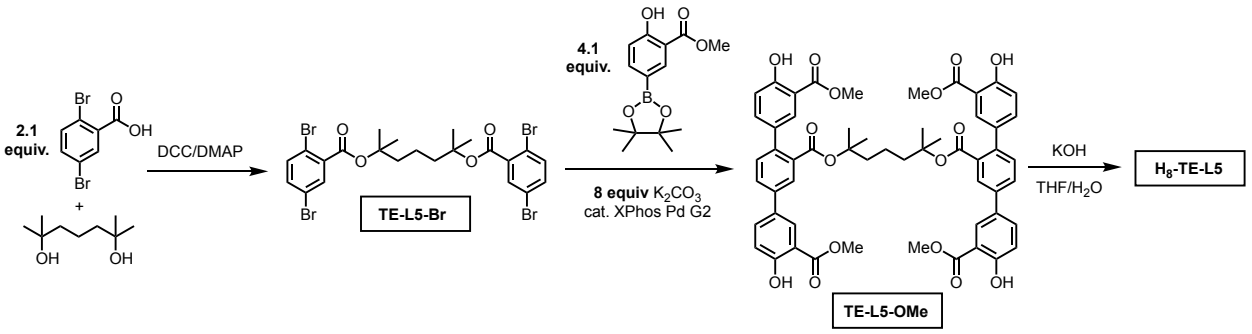

Scheme 2.S2 Overview of the synthesis of tertiary ester-based ligand dimers, **H_8-TE-L5**.

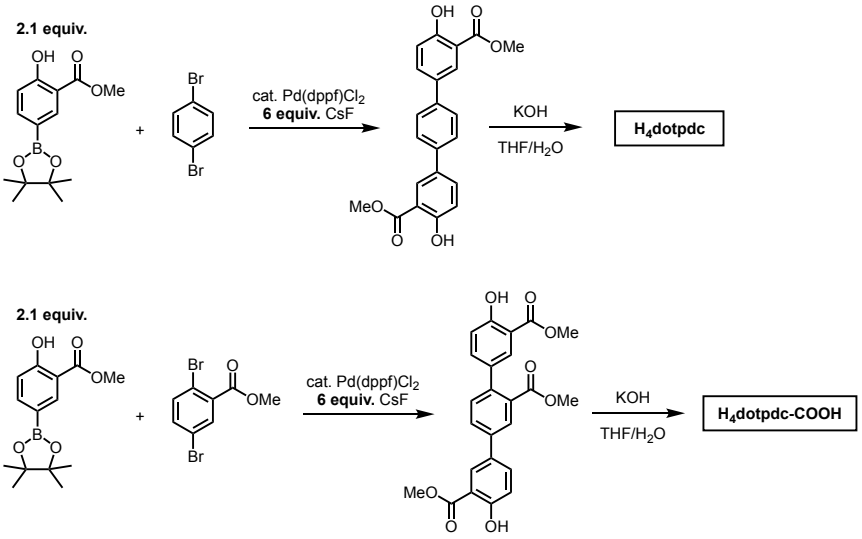

Scheme 3.S3 Overview of the synthesis of H_4dotpdc and H_4dotpdc-COOH.

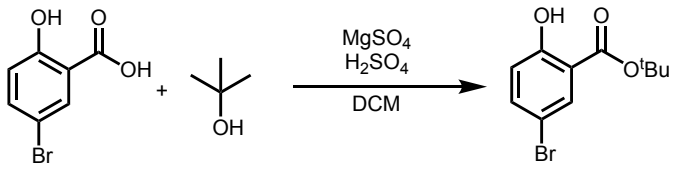

A 500 mL round bottom flask equipped with a stir bar was charged with $MgSO_4$ (19.3 g, 160 mmol, 4.00 equiv.) in dichloromethane (160 mL), followed by concentrated H_2SO_4 (2.22 mL, 40.0 mmol, 1.00 equiv.) and the solution was stirred at room temperature for 15 minutes. Next, 5-bromo-2-hydroxybenzoic acid (8.68 g, 40.0 mmol, 1.00 equiv) was added, followed by tert-butanol (19.1 mL, 50.0 mmol, 5.00 equiv). The flask was capped and the inhomogeneous solution was stirred at room temperature for 48 h. Subsequently, the mixture was filtered and neutralized with $NaHCO_3$. The organics were washed again with $NaHCO_3$ (100 mL), then deionized water (2x75 mL), dried over $MgSO_4$, filtered, and concentrated *in vacuo*. The resultant oily solid was brought up in minimal hexanes (5-10 mL) and re-concentrated to afford *tert*butyl 5-bromo-2-hydroxybenzoate (10.11 g, 93 % yield). ^{1}H NMR (300 MHz, $CDCl_3$): δ 11.00 (s, 1H), 7.86 (d, J = 2.5, 1H), 7.49 (dd, J = 8.8, 2.5, 1H), 6.85, (d, J = 8.8, 1H), 1.61 (s, 9H) ppm. ^{13}C NMR: (75 MHz, $CDCl_3$) δ 168.83, 160.98, 137.99, 132.50, 119.66, 115.51, 110.62, 83.83, 28.31 ppm.

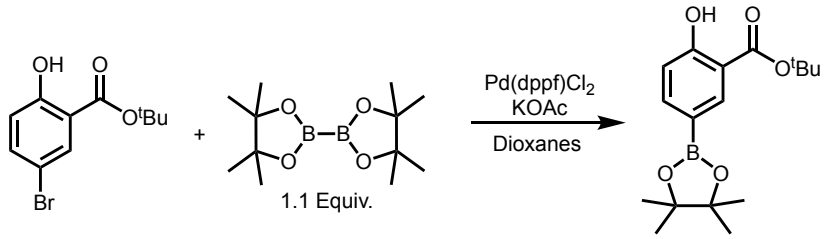

A 2-neck round bottom flask equipped with a stir bar and reflux condenser was charged with *tert*-butyl 5-bromo-2-hydroxybenzoate (8.00 g, 29.3 mmol, 1.00 equiv.), bis(pinacolato)diboron (8.18 g, 32.2 mmol, 1.10 equiv.), KOAc (8.63 g, 87.9 mmol, 3.00 equiv.) and 1,4-dioxane (75 mL). The solution was sparged with N_2 for 45 minutes, after which $Pd(dppf)Cl_2$ was added (0.429 g, 0.586 mmol, 0.020 equiv.) and the solution was stirred at 70 °C for 16 h during which time the solution

darkened considerably. The solution was cooled to room temperature and the dioxanes removed *in vacuo*. The resultant dark brown residue was brought up in deionized water (150 mL) and extracted with ethyl acetate (1x150 mL, 2x50 mL). The organics were dried over $MgSO_4$, filtered, concentrated, and the resultant oil triturated with hexanes to afford *tert*-butyl 2-hydroxy-5-(4,4,5,5-tetramethyl-1,3,2-dioxaborolan-2-yl)benzoate as an off white solid (6.70 g, 71% yield). ^{1}H NMR (300 MHz, $CDCl_3$): δ 11.37 (s, 1H), 8.20 (s, 1H), 7.85 (d, J = 8.3 Hz, 1H), 6.93 (d, J = 8.3 Hz, 1H), 1.63 (s, 9H), 1.34 (s, 12H) ppm. ^{13}C NMR (75 MHz, $CDCl_3$) δ 170.20, 164.49, 141.67, 137.44, 117.16, 113.70, 83.90, 83.12, 28.41, 24.98 ppm. MS (ESI/ion trap) *m/z*: $[M+NH_4]^+$ $C_{17}H_{26}BO_5NH_4$: 338.2; found: 338.1.

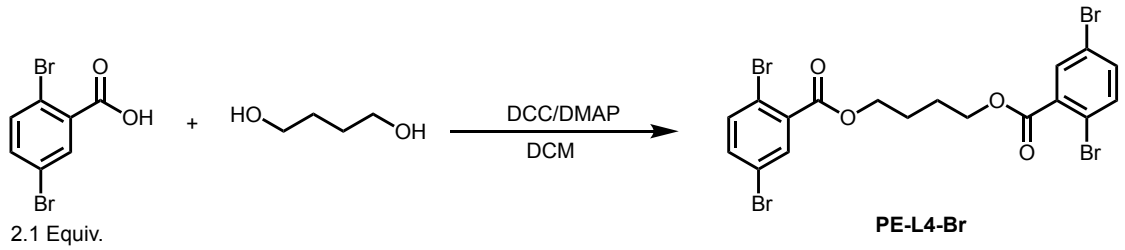

A 250 mL Schlenk flask under N_2 equipped with a stir bar was charged with 2,5-dibromobenzoic acid (1.00 g, 3.57 mmol, 2.10 equiv.), N,N′-dicyclohexylcarbodiimide (1.05 g, 5.10 mmol, 3.00 equiv.), and 4-(dimethylamino)pyridine (0.44 g, 3.57 mmol, 2.10 equiv.), and DCM (anhydrous, 40 mL). The inhomogeneous solution was stirred for 5 minutes, followed by addition of 1,4-butane diol via syringe (0.150 mL, 1.70 mmol, 1.00 equiv.). The solution was stirred overnight at room temperature, filtered over celite, washed with saturated $NaHCO_3$ (2x30 mL) and HCl (1M, 2x30 mL), dried over $MgSO_4$, concentrated, and the resultant oily solid washed with hexanes followed by methanol. The resultant **PE-L4-Br** solid (0.915 g, 88% yield) was used without further purification. ^{1}H NMR (300 MHz, $CDCl_3$) δ 7.90 (d, J = 2.4 Hz, 2H), 7.52 (d, J = 8.6 Hz, 2H), 7.44 (dd, J = 8.5, 2.4 Hz, 2H), 4.41 (bs, 4H), 1.96 (bs, 4H) ppm. ^{13}C NMR (75 MHz, $CDCl_3$) δ 164.98, 135.82, 135.57, 134.17, 121.17, 120.41, 65.51, 25.52 ppm.

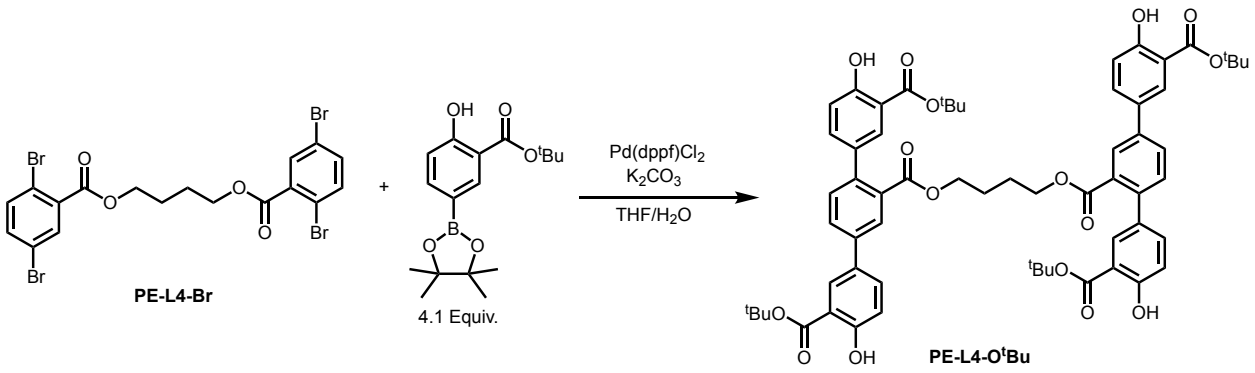

A 250 mL 2-neck round bottom flask equipped with a stir bar and reflux condenser under N_2 was charged with **PE-L4-Br** (1.00 g, 1.63 mmol, 1.00 equiv.), *tert*-butyl 2-hydroxy-5-(4,4,5,5-tetramethyl-1,3,2-dioxaborolan-2-yl)benzoate (2.14 g, 6.68 mmol, 4.1 equiv.), K_2CO_3 (1.80 g, 13.0 mmol, 8.00 equiv.), THF (60 mL) and deionized water (15 mL). The solution was sparged with N_2 for 40 minutes, followed by addition of $Pd(dppf)Cl_2$ (0.0360 g, 0.0490 mmol, 0.0300 equiv.). The solution was heated to 60 °C for 16 h. The reaction mixture was cooled to room temperature, followed by addition of deionized water (150 mL) and EtOAc (150 mL). The organics were separated, and the aqueous layer extracted with EtOAc (2x50 mL). The combined organics were dried over $MgSO_4$, filtered, and concentrated *in vacuo*, and the resultant dark brown residue was subjected to filtration through a pad of silica gel (DCM), and the filtrate concentrated to afford **PE-L4-O^{t}Bu** as an off white powder which was used without further purification (1.74 g, quant.). ^{1}H NMR (300 MHz, $CDCl_3$) δ 11.11 (s, 2H), 11.03 (s, 2H), 7.99 (dd, J = 15.1, 2.2 Hz, 4H), 7.81 – 7.63 (m, 6H), 7.47 – 7.33 (m, 4H), 7.14 – 6.88 (m, 4H), 4.00 (bs, 4H), 1.58 (s, 36H), 1.27 (bs, 4H) ppm. ^{13}C NMR (75 MHz, $CDCl_3$) δ 169.26, 168.14, 161.23, 160.84, 139.28, 138.86, 134.98, 133.45, 131.47, 131.00, 130.26, 129.05, 128.02, 127.67, 117.89, 116.92, 83.05, 82.84, 65.38, 64.06, 27.88, 24.54, 14.93 ppm. MS (ESI/ion trap) *m/z*: $[M–H]^-$ Calcd for $C_{26}H_{65}O_{16}$: 1066.2; found 1065.7.

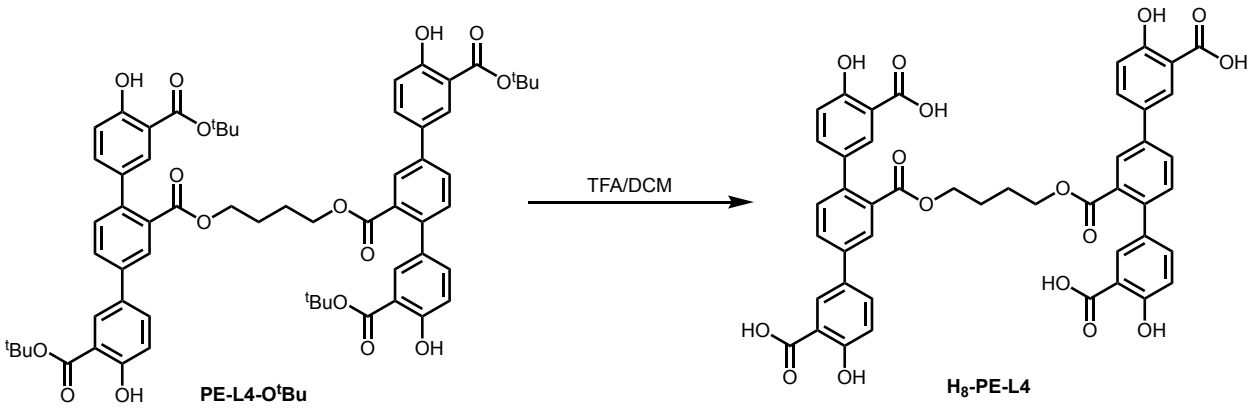

To a 100 mL round bottom flask equipped with a stir bar was added **PE-L4-O^{t}Bu** (1.74 g, 1.63 mmol). The flask was cooled to 0 °C in an ice bath, followed by addition of DCM (15 mL) and concentrated trifluoroacetic acid (15 mL). The solution was removed from the ice bath and allowed to stir at room temperature for 2 h, during which time no solids precipitated out. After, the solution was diluted with hexanes (40 mL), the resultant inhomogeneous mix centrifuged, and the mother liquor decanted. The solids were washed with hexanes repeatedly to remove remaining acid and afford **H_8-PE-L4** as an off-white solid (1.15 g, 84% yield). ^{1}H NMR (300 MHz, DMSO-d_6) δ 8.09 (d, J = 2.4 Hz, 2H), 7.99 – 7.80 (m, 6H), 7.69 (d, J = 2.4 Hz, 2H), 7.51 – 7.40 (m, 4H), 7.07 (d, J = 8.6 Hz, 2H), 6.97 (d, J = 8.5 Hz, 2H), 3.94 (s, 4H), 1.19 (s, 4H) ppm. ^{13}C NMR (75 MHz, DMSO-d_6) δ 171.93, 168.15, 161.36, 160.94, 138.85, 138.32, 135.50, 133.85, 131.66, 129.91, 129.06, 128.31, 127.23, 118.12, 117.17, 79.45, 79.04, 78.58, 64.38, 40.39, 40.33, 40.08, 39.81, 39.52, 39.23, 24.69 ppm. MS (ESI/ion trap) *m/z*: $[M–H]^-$ Calcd for $C_{46}H_{33}O_{16}$: 841.8; found 841.6.

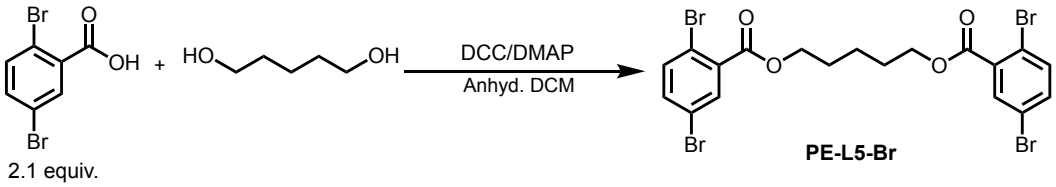

A 100 mL oven-dried Schlenk flask equipped with a stir bar was charged with 2,5-dibromobenzoic acid (0.500 g, 1.77 mmol, 2.10 equiv.), N,N'-dicyclohexylcarbodiimide (0.526 g, 5.31 mmol. 3.00 equiv.), 4-(dimethylamino)pyridine (0.218 g, 1.77 mmol, 2.10 equiv.) and anhydrous

dichloromethane (25 mL), and the slurry was allowed to stir for 5 minutes. Next, 1,5-pentanediol (0.178 mL, 0.84 mmol, 1.00 equiv.) was added via syringe. The inhomogeneous solution was allowed to stir for 24 h, cooled to 0 °C, filtered over celite, and the organics washed with $NaHCO_3$ (1x50 mL) and HCl (1M, 1x60 mL). The organics were then dried over $MgSO_4$, filtered and concentrated *in vacuo* to afford a pale yellow oil. The oil was brought up in fresh hexanes and cooled to 0 °C overnight before filtration over celite and concentration to afford **PE-L5-Br** as an oil which was used without further purification (0.500 g, 94% yield). ^{1}H NMR (300 MHz, $CDCl_3$): δ 7.89 (d, J = 2.4 Hz, 2H), 7.51 – 7.44 (m, 4H), 4.37 (t, J = 6.5 Hz, 4H), 1.86 (dt, J = 14.1, 6.8 Hz, 4H), 1.69 – 1.58 (m, 2H) ppm. ^{13}C NMR (75 MHz, $CDCl_3$) δ 165.03, 135.80, 135.50, 134.14, 121.15, 120.40, 65.85, 28.33, 22.80 ppm.

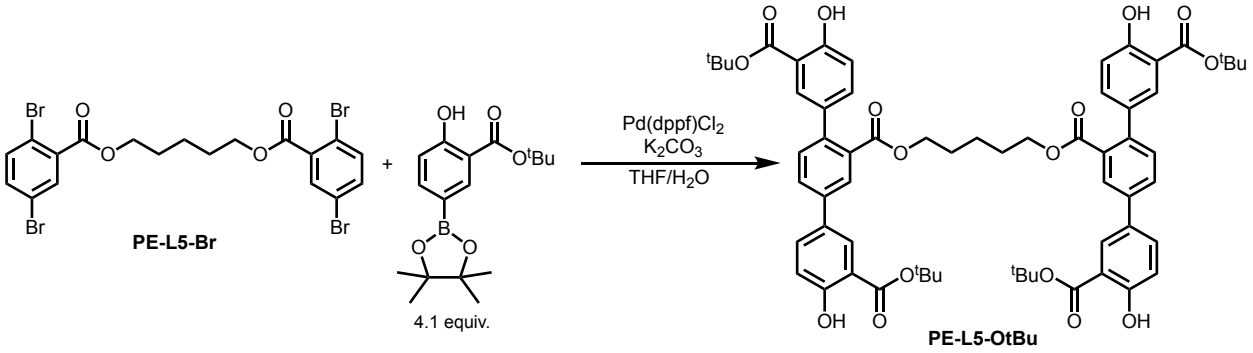

A 250 mL 2-neck round bottom flask equipped with a stir bar and reflux condenser was charged with **PE-L5-Br** (0.500 g, 0.800 mmol, 1.00 equiv.), *tert*-butyl 2-hydroxy-5-(4,4,5,5-tetramethyl-1,3,2-dioxaborolan-2-yl)benzoate (1.04 g, 3.28 mmol, 4.10 equiv.), K_2CO_3 (0.880 g, 6.40 mmol, 8.00 equiv.), THF (40 mL) and deionized water (10 mL). The solution was sparged for 45 minutes with N_2, charged with $Pd(dppf)Cl_2$ (0.0170 g, 0.0240 mmol, 0.0300 equiv.), and stirred at 60 °C 16 h, during which time the solution darkened noticeably to brown. The solution was cooled to room temperature, diluted with deionized water (150 mL) and EtOAc (100 mL). The aqueous layer was further extracted with EtOAc (2x50 mL) and the combined organics were dried over $MgSO_4$,

filtered, concentrated *in vacuo*, and subjected to filtration through a pad of silica gel (DCM). The filtrate was re-concentrated and further dried using Et_2O to afford **PE-L5-O^{t}Bu** as a beige solid and used without additional purification (0.844 g, 98% yield). ^{1}H NMR (300 MHz, $CDCl_3$): δ 11.12 (s, 2H), 11.04 (s, 2H), 8.01 (dd, J = 13.4, 2.2, 4H), 7.74 (d, J = 2.2, 2H), 7.69 (m, 4H), 7.40 (d, J = 7.8, 2H), 7.36 (d, J = 2.4, 2H), 7.06 (d, J = 8.6, 2H), 6.96 (d, J = 8.5, 2H), 4.04, (t, J = 6.5, 4H), 1.64 (s, 18H), 1.58 (s, 18H), 1.28 (bs, 4H), 0.88 (bs, 2H) ppm. ^{13}C NMR (75 MHz, $CDCl_3$) δ 169.77, 168.83, 161.79, 161.38, 139.76, 139.42, 135.46, 133.91, 131.93, 131.69, 131.33, 130.77, 129.76, 129.45, 128.50, 128.24, 118.38, 117.46, 114.31, 113.66, 83.43, 83.21, 65.93, 65.01, 28.38, 28.34, 24.97, 22.38, 15.38. MS (ESI/ion trap) *m/z*: $[M+Na]^+$ Calcd for $C_{63}H_{68}O_{16}Na$: 1103.4; found: 1103.6.

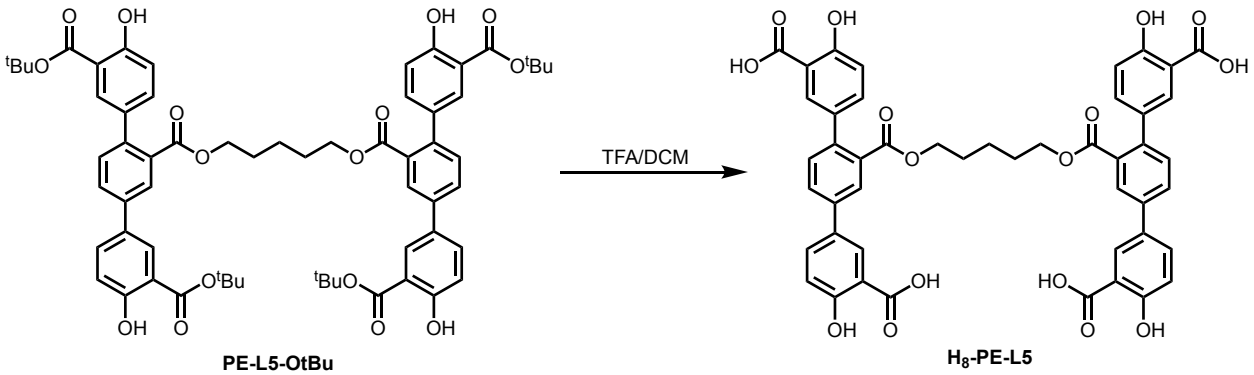

To a 100 mL round bottom flask equipped with a stir bar was added **PE-L5-O^{t}Bu** (0.844 g, 0.780 mmol). The flask was cooled to 0 °C in an ice bath, followed by addition of DCM (7 mL) and concentrated trifluoroacetic acid (7 mL). The solution was removed from the ice bath and allowed to stir at room temperature for 2 h, during which time no solids precipitated out. After, the solution was diluted with hexanes (40 mL), the resultant inhomogeneous mix centrifuged, and the mother liquor decanted. The solids were washed with hexanes repeatedly to remove remaining acid and afford **H$_8$-PE-L5** as an off-white solid (0.593 g, 87% yield). ^{1}H NMR (500 MHz, DMSO-d_6): δ

8.08 (d, J = 2.5, 2H), 7.9 (d, J = 2.1, 2H), 7.87 (dd, J = 8.7, 2.4, 2H), 7.81 (dd, J = 8.1, 2.1, 2H), 7.69 (d, J = 2.5, 2H), 7.43 (m, 4H), 7.06, (d, J = 8.6, 2H), 6.97 (d, J = 8.5, 2H), 3.97 (t, J = 6.2, 4H), 1.25 (dt, J = 15.8, 6.2, 4H), 0.74 (dt, J = 15.8, 6.2, 2H) ppm. ^{13}C NMR (75 MHz, DMSO-d_6) δ 171.73, 168.04, 161.07, 160.68, 138.56, 138.02, 135.29, 133.65, 131.53, 131.16, 130.97, 129.61, 128.82, 128.05, 126.92, 117.90, 117.00, 113.42, 112.66, 64.55, 27.52, 21.83 ppm. MS (ESI/ion trap) *m/z*: $[M–H]^-$ Calcd for $C_{47}H_{35}O_{16}$: 855.7; found: 855.6.

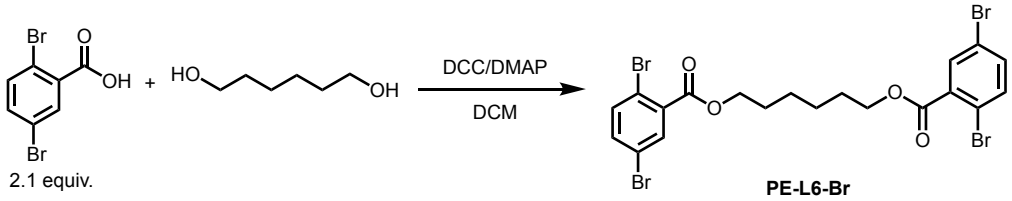

A 100 mL oven-dried Schlenk flask equipped with a stir bar was charged with 2,5-dibromobenzoic acid (1.00 g, 3.57 mmol, 2.10 equiv.), N,N'-dicyclohexylcarbodiimide (1.05 g, 5.09 mmol. 3.00 equiv.), 4-(dimethylamino)pyridine (0.436 g, 3.57 mmol, 2.10 equiv.) and anhydrous dichloromethane (40 mL), and the slurry was allowed to stir for 5 minutes. Next, 1,6-hexanediol (0.201 g, 1.70 mmol, 1.00 equiv.) was added. The inhomogeneous solution was allowed to stir for 24 h. The reaction was then filtered over celite and rinsed with DCM. The organics were washed with $NaHCO_3$ (1x50 mL) and HCl (1 M, 1x60 mL). The organics were then dried over $MgSO_4$, filtered and concentrated *in vacuo*. The resulting solid was rinsed with MeOH and filtered to afford **PE-L6-Br** as a white solid (0.980 g, 90% yield). ^{1}H NMR (500 MHz, $CDCl_3$) δ 7.89 (d, *J* = 2.4 Hz, 2H), 7.52 (d, *J* = 8.5 Hz, 2H), 7.44 (dd, *J* = 8.5, 2.4 Hz, 2H), 4.35 (t, *J* = 6.6 Hz, 4H), 2.41 – 1.69 (m, 4H), 1.67 – 0.57 (m, 4H). ^{13}C NMR (75 MHz, $CDCl_3$) δ 165.05, 135.80, 135.46, 134.31, 134.13, 121.14, 120.38, 66.05, 28.59, 25.81.

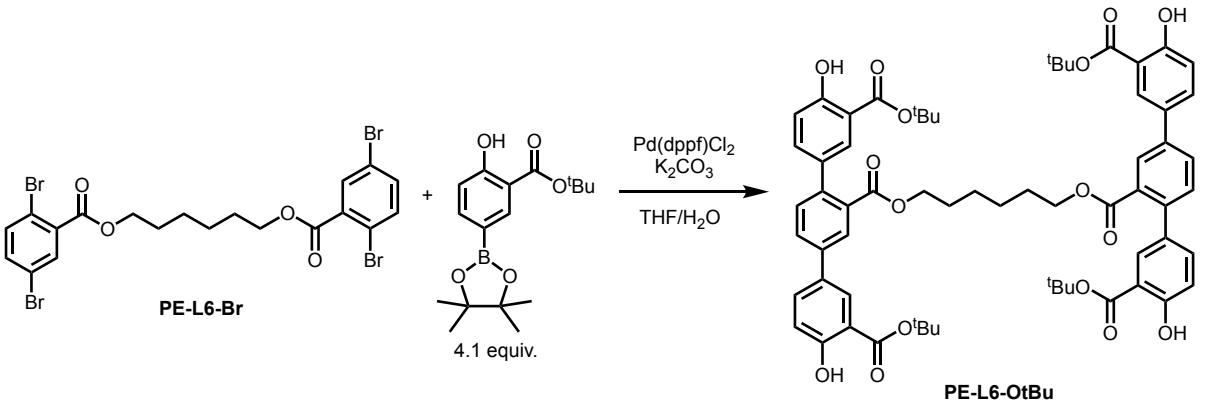

A 250 mL 2-neck round bottom flask equipped with a stir bar and reflux condenser was charged with **PE-L6-Br** (0.600 g, 0.935 mmol, 1.00 equiv.), *tert*-butyl 2-hydroxy-5-(4,4,5,5-tetramethyl-1,3,2-dioxaborolan-2-yl)benzoate (1.23 g, 3.84 mmol, 4.10 equiv.), K_2CO_3 (1.03 g, 7.47 mmol, 8.00 equiv.), THF (60 mL) and deionized water (15 mL). The solution was sparged for 45 minutes with N_2, charged with $Pd(dppf)Cl_2$ (0.0205 g, 0.0280 mmol, 0.0300 equiv.), and stirred at 60 °C 16 h, during which time the solution darkened noticeably to brown. The solution was cooled to room temperature, diluted with deionized water (150 mL) and Et_2O (100 mL). The aqueous layer was further extracted with Et_2O (2x50 mL) and the combined organics were dried over $MgSO_4$, filtered, and concentrated *in vacuo*. The resulting oil was further purified through a silica plug, eluting with DCM. The filtrate was rotovapped, and the oily solid was triturated with MeOH to obtain **PE-L6-O^{t}Bu** as an off-white solid (0.880 g, 86% yield). ^{1}H NMR (500 MHz, $CDCl_3$) δ 11.12 (s, 2H), 11.05 (s, 2H), 8.02 (d, J = 2.4 Hz, 2H), 7.98 (d, J = 2.1 Hz, 2H), 7.75 (d, J = 2.4 Hz, 2H), 7.69 (td, J = 8.4, 2.2 Hz, 4H), 7.44 – 7.37 (m, 4H), 7.06 (d, J = 8.6 Hz, 2H), 6.97 (d, J = 8.5 Hz, 2H), 4.06 (t, J = 6.5 Hz, 4H), 1.27 – 1.21 (m, 4H), 1.00 – 0.93 (m, 4H). ^{13}C NMR (75 MHz, $CDCl_3$) δ 169.80, 168.94, 161.80, 161.41, 139.76, 139.44, 135.49, 133.92, 131.97, 131.83, 131.34, 130.82, 129.80, 129.41, 128.52, 128.25, 118.40, 117.49, 114.35, 113.71, 83.44, 83.21, 28.40, 25.66. MS (ESI/ion trap) *m/z*: $[M+Cl]^-$ Calcd for $C_{64}H_{69}O_{16}Cl$: 1130.2; found: 1130.2.

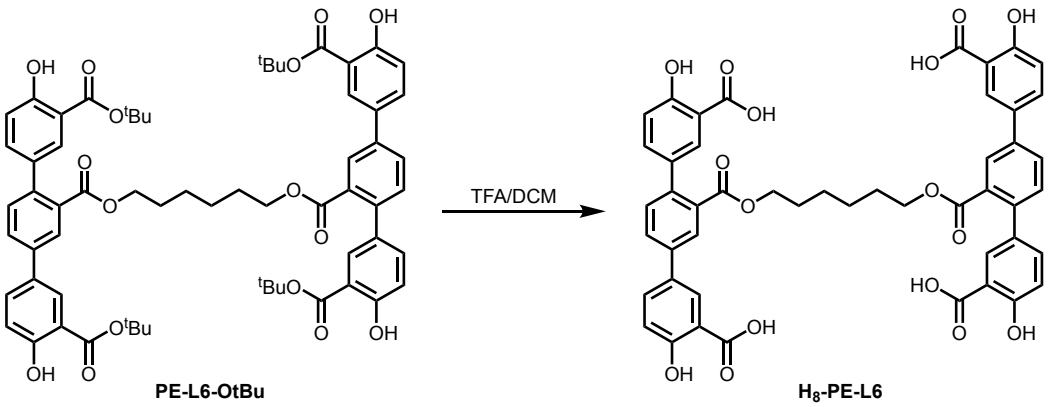

PE-L6-OtBu **H_8-PE-L6**

To a 100 mL round bottom flask equipped with a stir bar was added **PE-L6-O^{t}Bu** (0.750 g, 0.685 mmol). The flask was cooled to 0 °C in an ice bath, followed by addition of DCM (7 mL) and trifluoroacetic acid (7 mL). The solution was removed from the ice bath and allowed to stir at room temperature for 2 h, during solids precipitated out. After, the solution was diluted with hexanes (40 mL), the resultant inhomogeneous mix centrifuged, and the mother liquor decanted. The solids were washed with hexanes and DCM repeatedly to remove remaining acid and afford **H_8-PE-L6** as a white solid (0.534 g, 90% yield). ^{1}H NMR (500 MHz, DMSO) δ 8.09 (d, J = 2.5 Hz, 2H), 7.94 – 7.88 (m, 4H), 7.85 (dd, J = 8.0, 2.1 Hz, 2H), 7.70 (d, J = 2.5 Hz, 2H), 7.51 – 7.45 (m, 4H), 7.09 (d, J = 8.6 Hz, 2H), 7.01 (d, J = 8.6 Hz, 2H), 4.01 (t, J = 6.2 Hz, 4H), 1.28 (s, 4H), 0.85 (s, 4H). ^{13}C NMR (75 MHz, DMSO-d_6) δ 171.64, 168.18, 160.94, 160.59, 138.39, 137.94, 135.36, 133.74, 131.65, 131.12, 131.00, 129.68, 129.58, 128.86, 128.03, 126.83, 117.98, 117.15, 113.53, 112.76, 64.80, 27.68, 25.01. ppm. MS (ESI/ion trap) *m/*z: [M–H]$^-$ Calcd for $C_{48}H_{37}O_{16}$: 869.8; found: 869.4.

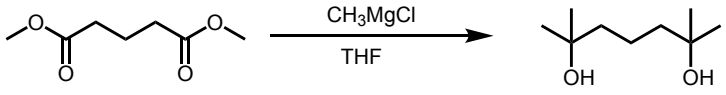

An oven-dried 250 mL 2-neck round bottom flask equipped with a stir bar and a reflux condenser was cooled to 0 °C under N_2. Methylmagnesium chloride (20.0 mL, 3M, 60.0 mmol) was canulaed in. Dimethyl glutarate (1.26 mL, 8.55 mmol) was added dropwise via syringe over the course of

15 minutes. While under N_2, the solution was allowed to warm to room temperature while stirring for 1h, during which time the solution became cloudy and began to thicken to a gel consistency. The solution as then refluxed for 2 h, during which time anhydrous THF (15 mL) was added because the solution had become to viscous to stir. The solution was then cooled to 0 °C, neutralized with excess saturated NH_4Cl (75 mL), and the THF was removed *in vacuo*. The aqueous solution was extracted with DCM (2x50 mL), dried with $MgSO_4$, filtered, and concentrated to yield Dimethyl-2,6-dihydroxyheptane as a semi-crystalline oil (1.33 g, 97% yield). ^{1}H NMR (300 MHz, $CDCl_3$): δ 1.46 (m, 6H), 1.23 (s, 12H). The spectrum is consistent with what is reported in the literature.[1]

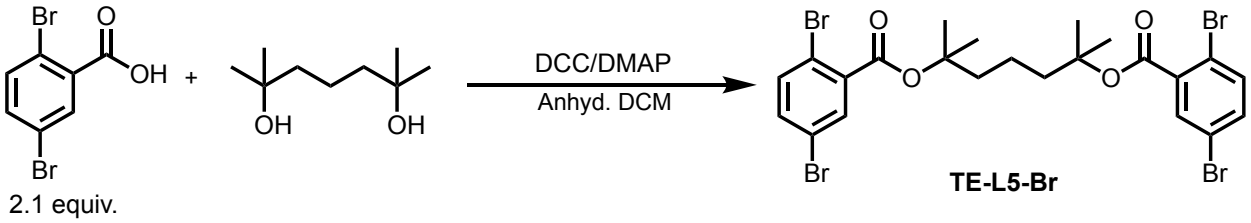

In a typical synthesis, an oven-dried Schlenk flask equipped with a reflux condenser was charged with anhydrous DCM (125 mL), 1,4-dibromobenzoic acid (4.59 g, 16.4 mmol, 2.10 equiv.), N,N′-dicyclohexylcarbodiimide (4.84 g, 23.4 mmol, 3.00 equiv), and 4-(dimethylamino)pyridine (2.00 g, 16.4 mmol, 2.10 equiv.), and the inhomogeneous solution was allowed to stir at room temperature for 5 minutes. Separately, dimethyl-2,6-dihydroxyheptane (1.25 g, 7.81 mmol, 1.00 equiv.) was placed under N_2, dissolved in anhydrous DCM (5 mL) and added to the Schlenk flask via canula. The inhomogeneous solution was refluxed for 48 h, cooled to 0 °C, and filtered over celite. The filtrate was then washed with 1 M HCl (1x 60 mL) and saturated $NaHCO_3$ (1x 100 mL), dried with $MgSO_4$, filtered, and concentrated *in vacuo* to afford a pale yellow oil with some solids present. To this hexanes was added, and chilled at 0 °C overnight, resulting in a white precipitate. The solution was filtered over celite, and the filtrate concentrated to afford **TE-L5-Br** as a yellow

oil which was used without further purification (4.33 g, 81% yield). ^{1}H NMR (300 MHz, $CDCl_3$): δ 7.73 (d, J = 2.3, 2H), 7.44 (s, 1H), 7.42 (s, 1H), 7.37 (d, J = 2.4, 1H), 7.34 (d, J = 2.4, 1H), 1.57 (m, 18H). ^{13}C NMR (75 MHz, $CDCl_3$): δ 164.2, 135.9, 135.5, 134.8, 133.6, 121.0, 119.7, 85.4, 55.7, 25.5, 18.6 ppm. A N,N'-dicyclohexyl urea impurity persisted, as evidenced by ^{13}C peaks at 41.1, 35.0, 26.2, and 24.8 ppm. We note that this impurity does not impact the subsequent synthetic steps.

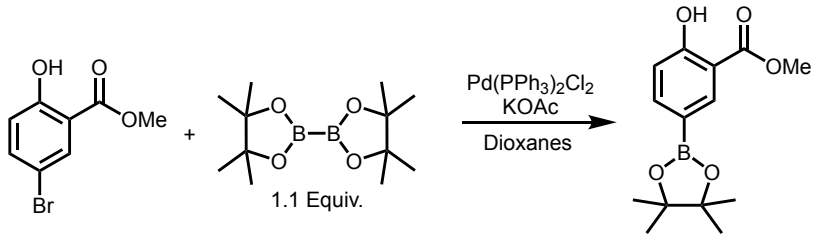

A 500 mL 2-neck round bottom flask equipped with a stir bar and reflux condenser under N_2 was charged with methyl 5-bromo-2-hydroxybenzoate (10.0 g, 43.3 mmol, 1.00 equiv.), bis(pinacolato)diboron (12.1 g, 47.6 mmol, 1.10 equiv.), potassium acetate (12.7 g, 130 mmol, 3.00 equiv.), and 1,4-dioxanes (150 mL). The solution was sparged with N_2 while stirring for 45 minutes, then $Pd(PPh_3)_2Cl_2$ (0.304 g, 0.433 mmol, 0.010 equiv.) was added the solution was refluxed for 18h, during which time the solution turned a dark brown and solids precipitated out. The solution was cooled too room temperature, and the dioxanes was removed *in vacuo*. The dark brown residue was brought up in EtOAc (200 mL) and deionized water (150 mL). The organics were separated off, and the aqueous remnants were extracted with EtOAc (2x70 mL). The organics were combined, dried over $MgSO_4$, filtered, and concentrated. The solids were washed with minimal hexanes to afford methyl 2-hydroxy-5-(4,4,5,5-tetramethyl-1,3,2-dioxaborolan-2-yl)benzoate as an off white solid. The hexanes wash was cooled overnight to afford a second crop of the product. (10.96 g, 91% yield). ^{1}H NMR (300 MHz, $CDCl_3$): δ 11.0 (s, 1H), 8.31 (d, J = 1.6,

1H), 7.88 (dd, J = 8.3, 1.6, 1H), 6.96 (d, J = 8.3, 1H), 3.94 (s, 3H), 1.34 (s, 12H). Spectrum is consistent with what is reported in the literature.[2]

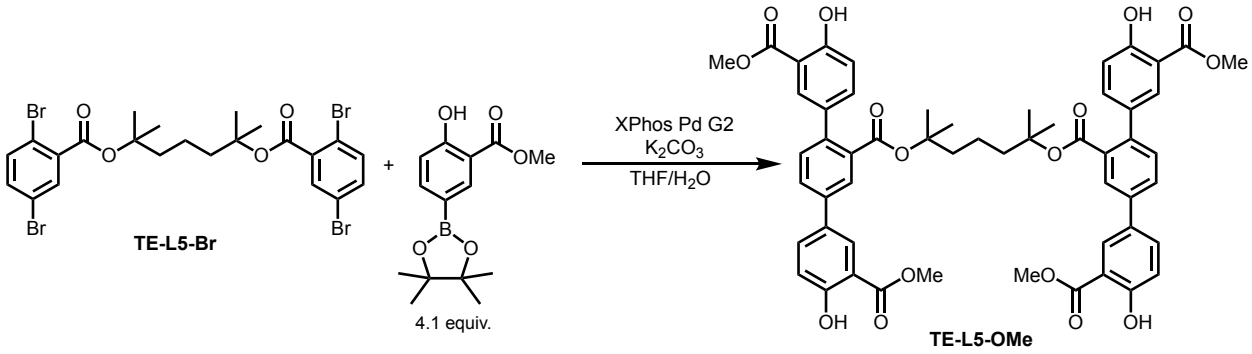

In a typical synthesis, a 500 mL 2-neck round bottom flask equipped with stir bar and reflux condenser was charged with the **TE-L5-Br** (1.30 g, 1.90 mmol. 1.00 equiv.), the aryl boronic pinacol ester (2.17 g, 7.79 mmol, 4.10 equiv.) and THF (124 mL). Separately, potassium carbonate (2.13 g, 15.4 mmol, 8.10 equiv.) was dissolved in deionized water (31 mL) and added to the round bottom flask. The solution was sparged with N_2 for 40 minutes before XPhos Pd G2 (0.0300 g, 0.0380 mmol. 0.0200 equiv.) was added and the solution was stirred at 60 °C for 14 h. The solution was then cooled to room temperature, and the THF was removed *in vacuo*. The aqueous remnants were diluted with ethyl acetate (200 mL) and additional deionized water (150 mL) before being extracted with ethyl acetate (2x70 mL). The organics were dried over $MgSO_4$, filtered, concentrated, and subjected to filtration through a pad of silica gel (9:1 DCM/EtOAc). The solvent was removed, and the resultant pale yellow residue was dissolved in minimal diethyl ether (~2 mL), triturated with hexanes (30 mL) and washed with additional hexanes to afford **TE-L5-OMe** as an off white powder (1.30 g, 70.6 % yield). ^{1}H NMR (300 MHz, $CDCl_3$): δ 10.8 (s, 2H), 10.75 (s, 2H), 8.07 (d, J = 2.3, 2H), 7.90 (d, J = 1.9, 2H), 7.80 (d, J = 2.2, 2H), 7.70 (dd, J = 8.7, 2.4, 2H), 7.61 (dd, J = 8.0, 1.9, 2H), 7.35 (dd, J = 8.5, 2.3, 2H), 7.3 (d, J = 8.0, 2H), 7.06 (d, J = 8.6, 2H), 6.98 (d, J = 8.5, 2H), 3.98 (s, 2H), 3.92 (s, 2H), 1.3 (m, 18H) ppm. ^{13}C NMR (75 MHz, $CDCl_3$): δ

170.5, 167.9, 161.5, 161.1, 139.2, 136.2, 134.3, 133.4, 132.5, 131.2, 129.8, 128.8, 128.2, 127.9, 118.4, 117.5, 112.8, 112.1, 83.6, 52.5, 52.4, 41.4, 25.6 ppm.

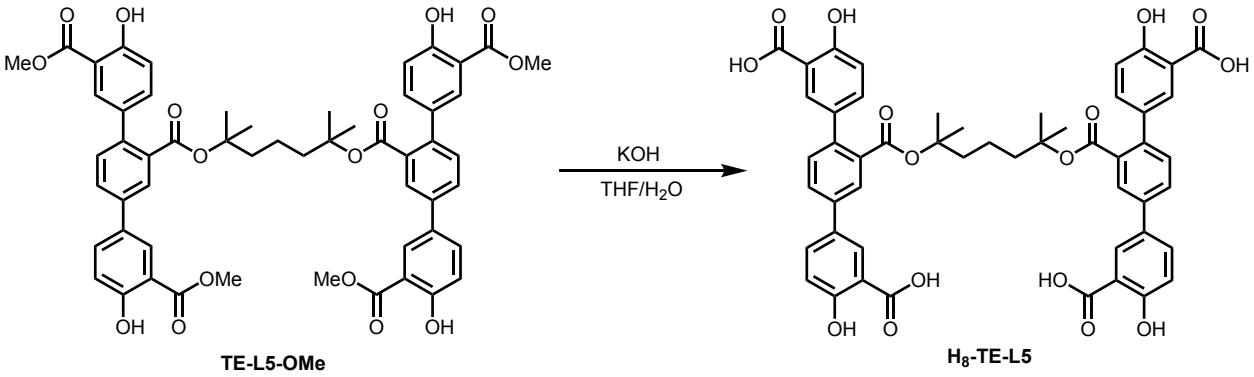

TE-L5-OMe **H_8-TE-L5**

A 250 mL round bottom flask equipped with a stir bar was charged with the tetraester dimer (1.3g, 1.30 mmol, 1.00 equiv.) dissolved in THF (35 mL). Separately, potassium hydroxide (0.960 g, 40.2 mmol, 30.0 equiv.) was dissolved in deionized water (35 mL) and added to the round bottom flask. The flask was capped and the solution was stirred at room temperature for 72 h. The solution was then acidified to pH<2, extracted with ethyl acetate (2x125 mL), dried over MgSO4, filtered, concentrated *in vacuo*, and triturated with minimal diethyl ether and hexanes and washed with additional hexanes to afford **H_8-TE-L5** as a pale yellow powder (1.18 g, 96% yield). ^{1}H NMR (500 MHz, DMSO-d_6): δ 8.0 (d, J=2.4, 2H), 7.80 (dd, J= 8.6, 2.4, 2H), 7.76 (d, J = 1.9, 2H), 7.74 (dd, J = 8.0, 2.0, 2H), 7.57 (d, J = 2.4, 2H), 7.26 (d, J = 8.0, 2H), 7.18 (dd, J = 8.5, 2.4, 2H), 7.03 (d, J = 8.6, 2H), 6.91 (d, J = 8.5, 2H), 1.24 (s, 12H), 1.20 (m, 6H) ppm. ^{13}C NMR (75 MHz, DMSO-d_6): δ 171.7, 167.3, 160.9, 160.5, 138.1, 137.8, 135.4, 133.7, 133.0, 131.3, 130.9, 129.7, 128.4, 127.9, 126.6, 117.9, 117.0, 113.5, 112.6, 83.0, 64.9, 24.9, 15.1 ppm. MS (ESI/ion trap) *m/*z: [M–H]$^-$ Calcd for $C_{51}H_{43}O_{16}$: 911.8; found: 911.6.

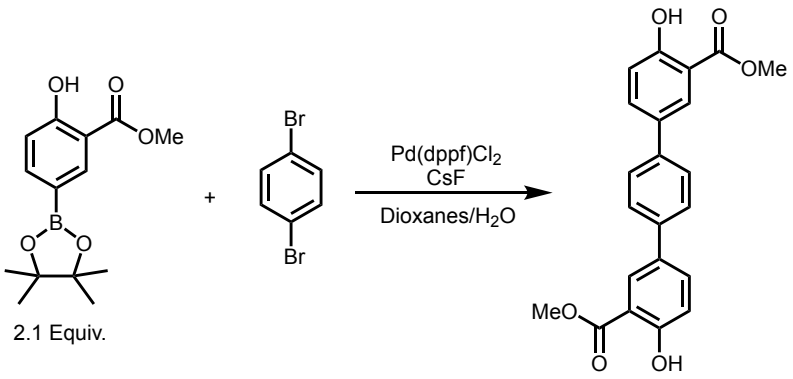

A 250 mL 2-neck round bottom flask equipped with a stir bar and reflux condenser was charged with methyl 2-hydroxy-5-(4,4,5,5-tetramethyl-1,3,2-dioxaborolan-2-yl)benzoate (2.00 g, 7.70 mmol, 2.10 equiv.), 1,4-dibromobenzene (0.808 g, 3.43 mmol, 1.00 equiv.), and cesium fluoride (3.12 g, 20.5 mmol, 6.00 equiv.). Next, 24 mL of 1,4-dioxane followed by 12 mL deionized water were added. While stirring, the solution was purged with nitrogen for 40 minutes. Subsequently $Pd(dppf)Cl_2$ (0.0752 g, 0.103 mmol, 0.030 equiv.) was added, and the solution was allowed to stir at reflux for 18 h, during which time the solution turned a dark grey with grey solids precipitating out. The solution was allowed to cool to room temperature under nitrogen. The solution diluted with deionized water (200. mL), and extracted with dichloromethane (3x 150. mL). The organics were dried using $MgSO_4$, filtered, and concentrated *in vacuo*. The resultant dark brown residue was brought up in minimal dichloromethane, and subjected to filtration through a pad of silica gel (9:1 DCM/EtOAc). The pale yellow filtrate was then concentrated *in vacuo*, and the resultant solids were washed with hexanes to afford 4,4''-dihydroxy-[1,1':4',1''-terphenyl]-3,3''-dicarboxylate (0.947 g, 73% yield) as an off-white solid, which was used without further purification. ^1H NMR (500 MHz, $CDCl_3$): δ 10.79 (s, 2H), 8.11 (d, J = 2.4Hz, 2H), 7.74 (dd, J = 8.6, 2.4Hz, 2H), 7.6 (s, 4H), 7.09 (d, J = 8.6, 2H), 4.00 (s, 6H). The spectrum is consistent with what is reported in the literature.[2]

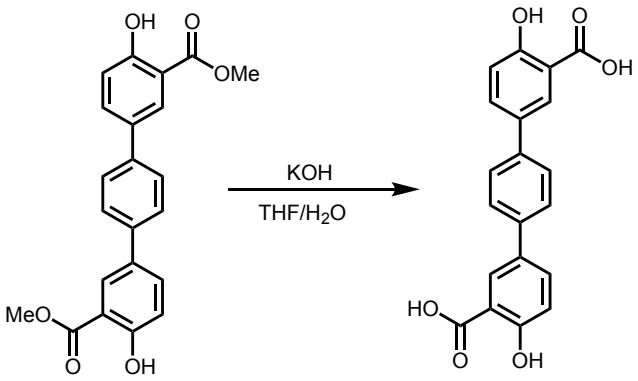

In a typical synthesis, a 500 mL round bottom flask equipped with a stir bar was charged with 4,4"-dihydroxy-[1,1':4',1"-terphenyl]-3,3"-dicarboxylate (2.01 g, 5.31 mmol, 1.00 equiv) and tetrahydrofuran (106 mL). Separately, potassium hydroxide (5.96 g, 106 mmol, 20.0 equiv) was dissolved in deionized water (106 mL) to give a 1 molar solution. The hydroxide solution was added to the round bottom flask containing the dicarboxylate. The inhomogeneous solution was stirred at 50 °C for 24 h, during which time the solution turned yellow and most of the solids dissolved. The solution was cooled to room temperature, and 1 M HCl was added to acidify to pH < 2, causing off-white solids to precipitate out. The tetrahydrofuran was removed *in vacuo*. The off-white solids were filtered, rinsed with copious water, and allowed to first air dry followed by heating at 150 °C for several hours to obtain H4dotpdc (4,4"-dihydroxy-[1,1':4',1"-terphenyl]-3,3"-dicarboxylic acid) as an off-white solid (1.77 g, 96% yield). ^{1}H NMR (500 MHz, DMSO-d_6): δ 8.08 (d, J = 2.45, 2H), 7.88 (dd, J = 8.6, 2.5, 2H), 7.70 (s, 4H), 7.08 (d, J = 8.6, 2H). The spectrum is consistent with what is reported in the literature.[2,3]

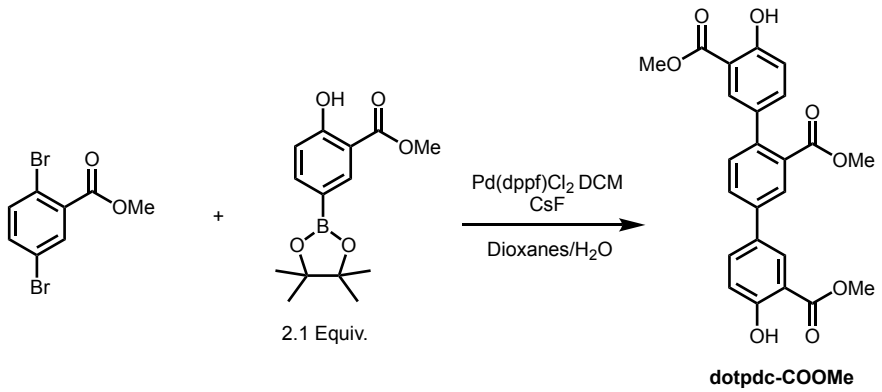

A 100 mL 2-neck roundbottom flask equipped with a stir bar and reflux condenser was charged with methyl 2,5-dibromobenzoate (0.252 g, 0.857 mmol, 1 equiv.), methyl 2-hydroxy-5-(4,4,5,5-tetramethyl-1,3,2-dioxaborolan-2-yl)benzoate (0.500 g, 1.80 mmol, 2.1 equiv.), cesium fluoride (0.780 g, 5.14 mmol, 6 equiv.), H_2O (6 mL) and 1,4-dioxanes (12 mL). The solution was sparged while stirring for 40 minutes, during which time the solids dissolved. $Pd(dppf)Cl_2$ DCM (0.0210 g, 0.0257 mmol, 0.0300 equiv.) and the solution was refluxed for 16 h during which time the solution darkened noticeably. The solution was cooled too room temperature, diluted with DCM (75 mL) and H_2O (75 mL), and the aqueous layer was extracted with DCM (2 x 75 mL). The combined organic layers were dried over $MgSO_4$, filtered over celite, and concentrated *in vacuo*. The resultant brown oil was subjected to filtration through a pad of silica (DCM), concentrated, triturated with MeOH/ hexanes, and filtered to afford dotpdc-COOMe as a white solid (0.215 g, 57% yield). ^{1}H NMR (300 MHz, $CDCl_3$) δ 10.81 (d, J = 6.7 Hz, 2H), 8.13 (s, 1H), 8.03 (s, 1H), 7.85 (s, 1H), 7.81 – 7.67 (m, 2H), 7.41 (t, J = 7.5 Hz, 2H), 7.10 (d, J = 8.5 Hz, 1H), 7.04 (d, J = 8.6 Hz, 1H), 4.01 (s, 3H), 3.96 (s, 3H), 3.71 (s, 3H) ppm. ^{13}C NMR (75 MHz, $CDCl_3$) δ 170.58, 170.50, 168.94, 161.61, 161.20, 139.94, 139.11, 136.03, 134.32, 132.09, 131.43, 130.94, 129.59, 129.45, 128.31, 128.23, 118.47, 117.49, 112.89, 112.25, 52.54, 52.44, 52.19 ppm.

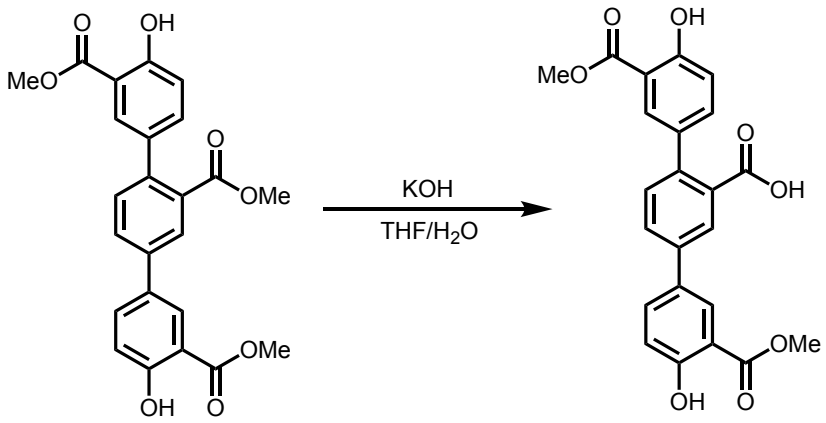

dotpdc-COOMe **H_4dotpdc-COOH**

A 100 mL round-bottom flask equipped with a stir bar was charged with dotpdc-COOMe (0.135 g, 0.310 mmol, 1 equiv.) and tetrahydrofuran (6 mL). Separately, KOH (0.337 g, 6.20 mmol, 20 equiv.) was dissolved in deionized water (6 mL) before being added to the round-bottom flask, causing the solution to immediately turn yellow. The solution was capped and stirred at 50 °C for 24 h, while monitored by TLC. The solution was cooled to room temperature, and acidified to pH < 2 with 1 M HCl, causing white precipitate to form. The tetrahydrofuran was removed *in vacuo*, and the aqueous remnants were extracted with EtOAc (2 x 50 mL), and the organics were combined, dried over $MgSO_4$, filtered, and concentrated *in vacuo* to afford H_4dotpdc-COOH as an off-white powder (0.125 g, 95% yield). ^{1}H NMR (300 MHz, $CDCl_3$) δ 8.09 (d, *J* = 2.5 Hz, 2H), 7.93 (d, *J* = 2.2 Hz, 2H), 7.90 (d, *J* = 2.5 Hz, 1H), 7.83 (dd, *J* = 8.0, 2.1 Hz, 2H), 7.77 (d, *J* = 2.4 Hz, 2H), 7.52 (dd, *J* = 8.5, 2.4 Hz, 2H), 7.47 (d, *J* = 8.0 Hz, 2H), 7.09 (d, *J* = 8.6 Hz, 2H), 7.02 (d, *J* = 8.5 Hz, 2H) ppm ^{13}C NMR (75 MHz, DMSO-d_6) δ 171.66, 171.57, 169.32, 160.86, 160.43, 138.38, 137.79, 135.59, 133.77, 132.56, 131.31, 131.06, 129.84, 129.70, 128.47, 127.96, 126.70, 117.98, 116.94, 113.53, 112.67 ppm. MS (ESI/ion trap) *m/z*: $[M+K-2H]^-$ Calcd for $C_{23}H_{18}O_8K$: 459.3; Found: 459.1.

3. Synthesis and characterization of cross-linked frameworks.

3.1 General procedure for Mg_2dotpdc-PE-LX-R% frameworks.

Mg_2dotpdc-PE-LX-R% frameworks were synthesized using adapted procedure from the literature.[1] A 20 mL scintillation vial was charged with 0.1***(**100-**x%**)** mmol H_4dotpdc and 0.1***x%** mmol **H_8-PE-LX** to give a total of 0.100 mmol ligand and $Mg(NO_3)_2 \cdot 6H_2O$ (2.50 equiv. per $dotpdc^{4-}$ unit), followed by MeOH (5.50 mL) and N,N-dimethylformamide (4.50 mL). The threads of the scintillation vial were wrapped with PTFE tape, capped, and taped with black electrical tape to prevent solvent evaporation. The vial was shaken to dissolve all solids and afford a pale-yellow solution. The solution was then heated in a dry bath at 120 °C for 16 h, after which the vial was cooled to room temperature, the mother liquor was decanted, and the solids re-immersed in fresh DMF and heated to 120 °C. After 3 h the mother liquor was syringed off and replaced with fresh DMF. This process was repeated a total of three times, then repeated three more times with MeOH, heated at 60 °C, to afford MeOH-solvated material. Powder X-ray diffraction measurements and digestion NMRs were taken of the MeOH-solvated material. For full list of reaction conditions with metal salt and ligand ratios, as well as predicted and observed percentages of cross-linked $dotpdc^{4-}$, see **Table S1**.

In a typical MOF digestion experiment to quantify ligand ratios, ~10–15 mg of MeOH-solvated material was suspended in 0.50 mL of DMSO-d_6, followed by addition of 1 drop of DCl in D_2O (20 wt. %). The solution was sonicated briefly to fully dissolve. ^{1}H NMR spectra were taken immediately following (~10 minutes).

3.2 General procedure for Mg_2dotpdc-TE-L5-R% frameworks.

Mg_2dotpdc-TE-L5-R% materials were synthesized the same as above, except the reaction was performed at 120 °C for just 3 h, and all subsequent DMF and MeOH washes were performed at

RT to prevent decomposition of the tertiary ester linkage. For full list of reaction conditions, see Table 1.

3.3 Syntheses of cross-linked frameworks.

Synthesis of Mg_2dotpdc-PE-L5-100% A 20 mL scintillation vial equipped with PTFE tape was charged with **H_8-PE-L5** (0.0857 g, 0.100 mmol, 1.00 equiv.) and $Mg(NO_3)_2 \cdot 6H_2O$ (0.128 g, 0.500 mmol, 5.00 equiv.). The general procedure shown above (see section 3.1) was followed. The ratio of cross-linked dotpdc^{4-} to total dotpdc^{4-} was 100%, as determined by ^{1}H NMR of digested samples. Anal. Calc for $Mg_2(C_{23.5}H_{14}O_8)(CH_3OH)_3(H_2O)_4(C_3H_7NO)_{0.1}$: C, 53.87; H, 4.38; N, 0.12. Found: C, 53.85; H, 4.46; N, 0.12.

Synthesis of Mg_2dotpdc-PE-L5-85% A 20 mL scintillation vial equipped with PTFE tape was charged with **H_8-PE-L5** (0.0643 g, 0.0750 mmol, 0.750 equiv.), H_4dotpdc (0.00880 g, 0.0250 mmol, 0.250 equiv.), and $Mg(NO_3)_2 \cdot 6H_2O$ (0.112 g, 0.438 mmol, 4.38 equiv.), followed by MeOH (5.50 mL) and N,N-dimethylformamide (4.50 mL). The general procedure shown above (see section 3.1) was followed. The ratio of cross-linked dotpdc^{4-} to total dotpdc^{4-} was 85%, as determined by ^{1}H NMR of digested samples. Anal. Calc for $Mg_2(C_{23}H_{13.29}O_{7.71})(CH_3OH)(H_2O)_5$: C, 53.27; H, 4.04. Found: C, 53.13; H, 4.07.

Synthesis of Mg_2dotpdc-PE-L5-66% A 20 mL scintillation vial equipped with PTFE tape was charged with **H_8-PE-L5** (0.0428 g, 0.0500 mmol, 0.500 equiv.), H_4dotpdc (0.0175 g, 0.0500 mmol, 0.500 equiv.), and $Mg(NO_3)_2 \cdot 6H_2O$ (0.0960 g, 0.375 mmol, 3.75 equiv.), followed by MeOH (5.5- mL) and N,N-dimethylformamide (4.50 mL). The general procedure shown above (see section 3.1) was followed. The ratio of cross-linked dotpdc^{4-} to total dotpdc^{4-} was 66%, as determined by ^{1}H NMR of digested samples. Anal. Calc. for

$Mg_2(C_{22.33}H_{12.33}O_{7.33})(CH_3OH)_1(H_2O)_6(C_3H_7NO)_{0.05}$: C, 51.15; H, 4.32; N, 0.09. Found: C, 51.02; H, 4.28; N, 0.11.

Synthesis of Mg_2dotpdc-PE-L5-40% A 20 mL scintillation vial equipped with PTFE tape was charged with **H_8-PE-L5** (0.0214 g, 0.0250 mmol, 0.250 equiv.), H_4dotpdc (0.0263 g, 0.0750 mmol, 0.750 equiv.), and $Mg(NO_3)_2{\cdot}6H_2O$ (0.0800 g, 0.313 mmol, 3.13 equiv.), followed by MeOH (5.50 mL) and N,N-dimethylformamide (4.50 mL). The general procedure shown above (see section 3.1) was followed. The ratio of cross-linked dotpdc^{4-} to total dotpdc^{4-} was 40%, as determined by ^{1}H NMR of digested samples. Anal. Calc. for $Mg_2(C_{21.4}H_{11}O_{6.8})(CH_3OH)_3(H_2O)_4(C_3H_7NO)_{0.05}$: C, 51.03; H, 4.88; N, 0.10. Found: C, 50.79; H, 4.45; N, 0.11.

Synthesis of Mg_2dotpdc-PE-L5-19% A 20 mL scintillation vial equipped with PTFE tape was charged with **H_8-PE-L5** (0.00860 g, 0.0100 mmol, 0.100 equiv.), H_4dotpdc (0.0315 g, 0.0900 mmol, 0.900 equiv.), and $Mg(NO_3)_2{\cdot}6H_2O$ (0.071 g, 0.275 mmol, 2.75 equiv.), followed by MeOH (5.50 mL) and N,N-dimethylformamide (4.50 mL). The general procedure shown above (see section 3.1) was followed. The ratio of cross-linked dotpdc^{4-} to total dotpdc^{4-} was 19%, as determined by ^{1}H NMR of digested samples. Anal. Calc. for $Mg_2(C_{20.64}H_{9.91}O_{6.36})(CH_3OH)_{1.5}(H_2O)_3(C_3H_7NO)_{0.05}$: C, 52.71; H, 4.22; N, 0.13. Found: C, 52.78; H, 4.19; N, 0.14.

Synthesis of Mg_2dotpdc-TE-L5-50% A 20 mL scintillation vial equipped with PTFE tape was charged with **H_8-TE-L5** (0.0228 g, 0.025 mmol, 0.250 equiv.), H_4dotpdc (0.0263 g, 0.0750 mmol, 0.750 equiv.), and $Mg(NO_3)_2{\cdot}6H_2O$ (0.080 g, 0.313 mmol, 3.13 equiv.), followed by MeOH (5.50 mL) and N,N-dimethylformamide (4.50 mL). The general procedure shown above (see section 3.2) was followed. The ratio of cross-linked dotpdc^{4-} to total dotpdc^{4-} was 50%, as determined by

^{1}H NMR of digested samples. Anal. Calc for $Mg_2(C_{22.79}H_{13.57}O_{7.01})(H_2O)_{6.00}(C_3H_7NO)_{0.10}$: C, 51.73; H, 4.35; N, 0.2. Found: C, 52.00; H, 4.33; N, 0.15.

Synthesis of Mg_2dotpdc-TE-L5-23% A 20 mL scintillation vial equipped with PTFE tape was charged with **H_8-PE-L5** (0.009 g, 0.010 mmol, 0.100 equiv.), H_4dotpdc (0.0031 g, 0.0900 mmol, 0.900 equiv.), and $Mg(NO_3)_2{\cdot}6H_2O$ (0.071 g, 0.275 mmol, 2.75 equiv.), followed by MeOH (5.50 mL) and N,N-dimethylformamide (4.50 mL). The general procedure shown above (see section 3.2) was followed. The ratio of cross-linked dotpdc^{4-} to total dotpdc^{4-} was 23%, as determined by ^{1}H NMR of digested samples.Anal. Calc. for $Mg_2(C_{21.35}H_{11.21}O_{6.49})(CH_3OH)_{2.00}(H_2O)_{3.00}$: C, 52.98; H, 4.52. Found: C, 52.93; H, 4.41.

4. Synthesis and characterization of thermolyzed frameworks.

4.1 General

The thermal deprotection method was adapted from the literature.[2] Samples were fully washed prior to thermolysis experiments. A typical reaction scale was 25 mg of MeOH solvated material. The material was transferred to a 10 mL reaction tube, to which was added 2-ethyl-1-hexanol (3.00 mL) and ethylene glycol (0.200 mL), which was found to be a necessary co-solvent. The heterogeneous mixture was subjected to 230 °C microwave heating for 1.00 min, cooled to room temperature, then centrifuged. The mother liquor was decanted, and the solids were immersed in DMF at 120 °C for 3 h, after which time the mother liquor was syringed off and replaced with fresh DMF. This hot DMF wash was repeated three times, followed by immersion in MeOH at 60 °C for 3x3 h washes. The resultant materials were analyzed by PXRD and gas sorption. Digested samples were analyzed by ^{1}H NMR.

In a typical MOF digestion experiment to quantify ligand content, ~10–15 mg of MeOH-solvated material was suspended in 0.500 mL of DMSO-d_6, followed by addition of 1 drop of DCl in D_2O (20 wt. %). The solution was sonicated briefly to fully dissolve. ^{1}H NMR spectra were taken immediately following (~10 minutes).

4.2 Procedures

Mg_2dotpdc-(t)-COOH-49% A washed microcrystalline sample of **Mg_2dotpdc-TE-L5-50%** was subjected to microwave heating and hot solvent washes as described above. The resultant off-white powder was analyzed by digestion ^{1}H NMR in its MeOH-solvated state. Cleavage of the diester moiety and thus conversion to the carboxylic acid was monitored by the loss of the doublet at 6.89 ppm and the growth of the doublet of doublets at 7.47 ppm in the digestion ^{1}H NMR, showing ca. 98% conversion to **Mg_2dotpdc-(t)-COOH-49%**. The found average dotpdc^{4-}/dotpdc^{4-}-COOH ratio of 1:0.96 corresponds to 49% functionalization with templated COOH groups. Anal. Calc. for $Mg_2C_{20.49}H_{9.49}O_{6.98}(H_2O)_{4.00}(C_3H_7NO)_{0.10}$: C, 50.4; H, 3.7; N, 0.28. Found: C, 50.58; H, 3.7; N, 0.16.

Mg_2dotpdc-(t)-COOH-23% A washed microcrystalline sample of **Mg_2dotpdc-TE-L5-23%**was subjected to microwave heating and hot solvent washes as described above. The resultant off-white powder was analyzed by digestion ^{1}H NMR in its MeOH-solvated state. Cleavage of the diester moiety and thus conversion to the carboxylic acid was monitored by the loss of the doublet at 6.89 ppm and the growth of the doublet of doublets at 7.47 ppm in the digestion ^{1}H NMR, showing ca. 99% conversion to **Mg_2dotpdc-(t)-COOH-23%**. The found average dotpdc^{4-}/dotpdc^{4-}-COOH ratio of 1:0.295 corresponds to 23% functionalization with templated COOH groups. Anal. Calc. for $Mg_2(C_{20.23}H_{9.23}O_{6.46})(H_2O)_5(C_3H_7NO)_{0.05}$: C, 49.18; H, 3.96; N, 0.14. Found: C, 49.11; H, 3.82; N, 0.12.

5. Sample activation and gas sorption analysis.

5.1 Activation of parent Mg_2dotpdc, PE cross-linked, and thermally deprotected materials

MeOH-solvated PE cross-linked and thermally deprotected samples were first immersed in DCM for 1 x 3h washes, followed by filtration. The samples were then transferred to a preweighed glass tube and subjected to drying under flowing N_2 at 85 °C for 1 h, and 150 °C for 1 h. After the initial N_2 purge, samples were capped with a Transeal and transferred to a Micromeritics Smart VacPrep instrument and heated under vacuum at 150 °C for overnight. Note that the initial, N_2 purge step was critical; framework collapse was occasionally observed if solvated samples were immediately placed under vacuum.

5.2 Activation of TE cross-linked materials

Due to the thermal sensitivity of the tertiary diester cross-linker, activation was carried out at room temperature. MeOH-solvated cross-linked MOF samples were first immersed in DCM for 1 x 3 h washes, followed by filtration. The samples were then transferred to a preweighed glass tube and subjected to drying under flowing N_2 at RT for 8 h. After the initial N_2 purge, samples were capped with a Transeal and transferred to a Micromeritics Smart VacPrep instrument and heated under dynamic vacuum at RT for overnight. The glass tube and Transeal were subsequently weighed to determine the final mass of the activated sample. Note that the initial, gentle N_2 purge step was critical; framework collapse was occasionally observed if solvated samples were immediately placed under vacuum.

5.3 N_2 adsorption measurements

For all gas adsorption measurements, ~50 mg of sample was transferred to a preweighed glass sample tube. Low-pressure N_2 adsorption experiments (up to 1 bar) were performed using a Micromimetics 3Flex Surface Characterization Analyzer. Ultrahigh purity N_2 (5.0 grade,

99.999%) was used in all adsorption experiments. N_2 adsorption measurements were performed using a liquid N_2 bath (77 K).

BET surface areas were calculated using data points between 0.02 and 0.08 P/P_0. In all cases, the following BET consistency criteria were followed: 1) the pressure range has values of $v(P_0–P)$ increasing with P/P_0, and 2) positive y intercept.[4] All correlation coefficients were ≥0.999.

6. Computational details.

Extended structures of Mg_2dotpdc were created using Mg_2dobdc (MOF-74-Mg) as a starting point, followed by geometry optimization using the Forcite module in Materials Studio.

The relative energies of two different configurations of the cross-linker down the pore channels were probed by density functional theory (DFT) using the Gaussian 16 program. The periodic structure obtained in Materials Studio was truncated to just two neighboring ligands, and a bridging cross-linker was added. The carbons and oxygens of the peripheral phenyl groups on the two ligands were frozen and only the central phenyl ring and bridging cross-linker were allowed to freely remove, mimicking the geometric constraints of the MOF lattice. The geometries of the cross-linker and central phenyl ring were optimized at the B3LYP/6-31+G(d) level of theory with empirical dispersion correction (D3BJ) and solvent correction via a polarization continuum model using methanol as the solvent. Frequency calculations were performed at this same level of theory to confirm that the final geometry was at a stationary point. Free energy corrections were determined at the B3LYP/6-31+G(d) level of theory at 298.15 K. Single point energies were computed at the B3LYP/6-311+G(d, p) level of theory with empirical dispersion correction (D3BJ) and solvent correction via polarization continuum using methanol as the solvent. All molecular structures were rendered in Diamond.

7. Supplementary tables.

Table 2.S1 | Summary of relative equivalents of metal salt and ligand used to synthesize Mg_2dotpdc, Mg_2dotpdc-PE-L5-R%, and Mg_2dotpdc-TE-L5-R%, including the predicted and observed percentages of cross-linked dotpdc^{4-} to total dotpdc^{4-} in the framework (R%).

	Mg^{2+} salt[1] (equiv)	**Cross-linked ligand** (equiv)	**H_4dotpdc** (equiv)	**Predicted**[2] **R%** (%)	**Observed**[3] **R%** (%)
Mg_2dotpdc	2.50	0	1.00	0%	0%
Mg_2dotpdc-PE-L5-R%	2.75	0.100	0.900	18%	19%
	3.13	0.250	0.750	40%	40%
	3.75	0.500	0.500	67%	66%
	4.38	0.750	0.250	86%	85%
	5.00	1.00	0.000	100%	100%
Mg_2dotpdc-TE-L5-R%	2.75	0.100	0.900	18%	23%
	3.13	0.250	0.750	40%	50%

[1] 2.5 equivalents of $Mg(NO3)_2 \cdot 6(H_2O)$ were added per dotpdc^{4-} unit. Note that each ligand dimer contains two dotpdc^{4-} units.
[2] The predicted percentage of cross-linked dotpdc^{4-} relative to the total amount of dotpdc^{4-} ligands in the framework.
[3] Observed percentages were determined by ^{1}H NMR characterization of frameworks digested in DCl/DMSO-d_6.

Table 2.S2 | Summary of BET and Langmuir surface areas of parent, cross-linked, and thermolyzed Mg_2dotpdc frameworks reported in this work. BET surface areas were calculated using data points between 0.02 and 0.08 P/P_0. In all cases, the following BET consistency criteria were followed: 1) the pressure range has values of $v(P_0–P)$ increasing with P/P_0, and 2) positive y intercept.[4] All correlation coefficients were ≥0.999.

	Langmuir SA (m^2/g)	**BET SA** (m^2/g)	**BET *y* intercept**	**BET Correlation Coefficient (R^2)**
Mg_2dotpdc (16 h)	5120 ± 30	2700 ± 40	0.00031	0.9994
Mg_2dotpdc (3 h)	4700 ± 20	2700 ± 30	0.00049	0.9998
Mg_2dotpdc-PE-L5-19%	4920 ± 20	2700 ± 40	0.00029	0.9993
Mg_2dotpdc-PE-L5-40%	4620 ± 14	2740 ± 50	0.00033	0.9995
Mg_2dotpdc-PE-L5-66%	3970 ± 40	2550 ± 50	0.00034	0.9996
Mg_2dotpdc-PE-L5-85%	2150 ± 10	1630 ± 30	0.00066	0.9998
Mg_2dotpdc-PE-L5-100%	1950 ± 8	1580 ± 20	0.00057	0.9997
Mg_2dotpdc-TE-L5-23%	3660 ± 20	2290 ± 50	0.00077	0.9995
Mg_2dotpdc-TE-L5-50%	3300 ± 10	2250 ± 60	0.00073	0.9993
Mg_2dotpdc-(t)-COOH-23%	4480 ± 40	2510 ± 40	0.00034	0.9994
Mg_2dotpdc-(t)-COOH-49%	3640 ± 40	2190 ± 30	0.00051	0.9995

Table 2.S3 | Comparison of standard BET and Langmuir surface areas (m^2/g) with those normalized on a per mol Mg basis (m^2/mmol Mg), to account for differences in the mass of the organic linkers.

	Langmuir SA (m^2/g)	**BET SA** (m^2/g)	**Normalized Langmuir SA** (m^2/mmol Mg)	**Normalized BET SA** (m^2/mmol Mg)
Mg_2dotpdc (16 h)	5120 ± 30	2700 ± 40	1011	533
Mg_2dotpdc (3 h)	4700 ± 20	2690 ± 60	928	533
Mg_2dotpdc-PE-L5-19%	4920 ± 20	2700 ± 40	1008	553
Mg_2dotpdc-PE-L5-40%	4620 ± 14	2740 ± 50	984	584
Mg_2dotpdc-PE-L5-66%	3970 ± 40	2550 ± 50	886	569
Mg_2dotpdc-PE-L5-85%	2150 ± 10	1630 ± 30	496	376
Mg_2dotpdc-PE-L5-100%	1950 ± 8	1580 ± 20	461	375
Mg_2dotpdc-TE-L5-23%	3660 ± 20	2290 ± 50	767	480
Mg_2dotpdc-TE-L5-50%	3300 ± 10	2250 ± 60	739	504

Mg_2dotpdc-(t)-COOH-23%	4480 ± 40	2510 ± 40	907	508
Mg_2dotpdc-(t)-COOH-49%	3640 ± 40	2190 ± 30	757	456

Table 2.S4 | Comparison of the peak widths (full width at half max, or FWHM) of the parent, cross-linked, and thermolyzed Mg_2dotpdc frameworks reported in this work. The FWHM measurements were performed on the second peak in the diffraction pattern, located at $2\theta \sim 6°$; the first peak was challenging to fit due to large background absorbance at low angles.

Framework	FWHM (°)
Mg_2dotpdc (16 h)	0.30
Mg_2dotpdc (3 h)	0.45
Mg_2dotpdc-PE-L5-19%	0.41
Mg_2dotpdc-PE-L5-40%	0.42
Mg_2dotpdc-PE-L5-66%	0.45
Mg_2dotpdc-PE-L5-85%	0.50
Mg_2dotpdc-PE-L5-100%	0.52
Mg_2dotpdc-TE-L5-23%	0.42
Mg_2dotpdc-TE-L5-50%	0.46
Mg_2dotpdc-(t)-COOH-23%	0.42
Mg_2dotpdc-(t)-COOH-49%	0.48

Table 2.S5 | Summary of electronic energies, free energy corrections, and final Gibbs free energies obtained from DFT calculations for the symmetric and offset cross-linker configurations. Calculations were performed at B3LYP/6-311+G(d,p)//B3LYP/6-31+G(d) with D3BJ dispersion correction and solvent correction (methanol).

	Symmetric configuration	**Offset configuration**
Electronic energy (Hartrees)	-3174.8457	-3174.8301
Free energy correction at 298.15 K (Hartrees)	0.6014	0.6036
G^0 at 298.15 K (Hartrees)	-3174.2443	-3174.2265
G^0 at 298.15 K (kcal/mol)	-1990251.187	-1990240.032

Table 2.S6 | DFT optimized structure of the "symmetric" cross-linker configuration.

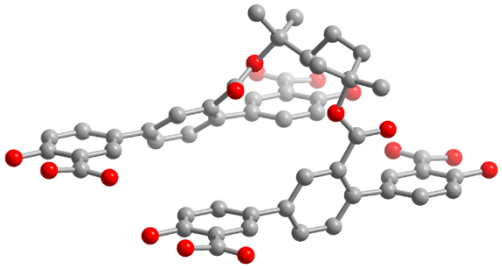

Symbol	**X**	**Y**	**Z**	O	2.920771	7.017883	-1.078704
O	-9.020144	2.971479	-0.375291	O	5.009355	6.131221	-1.364549
C	-6.969235	4.176431	-0.509922	O	5.205096	3.482187	-0.641792
C	-5.578928	4.254499	-0.537644	C	-4.159948	-1.898064	-1.425584
C	-7.461236	0.427044	0.064459	C	-2.769641	-1.819996	-1.453306
C	-6.856401	1.764437	-0.180854	C	-4.802313	3.097172	-0.397977
C	-5.44876	1.863519	-0.219055	C	-3.327499	3.164535	-0.451961
C	-7.622464	2.951898	-0.33058	C	-2.554639	2.41534	0.437472
O	-6.735932	-0.563974	0.061658	C	-1.158434	2.481521	0.440882
O	-8.824403	0.322445	0.347466	C	-4.651949	-5.647451	-0.851203
O	-6.210857	-3.103016	-1.290953	C	-4.047114	-4.310059	-1.096516
C	3.154187	2.277235	-0.507161	C	-2.639473	-4.210977	-1.134717
C	1.763767	2.19941	-0.479402	C	-4.813177	-3.122598	-1.246242
C	0.987265	3.356494	-0.619106	O	-3.926645	-6.638469	-0.854004
C	-0.488315	3.287292	-0.511372	O	-6.015116	-5.75205	-0.568196
C	-1.273426	4.0238	-1.412807	C	5.963474	-3.797261	-1.422823
C	-2.663415	3.981392	-1.379436	C	4.573054	-3.875086	-1.395064
C	3.646188	6.026622	-1.081542	C	3.796552	-2.718001	-1.534768
C	3.041353	4.689229	-0.836228	C	2.312809	-2.765582	-1.424757
C	1.633712	4.590147	-0.798028	C	1.559096	-2.732568	-2.603397
C	3.807416	3.501768	-0.686503	C	0.167294	-2.7928	-2.574156

C	6.455475	-0.047874	-1.997204	H	6.552939	-4.701375	-1.293087
C	5.85064	-1.385266	-1.75189	H	4.091412	-4.834534	-1.235541
C	4.442999	-1.484348	-1.71369	H	2.078412	-2.668855	-3.555134
C	6.616703	-2.572727	-1.602165	H	-0.397429	-2.77391	-3.501953
O	5.730058	0.943388	-1.994366	H	-0.280138	-2.951588	0.781737
O	7.818642	0.056726	-2.280211	H	-0.399242	1.091891	4.424623
O	8.014383	-2.592308	-1.557454	H	-0.160685	2.853993	4.481315
C	-1.993026	-2.977323	-1.313639	H	0.923764	1.787589	5.38436
C	-0.507788	-2.896285	-1.352226	H	1.997053	3.858141	3.547668
C	0.234975	-2.899662	-0.169799	H	3.024423	2.876404	2.478582
C	1.635897	-2.827952	-0.184479	H	3.053385	2.611254	4.236474
O	1.565248	-2.64484	2.160999	H	2.56501	0.49316	2.135609
C	2.38693	-2.813054	1.114262	H	1.018413	-0.205374	2.60027
O	3.598224	-2.937423	1.207108	H	1.778189	-0.286711	4.999381
C	-0.522149	1.719609	1.567985	H	3.330986	0.368873	4.525412
O	-1.007444	0.684417	2.004104	H	3.539473	-1.984581	4.845289
O	0.550265	2.336264	2.065521	H	3.824268	-1.629903	3.152751
C	1.290786	1.829118	3.252331	H	2.78871	-4.350578	4.823507
C	0.349984	1.885547	4.458186	H	3.660865	-4.220076	3.282478
C	2.412076	2.858051	3.385452	H	2.029469	-4.930362	3.329142
C	1.83725	0.419446	2.954042	H	0.103546	-3.540824	4.138794
C	2.494198	-0.246144	4.171931	H	0.192819	-1.769617	4.128444
C	3.047247	-1.656184	3.920674	H	0.971028	-2.68824	5.433794
C	2.043842	-2.772919	3.562043	H	-9.362692	2.081101	-0.164534
C	2.677874	-4.154999	3.751597	H	-6.548701	-3.999139	-1.101697
C	0.745787	-2.682813	4.362332	H	5.418325	5.240022	-1.260575
H	-7.574534	5.070847	-0.621477	H	5.523226	2.639637	-1.038735
H	-5.101985	5.221986	-0.658489	H	8.238185	-0.82759	-2.187998
H	3.750951	1.379353	-0.388394	H	8.33719	-3.506534	-1.612782
H	1.291652	1.230103	-0.359939	H	-4.871449	0.95332	-0.112051
H	-0.778818	4.620197	-2.173649	H	1.061001	5.505241	-0.88594
H	-3.233898	4.558449	-2.101339	H	-2.055978	-5.116306	-1.014473
H	-4.771592	-1.009241	-1.529393	H	3.863223	-0.575967	-1.82376
H	-2.28838	-0.854781	-1.581546	H	-9.019062	-0.627371	0.466831
H	-3.040027	1.800669	1.187436	H	-6.212331	-6.701594	-0.450785

Table 2.S7 | DFT optimized structure of the "offset" cross-linker configuration.

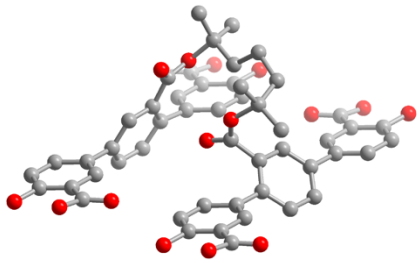

Symbol	X	Y	Z	C	2.65873	4.180958	-0.822637
O	8.439911	-3.528444	-0.965502	C	4.724737	2.933989	-1.136766
C	6.290494	-4.55009	-1.077363	O	4.158391	6.466857	-0.430196
C	4.898876	-4.513771	-1.03384	O	6.176074	5.395506	-0.328694
C	7.124732	-0.910545	-0.248123	C	-5.952189	4.483957	-0.664115
C	6.397892	-2.171032	-0.560371	C	-4.560477	4.447384	-0.707626
C	4.986736	-2.153357	-0.527915	C	-3.892183	3.246627	-0.977594
C	7.052742	-3.400326	-0.842045	C	-2.413797	3.202933	-1.002076
O	6.486397	0.132542	-0.135474	C	-1.660513	4.153843	-1.705735
O	8.50408	-0.93881	-0.033972	C	-0.269441	4.07978	-1.724026
O	6.111905	2.805871	-1.260223	C	-6.786427	0.844411	-1.493355
C	-3.624183	-1.850359	-0.369393	C	-6.059587	2.104898	-1.181107
C	-2.232471	-1.886932	-0.412904	C	-4.648431	2.087224	-1.213562
C	-1.564177	-3.087689	-0.682872	C	-6.714437	3.334192	-0.899433
C	-0.081381	-3.181691	-0.616754	O	-6.147999	-0.198929	-1.605992
C	0.593133	-3.520332	-1.801221	O	-8.165775	0.872676	-1.707505
C	1.982278	-3.580672	-1.867936	O	-8.101606	3.46231	-0.775976
C	-4.458421	-5.489904	-1.198634	C	1.902482	3.021555	-1.058606
C	-3.731581	-4.229417	-0.886385	C	0.420155	3.089974	-1.008142
C	-2.320425	-4.247092	-0.918841	C	-0.342369	2.184908	-0.243784
C	-4.386431	-3.000123	-0.604711	C	-1.73425	2.216373	-0.281007
O	-3.819993	-6.533244	-1.31127	O	0.677459	1.442462	1.878851
O	-5.837769	-5.46164	-1.412784	C	0.322764	1.158533	0.620469
O	-5.7736	-2.872005	-0.481255	O	0.581941	0.048372	0.18511
C	3.962488	1.784225	-1.372085	C	0.208055	-2.589825	1.928929
C	2.57087	1.820545	-1.328562	O	1.005911	-2.259545	2.796646
C	4.230488	-3.312761	-0.763884	O	-1.115164	-2.652406	2.13561
C	2.748143	-3.28441	-0.732329	C	-1.724598	-1.834888	3.239933
C	2.086134	-2.987066	0.453689	C	-1.182905	-2.224243	4.616428
C	0.688309	-2.944344	0.547349	C	-3.207504	-2.178094	3.155518
C	4.796726	5.42377	-0.542844	C	-1.421627	-0.38657	2.826612
C	4.069886	4.163283	-0.855093	C	-1.667546	0.747298	3.823718

C	-1.341611	2.123698	3.20569	H	-0.370663	-0.3538	2.561384
C	0.122793	2.450574	2.834797	H	-1.075445	0.591938	4.732501
C	0.235534	3.869389	2.275081	H	-2.718952	0.770035	4.137685
C	1.062334	2.276582	4.02704	H	-1.635009	2.903488	3.919765
H	6.812599	-5.477447	-1.293107	H	-1.97034	2.281367	2.323299
H	4.331979	-5.422796	-1.210409	H	-0.519174	4.082885	1.515976
H	-4.139247	-0.922218	-0.146953	H	1.228167	4.032471	1.844959
H	-1.653836	-0.990535	-0.225276	H	0.098648	4.581362	3.095676
H	0.005266	-3.709472	-2.694825	H	2.078938	2.578531	3.756014
H	2.471858	-3.827386	-2.806018	H	1.0885	1.235452	4.358977
H	4.488827	0.862072	-1.589344	H	0.722431	2.901299	4.859155
H	2.010764	0.914667	-1.524957	H	8.866342	-2.688971	-0.705335
H	2.662394	-2.780809	1.347205	H	6.533446	3.654254	-1.024292
H	-6.455073	5.417751	-0.427244	H	-6.163736	-4.551352	-1.219488
H	-3.994851	5.352374	-0.509336	H	-6.039119	-1.98011	-0.799875
H	-2.165296	4.928278	-2.275828	H	-8.505991	1.777157	-1.526793
H	0.297064	4.78892	-2.320493	H	-8.351145	4.40066	-0.751792
H	-0.175069	-1.850446	4.789389	H	4.487838	-1.217578	-0.30487
H	-1.177555	-3.314332	4.722503	H	-1.827015	-5.191869	-1.113659
H	-1.851279	-1.815398	5.382574	H	2.164457	5.115934	-0.587027
H	-3.377887	-3.229416	3.411336	H	-4.157566	1.152715	-1.456441
H	-3.599018	-1.993856	2.154159	H	-2.304421	1.498423	0.29771
H	-3.763136	-1.558338	3.867265	H	8.783462	-0.020267	0.146199
H	-1.993284	-0.184242	1.913078	H	6.458549	6.313796	-0.151924

8. Supplementary figures.

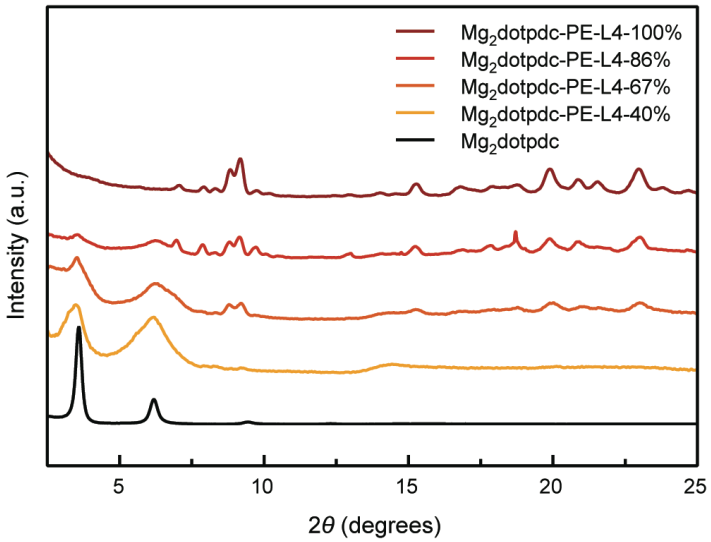

Fig. 2.S1 | PXRD patterns of materials made with varying amounts of H_8-PE-L4 showing broadened peaks and the presence of a new phase.

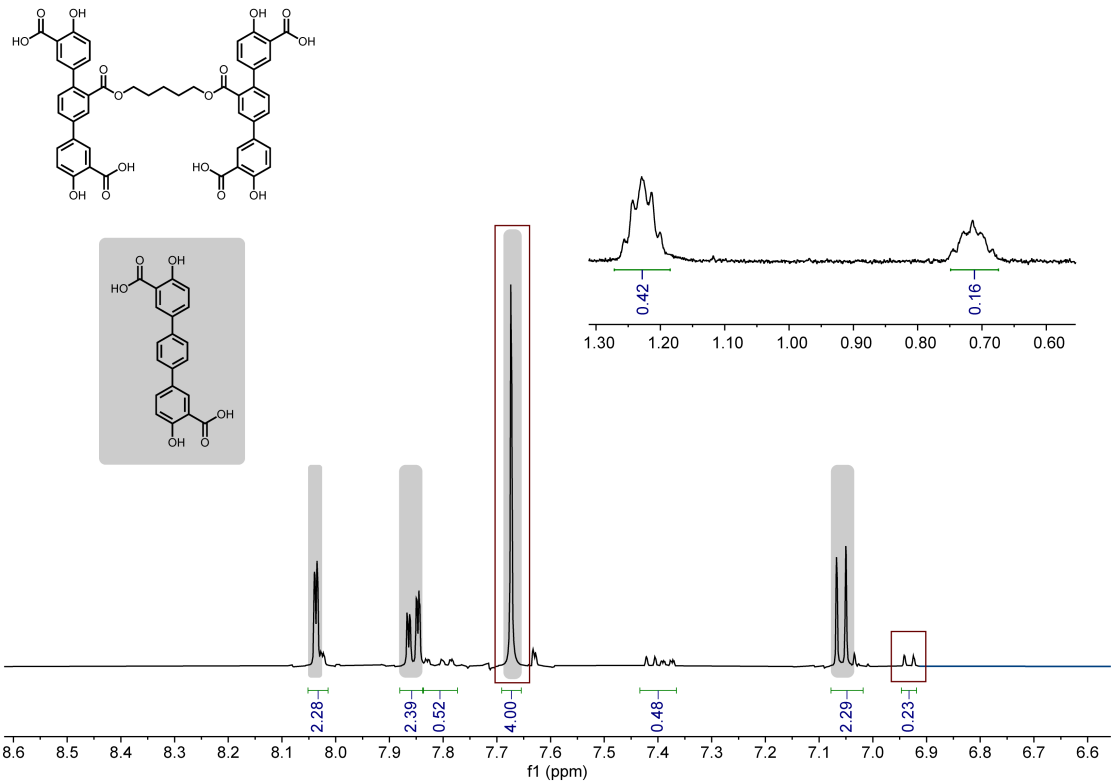

Fig. 2.S2 | The ^{1}H NMR spectra of MeOH-solvated **Mg_2dotpdc-PE-L5-19%** after digestion in DMSO-d_6/DCl. The relative ratio of 0.23:4.00 observed between the cross-linked dotpdc^{4-} doublet

at 6.93 ppm (1H per cross-linked dotpdc^{4-} unit) to the H_4dotpdc singlet at 7.67 ppm (4H) corresponds to a percentage of 19%.

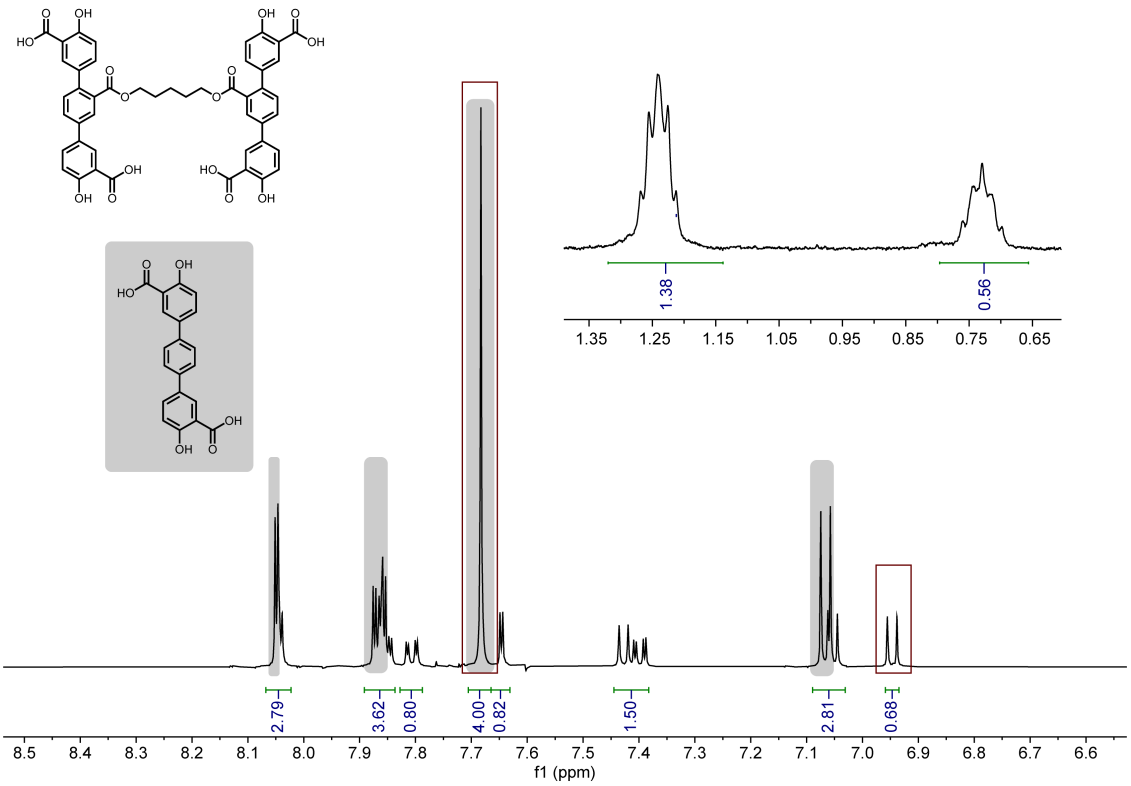

Fig. 2.S3 | ^{1}H NMR of MeOH-solvated **Mg_2dotpdc-PE-L5-40**% after digestion in DMSO-d_6/DCl. The relative ratio of 0.68:4.00 observed between the cross-linked dotpdc^{4-} doublet at 6.93 ppm (1H per cross-linked dotpdc^{4-} unit) to the H_4dotpdc singlet at 7.67 ppm (4H) corresponds to a percentage of 40%.

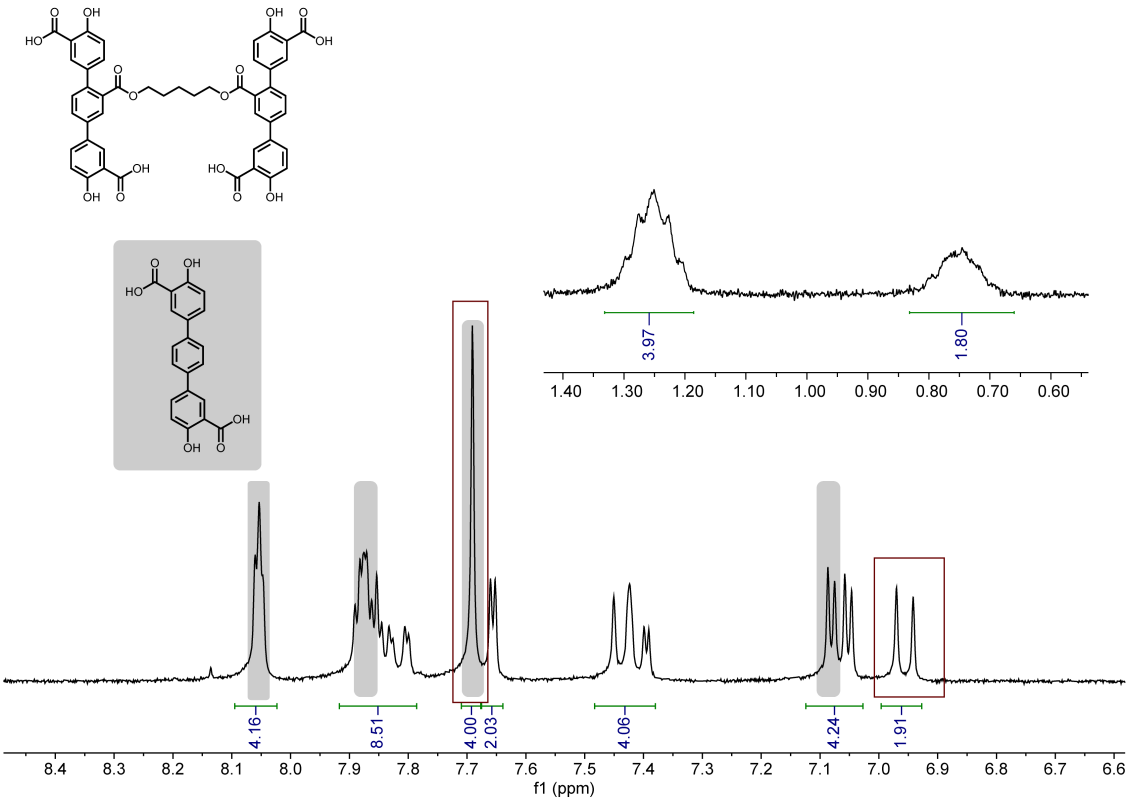

Fig. 2.S4 | ^{1}H NMR of MeOH-solvated **Mg_2dotpdc-PE-L5-66%** after digestion in DMSO-d_6/DCl. The relative ratio of 1.91:4.00 observed between the cross-linked dotpdc^{4-} doublet at 6.93 ppm (1H per cross-linked dotpdc^{4-} unit) to the H_4dotpdc singlet at 7.67 ppm (4H) corresponds to a percentage of 66%.

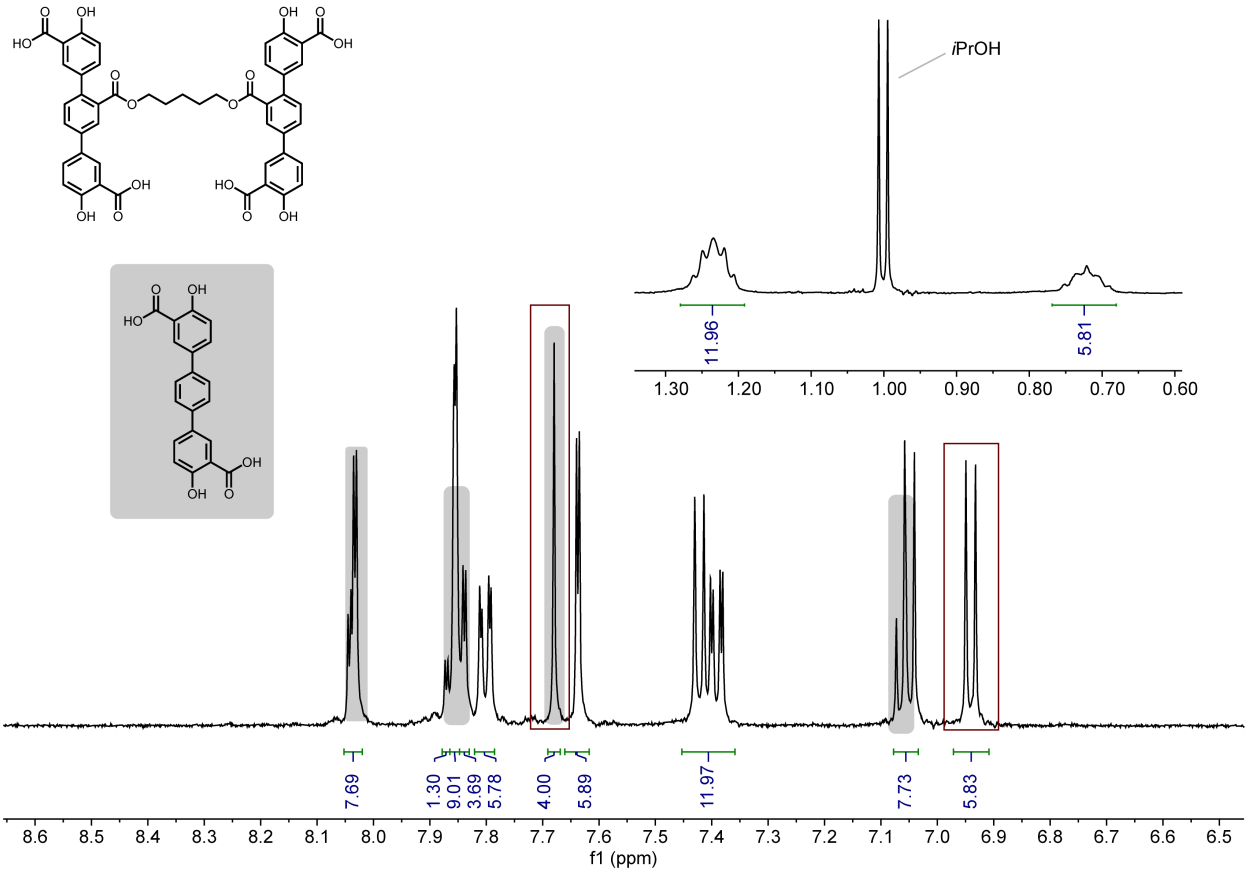

Fig. 2.S5 | ^{1}H NMR of MeOH-solvated **Mg_2dotpdc-PE-L5-85%** after digestion in DMSO-d_6/DCl. The relative ratio of 5.83:4.00 observed between the cross-linked dotpdc^{4-} doublet at 6.93 ppm (1H per cross-linked dotpdc^{4-} unit) to the H_4dotpdc singlet at 7.67 ppm (4H) corresponds to a percentage of 85%. An iPrOH impurity in this NMR sample is noted at 1.01 ppm.

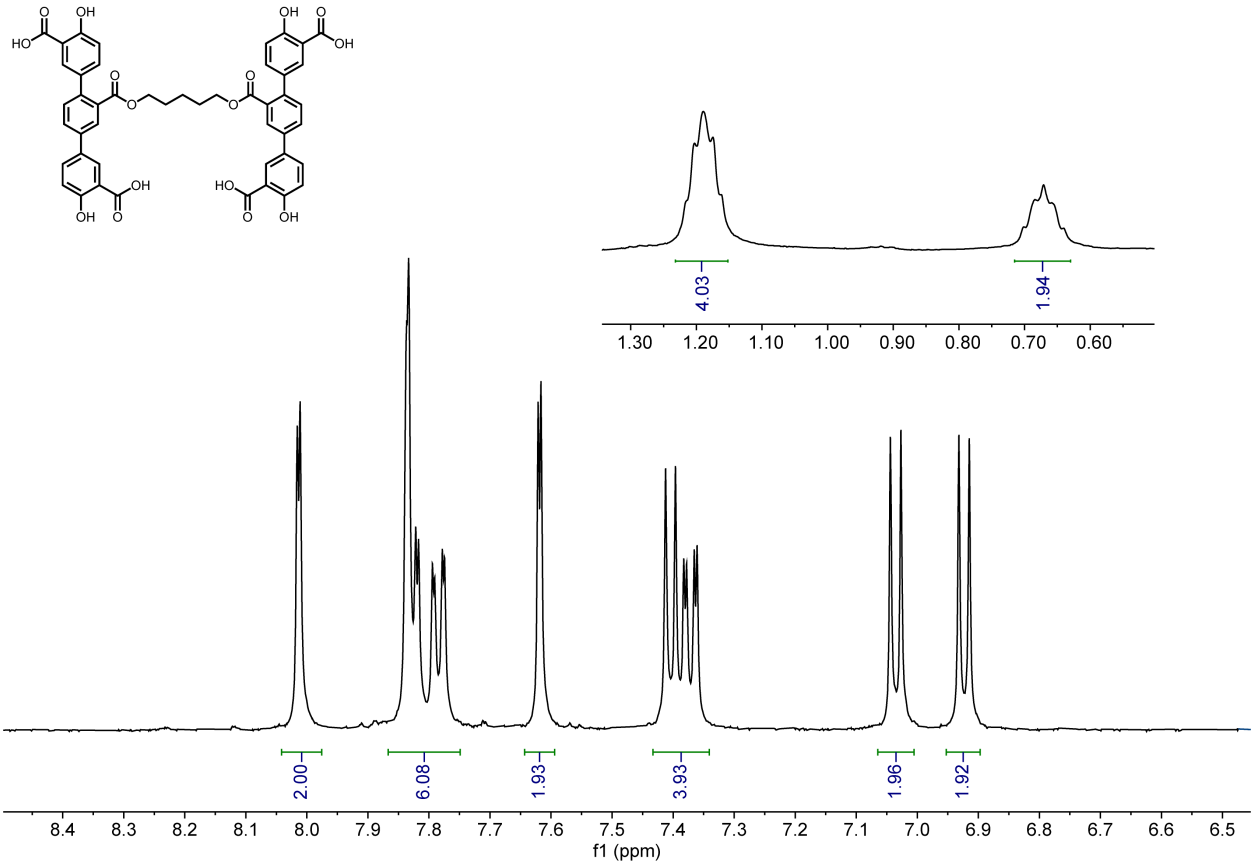

Fig. 2.S6 | ^{1}H NMR of MeOH-solvated **Mg_2dotpdc-PE-L5-100%** after digestion in DMSO-d_6/DCl showing 100% cross-linked dotpdc^{4-} present.

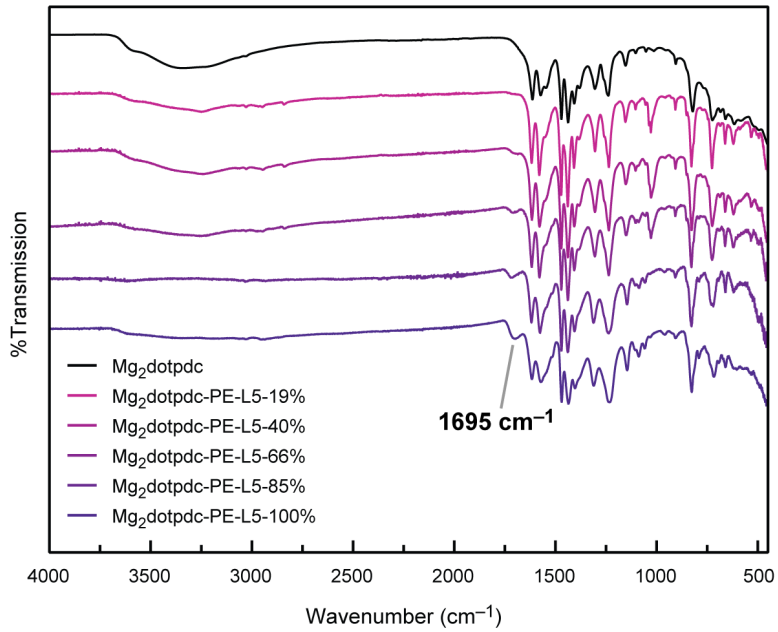

Fig. 2.S7 | FTIR spectrum of the frameworks Mg_2dotpdc, and Mg_2dotpdc-PE-L5-X% (X = 19–100). A new C=O stretch at ~1695 cm^{-1} grows in as the percentage of ester cross-linked ligands increases.

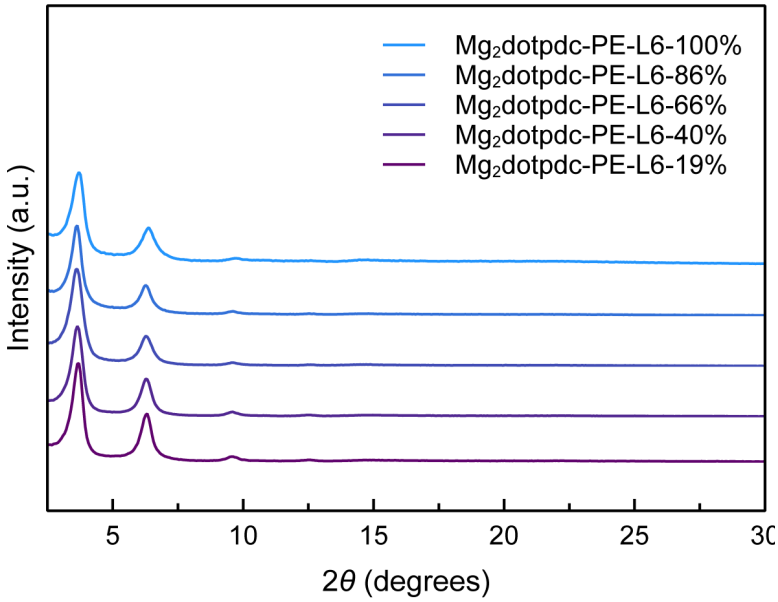

Fig. 2.S8 | PXRD patterns of materials made with varying amounts of H_8-PE-L6, showing the successful formation of the desired MOF-74 phase.

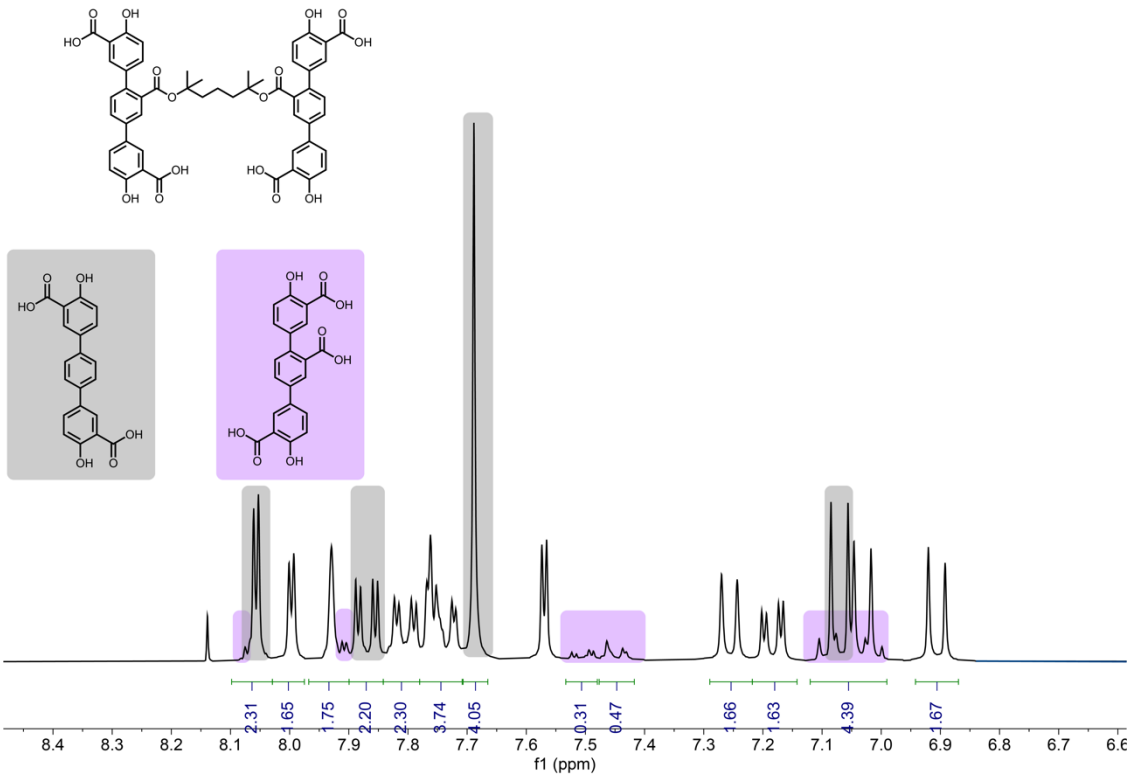

Fig. 2.S9 | ^{1}H NMR of **Mg_2dotpdc-TE-67%** synthesized using 16 h reaction conditions after digestion in DMSO-d_6/DCl. Approximately 20% decomposition to H_4dotpdc-COOH is observed and the associated NMR peaks are highlighted in purple.

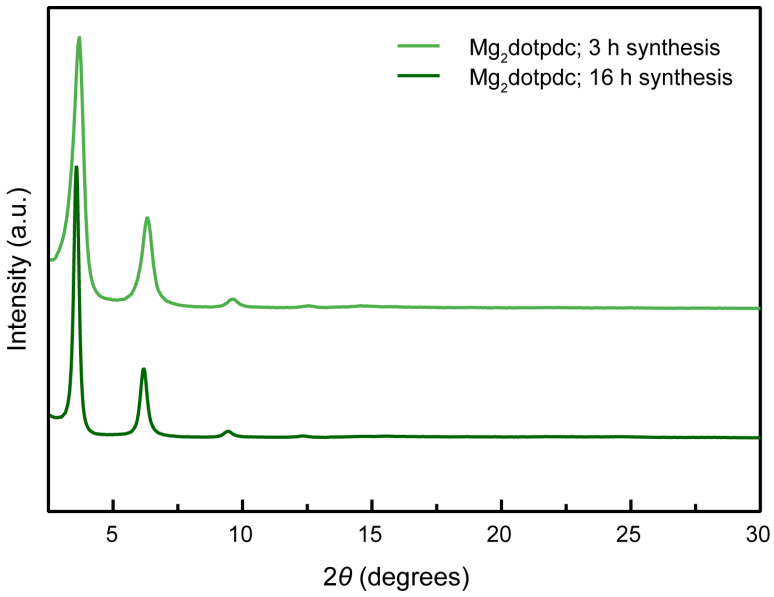

Fig. 2.S10 | PXRD pattern of Mg_2dotpdc synthesized under 3 h (top trace) and 16 h (bottom trace) reaction conditions.

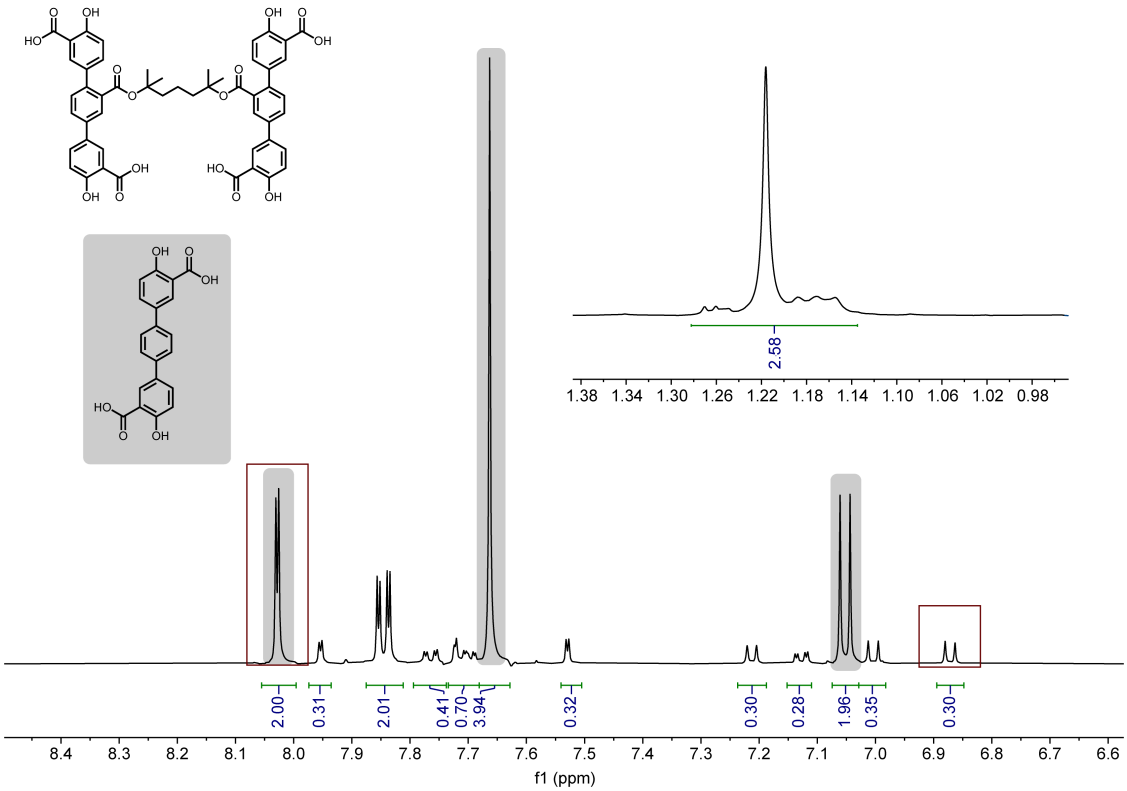

Fig. 2.S11 | ^{1}H NMR of MeOH-solvated **Mg$_2$dotpdc-TE-L5-23%** after digestion in DMSO-d_6/DCl. The relative ratio of 0.30:2.00 observed between the cross-linked dotpdc^{4-} doublet at 6.87 ppm (1H per cross-linked dotpdc^{4-} unit) to H$_4$dotpdc doublet at 8.04 ppm (2H) corresponds to a percentage of 23%.

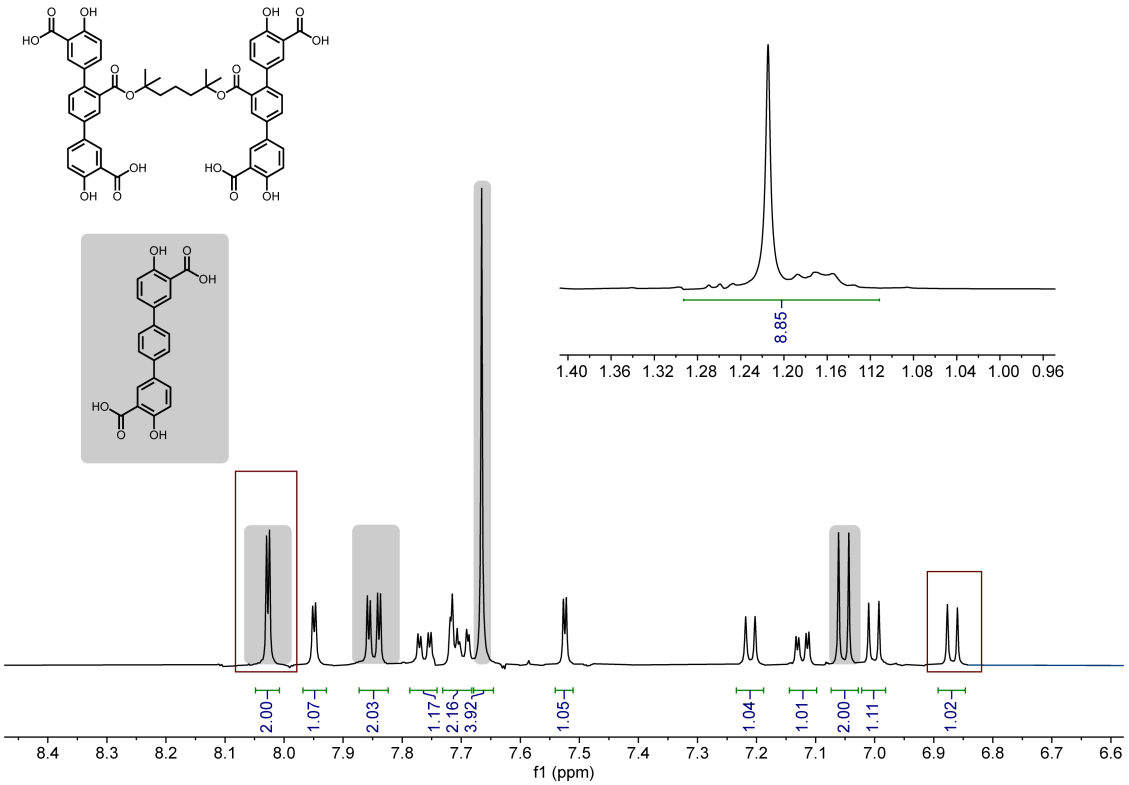

Fig. 2.S12 | ^{1}H NMR of MeOH-solvated **Mg$_2$dotpdc-TE-L5-50%** after digestion in DMSO-d_6/DCl. The relative ratio of 1.02:2.00 observed between the cross-linked dotpdc^{4-} doublet at 6.87 ppm (1H per cross-linked dotpdc^{4-} unit) to H$_4$dotpdc doublet at 8.04 ppm (2H) corresponds to a percentage of 50%.

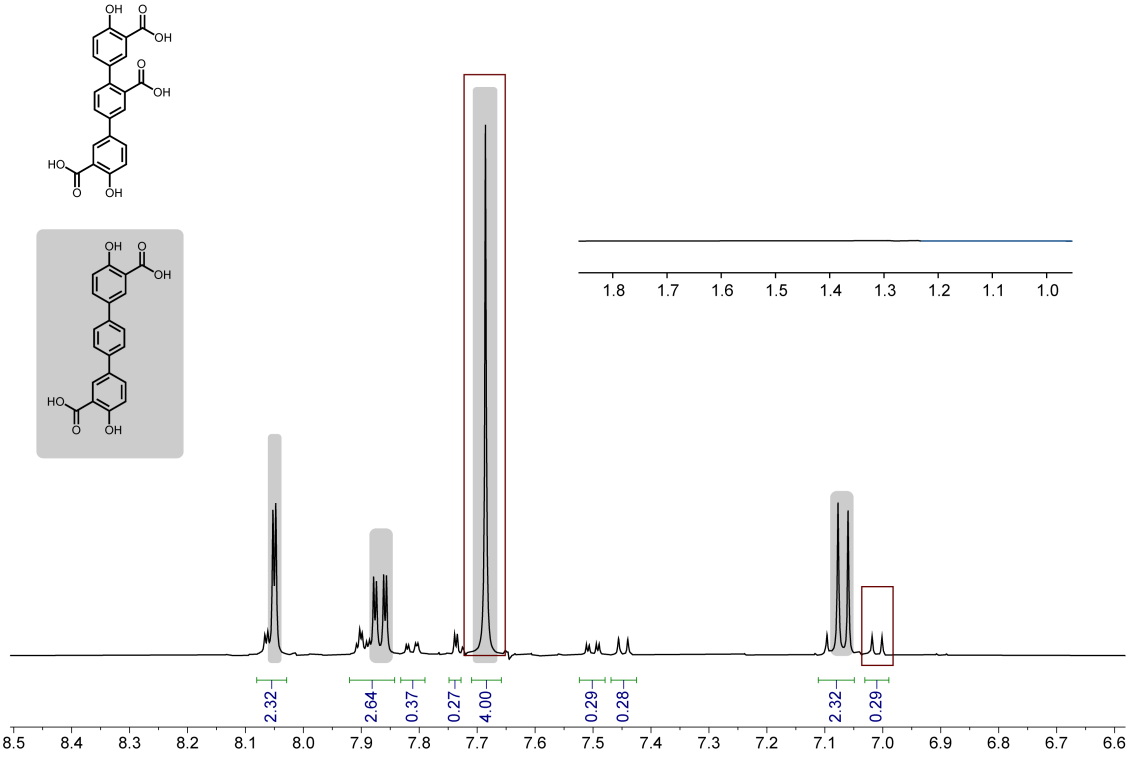

Fig. 2.S13 | ^{1}H NMR of MeOH-solvated **Mg_2dotpdc-(t)-COOH 23%** after digestion in DMSO-d_6/DCl. The relative ratio of 0.30:4.00 observed between the H_4dotpdc-COOH doublet of doublets at 7.5 ppm (1H) to H_4dotpdc singlet at 7.67 ppm (4H) corresponds to a percentage of 23%. The loss of the cross-linker alkyl peak at 1.22 ppm demonstrates complete cleavage.

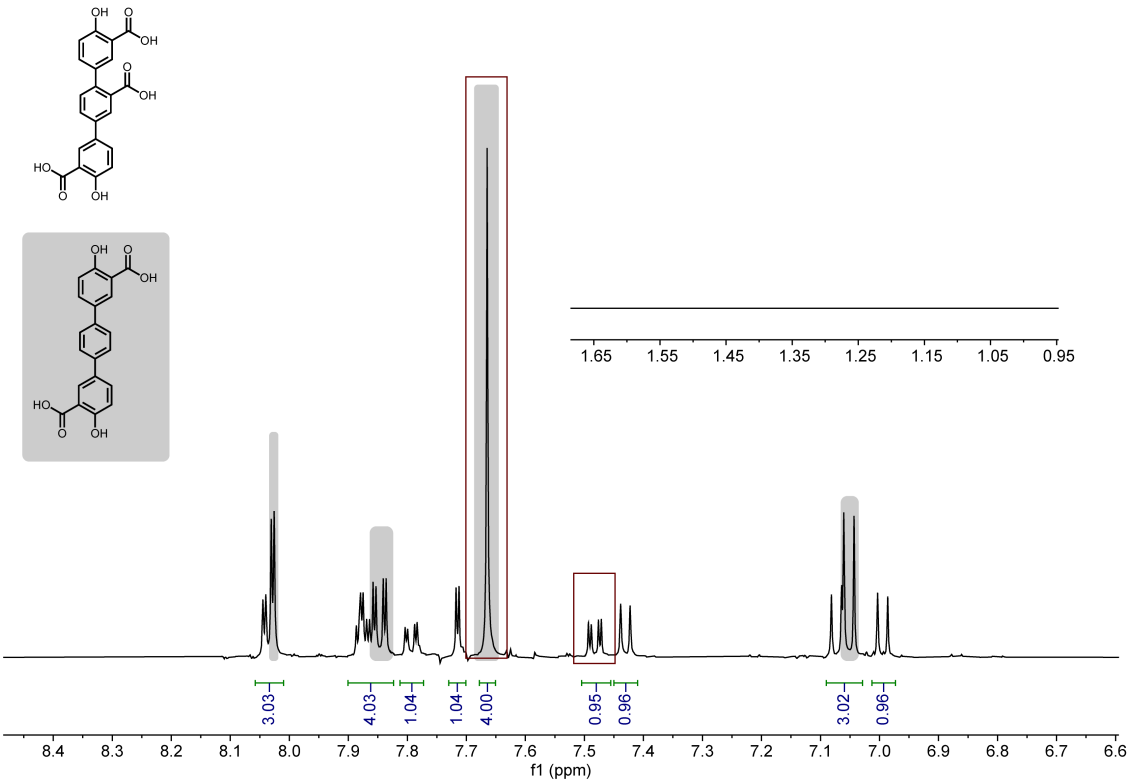

Fig. 2.S14 | ^{1}H NMR of MeOH-solvated **Mg_2dotpdc-(t)-COOH-49%** after digestion in DMSO-d_6/DCl. The relative ratio of 0.95:4.00 observed between the H_4dotpdc-COOH doublet of doublets at 7.5 ppm (1H) to the H_4dotpdc singlet at 7.67 ppm (4H) corresponds to a percentage of 49%.

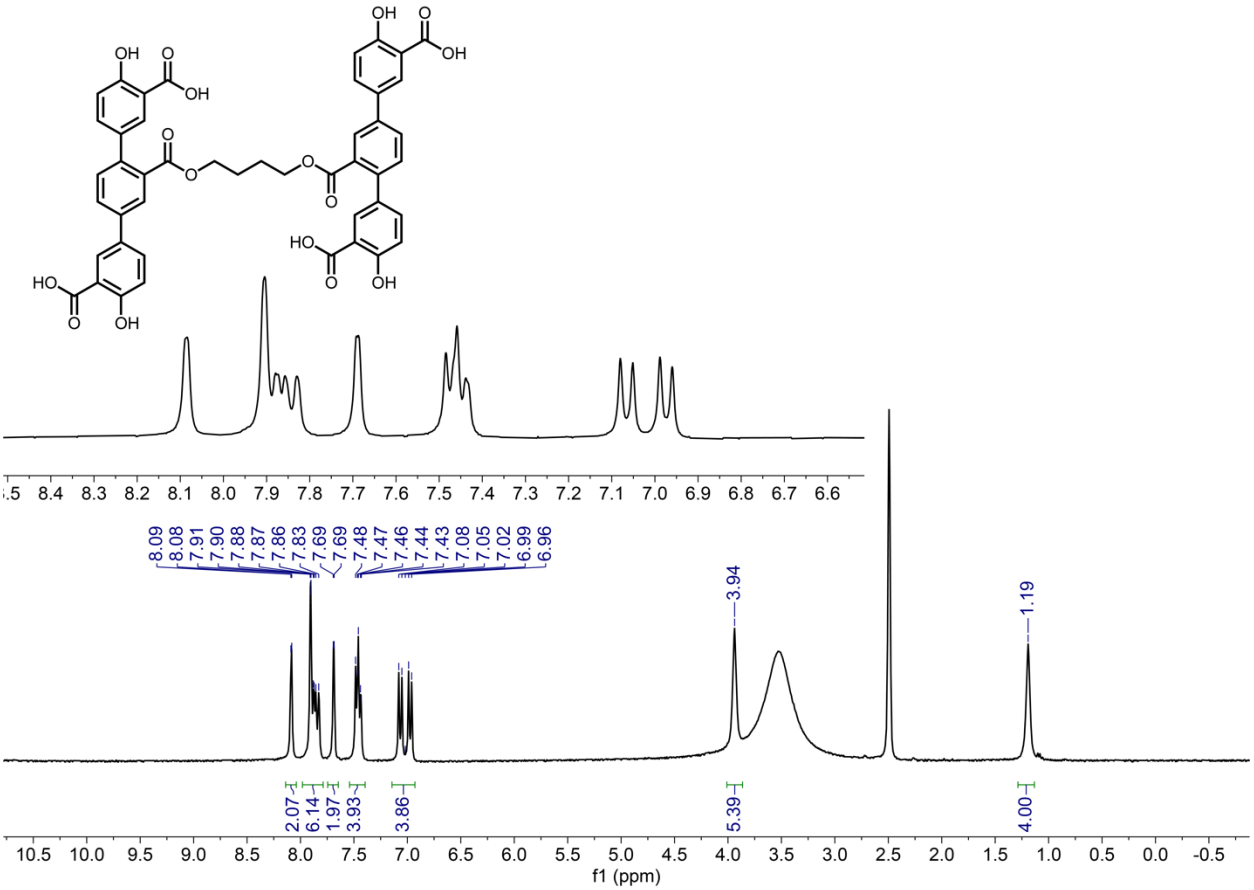

Fig. 2.S15 | ^{1}H NMR of **H$_8$-PE-L4** with aromatic region (inset).

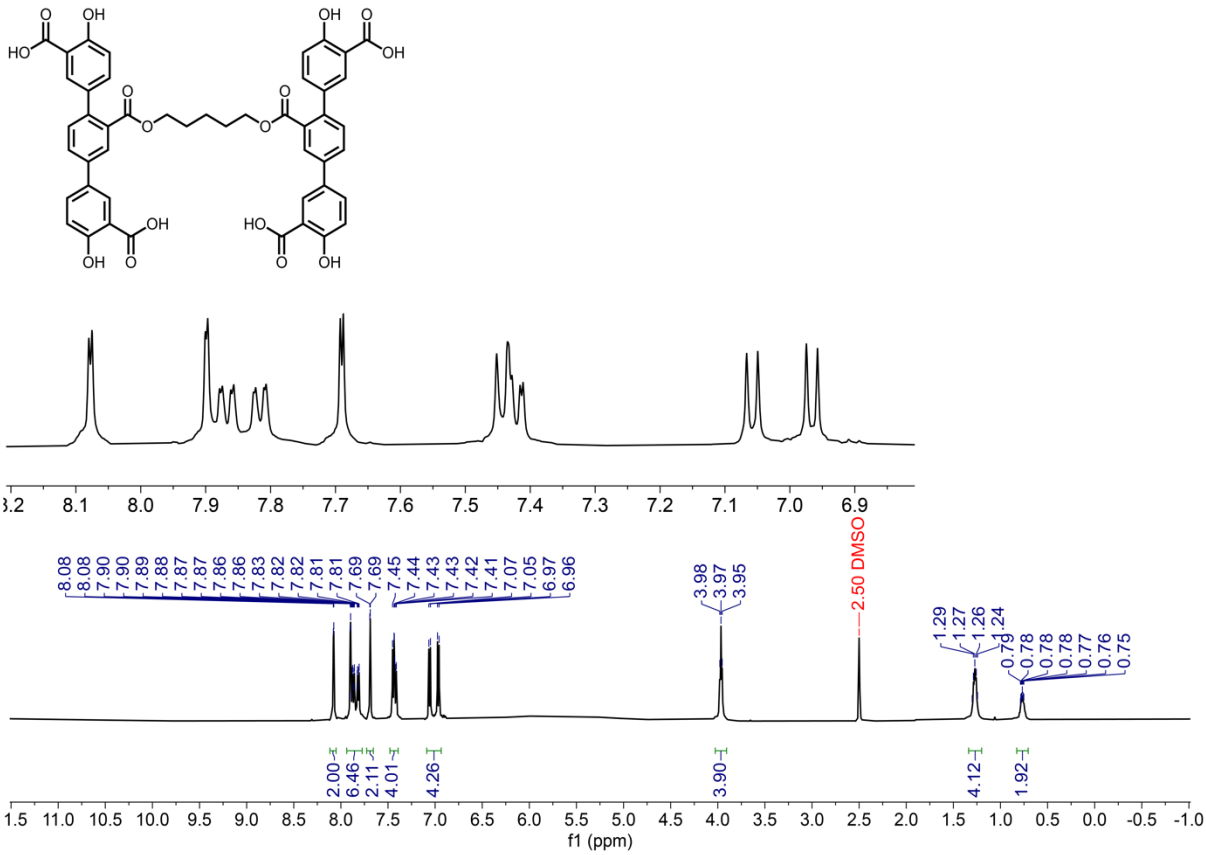

Fig. 2.S16 | ^{1}H NMR of **H_8-PE-L5** with aromatic region (inset).

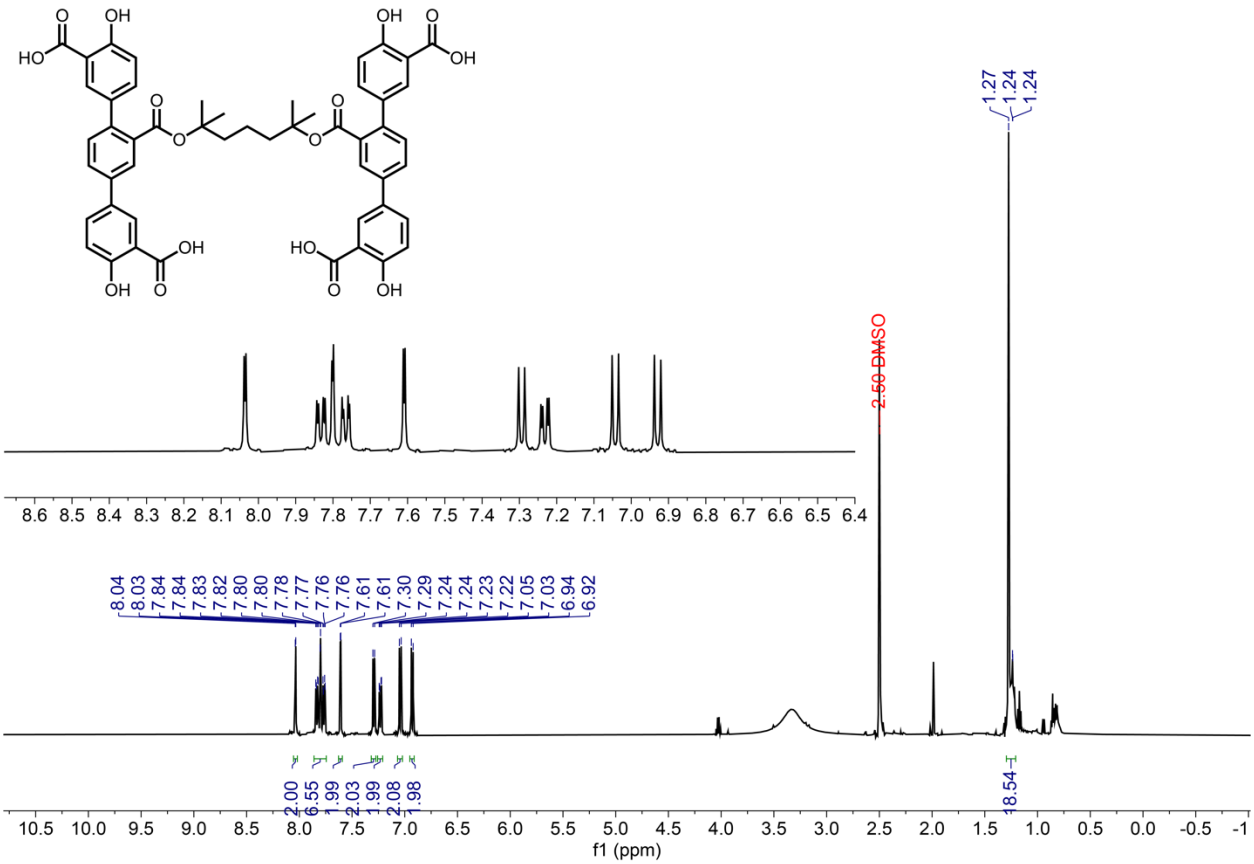

Fig. 2.S17 | ^{1}H NMR of **H_8-TE-L5** with aromatic region (inset).

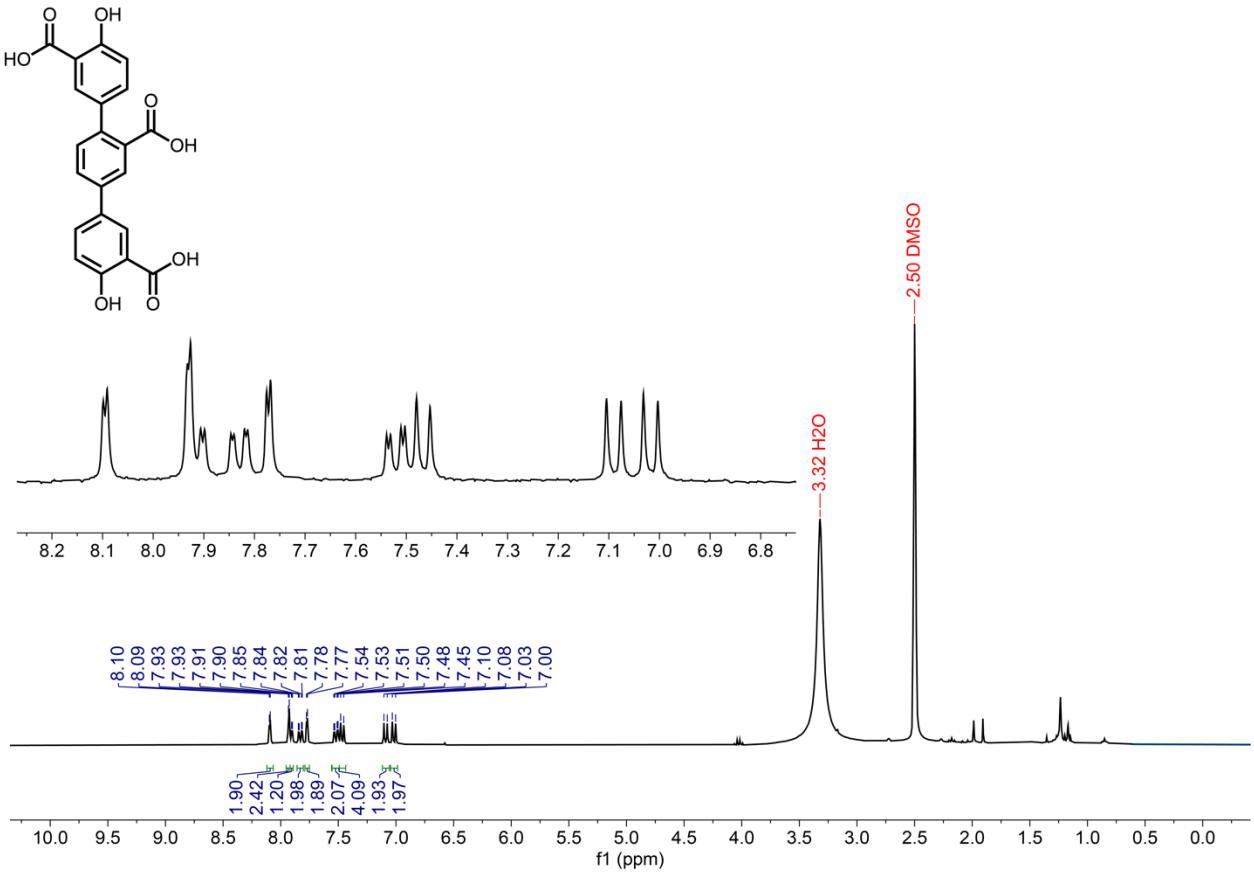

Fig. 2.S18 | ^{1}H NMR of H$_4$dotpdc-COOH with aromatic region (inset).

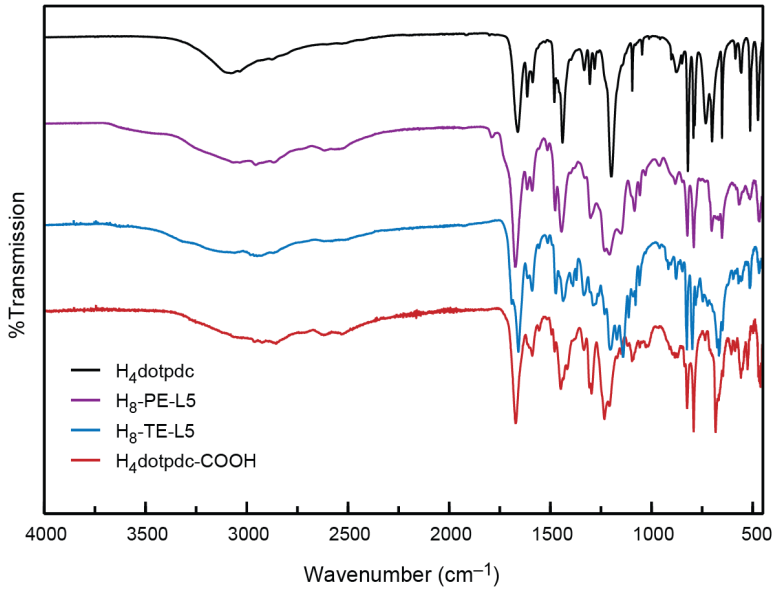

Fig. 2.S19 | FTIR spectrum of the ligands H_4dotpdc, H_8-PE-L5, H_8-TE-L5, and H_4dotpdc-COOH.

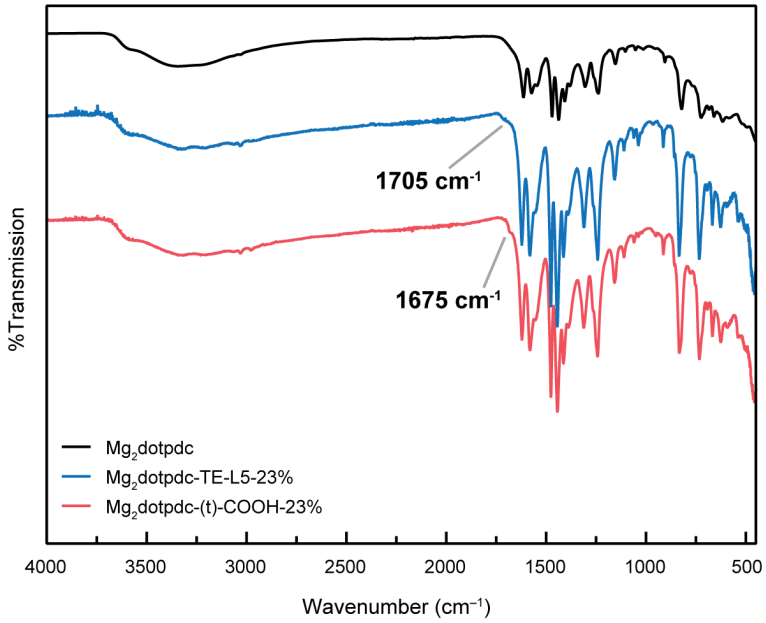

Fig. 2.S20 | FTIR spectrum of the frameworks Mg_2dotpdc, Mg_2dotpdc-TE-L5-23%, and thermolyzed Mg_2dotpdc-(t)-COOH-23%. Upon thermolysis, the ester peak at 1705 cm^{-1} disappears, while a new C=O stretch at 1675 cm^{-1} grows in.

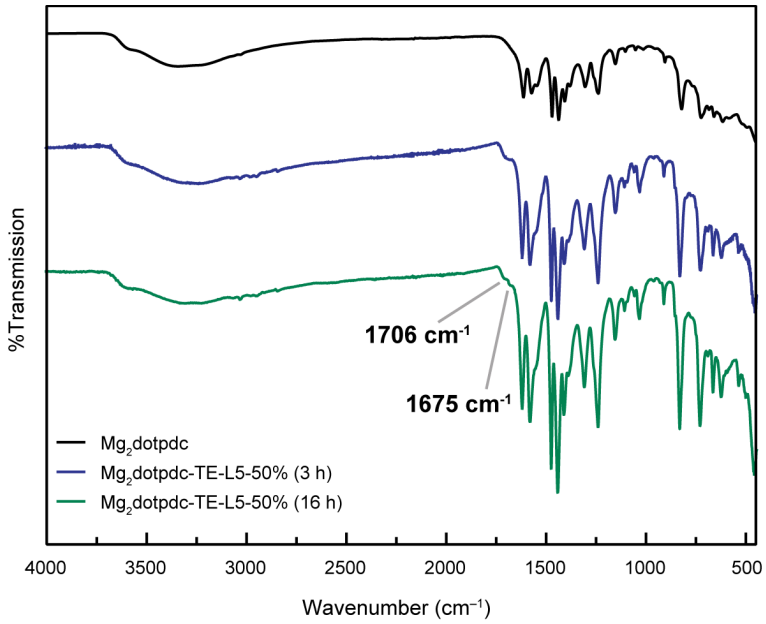

Fig. 2.S21 | FTIR spectrum of Mg_2dotpdc-TE-L5-50% synthesized over 16 vs 3 h. Two new C=O stretches are observed in the 16 h spectrum, consistent with partial decomposition of the cross-linker ester to H_4dotpdc-COOH.

9. References.

(1) Fischer, R.; Görls, H.; Langer, J.; Enke, M.; Westerhausen, M. Magnesiacycloalkanes with Different Ring Sizes. *Organometallics* **2016**, *35* (4), 587–594. https://doi.org/10.1021/acs.organomet.5b01010.

(2) Milner, P. J.; Martell, J. D.; Siegelman, R. L.; Gygi, D.; Weston, S. C.; Long, J. R. Overcoming Double-Step CO_2 Adsorption and Minimizing Water Co-Adsorption in Bulky Diamine-Appended Variants of Mg_2 (Dobpdc). *Chem. Sci.* **2018**, *9* (1), 160–174. https://doi.org/10.1039/C7SC04266C.

(3) Fracaroli, A. M.; Furukawa, H.; Suzuki, M.; Dodd, M.; Okajima, S.; Gándara, F.; Reimer, J. A.; Yaghi, O. M. Metal-Organic Frameworks with Precisely Designed Interior for Carbon Dioxide Capture in the Presence of Water. *Journal of the American Chemical Society* **2014**, *136* (25), 8863–8866. https://doi.org/10.1021/ja503296c.

(4) Walton, K. S.; Snurr, R. Q. Applicability of the BET Method for Determining Surface Areas of Microporous Metal−Organic Frameworks. *J. Am. Chem. Soc.* **2007**, *129* (27), 8552–8556. https://doi.org/10.1021/ja07

Chapter 3. Modular Synthesis of Templated Bimetallic Sites in Metal–Organic Framework Pores

3.1 Introduction.

Enzymes often use two or more metal sites to catalyze difficult oxidative, reductive, and redox-neutral transformations. For example, nature uses diiron and dicopper sites to activate O_2 and oxygenate substrates,[1,2] as well as diiron and [NiFe] centers to reversibly form and split H_2.[3,4] Two metal cations can also work jointly to increase the electrophilicity and nucleophilicity of reaction partners, such as in the hydrolysis of phosphate ester and amide bonds.[5,6] We have been interested in translating these bioinspired concepts to a heterogeneous platform, to leverage the greater stability, recyclability, and unique microenvironments found in porous materials.

An ideal heterogeneous scaffold would, like enzymes, offer precise control over the active site nuclearity and metal–metal distance, as well as the identity and flexibility of the primary coordination sphere. These complex structural requirements represent an exciting opportunity for metal–organic frameworks (MOFs), a class of porous materials characterized by high structural and chemical tunability. Multiple strategies to install homo- and heterobinuclear metal active sites on MOF surfaces have been reported, and these prior examples can be roughly divided into two categories. In the first approach, multinuclear metal nodes are used directly as the catalytic centers. Coordinatively unsaturated binuclear metal nodes can be used without further modification,[7] while larger nuclearity nodes, such as 1D chains, must be converted into site-isolated bimetallic sites through the synthesis of mixed-metal variants.[8] In the second approach, bimetallic active sites are postsynthetically grafted onto the pore walls. Reactive surface hydroxyl sites,[9–11] Lewis acidic metal cations,[12] or organic functional groups on the ligand struts[13,14] have all been used as the

points of attachment. However, in the absence of pre-formed clusters[9,13] or highly constrained binding pockets,[11] complex metal speciation is often observed in both approaches.

Grafting bimetallic active sites to MOFs via covalent attachment to the ligand strut is a particularly appealing approach (**Fig. 3.1**), as it not only provides a robust connection to the framework surface but can also be adapted to diverse ligand environments, metal precursors, and pore structures. For example, amine-functionalized frameworks have been used to attach salicylidene,[15] iminopyridine,[16,17] and NNN-pincer[18] complexes to pore walls, as well as iminocatecholate-bound Ru(II) metathesis catalysts (**Fig. 3.1a**).[19] Furthermore, amine groups are readily incorporated into many common MOF structure types.[20] However, while postsynthetic covalent grafting offers a large selection of possible ligand and pore environments, an unresolved challenge is controlling the active site nuclearity. Grafting at low surface coverages results in predominantly mononuclear sites, while higher loadings risk the formation of larger nuclearity clusters (**Fig. 3.1b**).

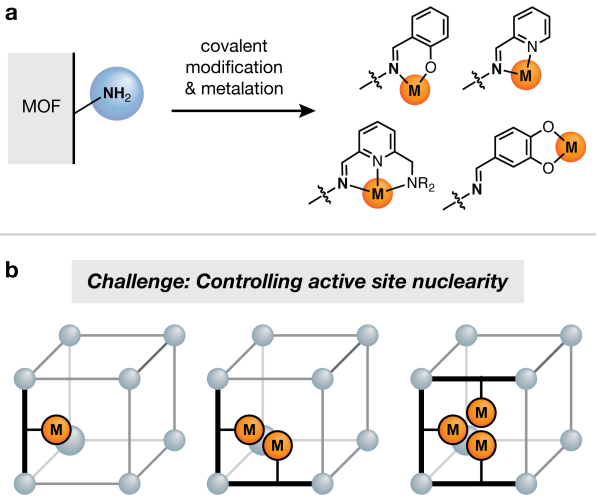

Figure 3.1. (a) Previously reported strategies to graft metal complexes onto amine-functionalized metal–organic frameworks. The free amine group can be covalently modified and converted into chelating ligands. (b) Adapting covalent grafting strategies to the construction of binuclear metal active sites introduces new challenges, such as controlling active site nuclearity.

Here, we describe a templating approach to circumvent these challenges and install well-defined binuclear metal active sites in framework pores, irrespective of the active site density (**Fig. 3.2**). Thermolabile tertiary carbamate cross-linkers are used to tether pairs of amine functional groups during framework synthesis. Postsynthetic cross-linker cleavage reveals templated aryl- and alkylamines that can be used to graft atomically precise bimetallic iminopyridine and bis(2-pyridylmethyl)amine complexes with a variety of metals (e.g., Mn(II), Fe(II), Co(II), Ni(II), Cu(I), and Cu(II)). The structural integrity of the frameworks is confirmed by powder X-ray diffraction

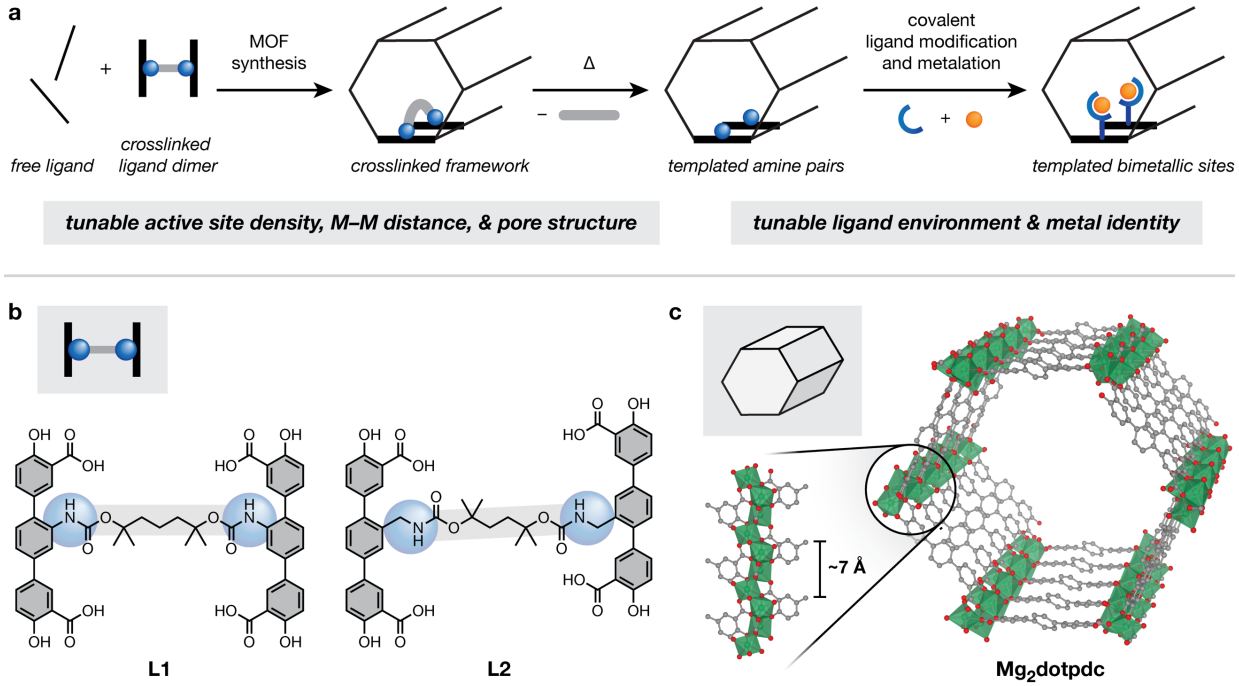

Figure 3.2. (a) Overview of the templating strategy employed in this work, which leverages thermolabile cross-linkers to install pairwise bimetallic active sites. (b) Structures and abbreviations of ligands and cross-linked ligand dimers used in this work. **L1** and **L2** contain N-aryl and N-alkylcarbamate linkages, respectively. (c) Structure of Mg_2dotpdc, a mesoporous MOF which possesses an interligand spacing of ~7 Å down the hexagonal pore channels.

and gas sorption measurements, while the local structure of the metal centers is probed by density functional theory (DFT), extended X-ray absorption fine structure (EXAFS) spectroscopy, and electron paramagnetic resonance (EPR) spectroscopy.

3.2 Results and discussion.

3.2.1 Synthesis of templated amine-functionalized frameworks.

We recently showed that cleavable covalent cross-linkers can be used to template functional group pairs in multicomponent metal–organic frameworks.[21] Specifically, thermolabile tertiary ester cross-linkers can be used to install well-defined carboxylic acid pairs within the terphenyl-expanded MOF-74 framework, also known as Mg_2dotpdc (dotpdc^{4-} = 4,4″-dioxido-[1,1′:4′,1″-terphenyl]-3,3″-dicarboxylate). When short pentyl cross-linkers are used, modeling studies showed that the carboxylic acids are installed in a single configuration down the pore channels, spaced ~7 Å apart.

Given the thermal instability of tertiary carbamates,[22] we hypothesized that a similar strategy could be used to template pairs of amines within framework pores (**Fig. 2a**). Amines are ideal entry points to more complex structures thanks to their rich postsynthetic chemistry.[23] They have been shown to undergo a multitude of reactions within MOF pores, including imine formation,[16] urea formation,[24,25] alkylation,[26] and acylation.[27] In principle, it should be possible to convert templated amine pairs into diverse site-isolated bimetallic sites via established postsynthetic ligand modification and metalation steps.

Towards this goal, we synthesized two distinct cross-linked ligand dimers, each containing thermolabile tertiary carbamate linkages (**Fig. 3.2b**). The lengths of both cross-linkers were designed to span the short ~7 Å interligand distance down the pore channel of Mg_2dotpdc (**Fig. 3.2c**). The ligand dimer **L1** is constructed from *N*-aryl carbamate linkages, which should produce arylamines after thermolysis. In contrast, **L2** contains *N*-alkylcarbamate linkages, which should template more nucleophilic alkylamine pairs. Both ligand dimers were synthesized in 4–5 steps in good overall yield (42–60%, see SI for experimental details, **Fig. 3.S-3.S2** for final ligand NMRs).

With spatially separated, site-isolated bimetallic pairs in mind, we targeted the synthesis of carbamate-cross-linked Mg_2dotpdc at relatively low cross-linker loadings (<20 mol%). Heating a mixture of cross-linked ligand dimer (0.100 equiv), H_4dotpdc (0.900 equiv), and $Mg(NO_3)_2 \cdot 6H_2O$ (2.75 equiv) in a solution of DMF and MeOH produced microcrystalline powders with the desired Mg_2dotpdc structure. Keeping in mind that each equivalent of **L1** or **L2** contains two ligand monomers, this reaction mixture should theoretically lead to ~18% functional group loading. The exact composition of the framework was quantified by digestion ^{1}H NMR (**Table 3.S1**). Consistent with previous work,[21] the experimentally observed incorporation of **L1** or **L2** varied slightly, but was typically slightly higher than the value expected based on the initial ratio of starting materials. Using the ligand dimer **L1**, we obtained a framework containing 18% cross-linked (i.e., functionalized) ligand, which we have abbreviated as **1-XL-18%** (**Fig. 3.S3**). Similarly, using the ligand dimer **L2** under these conditions produced a material containing 23% cross-linked ligand, which we have abbreviated **2-XL-23%** (**Fig. 3.S4**). Both chemically cross-linked frameworks are permanently porous, displaying high Brunauer–Emmett–Teller (BET) surface areas of 2370 m^2/g and 2400 m^2/g for **1-XL-18%** and **2-XL-23%**, respectively (**Fig.3.S5)**.

Due to the short length of the cross-linking tether, the ligand monomers in **L1** and **L2** should lie directly adjacent down the pore channels (**Fig. 3.2a**). DFT modeling studies suggest that the conformation shown in **Fig. 3.3a**, where the amine groups are oriented in the same direction rather than offset, is most favorable for both dimers (**Fig. 3.S6** and **Table 3.S2**, see SI for additional modeling details).

With the desired cross-linked frameworks in hand, we next sought to cleave the carbamate linkage and reveal exposed amine pairs. The thermal cleavage of tertiary carbamates has been successfully demonstrated not only in simple organic compounds[22] but also in solid-state porous

materials including silica[28,29] and metal–organic frameworks.[30–32] Thermogravimetric analyses confirmed the thermal lability of the cross-linkers (**Fig. 3.S7–3.S8)**. Excitingly, subjecting **1-XL-18%** to microwave heating at 230 °C in a mixture of 2-ethyl-1-hexanol and ethylene glycol for 10 minutes resulted in quantitative carbamate cleavage and formation of **1-NH_2-18%**, a framework containing templated arylamines (**Fig. 3.3a**). No loss in crystallinity was detected by powder X-ray diffraction (PXRD) (**Fig. 3.3b**), and a large increase in the BET surface area from 2370 m^2/g to 2650 m^2/g was observed (**Fig. 3.S9**). This value is very close to the reported surface area for unfunctionalized Mg_2dotpdc (~2700 m^2/g).[21] Full cross-linker removal was further confirmed by digestion ^{1}H NMR. No peaks associated with the cross-linker could be detected, and the amount of H_4dotpdc-NH_2 found was consistent with the starting amount of **L1** (**Fig. 3.S10**).

The carbamates in **2-XL-23%** could be cleaved using either microwave heating under air-free conditions, or conventional heating in the solid state under flowing N_2. Similar conditions have been previously used to remove tert-butoxycarbonyl (Boc) protecting groups in MOFs.[32] Heating samples of **2-XL-23%** at 250 °C for two days under flowing N_2 resulted in clean conversion to **2-CH_2NH_2-23%**. Like **1-NH_2-18%**, no

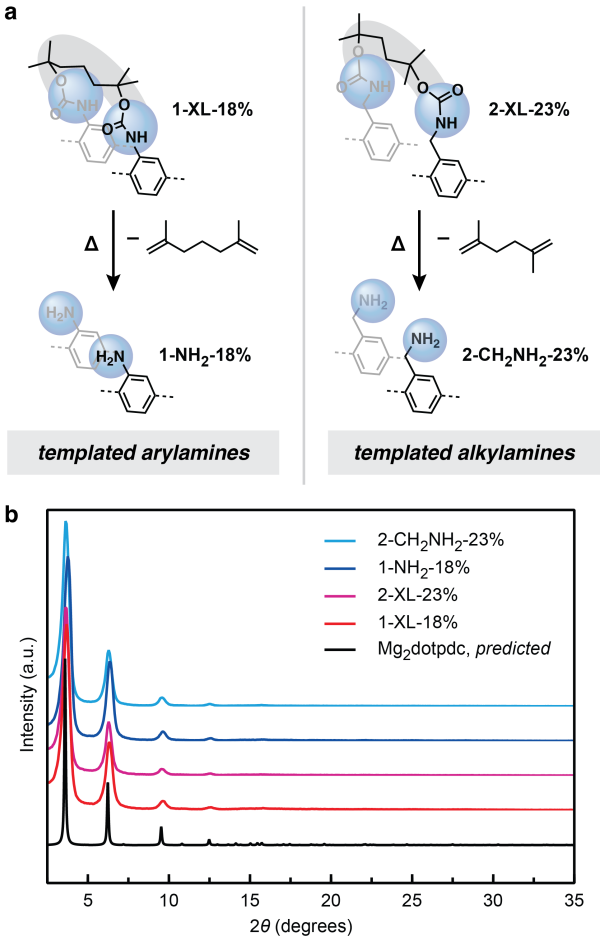

Figure 3.3. (a) Overview of thermolysis conditions to generate templated arylamine and alkylamine pairs. Powder X-ray diffraction data (b) and 77 K nitrogen adsorption data (c) for the cross-linked materials **1-XL-18%** and **2-XL-23%**, and the thermolyzed frameworks **1-NH_2-18%** and **2-CH_2NH_2-23%**.

loss in crystallinity was observed (**Fig. 3.3b**), and the BET surface area increased from 2400 m^2/g to 2610 m^2/g (**Fig. 3.S11**). Digestion ^1H NMR analysis confirmed quantitative cross-linker removal and the clean conversion of **L2** to two equivalents of H_4dotpdc-CH_2NH_2 (**Fig. 3.S12**).

3.2.2 Postsynthetic imine formation and metalation.

The ability to template amine pairs in MOF pores provides the opportunity to create bimetallic active sites where all structural parameters, from the ligand environment and metal identity to the metal–metal distances and pore environment, can be carefully controlled (**Fig. 3.2a**). Motivated by the widespread use of iminopyridine ligands in organometallic chemistry,[33–35] we envisioned that the templated arylamines in **1-NH_2-18%** could be converted into bimetallic iminopyridine complexes (**Fig. 3.4a**).

Iminopyridine formation and metalation in MOFs has been previously demonstrated by several groups,[16,17,36,37] and both stepwise and one-pot synthetic approaches have been explored. In the stepwise approach, excess 2-pyridinecarboxaldehyde (PyCHO) is first added to the amine-functionalized framework to form discrete MOF-supported iminopyridine sites, which are subsequently metalated in a second step.[16,37] In the one-pot approach, excess PyCHO and metal halide salt (e.g., $NiCl_2$) are combined together to form a molecular (PyCHO)MX_2 complex, which is then combined with the framework to form the desired metalated iminopyridine species.[17,36]

We first tested the one-pot condensation and metalation of **1-NH_2** with 10 equiv of 2-pyridinecarboxaldehyde and metal salt ($NiCl_2$ or CuCl) in methanol. Excitingly, we observed near-quantitative conversion of **1-NH_2** to **1-(IP)M** (M = $NiCl_2$, CuCl), a framework containing surface-

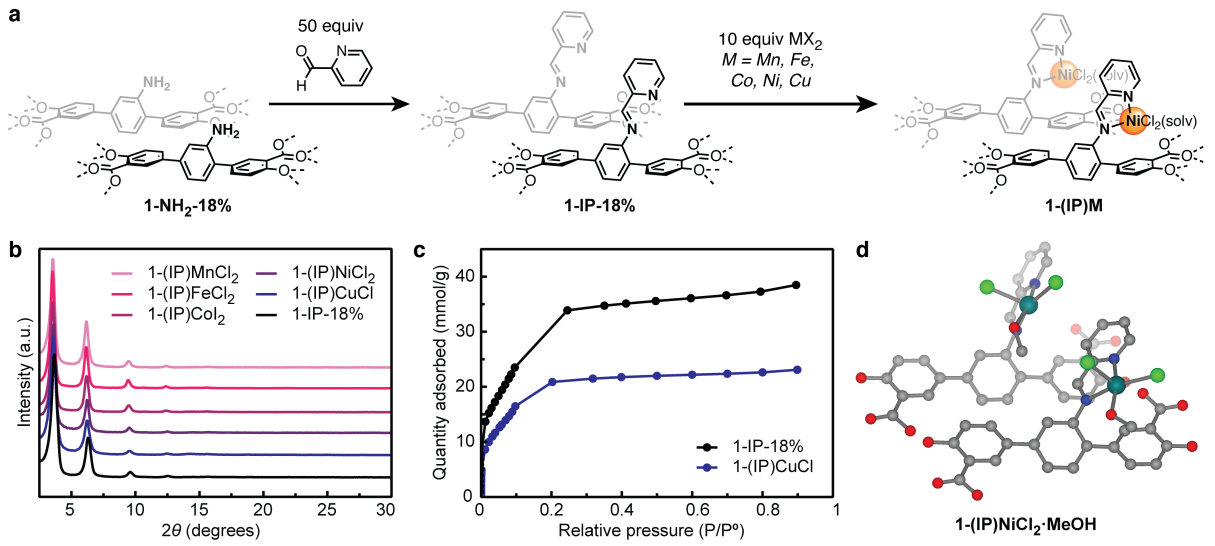

Figure 3.4. (a) Overview of the stepwise route to generate **1-(IP)M** from **1-NH$_2$-18%**. Powder X-ray diffraction data (b) and 77 K nitrogen adsorption data (c) for postsynthetically modified **1-IP-18%**, and metalated **1-(IP)M**. (d) Optimized structure for the metal sites in **1-(IP)NiCl$_2$·MeOH** obtained via DFT using a split B3LYP/6-31+G(d), B3LYP/LANL2DZ basis set. Additional ligand layers omitted for clarity.

supported bimetallic metal iminopyridine complexes (90% yield for $NiCl_2$ and 100% for CuCl) (**Table 3.S3, Table 3.1**). Successful iminopyridine formation and metalation were quantified by ^{1}H NMR and ICP analysis of digested frameworks, respectively (**Table 3.S3**). Both crystallinity and surface area were maintained in the metalated frameworks (**Fig. 3.4b**), and a BET surface area of 1700 m^2/g was observed for **1-(IP)CuCl** (**Fig. 3.4c**).

While the one-pot approach worked well for Ni(II) and Cu(I), generalizing this strategy to other metal cations was challenging due to the precipitation of insoluble PyCHO-containing metal species.[38,39] In an effort to expand our metalation catalogue, we returned to the stepwise route. Initial attempts to form iminopyridine species in the absence of Lewis acidic transition metal salts yielded poor conversion to the imine (e.g., <50% yield after 7 days).[16] Surprisingly, simply switching from the nonpolar solvents commonly used in the MOF literature (e.g., DCM, toluene) to a more polar solvent such as methanol greatly improved the yield. Heating **1-NH$_2$-18%** in methanol with a large excess of 2-pyridinecarboxaldehyde (50 equiv) resulted in the clean formation of **1-IP-18%**, with a BET surface area of 2450 m^2/g (**Fig. 3.4c**). The reaction could be

tracked by digestion ^{1}H NMR. Though the digestion conditions hydrolyze the imine, the observed 1:1 ratio of 2-pyridinecarboxaldehyde to H_4dotpdc-NH_2 is consistent with quantitative imine formation (**Fig. 3.S13**). The loss of the broad amine N–H stretch is clearly observed in the ATR-FTIR spectra, further supporting the conversion of the amine to the imine (**Fig. 3.S14**).

With the iminopyridine-functionalized framework in hand, metalation proceeded smoothly with a variety of M(I) and M(II) salts (e.g., $MnCl_2$, $FeCl_2$, CoI_2, $NiCl_2$, $NiBr_2$, CuCl) to generate **1-(IP)M-18%** (**Table 3.1**). The crystallinity of the metalated materials was confirmed by PXRD (**Fig. 3.4b**), and metalation was quantified by ICP analysis (**Table 3.S3**). While nearly all transition metals tested led to >90% metalation, a notable exception was Cu(II), which leached in acetonitrile and formed side products in methanol. Overall, this work establishes a remarkably general route to achieve bimetallic iminopyridine species with diverse metal cations.

3.2.3 Postsynthetic alkylation and metalation.

Given the increased nucleophilicity and flexibility of alkylamines, we hypothesized that new MOF-supported multidentate ligand scaffolds could be accessed through S_N2 alkylation of **2-CH_2NH_2-23%** (**Fig. 3.5**). In particular, alkylation is a common way to achieve polypyridyl ligand scaffolds. For example, double alkylation of the amine sites in **2-CH_2NH_2-23%** with 2-(bromomethyl)pyridine should generate tridentate bis(2-pyridylmethyl)amine ligands, also commonly known as di-(2-picolyl)amine (DPA) (**Fig. 3.5a**). While polypyridylamine ligands are found throughout inorganic chemistry, particularly in the study of biomimetic dicopper and diiron–oxo and dioxygen chemistry,[40,41] to our knowledge no polypyridylamine complexes have been previously grafted in a metal–organic framework.

Gratifyingly, double alkylation of the alkylamine sites in **2-CH_2NH_2-23%** with 2-(bromomethyl)pyridine hydrobromide proceeded smoothly in the presence of diisopropylethylamine in acetonitrile. The ^{1}H NMR spectrum of the digested framework shows the appearance of diagnostic pyridyl and methylene peaks, along with the complete disappearance of signals corresponding to the unalkylated benzylamine ligand, H_4dotpdc-CH_2NH_2 (**Fig. 3.S15**). The resultant material, abbreviated **2-DPA-23%**, is readily metalated with a number of first row transition metals (M = Fe(II), Co(II), Ni(II), and Cu(II), see **Table 3.1**) in 90–100% yield. Both **2-DPA-23%** and the metalated materials retain crystallinity and porosity (**Fig. 3.5b**), with **2-DPA-23%** possessing a BET surface area of 2540 m^2/g and **2-(DPA)$FeCl_2$** possessing a BET surface area of 1760 m^2/g (**Fig. 3.5c**).

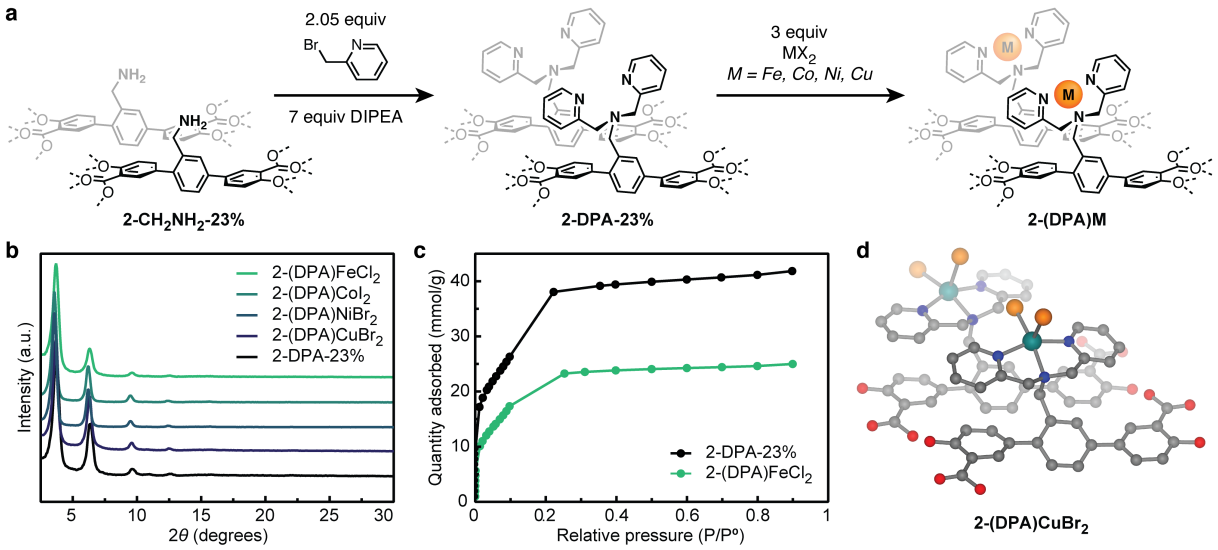

Figure 3.5. Overview of postsynthetic reactions to generate **2-(DPA)M** from **2-CH_2NH_2-23%**. Powder X-ray diffraction data (b) and 77 K nitrogen adsorption data (c) for postsynthetically modified **2-DPA-23%**, and metalated **2-(DPA)M**. (d) Optimized structure for the metal sites in **2-(DPA)$CuBr_2$** obtained via DFT using a split B3LYP/6-31+G(d), B3LYP/LANL2DZ basis set. Additional ligand layers omitted for clarity.

Table 3.1 | Metalations summary as determined by ICP-OES.

Framework	Metal Identity	Metalation Yield (%)
1-IP-18%	$MnCl_2$[b]	100
	$FeCl_2$[b]	100
	CoI_2[b]	89
	$NiBr_2$[b]	89
	CuCl[a]	100

2-DPA-23%	$FeCl_2$	100
	CoI_2	100
	$NiBr_2$	83
	$CuBr_2$	100
2-DPA-5%	$CuCl_2$	100
	$Cu(OTf)_2$	100

[a] Synthesized using the one-pot method.

[b] Synthesized using the stepwise method

3.2.4 Spectroscopic characterization of bimetallic sites.

We next carried out a combination of extended X-ray absorption fine structure (EXAFS), density functional theory (DFT), and electron paramagnetic resonance (EPR) studies to structurally interrogate the metal sites in **1-(IP)M and 2-(DPA)M**. Two air-stable materials, **1-(IP)$NiCl_2$** and **2-(DPA)CuX_2** (X =Br, OSO_2CF_3), were selected as representative frameworks for these studies.

Excitingly, EXAFS studies on both frameworks confirm that the MOF-supported metal sites reside in well-defined ligand environments that closely resemble their molecular counterparts. The Ni K-edge EXAFS spectrum of **1-(IP)$NiCl_2$** is shown in **Fig. 3.S16**. The EXAFS data was best fit with three N/O atoms at a distance of 2.03(6) Å and two Cl atoms at 2.29(7) Å (**Table 3.S4**). The presence of an additional ligand is expected, as coordinating methanol is used in the metalation and washing procedure. These bond distances are consistent with the DFT optimized structure for **1-(IP)$NiCl_2$** (**Fig. 3.4d**, **Table 3.S5**), as well as with previously reported five-coordinate nickel(II) iminopyridine complexes, which show average Ni–N/O and Ni–Cl distances of ~2.0–2.1 Å and ~2.3 Å, respectively (see **Table 3.S6** for a tabulation of reference compounds).

The Cu K-edge EXAFS spectrum of **2-(DPA)CuBr$_2$**, shown in **Fig. 3.6a**, was best fit with two pyridyl N atoms at 2.01(1) Å, one alkyl N atom at 2.14(1) Å, one Br atom at 2.40(1) Å, and a second Br atom at 2.79(1) Å (**Table 3.S7**). This is consistent with previously reported bis(2-pyridylmethyl)amine-ligated Cu(II) molecular complexes, which often adopt distorted square pyramidal geometries featuring one shorter basal Cu–Br bond (~2.40 Å) and one significantly longer apical Cu–Br bond (~2.70 Å) (see **Table 3.S8** for tabulation of reference compounds). The bond lengths observed by EXAFS are also consistent with DFT-optimized structural models (**Fig. 3.5d** and **Table 3.S9**).

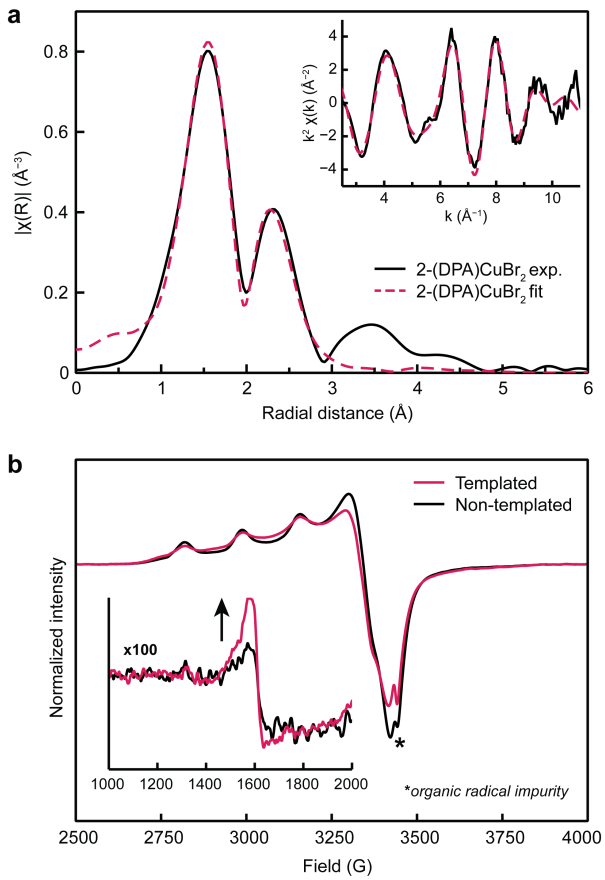

Figure 3.6. (a) Fit (red dashed lines) to EXAFs spectrum of **2-(DPA)CuBr$_2$** (solid black line). (Inset) Corresponding k^2-weighted oscillations. See SI for fit parameters. (b) 100K X-band EPR spectra for **2-(DPA)Cu(OTf)$_2$** and the non-templated control framework, Mg$_2$dotpdc-DPA-Cu(OTf)$_2$. The forbidden $Dm_s = 2$ transition at 100x magnification is shown in the inset. The framework organic radical that appears after thermolysis is marked with an asterisk.

Notably, no evidence of strong M–M scattering was observed in any of the EXAFS spectra. Indeed, the EXAFS spectra of templated frameworks and their non-templated analogues are nearly identical (**Fig. 3.S17, 3.S18**). Given the ~7 Å distance between ligand struts and the lack of strong bridging ligands between the two metal centers, the M–M distances are likely beyond the ~4–5 Å distance detectable by EXAFS. Therefore, we turned to EPR spectroscopy as a more sensitive probe of proximal paramagnetic centers.

Electron paramagnetic resonance spectroscopy is highly sensitive to the interactions between unpaired electrons, and is widely used to probe interspin distances.[42,43] These interactions may be either exchange (through orbital overlap) or dipolar (through space) interactions. Given the expected ~7 Å distance between our metal centers by DFT, the lack of short M–M distances observed in our EXAFS data, and the absence of strong bridging ligands, we only expect spin-spin interactions through dipolar coupling. Because our templated frameworks have shorter average M–M distances than non-templated controls, this should lead to two distinct differences: 1) the EPR features for the templated samples should show greater homogeneous line broadening, and 2) the relative intensity of the forbidden $\Delta m_s = 2$ half-field transition should increase.[44,45]

To simplify the analysis, all EPR studies were carried out on **2-(DPA)Cu(OTf)$_2$**, an $S = ½$ system. Due to the high sensitivity of EPR towards dipolar interactions, low amine loadings of 5% were targeted. Two frameworks were synthesized, the templated framework **2-(DPA)Cu(OTf)$_2$-5%** and the non-templated control, Mg$_2$dotpdc-(DPA)Cu(OTf)$_2$-5%. Briefly, the non-templated framework was synthesized using H$_4$dotpdc-CH$_2$NHBoc, a non-cross-linked ligand containing Boc-protected benzylamine groups. The protected framework was then subjected to thermolysis, post-synthetic alkylation, and metalation to yield randomly distributed mononuclear (DPA)Cu(OTf)$_2$ sites throughout the framework (see SI for more experimental details).

Unexpectedly, a sharp isotropic feature at $g = 2.002$ was observed in all thermolyzed samples. We assign this feature to a ligand-based organic radical generated during the thermal deprotection step, as it is observed even in the unfunctionalized Mg$_2$dotpdc after thermal treatment (**Fig. 3.S19**). We note that careful air-free thermolysis under microwave conditions minimizes, but does not fully eliminate, the presence of this radical species, suggesting it arises due to oxidation of the framework backbone at high temperatures.

The X-band EPR spectra of the templated **2-(DPA)Cu(OTf)$_2$-5%** and the non-templated Mg$_2$dotpdc-(DPA)Cu(OTf)$_2$-5% control were collected at 100 K and analyzed (**Fig. 3.6b**). The Cu(II) features in both spectra are best fit using two distinct *g*-values (2.06 and 2.24, see **Fig. 3.S20–3.S21**). Similar values have been observed in molecular (DPA)Cu(OTf)$_2$ complexes.[46,47] To control for slight variations in copper loading between the samples, both spectra were normalized to the double integral of the allowed $\Delta m_s = 1$ transition.

Excitingly, both greater line broadening as well as an increase in the intensity of the forbidden transition at g ~ 4 is observed in **2-(DPA)Cu(OTf)$_2$-5%** relative to the non-templated analogue (**Fig. 3.6b** and **Table 3.S10**). While subtle, this data provides evidence that the templated framework has shorter average M–M distances. Greater differences in both the EPR and EXAFS data and more quantitative analysis should be possible with the addition of bridging ligands to tether the two metal sites closer together (<4 Å), and work along this vein is underway.

3.3 Conclusion.

In summary, we have developed a strategy to precisely template pairs of aryl- and alkylamines in a mesoporous metal–organic framework. The templated amines can be further elaborated to achieve atomically precise bimetallic active sites with tunable ligand environments. The iminopyridine and bis(2-pyridylmethyl)amine ligand scaffolds illustrated here have a rich history in organometallic and bioinorganic chemistry, as well as the potential to support unusual bimetallic reactivity. For example, dinucleating iminopyridine ligands have been previously explored in the context of olefin polymerization,[48] while dinucleating polypyridyl scaffolds have been studied for bimetallic O_2 activation,[1,2,40,41] anion sensing,[49] and nucleotide hydrolysis.[50]

Finally, we note that previous routes to achieve well-defined bimetallic sites in metal–organic frameworks have focused on active sites with highly constrained metal–metal

distances.[9,11,13] Our templated sites, which are conformationally flexible, represent a distinct and complementary alternative to the more rigid, static ligand environments described in earlier reports. Overall, the synthetic precision and flexibility of the templating approach described here will allow researchers to re-examine molecular and enzymatic bimetallic motifs in a heterogeneous context, as well uncover new modes of reactivity.

3.4 Acknowledgements

Initial ligand synthesis studies were supported by the donors of ACS Petroleum Research Fund under PRF# 61949-DNI3. Subsequent framework synthesis, post-synthetic modification and metalation were supported by the National Science Foundation (NSF) under Grant No. 2142798 and the David and Lucile Packard Foundation. This research used the beamline 12-BM of the Advanced Photon Source (APS), a U.S. Department of Energy (DOE) Office of Science user facility operated for the DOE Office of Science by Argonne National Laboratory under Contract No. DE-AC02-06CH11357. Part of this work was conducted at the Molecular Analysis Facility, a National Nanotechnology Coordinated Infrastructure (NNCI) site at the University of Washington, which is supported in part by funds from the National Science Foundation (awards NNCI-2025489, NNCI-1542101), the Molecular Engineering & Sciences Institute, and the Clean Energy Institute. In addition, the authors acknowledge the use of facilities and instrumentation supported by the U.S. National Science Foundation through the UW Molecular Engineering Materials Center (MEM-C), a Materials Research Science and Engineering Center (DMR171797). JCG is supported by an NSF graduate research fellowship. We thank Dr. Sungsik Lee for assisting with the collection of synchrotron XAS data at APS beamline 12-BM. We thank the Mary Gates research scholarship for supporting JPA. The NMR facility at the UW Department of Chemistry is

supported by NIH Award Number S10OD030224-01A1. This work utilized the computational infrastructure of the Hyak supercomputer system at the UW.

3.5 References

(1) Jasniewski, A. J.; Que, L. Dioxygen Activation by Nonheme Diiron Enzymes: Diverse Dioxygen Adducts, High-Valent Intermediates, and Related Model Complexes. *Chem. Rev.* **2018**, *118* (5), 2554–2592. https://doi.org/10.1021/acs.chemrev.7b00457.

(2) Solomon, E. I.; Heppner, D. E.; Johnston, E. M.; Ginsbach, J. W.; Cirera, J.; Qayyum, M.; Kieber-Emmons, M. T.; Kjaergaard, C. H.; Hadt, R. G.; Tian, L. Copper Active Sites in Biology. *Chem. Rev.* **2014**, *114* (7), 3659–3853. https://doi.org/10.1021/cr400327t.

(3) Fontecilla-Camps, J. C.; Volbeda, A.; Cavazza, C.; Nicolet, Y. Structure/Function Relationships of [NiFe]- and [FeFe]-Hydrogenases. *Chem. Rev.* **2007**, *107* (10), 4273–4303. https://doi.org/10.1021/cr050195z.

(4) Lubitz, W.; Ogata, H.; Rüdiger, O.; Reijerse, E. Hydrogenases. *Chem. Rev.* **2014**, *114* (8), 4081–4148. https://doi.org/10.1021/cr4005814.

(5) Wilcox, D. E. Binuclear Metallohydrolases. *Chem. Rev.* **1996**, *96* (7), 2435–2458. https://doi.org/10.1021/cr950043b.

(6) Mitić, N.; Smith, S. J.; Neves, A.; Guddat, L. W.; Gahan, L. R.; Schenk, G. The Catalytic Mechanisms of Binuclear Metallohydrolases. *Chem. Rev.* **2006**, *106* (8), 3338–3363. https://doi.org/10.1021/cr050318f.

(7) Wang, C.-H.; Das, A.; Gao, W.-Y.; Powers, D. C. Probing Substrate Diffusion in Interstitial MOF Chemistry with Kinetic Isotope Effects. *Angew. Chem. Int. Ed.* **2018**, *57* (14), 3676–3681. https://doi.org/10.1002/anie.201713244.

(8) Osadchii, D. Y.; Olivos-Suarez, A. I.; Szécsényi, Á.; Li, G.; Nasalevich, M. A.; Dugulan, I. A.; Crespo, P. S.; Hensen, E. J. M.; Veber, S. L.; Fedin, M. V.; Sankar, G.; Pidko, E. A.; Gascon, J. Isolated Fe Sites in Metal Organic Frameworks Catalyze the Direct Conversion of Methane to Methanol. *ACS Catalysis* **2018**, *8* (6), 5542–5548. https://doi.org/10.1021/ACSCATAL.8B00505.

(9) Desai, S. P.; Malonzo, C. D.; Webber, T.; Duan, J.; Thompson, A. B.; Tereniak, S. J.; DeStefano, M. R.; Buru, C. T.; Li, Z.; Penn, R. L.; Farha, O. K.; Hupp, J. T.; Stein, A.; Lu, C. C. Assembly of Dicobalt and Cobalt–Aluminum Oxide Clusters on Metal–Organic Framework and Nanocast Silica Supports. *Faraday Discuss.* **2017**, *201*, 287–302. https://doi.org/10.1039/C7FD00055C.

(10) Zheng, J.; Ye, J.; Ortuño, M. A.; Fulton, J. L.; Gutiérrez, O. Y.; Camaioni, D. M.; Motkuri, R. K.; Li, Z.; Webber, T. E.; Mehdi, B. L.; Browning, N. D.; Penn, R. L.; Farha, O. K.; Hupp, J. T.; Truhlar, D. G.; Cramer, C. J.; Lercher, J. A. Selective Methane Oxidation to Methanol on Cu-Oxo Dimers Stabilized by Zirconia Nodes of an NU-1000 Metal–Organic Framework. *J. Am. Chem. Soc.* **2019**, *141* (23), 9292–9304. https://doi.org/10.1021/jacs.9b02902.

(11) Feng, X.; Song, Y.; Chen, J. S.; Xu, Z.; Dunn, S. J.; Lin, W. Rational Construction of an Artificial Binuclear Copper Monooxygenase in a Metal–Organic Framework. *J. Am. Chem. Soc.* **2021**, *143* (2), 1107–1118. https://doi.org/10.1021/jacs.0c11920.

(12) Baek, J.; Rungtaweevoranit, B.; Pei, X.; Park, M.; Fakra, S. C.; Liu, Y.-S.; Matheu, R.; Alshmimri, S. A.; Alshehri, S.; Trickett, C. A.; Somorjai, G. A.; Yaghi, O. M. Bioinspired Metal–Organic Framework Catalysts for Selective Methane Oxidation to Methanol. *J. Am. Chem. Soc.* **2018**, *140* (51), 18208–18216. https://doi.org/10.1021/jacs.8b11525.

(13) Pullen, S.; Fei, H.; Orthaber, A.; Cohen, S. M.; Ott, S. Enhanced Photochemical Hydrogen Production by a Molecular Diiron Catalyst Incorporated into a Metal–Organic Framework. *J. Am. Chem. Soc.* **2013**, *135* (45), 16997–17003. https://doi.org/10.1021/ja407176p.
(14) Wang, Z.; Yeary, P.; Feng, X.; Lin, W. Self-Adaptive Metal–Organic Framework Assembles Di-Iron Active Sites to Mimic Monooxygenases. *J. Am. Chem. Soc.* **2023**, *145* (15), 8647–8655. https://doi.org/10.1021/jacs.3c01498.
(15) Ingleson, M. J.; Perez Barrio, J.; Guilbaud, J.-B.; Khimyak, Y. Z.; Rosseinsky, M. J. Framework Functionalisation Triggers Metal Complex Binding. *Chem. Commun.* **2008**, No. 23, 2680. https://doi.org/10.1039/b718367d.
(16) Doonan, C. J.; Morris, W.; Furukawa, H.; Yaghi, O. M. Isoreticular Metalation of Metal−Organic Frameworks. *J. Am. Chem. Soc.* **2009**, *131* (27), 9492–9493. https://doi.org/10.1021/ja903251e.
(17) Canivet, J.; Aguado, S.; Schuurman, Y.; Farrusseng, D. MOF-Supported Selective Ethylene Dimerization Single-Site Catalysts through One-Pot Postsynthetic Modification. *J. Am. Chem. Soc.* **2013**, *135* (11), 4195–4198. https://doi.org/10.1021/ja312120x.
(18) Rasero-Almansa, A. M.; Corma, A.; Iglesias, M.; Sánchez, F. One-Pot Multifunctional Catalysis with NNN-Pincer Zr-MOF: Zr Base Catalyzed Condensation with Rh-Catalyzed Hydrogenation. *ChemCatChem* **2013**, *5* (10), 3092–3100. https://doi.org/10.1002/cctc.201300371.
(19) Yuan, J.; Fracaroli, A. M.; Klemperer, W. G. Convergent Synthesis of a Metal–Organic Framework Supported Olefin Metathesis Catalyst. *Organometallics* **2016**, *35* (12), 2149–2155. https://doi.org/10.1021/acs.organomet.6b00365.
(20) Lin, Y.; Kong, C.; Chen, L. Amine-Functionalized Metal–Organic Frameworks: Structure, Synthesis and Applications. *RSC Adv.* **2016**, *6* (39), 32598–32614. https://doi.org/10.1039/C6RA01536K.
(21) Geary, J.; Wong, A. H.; Xiao, D. J. Thermolabile Cross-Linkers for Templating Precise Multicomponent Metal–Organic Framework Pores. *J. Am. Chem. Soc.* **2021**, *143* (27), 10317–10323. https://doi.org/10.1021/jacs.1c04030.
(22) Protection for the Amino Group. In *Greene's Protective Groups in Organic Synthesis*; John Wiley & Sons, Ltd, 2006; pp 696–926. https://doi.org/10.1002/9780470053485.ch7.
(23) Cohen, S. M. Postsynthetic Methods for the Functionalization of Metal–Organic Frameworks. *Chem. Rev.* **2012**, *112* (2), 970–1000. https://doi.org/10.1021/cr200179u.
(24) Costa, J. S.; Gamez, P.; Black, C. A.; Roubeau, O.; Teat, S. J.; Reedijk, J. Chemical Modification of a Bridging Ligand Inside a Metal–Organic Framework While Maintaining the 3D Structure. *Eur. J. Inorg. Chem.* **2008**, *2008* (10), 1551–1554. https://doi.org/10.1002/ejic.200800002.
(25) Dugan, E.; Wang, Z.; Okamura, M.; Medina, A.; Cohen, S. M. Covalent Modification of a Metal–Organic Framework with Isocyanates: Probing Substrate Scope and Reactivity. *Chem. Commun.* **2008**, No. 29, 3366. https://doi.org/10.1039/b806150e.
(26) Taylor-Pashow, K. M. L.; Della Rocca, J.; Xie, Z.; Tran, S.; Lin, W. Postsynthetic Modifications of Iron-Carboxylate Nanoscale Metal−Organic Frameworks for Imaging and Drug Delivery. *J. Am. Chem. Soc.* **2009**, *131* (40), 14261–14263. https://doi.org/10.1021/ja906198y.
(27) Tanabe, K. K.; Wang, Z.; Cohen, S. M. Systematic Functionalization of a Metal−Organic Framework via a Postsynthetic Modification Approach. *J. Am. Chem. Soc.* **2008**, *130* (26), 8508–8517. https://doi.org/10.1021/ja801848j.

(28) Ki, C. D.; Oh, C.; Oh, S.-G.; Chang, J. Y. The Use of a Thermally Reversible Bond for Molecular Imprinting of Silica Spheres. *J. Am. Chem. Soc.* **2002**, *124* (50), 14838–14839. https://doi.org/10.1021/ja0277881.
(29) Bass, J. D.; Katz, A. Thermolytic Synthesis of Imprinted Amines in Bulk Silica. *Chem. Mater.* **2003**, *15* (14), 2757–2763. https://doi.org/10.1021/cm021822t.
(30) Deshpande, R. K.; Minnaar, J. L.; Telfer, S. G. Thermolabile Groups in Metal-Organic Frameworks: Suppression of Network Interpenetration, Post-Synthetic Cavity Expansion, and Protection of Reactive Functional Groups. *Angew. Chem. Int. Ed.* **2010**, *49* (27), 4598–4602. https://doi.org/10.1002/anie.200905960.
(31) Lun, D. J.; Waterhouse, G. I. N.; Telfer, S. G. A General Thermolabile Protecting Group Strategy for Organocatalytic Metal−Organic Frameworks. *J. Am. Chem. Soc.* **2011**, *133* (15), 5806–5809. https://doi.org/10.1021/ja202223d.
(32) Fracaroli, A. M.; Furukawa, H.; Suzuki, M.; Dodd, M.; Okajima, S.; Gándara, F.; Reimer, J. A.; Yaghi, O. M. Metal–Organic Frameworks with Precisely Designed Interior for Carbon Dioxide Capture in the Presence of Water. *J. Am. Chem. Soc.* **2014**, *136* (25), 8863–8866. https://doi.org/10.1021/ja503296c.
(33) Mu, H.; Pan, L.; Song, D.; Li, Y. Neutral Nickel Catalysts for Olefin Homo- and Copolymerization: Relationships between Catalyst Structures and Catalytic Properties. *Chem. Rev.* **2015**, *115* (22), 12091–12137. https://doi.org/10.1021/cr500370f.
(34) McNeill, E.; Ritter, T. 1,4-Functionalization of 1,3-Dienes With Low-Valent Iron Catalysts. *Acc. Chem. Res.* **2015**, *48* (8), 2330–2343. https://doi.org/10.1021/acs.accounts.5b00050.
(35) Wang, Z.; Liu, Q.; Solan, G. A.; Sun, W.-H. Recent Advances in Ni-Mediated Ethylene Chain Growth: Nimine-Donor Ligand Effects on Catalytic Activity, Thermal Stability and Oligo-/Polymer Structure. *Coordination Chemistry Reviews* **2017**, *350*, 68–83. https://doi.org/10.1016/j.ccr.2017.06.003.
(36) Liu, B.; Jie, S.; Bu, Z.; Li, B.-G. Postsynthetic Modification of Mixed-Linker Metal–Organic Frameworks for Ethylene Oligomerization. *RSC Adv.* **2014**, *4* (107), 62343–62346. https://doi.org/10.1039/C4RA10605A.
(37) Liu, J.; Zhang, X.; Yang, J.; Wang, L. Postsynthetic Modification of IRMOF-3 with a Copper Iminopyridine Complex as Heterogeneous Catalyst for the Synthesis of 2-Aminobenzothiazoles. *Applied Organometallic Chemistry* **2014**, *28* (3), 198–203. https://doi.org/10.1002/aoc.3109.
(38) Müller, B.; Vahrenkamp, H. Zinc Complexes of Chelating Aldehydes. *European Journal of Inorganic Chemistry* **1999**, *1999* (1), 137–144. https://doi.org/10.1002/(SICI)1099-0682(199901)1999:1<137::AID-EJIC137>3.0.CO;2-T.
(39) Lumb, I.; Sran, B. S.; Sood, H.; Arora, D. S.; Hundal, G. Coordination Chemistry of Cu(II), Co(II), Zn(II) and Ag(I) Complexes of Isomeric Pyridine 2- and 4-Carboxamides and Their Biological Activity Evaluation. *Polyhedron* **2017**, *127*, 153–166. https://doi.org/10.1016/j.poly.2017.01.063.
(40) Mirica, L. M.; Ottenwaelder, X.; Stack, T. D. P. Structure and Spectroscopy of Copper−Dioxygen Complexes. *Chem. Rev.* **2004**, *104* (2), 1013–1046. https://doi.org/10.1021/cr020632z.
(41) Tshuva, E. Y.; Lippard, S. J. Synthetic Models for Non-Heme Carboxylate-Bridged Diiron Metalloproteins: Strategies and Tactics. *Chem. Rev.* **2004**, *104* (2), 987–1012. https://doi.org/10.1021/cr020622y.

(42) Eaton, S. S.; Eaton, G. R. Distance Measurements by CW and Pulsed EPR. In *Distance Measurements in Biological Systems by EPR*; Berliner, L. J., Eaton, G. R., Eaton, S. S., Eds.; Biological Magnetic Resonance; Springer US: Boston, MA, 2002; Vol. 19, pp 1–27. https://doi.org/10.1007/0-306-47109-4_1.
(43) Eaton, G. R.; Eaton, S. S. Measurement of Interspin Distances by EPR. In *Electron Paramagnetic Resonance*; Gilbert, B. C., Ed.; Royal Society of Chemistry: Cambridge, 2008; Vol. 21, pp 59–75. https://doi.org/10.1039/b709149b.
(44) Eaton, G. R.; Eaton, S. S. Resolved Electron-Electron Spin-Spin Splittings in EPR Spectra. In *Spin Labeling*; Berliner, L. J., Reuben, J., Eds.; Biological Magnetic Resonance; Springer US: Boston, MA, 1989; Vol. 8, pp 339–397. https://doi.org/10.1007/978-1-4613-0743-3_7.
(45) Grigoropoulou, G.; Christoforidis, K. C.; Louloudi, M.; Deligiannakis, Y. Structure-Catalytic Function Relationship of SiO2-Immobilized Mononuclear Cu Complexes: An EPR Study. *Langmuir* **2007**, *23* (20), 10407–10418. https://doi.org/10.1021/la700815d.
(46) Niklas, N.; Alsfasser, R. The Chemistry of Nitrogen Coordinated Tertiary Carboxamides: A Spectroscopic Study on Bis(Picolyl)Amidecopper(II) Complexes. *Dalton Trans.* **2006**, No. 26, 3188–3199. https://doi.org/10.1039/B516875A.
(47) Ghosh, S.; Lawless, M. J.; Brubaker, H. J.; Singewald, K.; Kurpiewski, M. R.; Jen-Jacobson, L.; Saxena, S. Cu2+-Based Distance Measurements by Pulsed EPR Provide Distance Constraints for DNA Backbone Conformations in Solution. *Nucleic Acids Research* **2020**, *48* (9), e49. https://doi.org/10.1093/nar/gkaa133.
(48) Delferro, M.; Marks, T. J. Multinuclear Olefin Polymerization Catalysts. *Chem. Rev.* **2011**, *111* (3), 2450–2485. https://doi.org/10.1021/cr1003634.
(49) Ngo, H. T.; Liu, X.; Jolliffe, K. A. Anion Recognition and Sensing with Zn(Ii)–Dipicolylamine Complexes. *Chem. Soc. Rev.* **2012**, *41* (14), 4928. https://doi.org/10.1039/c2cs35087d.
(50) Niittymäki, T.; Lönnberg, H. Artificial Ribonucleases. *Org. Biomol. Chem.* **2006**, *4* (1), 15–25. https://doi.org/10.1039/B509022A.
(51) *EasySpin - EPR spectrum simulation*. https://easyspin.org/ (accessed 2024-03-21).
(52) Newville, M. Larch: An Analysis Package for XAFS and Related Spectroscopies. *J. Phys.: Conf. Ser.* **2013**, *430*, 012007. https://doi.org/10.1088/1742-6596/430/1/012007.

3.6 Supplementary Information

1. General materials and methods.

Reagents and solvents were purchased from commercial vendors (Millipore Sigma, TCI America, Alfa Aesar, Fisher, Oakwood Chemical, Combi-Blocks) and used without purification unless otherwise noted. Deuterated solvents ($CDCl_3$, DMSO-d_6) were purchased from Cambridge Isotope Laboratories. NMR spectra were acquired on Bruker AV300, AV301, GG500 or NEO500 instruments. ^{1}H and ^{13}C NMR spectra were referenced to residual deuterated solvent peaks. High resolution mass spectrometry data of ligands and their intermediates were collected on a Thermo

Scientific LTQ Orbitrap XL instrument in positive ion mode. C, H, N combustion analysis was conducted by Atlantic Microlabs Inc. FT-IR spectra were collected using a Perkin-Elmer Frontier spectrometer equipped with an ATR crystal. Thermogravimetric analysis data were collected using a TA Instruments Q Series analyzer. Inductively coupled plasma-optical emission spectroscopy (ICP-OES) was performed using a Perkin Elmer Optima 8300 Inductively Coupled Plasma - Optical Emission Spectrophotometer. XAS measurements were conducted using the mail-in program at the Advanced Photon Source on beamline 12-BM. Electron paramagnetic resonance measurements were performed on a Bruker EMXNano instrument at 100K.

Powder X-ray diffraction data were collected on either a Bruker D8 Discover powder X-ray diffractometer located in University of Washington's Molecular Analysis Facility, or a Bruker D2 PHASER benchtop diffractometer.

Microwave reactions were carried out using a CEM Discover SP Microwave synthesizer housed in the University of Washington Molecular Engineering Materials Center (MEM-C).

2. Ligand syntheses.

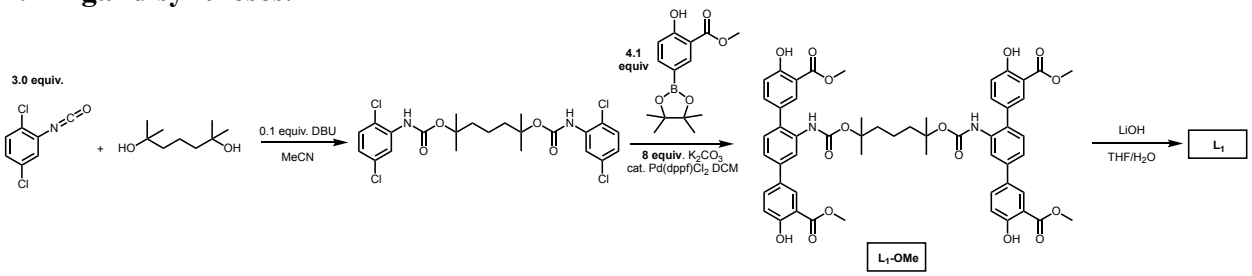

Scheme 3.S1. Overview of the synthesis of the aryl amine cross-linked ligand dimer, $\mathbf{L_1}$.

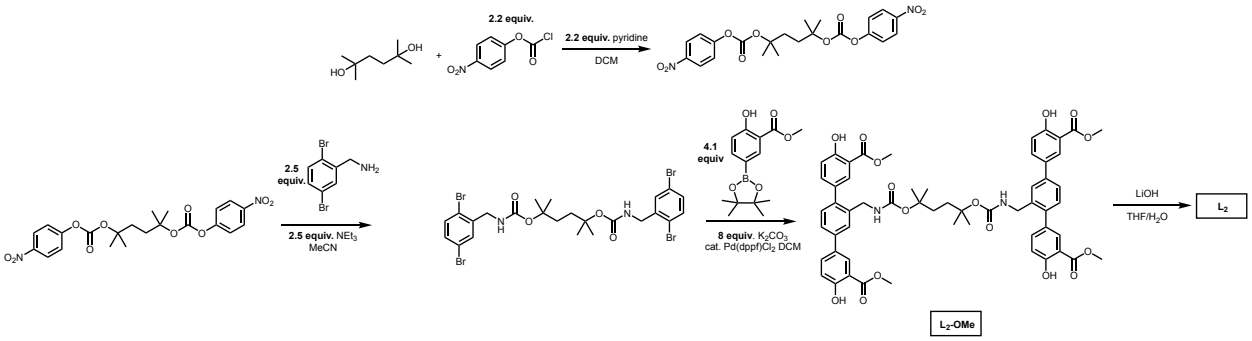

Scheme 3.S2. Overview of the synthesis of the alkyl amine cross-linked ligand dimer, $\mathbf{L_2}$.

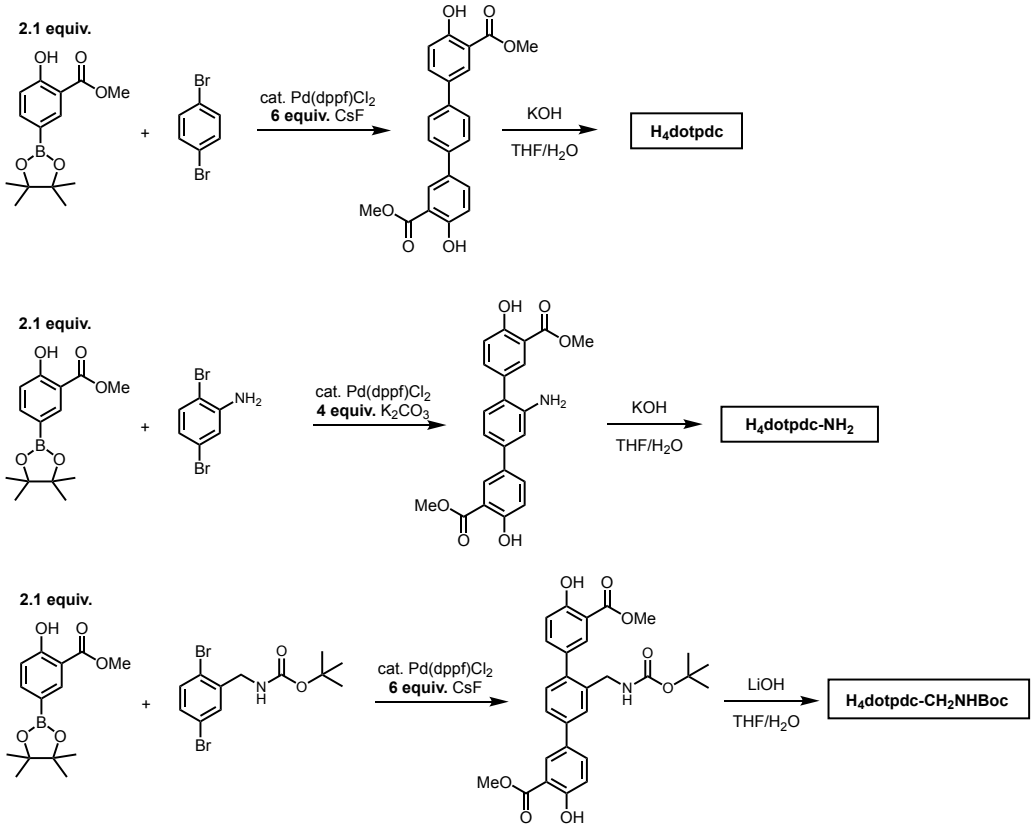

Scheme 3.S3. Overview of the synthesis of H_4dotpdc, H_4dotpdc-NH_2, and H_4dotpdc-CH_2NHBoc.

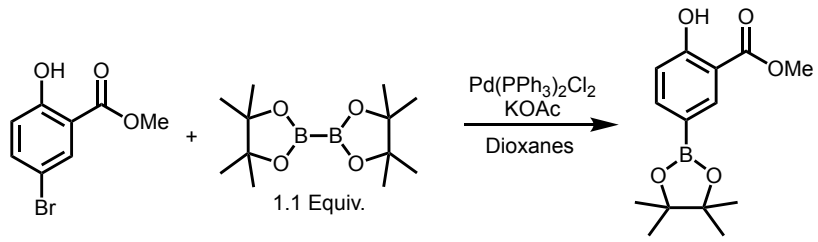

A 500 mL 2-neck round bottom flask equipped with a stir bar and reflux condenser under N_2 was charged with methyl 5-bromo-2-hydroxybenzoate (10.0 g, 43.3 mmol, 1.00 equiv.), bis(pinacolato)diboron (12.1 g, 47.6 mmol, 1.10 equiv.), potassium acetate (12.7 g, 130 mmol, 3.00 equiv.), and 1,4-dioxanes (150 mL). The solution was sparged with N_2 while stirring for 45 minutes, then $Pd(PPh_3)_2Cl_2$ (0.304 g, 0.433 mmol, 0.010 equiv.) was added the solution was refluxed for 18h, during which time the solution turned a dark brown and solids precipitated out. The solution was cooled too room temperature, and the dioxanes was removed *in vacuo*. The dark brown residue was brought up in EtOAc (200 mL) and deionized water (150 mL). The organics were separated off, and the aqueous remnants were extracted with EtOAc (2x70 mL). The organics were combined, dried over $MgSO_4$, filtered, and concentrated. The solids were washed with minimal hexanes to afford methyl 2-hydroxy-5-(4,4,5,5-tetramethyl-1,3,2-dioxaborolan-2-yl)benzoate as an off white solid. The hexanes wash was cooled overnight to afford a second crop of the product (10.96 g, 91% yield). ^{1}H NMR (300 MHz, $CDCl_3$): δ 11.0 (s, 1H), 8.31 (d, J = 1.6, 1H), 7.88 (dd, J = 8.3, 1.6, 1H), 6.96 (d, J = 8.3, 1H), 3.94 (s, 3H), 1.34 (s, 12H). Spectrum is consistent with what is reported in the literature.[1]

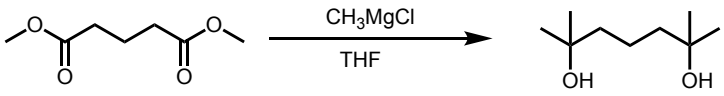

An oven-dried 250 mL 2-neck round bottom flask equipped with a stir bar and a reflux condenser was cooled to 0 °C under N_2. Methylmagnesium chloride (20.0 mL, 3M, 60.0 mmol) was canulaed in. Dimethyl glutarate (1.26 mL, 8.55 mmol) was added dropwise via syringe over the course of

15 minutes. While under N_2, the solution was allowed to warm to room temperature while stirring for 1h, during which time the solution became cloudy and began to thicken to a gel consistency. The solution was then refluxed for 2 h, during which time anhydrous THF (15 mL) was added because the solution had become to viscous to stir. The solution was then cooled to 0 °C, neutralized with excess saturated NH_4Cl (75 mL), and the THF was removed *in vacuo*. The aqueous solution was extracted with DCM (2x50 mL), dried with $MgSO_4$, filtered, and concentrated to yield Dimethyl-2,6-dihydroxyheptane as a semi-crystalline oil (1.33 g, 97% yield). ^{1}H NMR (300 MHz, $CDCl_3$): δ 1.46 (m, 6H), 1.23 (s, 12H). The spectrum is consistent with what is reported in the literature.[2]

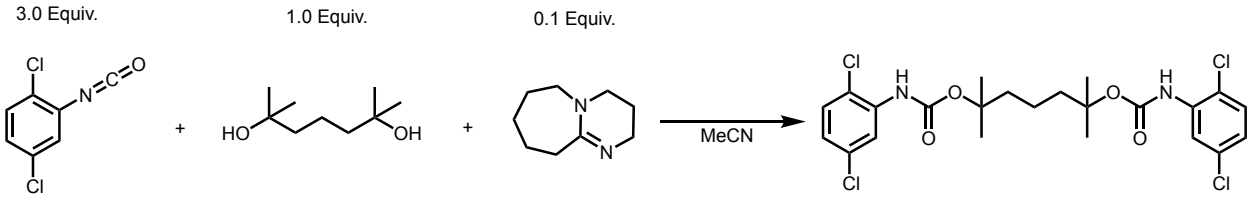

In a glovebox, a 20 mL scintillation vial equipped with a stir bar was charged with dimethyl-2,6-dihydroxyheptane (0.192 g, 1.20 mmol, 1.00 equiv.) and MeCN (4.0 mL). Separately, 2,5-dichlorophenyl isocyanate (0.677 g, 3.60 mmol, 3.00 equiv.) was dissolved in MeCN (4.0 mL), then added to the vial containing the dimethyl-2,6-dihydroxyheptane solution. The combined solution was allowed to stir at room temperature for 15 minutes, after which 1,8-Diazabicyclo[5.4.0]undec-7-ene (0.100 mL of 1.2 M solution in MeCN, 0.12 mmol, 0.10 equiv.) was added. The vial was capped and the solution was stirred at 40 ºC inside the glovebox for 18 h, during which time white solids precipitated out. The solution was cooled at -18 ºC for 2 hours, during which time more white solids precipitated out. The solution was filtered, the solids were rinsed with MeCN, and dried under N_2 to afford 2,6-dimethylheptane-2,6-diyl bis((2,5-dichlorophenyl)carbamate) as a white solid (0.407 g, 63.2% yield). ^{1}H NMR (300 MHz, $CDCl_3$) δ

8.23 (d, *J* = 2.5 Hz, 2H), 7.24 (d, *J* = 14.3 Hz, 2H), 6.99 (s, 2H), 6.93 (dd, *J* = 8.6, 2.5 Hz, 2H), 1.94 – 1.79 (m, 6H), 1.53 (s, 12H). ^{13}C NMR (126 MHz, $CDCl_3$) δ 151.86, 135.98, 133.57, 129.61, 123.19, 119.77, 119.55, 83.68, 41.04, 26.25, 18.45.

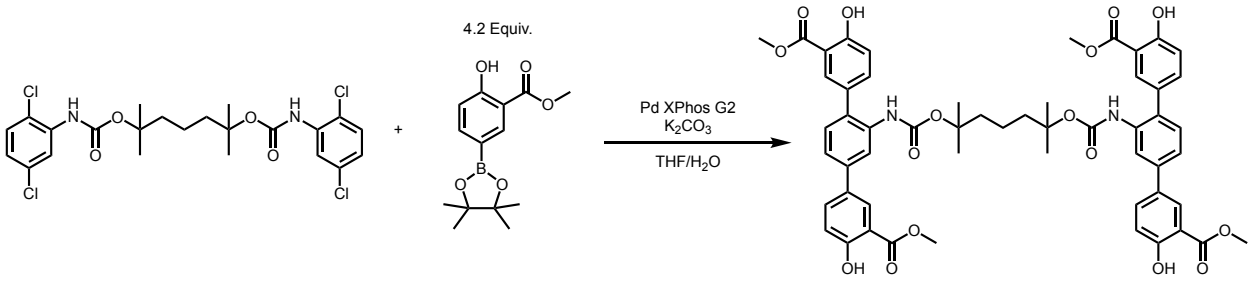

In a typical synthesis, to a 250 mL 2-neck round bottom flask equipped with a stir bar and reflux condenser under N_2 was added 2,6-dimethylheptane-2,6-diyl bis((2,5-dichlorophenyl)carbamate) (0.500 g, 0.932 mmol, 1.00 equiv.), methyl 2-hydroxy-5-(4,4,5,5-tetramethyl-1,3,2-dioxaborolan-2-yl)benzoate (1.089 g, 3.91 mmol, 4.20 equiv.), K_2CO_3 (1.031 g, 7.46 mmol, 8.00 equiv.), THF (60 mL) and H_2O (15 mL). The solution was sparged with N_2 for 45 minutes, after which time Pd XPhos G2 (0.0147 g, 0.019 mmol, 0.02 equiv.) was added, and the solution was allowed to stir at 60 ºC for 18 h, during which time the solution darkened and pale grey solids precipitated. After cooling to room temperature, the solution was poured into cold DI H_2O (75 mL) and the solids were filtered and further washed with H_2O and minimal MeOH to afford **L_1-(OMe)** as a an off-white solid (0.67 g, 72% yield). ^{1}H NMR (500 MHz, DMSO) δ 10.54 (s, 2H), 10.50 (s, 2H), 8.47 (s, 2H), 7.98 (s, 2H), 7.78 (s, 2H), 7.53 (d, *J* = 8.2 Hz, 2H), 7.49 (s, 2H), 7.47 (d, *J* = 8.3 Hz, 2H), 7.32 (d, *J* = 7.9 Hz, 2H), 7.07 (d, *J* = 8.7 Hz, 2H), 7.03 (d, *J* = 8.4 Hz, 2H), 3.91 (s, 6H), 3.87 (s, 6H), 1.51-1.24 (m, 18H). ^{13}C NMR (126 MHz, DMSO) δ 169.11, 168.90, 159.51, 159.18, 138.27, 135.81, 135.62, 133.55, 130.58, 130.47, 130.19, 129.88, 127.52, 123.42, 118.20, 117.36, 113.60, 112.88, 80.60, 73.52, 52.52, 52.43, 25.74, 24.95. Due to solubility reasons, no mass spectrum was collected.

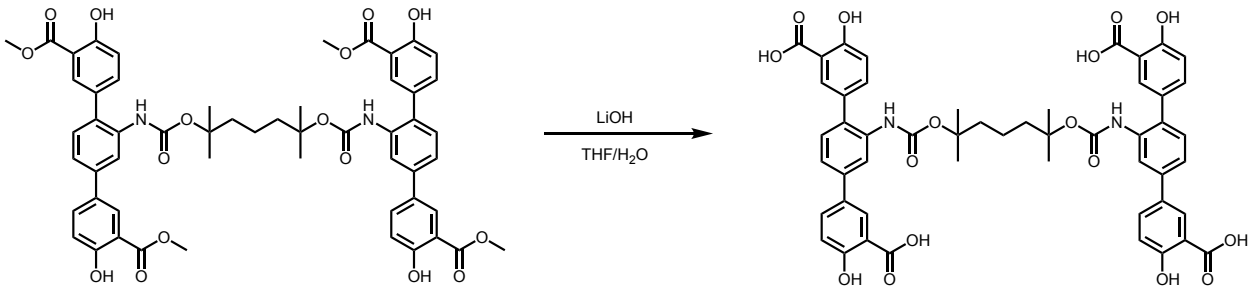

In a typical synthesis, to a 250 mL roundbottom flask equipped with a stir bar was added L_1-$(OMe)_4$ (0.4100 g, 0.410 mmol, 1.00 equiv.) along with THF (11 mL). Separately, LiOH (0.2949 g, 12.31 mmol, 30 equiv.) was dissolved in H_2O (11 mL) and then added to the flask. The solution was stirred at room temperature for 48 h, after which the solution was acidified to pH <2 and extracted with DCM (2x75 mL). The organics were dried over $MgSO_4$, filtered, and concentrated *in vacuo*. Trituration with Et_2O and hexanes afforded **L_1** as an off-white solid (0.356 g, 92% yield). ^{1}H NMR (500 MHz, DMSO) δ 8.46 (s, 2H), 8.02 (d, J = 2.4 Hz, 2H), 7.84 – 7.77 (m, 4H), 7.56 – 7.46 (m, 6H), 7.34 (d, J = 7.9 Hz, 2H), 7.05 (d, J = 8.6 Hz, 2H), 6.99 (d, J = 8.5 Hz, 2H), 1.50 (bs, 4H), 1.26 – 1.21 (m, 16H). HRMS (ESI/ion trap) *m/*z: $[M+H]^+$ Calcd for $C_{51}H_{46}N_2O_{16}$: 941.2764 ; found 941.2779.

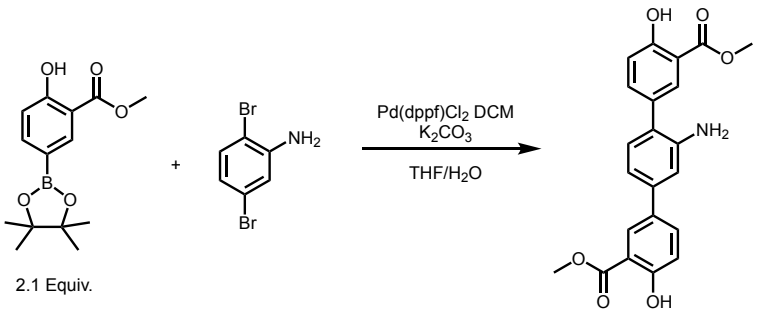

In a typical synthesis, to a 250 mL roundbottom flask equipped with a stir bar and reflux condenser under N_2 was added 2,5-dibromoaniline (0.86 g, 3.42 mmol, 1.00 equiv.), methyl 2-hydroxy-5-(4,4,5,5-tetramethyl-1,3,2-dioxaborolan-2-yl)benzoate (2.00 g, 7.20 mmol, 2.1 equiv.), K_2CO_3 (1.89 g, 13.68 mmol, 4.00 equiv.), THF (40 mL) and H_2O (10 mL). The solution was sparged with

N_2 for 30 minutes, followed by addition of Pd(dppf)Cl_2 DCM (0.06 g, 0.068 mmol, 0.02 equiv.). The solution was heated under N_2 at 60 ºC for 18 hours, during which time the solution darkened substantially. The solution was allowed to cool to room temperature under nitrogen. The solution was diluted with ~150 mL deionized water and ~200 mL dichloromethane. The aqueous layer was extracted with dichloromethane (2x 75 mL). The combined organics were dried over $MgSO_4$, filtered, and concentrated *in vacuo*. The resultant dark brown residue was brought up in minimal dichloromethane, and subjected to filtration through a pad of silica gel (9:1 DCM/EtOAc). The pale yellow filtrate was then concentrated *in vacuo*, and the resultant solids were washed with hexanes to afford [1,1′:4′,1″-Terphenyl]-4,4″-dicarboxylic acid, 2′-amino-3,3″-dihydroxy-, 4,4″-dimethyl ester as an off-white solid (1.32 g, 98% yield). ^{1}H NMR (300 MHz, $CDCl_3$) δ 10.78 (d, J = 10.2 Hz, 2H), 8.08 (d, J = 2.4 Hz, 1H), 7.97 (d, J = 2.3 Hz, 1H), 7.71 (dd, J = 8.6, 2.4 Hz, 1H), 7.60 (dd, J = 8.6, 2.4 Hz, 1H), 7.16 (d, J = 7.8 Hz, 1H), 7.12 – 6.95 (m, 4H), 4.04 – 3.98 (s, 3H), 3.96 (s, 3H). The data is consistent with that reported in the literature.[3]

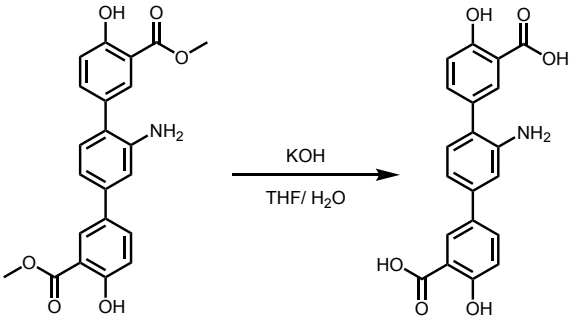

To a 250 mL roundbottom flask equipped with a stir bar was added [1,1′:4′,1″-Terphenyl]-4,4″-dicarboxylic acid, 2′-amino-3,3″-dihydroxy-, 4,4″-dimethyl ester (1.32 g, 3.35 mmol, 1.00 equiv.) and THF (50 mL). Separately, KOH (3.76 g, 67.0 mmol, 20 equiv.) was dissolved in 50 mL of H_2O. While stirring, the KOH solution was added to the solution containing the diester. The combined solution was then allowed to stir at 50 ºC for 24 h. After, the solution was cooled to room temperature and acidified to pH <1 using 1M HCl. The solution was extracted using EtOAc

(2x 150 mL), and the combined organics were dried over $MgSO_4$, filtered, and concentrated *in vacuo* to afford H_4dotpdc-NH_2 as an off-white solid (1.10 g, 90% yield). ^{1}H NMR (500 MHz, DMSO) δ 8.03 (d, *J* = 2.4 Hz, 1H), 7.87 (d, *J* = 2.2 Hz, 1H), 7.79 (dd, *J* = 8.7, 2.4 Hz, 1H), 7.61 (dd, *J* = 8.5, 2.3 Hz, 1H), 7.20-7.1 (m, 2H), 7.06 (dd, *J* = 8.5, 6.2 Hz, 3H). This spectrum is consistent with what is reported in literature.[3]

To an oven-dried 200 mL Schlenk flask equipped with a stir bar was added 2,5-Dimethyl-2,5-hexanediol (0.585 g, 4.00 mmol, 1.00 equiv.) and 40 mL of anhydrous DCM. The flask was cooled to 0 ºC under N_2. Pyridine (0.709 mL, 8.80 mmol, 2.20 equiv.) followed by 4-nitrophenyl chloroformate (1.77 g, 8.80 mmol, 2.20 equiv.) were added. The solution was stirred at 0 ºC for 10 minutes, then warmed to room temperature and stirred for 24 h, after which time the solution was transferred to a separatory funnel, washed once with 0.5 M HCl (20 mL), then with saturated aqueous $NaHCO_3$. The organics were dried with $MgSO_4$, filtered, and concentrated *in vacuo*. The resultant residue was triturated with MeOH, and the solids were filtered to obtain 2,5-dimethylhexane-2,5-diyl bis(4-nitrophenyl) bis(carbonate) as a white powder (1.835 g, 96% yield). ^{1}H NMR (500 MHz, $CDCl_3$): δ 8.19 (d, J = 8.8 Hz, 4H), 7.32 (d, J = 8.8 Hz, 4H), 1.99 (s, 4H), 1.57 (s, 12H). ^{13}C NMR (126 MHz, $CDCl_3$) δ 155.86, 150.74, 145.52, 125.44, 122.35, 86.35, 34.19, 26.13.

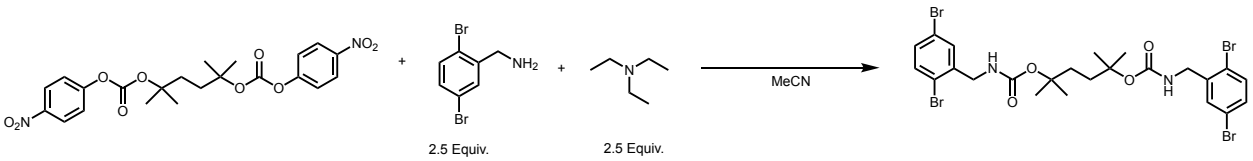

Dibromobenzylamine was first synthesized using the reported procedure.[4,5] In a typical reaction, to a 2-neck flask equipped with a stir bar and reflux condenser under N_2 was added the carbonate product (1.187 g, 2.49 mmol, 1.00 equiv.) and MeCN (20 mL). The solution was cooled to 0 ºC, followed by addition of 2,5-dibromobenzylamine (1.650 g, 6.23 mmol, 2.50 equiv.) and triethylamine (0.868 mL, 6.23 mmol, 2.50 equiv.). The solution was stirred at 0 ºC for 15 minutes, then warmed to 80 ºC and stirred 24 h. After, the inhomogeneous solution was cooled to room temperature, the solids were filtered, washed with MeOH, and dried under vacuum to afford 2,5-dimethylhexane-2,5-diyl bis((2,5-dibromobenzyl)carbamate) as a white powder (1.294 g, 71% yield). ^{1}H NMR (500 MHz, DMSO) δ 7.54 (d, J = 8.8 Hz, 2H), 7.49 (t, J = 6.0 Hz, 2H), 7.39 (d, J = 6.2 Hz, 4H), 4.13 (d, J = 6.1 Hz, 4H), 1.81 (s, 4H), 1.50 – 1.15 (m, 12H). ^{13}C NMR (126 MHz, DMSO) δ 155.51, 140.99, 134.23, 134.21, 131.43, 131.35, 130.65, 120.90, 120.85, 80.03, 43.55, 34.16, 26.39.

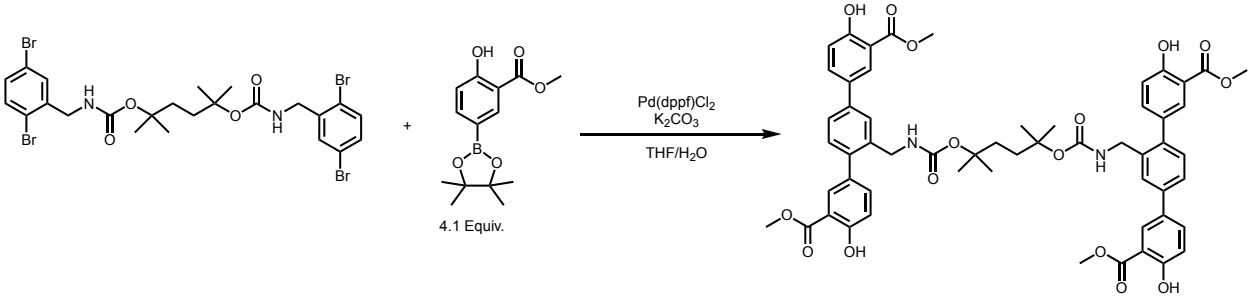

In a typical reaction, to a 2-neck flask equipped with a stir bar and reflux condenser under N_2 was added 2,5-dimethylhexane-2,5-diyl bis((2,5-dibromobenzyl)carbamate) (1.294 g, 1.78 mmol, 1.00 equiv.), methyl 2-hydroxy-5-(4,4,5,5-tetramethyl-1,3,2-dioxaborolan-2-yl)benzoate (2.026 g, 7.28 mmol, 4.10 equiv.), K_2CO_3 (1.965 g, 14.22 mmol, 8.00 equiv.), THF (120 mL) and H_2O (30 mL).

The solution was sparged with N_2 for 30 minutes, after which time Pd(dppf)Cl_2 DCM (0.043 g, 0.05 mmol, 0.03 equiv.) was added. The solution was then stirred at 60 ºC under N_2 for 18 h, during which time the color darkened. After, the solution was cooled to room temperature, diluted with H_2O (100 mL), extracted with EtOAc (2x100 mL), followed by DCM (1x100 mL). The combined organics were dried over $MgSO_4$, filtered, and concentrated *in vacuo*. Trituration with Et_2O and hexanes afforded **L_2-(OMe)** as an off-white powder (1.60 g, 89% yield). ^{1}H NMR (300 MHz, DMSO) δ 10.54 (s, 4H), 8.01 (s, 2H), 7.81 (d, *J* = 8.7 Hz, 2H), 7.70 (s, 2H), 7.59 (s, 2H), 7.52 (d, *J* = 8.6 Hz, 4H), 7.34 (bs, 2H), 7.24 (d, *J* = 7.9 Hz, 2H), 7.09 (d, *J* = 8.7 Hz, 2H), 7.04 (d, *J* = 8.6 Hz, 2H), 4.07 (d, *J* = 5.8 Hz, 4H), 3.9 (s, 6H), 3.88 (s, 6H), 1.69 (s, 4H), 1.25 (s, 12H). ^{13}C NMR (126 MHz, DMSO) δ 168.98, 168.96, 159.50, 159.12, 137.93, 136.17, 133.61, 131.14, 130.97, 130.32, 130.18, 127.47, 125.12, 124.51, 118.18, 117.34, 113.52, 113.03, 79.51, 73.50, 52.49, 52.45, 24.93. MS (ESI/ion trap) *m/z*: $[M–Na]^+$ Calcd for $C_{56}H_{56}N_2O_{16}Na$: 1035.35; found 1035.3.

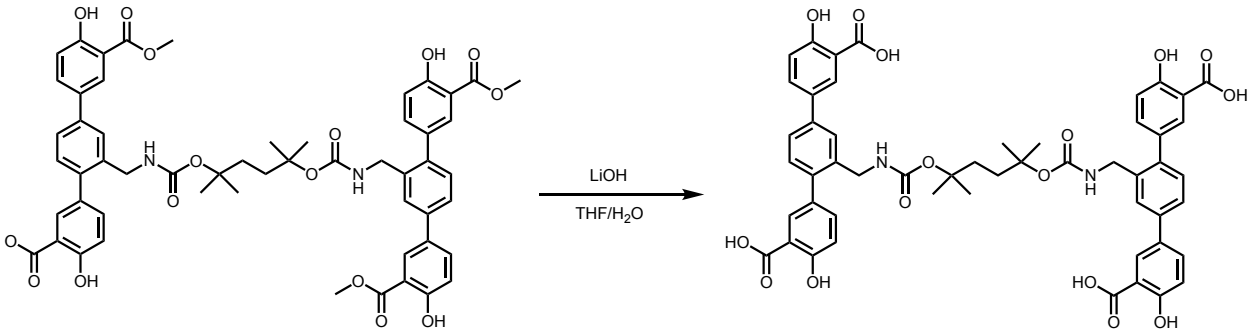

In a typical synthesis, to a 250 mL roundbottom flask equipped with a stir bar was added L_2-$(OMe)_4$ (0.7007 g, 0.69 mmol, 1.00 equiv.) along with THF (20 mL). Separately, LiOH (0.497 g, 20.75 mmol, 30 equiv.) was dissolved in H_2O (20 mL) and then added to the flask. The solution was stirred at room temperature for 48 h, after which the solution was acidified to pH <2 and extracted with DCM (2x75 mL). The organics were dried over $MgSO_4$, filtered, and concentrated *in vacuo*. Trituration with Et_2O and hexanes afforded **L_2** as an off-white solid (0.613 g, 93% yield).

^{1}H NMR (500 MHz, DMSO) δ 8.07 (s, 2H), 7.80 (dt, *J* = 9.3, 4.7 Hz, 2H), 7.72 (s, 2H), 7.60 (s, 2H), 7.53 (t, *J* = 7.6 Hz, 4H), 7.37 (q, *J* = 7.8 Hz, 2H), 7.25 (d, *J* = 7.9 Hz, 2H), 7.06 (d, *J* = 8.6 Hz, 2H), 7.01 (d, *J* = 8.6 Hz, 2H), 4.10 (s, 4H), 1.68 (s, 4H), 1.24 (s, 12H). ^{13}C NMR (126 MHz, DMSO) δ 171.78, 160.70, 160.30, 155.55, 138.05, 138.00, 137.65, 136.25, 133.59, 130.93, 130.77, 130.40, 130.36, 127.82, 125.09, 124.50, 117.86, 117.06, 113.55, 112.95, 79.57, 28.38. HRMS (ESI/ion trap) *m/z*: $[M+H]^+$ Calcd for $C_{52}H_{48}N_2O_{16}$: 955.2920; found 955.2933.

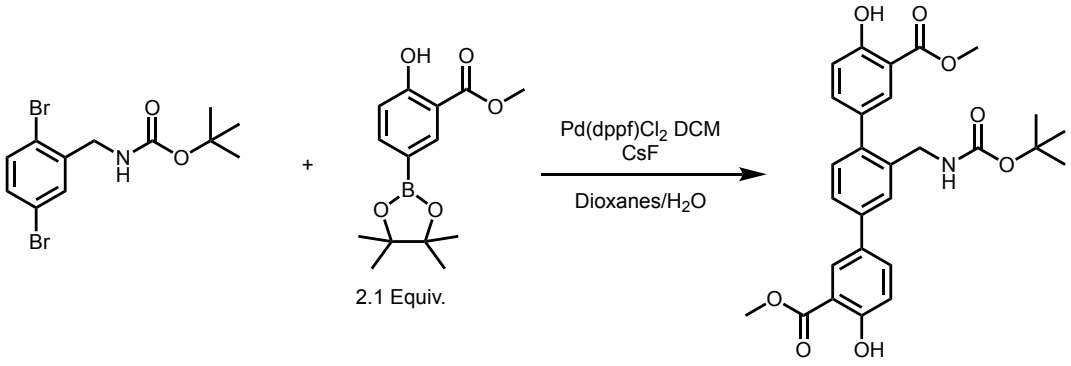

^{t}butyl-2,5-dibromobenzylcarbamate was first synthesized using the method reported in the literature.[6] A 100 mL 2-neck round bottom flask equipped with a stir bar and reflux condenser was charged with methyl 2-hydroxy-5-(4,4,5,5-tetramethyl-1,3,2-dioxaborolan-2-yl)benzoate (0.619 g, 2.23 mmol, 2.10 equiv.), ^{t}butyl-2,5-dibromobenzylcarbamate (0.387 g, 1.06 mmol, 1.00 equiv.), and cesium fluoride (0.966 g, 6.36 mmol, 6.00 equiv.). Next, 10 mL 1,4-dioxane followed by 5 mL deionized water were added. While stirring, the solution was sparged with nitrogen for 40 minutes. Subsequently, Pd(dppf)Cl_2 DCM (0.017 g, 0.021 mmol, 0.02 equiv.) was added, and the solution was allowed to reflux at 90 ºC for 18 hours, during which time the solution darkened. The solution was allowed to cool to room temperature under nitrogen. The solution was diluted with ~50 mL deionized water, and extracted with dichloromethane (2x50 mL) and ethyl acetate (1x50 mL). The combined organics were dried over $MgSO_4$, filtered, and concentrated *in vacuo*. The resultant residue was triturated with methanol, and the solids filtered to yield dimethyl 2'-(((*tert*-

butoxycarbonyl)amino)methyl)-4,4''-dihydroxy-[1,1':4',1''-terphenyl]-3,3''-dicarboxylate (0.443 g, 82 % yield) as a beige solid which was used without further purification. ^{1}H NMR (500 MHz, $CDCl_3$) δ 10.79 (s, 2H), 8.10 (d, *J* = 2.3 Hz, 1H), 7.81 (d, *J* = 2.2 Hz, 1H), 7.73 (dd, *J* = 8.6, 2.4 Hz, 1H), 7.59 (d, *J* = 1.9 Hz, 1H), 7.52 (dd, *J* = 8.6, 2.3 Hz, 1H), 7.43 (dd, *J* = 8.6, 2.3 Hz, 1H), 7.28 (s, 1H), 7.07 (m, 2H), 4.32 (s, 2H), 3.99 (s, 3H), 3.95 (s, 3H), 1.43 (s, 9zH). ^{13}C NMR (126 MHz, DMSO) δ 168.95, 159.48, 159.10, 155.77, 137.94, 137.89, 137.69, 137.34, 136.19, 133.62, 131.13, 130.97, 130.37, 130.22, 128.89, 128.19, 127.45, 125.31, 125.00, 124.51, 118.27, 117.42, 113.69, 113.12, 77.91, 52.55, 52.50, 41.39, 28.18.

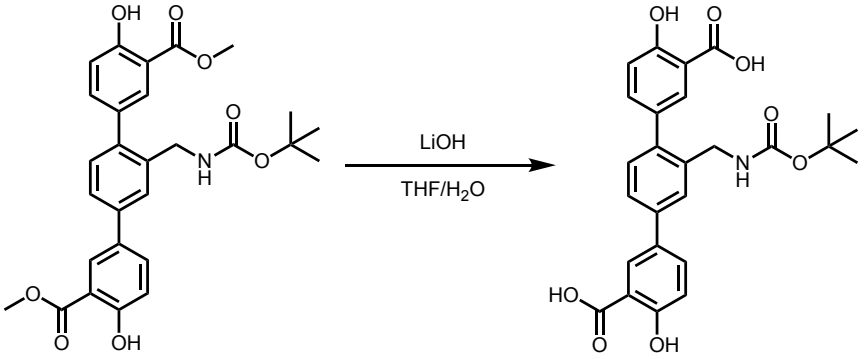

A 250 mL round bottom flask equipped with a stir bar was charged with dimethyl 2'-(((*tert*-butoxycarbonyl)amino)methyl)-4,4''-dihydroxy-[1,1':4',1''-terphenyl]-3,3''-dicarboxylate (0.443 g, 0.873 mmol, 1.00 equiv.) and 25 mL of tetrahydrofuran. Separately, lithium hydroxide (0.627 g, 26.19 mmol, 30.00 equiv.) was dissolved in 25 mL of deionized water. While stirring, the lithium hydroxide solution was added to the round bottom flask, and the combined solution was allowed to stir at room temperature over 48 hours. The tetrahydrofuran was removed under reduced pressure, the aqueous solution was acidified with 1M HCl and extracted with ethyl acetate (2x100 mL). The combined organics were washed with brine, dried over $MgSO_4$, filtered, and concentrated *in vacuo*. The resultant oil was triturated with hexanes, and the solids filtered to afford H_4dotpdc-CH_2NHBOC (2'-(((*tert*-butoxycarbonyl)amino)methyl)-4,4''-dihydroxy-[1,1':4',1''-

terphenyl]-3,3"-dicarboxylic acid) (0.346 g, 83 % yield) as an off-white solid. ^{1}H NMR (300 MHz, DMSO) δ 8.09 (d, *J* = 2.4 Hz, 1H), 7.85 (dd, *J* = 8.7, 2.5 Hz, 1H), 7.73 (d, *J* = 2.3 Hz, 1H), 7.61 (s, 1H), 7.55 (td, *J* = 7.7, 2.1 Hz, 2H), 7.42 (t, *J* = 6.0 Hz, 1H), 7.27 (d, *J* = 7.9 Hz, 1H), 7.07 (dd, *J* = 16.3, 8.6 Hz, 2H), 4.12 (d, *J* = 5.9 Hz, 2H), 1.38 (s, 9H). MS (ESI/ion trap) *m/*z: $[M–H]^-$ Calcd for $C_{26}H_{25}NO_8$: 478.1496. Found: 478.1500.

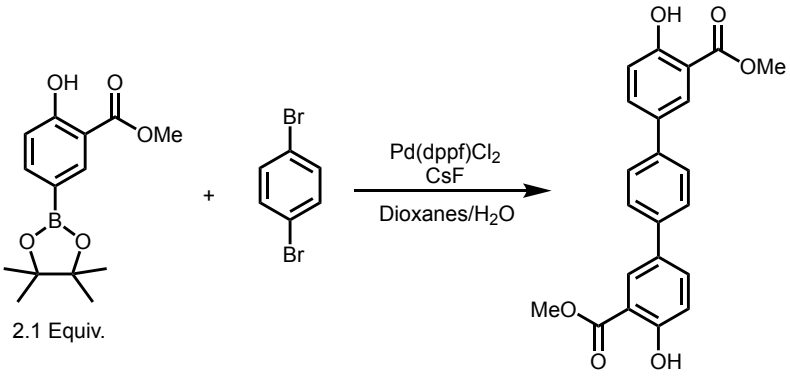

A 250 mL 2-neck round bottom flask equipped with a stir bar and reflux condenser was charged with methyl 2-hydroxy-5-(4,4,5,5-tetramethyl-1,3,2-dioxaborolan-2-yl)benzoate (2.00 g, 7.70 mmol, 2.10 equiv.), 1,4-dibromobenzene (0.808 g, 3.43 mmol, 1.00 equiv.), and cesium fluoride (3.12 g, 20.5 mmol, 6.00 equiv.). Next, 24 mL of 1,4-dioxane followed by 12 mL deionized water were added. While stirring, the solution was purged with nitrogen for 40 minutes. Subsequently $Pd(dppf)Cl_2$ (0.0752 g, 0.103 mmol, 0.03 equiv.) was added, and the solution was allowed to stir at reflux for 18 h, during which time the solution turned a dark grey with grey solids precipitating out. The solution was allowed to cool to room temperature under nitrogen. The solution diluted with deionized water (200 mL), and extracted with dichloromethane (3x 150. mL). The organics were dried using $MgSO_4$, filtered, and concentrated *in vacuo*. The resultant dark brown residue was brought up in minimal dichloromethane, and subjected to filtration through a pad of silica gel (9:1 DCM/EtOAc). The pale yellow filtrate was then concentrated *in vacuo*, and the resultant solids were washed with hexanes to afford 4,4"-dihydroxy-[1,1':4',1"-terphenyl]-3,3"-

dicarboxylate (0.947 g, 73% yield) as an off-white solid, which was used without further purification. ^{1}H NMR (500 MHz, $CDCl_3$): δ 10.79 (s, 2H), 8.11 (d, J = 2.4Hz, 2H), 7.74 (dd, J = 8.6, 2.4Hz, 2H), 7.6 (s, 4H), 7.09 (d, J = 8.6, 2H), 4.00 (s, 6H). The spectrum is consistent with what is reported in the literature.[1]

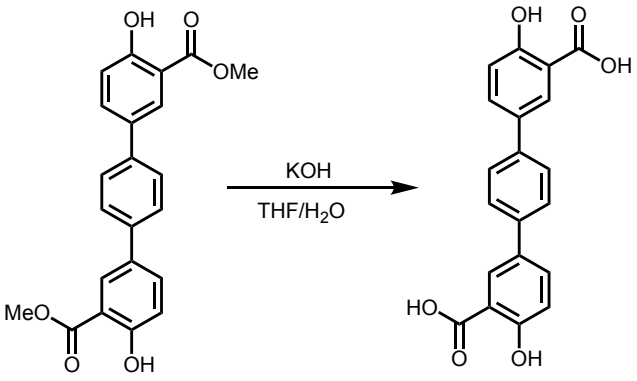

In a typical synthesis, a 500 mL round bottom flask equipped with a stir bar was charged with 4,4"-dihydroxy-[1,1':4',1"-terphenyl]-3,3"-dicarboxylate (2.01 g, 5.31 mmol, 1.00 equiv) and tetrahydrofuran (106 mL). Separately, potassium hydroxide (5.96 g, 106 mmol, 20.0 equiv) was dissolved in deionized water (106 mL) to give a 1 molar solution. The hydroxide solution was added to the round bottom flask containing the dicarboxylate. The inhomogeneous solution was stirred at 50 °C for 24 h, during which time the solution turned yellow and most of the solids dissolved. The solution was cooled to room temperature, and 1 M HCl was added to acidify to pH < 2, causing off-white solids to precipitate out. The tetrahydrofuran was removed *in vacuo*. The off-white solids were filtered, rinsed with copious water, and allowed to first air dry followed by heating at 150 °C for several hours to obtain H4dotpdc (4,4"-dihydroxy-[1,1':4',1"-terphenyl]-3,3"-dicarboxylic acid) as an off-white solid (1.77 g, 96% yield). ^{1}H NMR (500 MHz, DMSO-d_6): δ 8.08 (d, J = 2.45, 2H), 7.88 (dd, J = 8.6, 2.5, 2H), 7.70 (s, 4H), 7.08 (d, J = 8.6, 2H). The spectrum is consistent with what is reported in the literature.[1,6]

3. Synthesis and characterization of cross-linked frameworks.

3.1 General procedure for 1-XL-R% frameworks.

1-XL-R% frameworks were synthesized using an adapted procedure from the literature.[1,7] A 20 mL scintillation vial was charged with 0.1*(100-x%) mmol H_4dotpdc and 0.1*x% mmol L_1 to give a total of 0.100 mmol ligand and $Mg(NO_3)_2 \cdot {}_6H_2O$ (2.50 equiv. per dotpdc^{4-} unit), followed by MeOH (5.50 mL) and N,N-dimethylformamide (4.50 mL). The threads of the scintillation vial were wrapped with PTFE tape, capped, and taped with black electrical tape to prevent solvent evaporation. The vial was shaken to dissolve all solids and afford a pale-yellow solution. The solution was then heated in a dry bath at 120 °C for 3 h, after which the vial was cooled to room temperature, the mother liquor was decanted, and the solids re-immersed in fresh DMF and allowed to soak at room temperature. After 3 h the mother liquor was syringed off and replaced with fresh DMF. This process was repeated a total of three times, then repeated three more times with MeOH, also at room temperature, to afford MeOH-solvated material. Powder X-ray diffraction measurements and digestion NMRs were taken of the MeOH-solvated material. Scale ups of material were performed via batch. For full list of reaction conditions with metal salt and ligand ratios, as well as predicted and observed percentages of cross-linked dotpdc^{4-}, see Table S1.

3.1a Synthesis of 1-XL-18%.

A 20 mL scintillation vial was charged with H_4dotpdc (0.032 g, 0.090 mmol, 0.90 equiv.) and L_1 (0.010 g, 0.01 mmol, 0.10 equiv.) to give a total of 0.100 mmol ligand and $Mg(NO_3)_2 \cdot 6H_2O$ (0.071 g, 0.275 mmol, 2.50 equiv. per dotpdc^{4-} unit), followed by MeOH (5.50 mL) and N,N-dimethylformamide (4.50 mL). The threads of the scintillation vial were wrapped with PTFE tape, capped, and taped with black electrical tape to prevent solvent evaporation. The vial was shaken

to dissolve all solids and afford a pale-yellow solution. The solution was then heated in a dry bath at 120 °C for 3 h, after which the vial was cooled to room temperature, the mother liquor was decanted, and the solids re-immersed in fresh DMF and allowed to soak at room temperature. After 3 h the mother liquor was syringed off and replaced with fresh DMF. This process was repeated a total of three times, then repeated three more times with MeOH, also at room temperature, to afford MeOH-solvated material. Powder X-ray diffraction measurements and digestion NMRs were taken of the MeOH-solvated material. The relative ratio of 0.23:1 observed between the cross-linked dotpdc^{4-} and H_4dotpdc in the digestion ^{1}H NMR spectrum corresponds to an incorporation of 18%.

3.1b Synthesis of 1-XL-34%

A 20 mL scintillation vial was charged with H_4dotpdc (0.026 g, 0.075 mmol, 0.75 equiv.) and L_1 (0.024 g, 0.025 mmol, 0.25 equiv.) to give a total of 0.100 mmol ligand and $Mg(NO_3)_2 \cdot 6H_2O$ (0.080 g, 0.313 mmol, 2.50 equiv. per dotpdc^{4-} unit), followed by MeOH (5.50 mL) and N,N-dimethylformamide (4.50 mL). The threads of the scintillation vial were wrapped with PTFE tape, capped, and taped with black electrical tape to prevent solvent evaporation. The vial was shaken to dissolve all solids and afford a pale-yellow solution. The solution was then heated in a dry bath at 120 °C for 3 h, after which the vial was cooled to room temperature, the mother liquor was decanted, and the solids re-immersed in fresh DMF and allowed to soak at room temperature. After 3 h the mother liquor was syringed off and replaced with fresh DMF. This process was repeated a total of three times, then repeated three more times with MeOH, also at room temperature, to afford MeOH-solvated material. Powder X-ray diffraction measurements and digestion NMRs were taken of the MeOH-solvated material. The relative ratio of 0.51:1 observed between the cross-

linked dotpdc^{4-} and H_4dotpdc in the digestion ^{1}H NMR spectrum corresponds to an incorporation of 34%.

3.2 General procedure for Mg_2dotpdc-NH_2-R%.

Mg_2dotpdc-NH_2-R% frameworks were synthesized using an adapted procedure from the literature.[1,7] A 20 mL scintillation vial was charged with 0.1*(100-x%) mmol H_4dotpdc and 0.1*x% mmol H_2dotpdc-NH_2 to give a total of 0.100 mmol ligand and $Mg(NO_3)_2 \cdot 6H_2O$ (2.50 equiv. per dotpdc^{4-} unit), followed by MeOH (5.50 mL) and N,N-dimethylformamide (4.50 mL). The threads of the scintillation vial were wrapped with PTFE tape, capped, and taped with black electrical tape to prevent solvent evaporation. The vial was shaken to dissolve all solids and afford a pale-yellow solution. The solution was then heated in a dry bath at 120 °C for 3 h, after which the vial was cooled to room temperature, the mother liquor was decanted, and the solids re-immersed in fresh DMF and allowed to soak at room temperature. After 3 h the mother liquor was syringed off and replaced with fresh DMF. This process was repeated a total of three times, then repeated three more times with MeOH, also at room temperature, to afford MeOH-solvated material. Powder X-ray diffraction measurements and digestion NMRs were taken of the MeOH-solvated material. Scale ups of material were performed via batch. All subsequent reactions were performed using the same conditions as for the cross-linked/ templated materials.

3.3 General procedure for 2-XL-R% frameworks.

2-XL-R% frameworks were synthesized using an adapted procedure from the literature.[1,7] A 20 mL scintillation vial was charged with 0.1*(100-x%) mmol H_4dotpdc and 0.1*x% mmol L_2 to give a total of 0.100 mmol ligand and $Mg(NO_3)_2 \cdot 6H_2O$ (2.50 equiv. per dotpdc^{4-} unit), followed by MeOH (5.50 mL) and N,N-dimethylformamide (4.50 mL). The threads of the scintillation vial were wrapped with PTFE tape, capped, and taped with black electrical tape to prevent solvent

evaporation. The vial was shaken to dissolve all solids and afford a pale-yellow solution. The solution was then heated in a dry bath at 120 °C for 3 h, after which the vial was cooled to room temperature, the mother liquor was decanted, and the solids re-immersed in fresh DMF and allowed to soak at room temperature. After 3 h the mother liquor was syringed off and replaced with fresh DMF. This process was repeated a total of three times, then repeated three more times with MeOH, also at room temperature, to afford MeOH-solvated material. Powder X-ray diffraction measurements and digestion NMRs were taken of the MeOH-solvated material. Scale ups of material were performed via batch. For full list of reaction conditions with metal salt and ligand ratios, as well as predicted and observed percentages of cross-linked dotpdc^{4-}, see Table S1.

3.3a Synthesis of 2-XL-5%

A 20 mL scintillation vial was charged with H_4dotpdc (0.034 g, 0.0975 mmol, 0.975 equiv.) and L_2 (0.002 g, 0.0025 mmol, 0.025 equiv.) to give a total of 0.100 mmol ligand and $Mg(NO_3)_2 \cdot 6H_2O$ (0.066 g, 0.256 mmol, 2.50 equiv. per dotpdc4– unit), followed by MeOH (5.50 mL) and N,N-dimethylformamide (4.50 mL). The threads of the scintillation vial were wrapped with PTFE tape, capped, and taped with black electrical tape to prevent solvent evaporation. The vial was shaken to dissolve all solids and afford a pale-yellow solution. The solution was then heated in a dry bath at 120 °C for 3 h, after which the vial was cooled to room temperature, the mother liquor was decanted, and the solids re-immersed in fresh DMF and allowed to soak at room temperature. After 3 h the mother liquor was syringed off and replaced with fresh DMF. This process was repeated a total of three times, then repeated three more times with MeOH, also at room temperature, to afford MeOH-solvated material. Powder X-ray diffraction measurements and digestion NMRs were taken of the MeOH-solvated material. The relative ratio of 0.055:1 observed between the cross-

linked dotpdc^{4-} and H_4dotpdc in the digestion ^{1}H NMR spectrum corresponds to an incorporation of 5%.

3.3b Synthesis of 2-XL-23%

A 20 mL scintillation vial was charged with H_4dotpdc (0.026 g, 0.075 mmol, 0.75 equiv.) and L_1 (0.024 g, 0.025 mmol, 0.25 equiv.) to give a total of 0.100 mmol ligand and $Mg(NO_3)_2 \cdot 6H_2O$ (0.080 g, 0.313 mmol, 2.50 equiv. per dotpdc^{4-} unit), followed by MeOH (5.50 mL) and N,N-dimethylformamide (4.50 mL). The threads of the scintillation vial were wrapped with PTFE tape, capped, and taped with black electrical tape to prevent solvent evaporation. The vial was shaken to dissolve all solids and afford a pale-yellow solution. The solution was then heated in a dry bath at 120 °C for 3 h, after which the vial was cooled to room temperature, the mother liquor was decanted, and the solids re-immersed in fresh DMF and allowed to soak at room temperature. After 3 h the mother liquor was syringed off and replaced with fresh DMF. This process was repeated a total of three times, then repeated three more times with MeOH, also at room temperature, to afford MeOH-solvated material. Powder X-ray diffraction measurements and digestion NMRs were taken of the MeOH-solvated material. The relative ratio of 0.30:1 observed between the cross-linked dotpdc^{4-} and H_4dotpdc in the digestion ^{1}H NMR spectrum corresponds to an incorporation of 23%.

3.4 Synthesis of Mg_2dotpdc-CH_2NHBoc-R%.

Mg_2dotpdc-CH_2NHBoc-R% frameworks were synthesized using an adapted procedure from the literature.[1,7] A 20 mL scintillation vial was charged with 0.1*(100-x%) mmol H_4dotpdc and 0.1*x% mmol H_2dotpdc-CH_2NHBoc to give a total of 0.100 mmol ligand and $Mg(NO_3)_2 \cdot 6H_2O$ (2.50 equiv. per dotpdc^{4-} unit), followed by MeOH (5.50 mL) and N,N-dimethylformamide (4.50 mL). The threads of the scintillation vial were wrapped with PTFE tape, capped, and taped with

black electrical tape to prevent solvent evaporation. The vial was shaken to dissolve all solids and afford a pale-yellow solution. The solution was then heated in a dry bath at 120 °C for 3 h, after which the vial was cooled to room temperature, the mother liquor was decanted, and the solids re-immersed in fresh DMF and allowed to soak at room temperature. After 3 h the mother liquor was syringed off and replaced with fresh DMF. This process was repeated a total of three times, then repeated three more times with MeOH, also at room temperature, to afford MeOH-solvated material. Powder X-ray diffraction measurements and digestion NMRs were taken of the MeOH-solvated material. Scale ups of material were performed via batch. All subsequent reactions were performed using the same conditions as for the cross-linked/ templated materials.

4. Synthesis and characterization of thermolyzed frameworks.

4.1 General procedure for thermolysis of 1-XL-R% frameworks.

The thermal deprotection method was adapted from the literature[1]. Samples were fully washed prior to thermolysis experiments. A typical reaction scale was 25 mg of MeOH solvated material. The material was transferred to a 10 mL reaction tube, to which was added 2-ethyl-1-hexanol (3.00 mL) and ethylene glycol (0.300 mL), which was found to be a necessary co-solvent. The heterogeneous mixture was subjected to 230 °C microwave heating for 10.00 min, cooled to room temperature, then centrifuged. The mother liquor was decanted, and the solids were immersed in DMF at 120 °C for 3 h, after which time the mother liquor was syringed off and replaced with fresh DMF. This hot DMF wash was repeated three times, followed by immersion in MeOH at 60 °C for 3x3 h washes. The resultant materials were analyzed by PXRD and gas sorption. Digested samples were analyzed by ^{1}H NMR.

In a typical MOF digestion experiment to quantify ligand content, ~10–15 mg of MeOH-solvated material was suspended in 0.500 mL of DMSO-d_6, followed by addition of 1 drop of DCl in D_2O (20 wt. %). The solution was sonicated briefly to fully dissolve. ^{1}H NMR spectra were taken immediately following (~10 minutes).

4.2 General procedure for thermolysis of 2-XL-R% frameworks under N_2.

Samples were fully washed prior to thermolysis experiments. A typical reaction scale was 100 mg of MeOH solvated material. The material was transferred to a 40 mL scintillation vial and placed under flowing N_2 at room temperature for several hours. This initial N_2 purge was found to be critical to mitigating oxidation of H_4dotpdc-CH_2NH_2. After, the materials were heated to 250 ºC for 48 h, then cooled to room temperature under continuous N_2 flow. The resultant materials were immediately transferred to a nitrogen glovebox for storage. The materials were analyzed by PXRD and gas sorption. Digested samples were analyzed by ^{1}H NMR.

In a typical MOF digestion experiment to quantify ligand content, ~10–15 mg of MeOH-solvated material was suspended in 0.500 mL of DMSO-d_6, followed by addition of 1 drop of DCl in D_2O (20 wt. %). The solution was sonicated briefly to fully dissolve. ^{1}H NMR spectra were taken immediately following (~10 minutes).

4.3 Microwave thermolysis of 2-XL-2% materials.

In a typical procedure, in a nitrogen filled purge box 35.0 mg of MeOH solvated 2-XL-2% was placed inside a microwave reaction vessel, followed by 2-ethyl-1-hexanol (3.00 mL) and ethylene glycol (0.30 mL). Butylated hydroxytoluene (0.150 g, 0.681 mmol, 7.68 equiv.) was then added. The vessel was capped, then subjected to 230 ºC microwave heating for 10.00 min, cooled to room temperature, then centrifuged. The mother liquor was decanted, and the solids were immersed in

DMF at 120 °C for 3 h, after which time the mother liquor was syringed off and replaced with fresh DMF. This hot DMF wash was repeated three times, followed by immersion in MeOH at 60 °C for 3x3 h washes. The resultant materials were analyzed by PXRD and gas sorption. Digested samples were analyzed by ^{1}H NMR.

In a typical MOF digestion experiment to quantify ligand content, ~10–15 mg of MeOH-solvated material was suspended in 0.500 mL of DMSO-d_6, followed by addition of 1 drop of DCl in D_2O (20 wt. %). The solution was sonicated briefly to fully dissolve. ^{1}H NMR spectra were taken immediately following (~10 minutes).

5. Post-synthetic Schiff base condensations and metalations of 1-NH_2-R% frameworks.

5.1 General procedure for one-step imine condensation/metalation in 1-NH_2-R%. frameworks with CuCl and $NiCl_2$.

In a typical reaction, 25 mg of MeOH solvated material was suspended in 2 mL MeOH in a scintillation vial charged with a stir bar. Separately, an equimolar solution of 2-pyridinecarboxaldehyde and metal salt was prepared in acetonitrile and allowed to stir, during which time the solution turned a clear dark yellow. The solution was concentrated *in vacuo*, then brought back up in 2mL of MeOH to afford a clear, dark yellow solution. The M-aldehyde solution was then added to the scintillation vial (10 EQ vs -NH_2), and the inhomogeneous solution was allowed to stir overnight. The mother liquor was decanted and replaced with fresh MeOH and allowed to sit for 3 h, after which time the mother liquor was decanted and replaced with fresh MeOH. This MeOH wash was repeated three times, followed by drying under vacuum at room temperature to afford 1-(IP)CuCl-R% or 1-(IP)$NiCl_2$-R%.

5.1a Synthesis of 1-(IP)CuCl-18%.

25.0 mg of MeOH solvated 1-NH_2-18% was suspended in 2mL of MeOH in a scintillation vial charged with a stir bar. Separately, 2-pyridinecarboxaldehyde (0.011 mL, 0.113 mmol, 10.0 Equiv.) and anhydrous CuCl (0.011 g, 0.113 mmol, 10.0 Equiv.) were dissolved in 1 mL acetonitrile, and allowed to stir until a clear dark yellow solution was obtained. The solution was concentrated *in vacuo*, then brought back up in 2 mL of MeOH to afford a clear dark yellow solution. The CuCl-aldehyde solution was then added to the scintillation vial containing 1-IP-18%, and the inhomogeneous solution was allowed to stir overnight. The mother liquor was decanted and replaced with fresh MeOH and allowed to sit for 3 h, after which time the mother liquor was decanted and replaced again with fresh MeOH. This MeOH wash procedure was repeated three times, followed by drying under vacuum at room temperature to afford 1-(IP)CuCl-18%. The ratio of H_4dotpdc-NH_2/2-pyridinecarboxaldehyde of 1:1 observed by digestion ^{1}H NMR confirms the formation of the imine, while the Cu/Mg ratio of 0.09 observed by ICP-OES confirms quantitative metalation of the imine sites.

5.1b Synthesis of 1-(IP)$NiCl_2$-34%.

25.0 mg of MeOH solvated 1-NH_2-34% was suspended in 2mL of MeOH in a scintillation vial charged with a stir bar. Separately, 2-pyridinecarboxaldehyde (0.020 mL, 0.210 mmol, 10.0 Equiv.) and anhydrous $NiCl_2$ (0.027 g, 0.210 mmol, 10.0 Equiv.) were dissolved in 1 mL acetonitrile, and allowed to stir until a clear green solution was obtained. The solution was concentrated *in vacuo*, then brought back up in 2 mL of MeOH to afford a clear green solution. The $NiCl_2$-aldehyde solution was then added to the scintillation vial containing 1-IP-34%, and the inhomogeneous solution was allowed to stir overnight. The mother liquor was decanted and replaced with fresh MeOH and allowed to sit for 3 h, after which time the mother liquor was decanted and replaced again with fresh MeOH. This MeOH wash procedure was repeated three

times, followed by drying under vacuum at room temperature to afford 1-(IP)$NiCl_2$-34%. The ratio of H_4dotpdc-NH_2/2-pyridinecarboxaldehyde of 1:1 observed by digestion ^{1}H NMR confirms the formation of the imine, while the Ni/Mg ratio of 0.16 observed by ICP-OES confirms metalation of 94% of the imine sites.

5.2 General procedure for direct imine condensation in 1-NH_2-R% frameworks.

In a typical synthesis, 50 mg of MeOH solvated material was suspended in 5 mL MeOH in a scintillation vial charged with a stir bar. To that vial, 2-pyridine carboxaldehyde was added directly (50 EQ vs R%). The threads of the vial were lined with PTFE tape, and the vial was sealed and stirred at 60 ºC for 18 h. The mother liquor was decanted and replaced with fresh MeOH and allowed to sit for 3 h, after which time the mother liquor was decanted and replaced with fresh MeOH. This MeOH wash was repeated three times, followed by drying under vacuum at room temperature to afford 1-(IP)-R%. Conversion was confirmed by digestion ^{1}H NMR, and crystallinity was confirmed by PXRD.

5.2a Synthesis of 1-IP-18%.

50.0 mg of MeOH solvated 1-NH_2-18% was suspended in 5 mL of MeOH in a scintillation vial charged with a stir bar. To that vial, 2-pyridine carboxaldehyde (0.594 mL, 6.25 mmol, 50.0 equiv.) was added. The threads of the vial were wrapped twice with PTFE tape, the vial was sealed and allowed to stir at 60 ºC for 18 h, then cooled to room temperature. The mother liquor was decanted and replaced with fresh MeOH and allowed to sit at room temperature for 3 h, after which time the mother liquor was decanted and replaced with fresh MeOH. This washing procedure was repeated three times, followed by drying under vacuum to afford 1-IP-18%. The observed H_4dotpdc-NH_2/2-pyridinecarboxaldehyde ratio of 1:1 in the digestion ^{1}H NMR spectrum confirms quantitative conversion to the imine.

5.3 General procedure for metalation of 1-(IP)-R%.

In a typical procedure, 20 mg of MeOH solvated 1-IP-R% was suspended in 2 mL of MeOH in a scintillation vial. To that vial was added the anhydrous metal salt, MX_2, (10 equiv. vs R% as a 0.1M stock solution). The inhomogeneous solution was then stirred at room temperature for one day. The mother liquor was decanted and replaced with fresh MeOH and allowed to sit at room temperature for 3 h, after which time the mother liquor was decanted and replaced with fresh MeOH. This washing procedure was repeated three times, followed by drying under vacuum to afford 1-(IP)MX_2-R%. Metalation was confirmed by ICP-OES.

5.3a Synthesis of 1-(IP)CoI_2-18%.

20.0 mg of MeOH solvated 1-IP-18% was suspended in 2 mL of MeOH in a scintillation vial. Anhydrous CoI_2 (0.85 mL of 0.10 M stock solution, 0.085 mmol, 10 equiv.) was added, and the inhomogeneous solution was stirred for one day. The mother liquor was decanted and replaced with fresh MeOH and allowed to sit at room temperature for 3 h, after which time the mother liquor was decanted and replaced with fresh MeOH. This washing procedure was repeated three times, followed by drying under vacuum to afford **1-(IP)CoI_2-18%**. The observed Co/Mg ratio of 0.08 confirms metalation of 89% of the iminopyridine sites.

5.3b Synthesis of 1-(IP)$NiBr_2$-18%.

20.0 mg of MeOH solvated 1-IP-18% was suspended in 2 mL of MeOH in a scintillation vial. Anhydrous $NiBr_2$ (0.85 mL of 0.10 M stock solution, 0.085 mmol, 10 equiv.) was added, and the inhomogeneous solution was stirred for one day. The mother liquor was decanted and replaced with fresh MeOH and allowed to sit at room temperature for 3 h, after which time the mother liquor was decanted and replaced with fresh MeOH. This washing procedure was repeated three times,

followed by drying under vacuum to afford **1-(IP)NiBr$_2$-18%**. The observed Ni/Mg ratio of 0.08 confirms metalation of 89% of the iminopyridine sites.

5.3c Synthesis of 1-(IP)FeCl$_2$-18%.

20.0 mg of MeOH solvated 1-IP-18% was suspended in 2 mL of MeOH in a scintillation vial. Anhydrous $FeCl_2$ (0.85 mL of 0.10 M stock solution, 0.085 mmol, 10 equiv.) was added, and the inhomogeneous solution was stirred for one day. The mother liquor was decanted and replaced with fresh MeOH and allowed to sit at room temperature for 3 h, after which time the mother liquor was decanted and replaced with fresh MeOH. This washing procedure was repeated three times, followed by drying under vacuum to afford **1-(IP)FeCl$_2$-18%**. The observed Fe/Mg ratio of 0.09 confirms quantitative metalation of the iminopyridine sites.

6. Post-synthetic alkylation and metalation of 2-CH$_2$NH$_2$-R% frameworks.

6.1 General procedure for alkylation of 2-CH$_2$NH$_2$-R% frameworks.

In a typical reaction, in a nitrogen filled glovebox 50.0 mg of 2-CH_2NH_2-R% was suspended in 5 mL of anhydrous MeCN. Diisopropylethylamine (7.0 EQ vs R%) was then added, followed by 2-pyridylbromide hydrobromide (2.05 EQ vs R%). The inhomogeneous solution was stirred at room temperature for 48 h. After, the mother liquor was removed, and replaced with fresh MeCN and allowed to sit at room temperature for 3 h, after which time the mother liquor was replaced with fresh MeCN again. This washing procedure was repeated three times, followed by drying under vacuum to afford **2-DPA-R%**. Conversion was confirmed by digestion ^{1}H NMR, and crystallinity was confirmed by PXRD.

6.1a Synthesis of 2-DPA-23%.

In a nitrogen filled glovebox, 50.0 mg of 2-CH_2NH_2-23% was suspended in 5 mL MeCN in a scintillation vial. Diisopropylethylamine (0.028 mL, 0.162 mmol, 7.00 equiv.) was added,

followed by 2-pyridylbromide hydrobromide (0.012 g, 0.048 mmol, 2.05 equiv.). The inhomogeneous solution was stirred at room temperature for 48 h. After, the mother liquor was removed, and replaced with fresh MeCN and allowed to sit at room temperature for 3 h, after which time the mother liquor was replaced with fresh MeCN again. This washing procedure was repeated three times, followed by drying under vacuum to afford **2-DPA-23%**. The observed H_4dotpdc-DPA/H_4dotpdc ratio of 0.58:1.00 corresponds to overall functionalization of 23%.

6.1b Synthesis of 2-DPA-5%.

In a nitrogen filled glovebox, 50.0 mg of 2-CH_2NH_2-5% was suspended in 5 mL MeCN in a scintillation vial. Diisopropylethylamine (0.378 mL of 0.10 M in MeCN stock, 0.038 mmol, 7.00 equiv.) was added, followed by 2-pyridylbromide hydrobromide (0.111 mL of 0.10 M in MeCN stock, 0.011 mmol, 2.05 equiv.). The inhomogeneous solution was stirred at room temperature for 48 h. After, the mother liquor was removed, and replaced with fresh MeCN and allowed to sit at room temperature for 3 h, after which time the mother liquor was replaced with fresh MeCN again. This washing procedure was repeated three times, followed by drying under vacuum to afford **2-DPA-5%**. The observed H_4dotpdc-DPA/H_4dotpdc ratio of 0.05:1.00 corresponds to overall functionalization of 5%.

6.2 General procedure for metalation of 2-DPA-R% materials.

In a typical reaction, 20 mg of **2-DPA-R%** was suspended in 2 mL of MeCN in a PTFE wrapped scintillation vial charged with a stir bar. To that vial was added the anhydrous metal salt, MX_2, (3 equiv. vs R% as a 0.1M stock solution). The inhomogeneous solution was then stirred at 80 ºC for one day. The mother liquor was decanted and replaced with fresh MeCN and allowed to sit at 80 ºC for 3 h, after which time the mother liquor was decanted and replaced with fresh MeCN. This

washing procedure was repeated three times, followed by drying under vacuum to afford 2-(DPA)MX_2-R%. Metalation was confirmed by ICP-OES.

6.2a Synthesis of 2-(DPA)CoI_2-23%.

20.0 mg of MeCN solvated 2-DPA-23% was suspended in 2 mL of MeCN in a PTFE wrapped scintillation vial charged with a stir bar. Anhydrous CoI_2 (0.23 mL of 0.10 M stock solution, 0.023 mmol, 3 equiv.) was added, and the inhomogeneous solution was stirred for one day at 80 ºC. The mother liquor was decanted and replaced with fresh MeCN and allowed to sit at 80 ºC for 3 h, after which time the mother liquor was decanted and replaced with fresh MeCN. This washing procedure was repeated three times, followed by drying under vacuum to afford **2-(DPA)CoI_2-23%**. The observed Co/Mg ratio of 0.12 by ICP-OES confirms quantitative metalation of the bis(2-pyridylmethyl)amine sites.

6.2b Synthesis of 2-(DPA)$CuBr_2$-23%.

20.0 mg of MeCN solvated 2-DPA-23% was suspended in 2 mL of MeCN in a PTFE wrapped scintillation vial charged with a stir bar. Anhydrous $CuBr_2$ (0.23 mL of 0.10 M stock solution, 0.023 mmol, 3 equiv.) was added, and the inhomogeneous solution was stirred for one day at 80 ºC. The mother liquor was decanted and replaced with fresh MeCN and allowed to sit at 80 ºC for 3 h, after which time the mother liquor was decanted and replaced with fresh MeCN. This washing procedure was repeated three times, followed by drying under vacuum to afford **2-(DPA)$CuBr_2$-23%**. The observed Cu/Mg ratio by ICP-OES of 0.12 confirms quantitative metalation of the bis(2-pyridylmethyl)sites.

6.2c Synthesis of 2-(DPA)$FeCl_2$-23%.

20.0 mg of MeCN solvated 2-DPA-23% was suspended in 2 mL of MeCN in a PTFE wrapped scintillation vial charged with a stir bar. Anhydrous $FeCl_2$ (0.23 mL of 0.10 M stock solution,

0.023 mmol, 3 equiv.) was added, and the inhomogeneous solution was stirred for one day at 80 ºC. The mother liquor was decanted and replaced with fresh MeCN and allowed to sit at 80 ºC for 3 h, after which time the mother liquor was decanted and replaced with fresh MeCN. This washing procedure was repeated three times, followed by drying under vacuum to afford **2-(DPA)$FeCl_2$-23%**. The observed Fe/Mg ratio by ICP-OES of 0.12 confirms quantitative metalation of the bis(2-pyridylmethyl) sites.

6.2d Synthesis of 2-(DPA)$NiBr_2$-23%.

20.0 mg of MeCN solvated 2-DPA-23% was suspended in 2 mL of MeCN in a PTFE wrapped scintillation vial charged with a stir bar. Anhydrous $NiBr_2$ (0.23 mL of 0.10 M stock solution, 0.023 mmol, 3 equiv.) was added, and the inhomogeneous solution was stirred for one day at 80 ºC. The mother liquor was decanted and replaced with fresh MeCN and allowed to sit at 80 ºC for 3 h, after which time the mother liquor was decanted and replaced with fresh MeCN. This washing procedure was repeated three times, followed by drying under vacuum to afford **2-(DPA)$NiBr_2$-23%**. The observed Ni/Mg ratio by ICP-OES of 0.10 confirms metalation of 83% of the bis(2-pyridylmethyl)sites.

6.2e Synthesis of 2-(DPA)$CuCl_2$-5%.

20.0 mg of MeCN solvated 2-DPA-5% was suspended in 1.5 mL of MeCN in a PTFE wrapped scintillation vial charged with a stir bar. Anhydrous $CuCl_2$ (0.06 mL of 0.10 M stock solution, 0.006 mmol, 3 equiv.) was added, and the inhomogeneous solution was stirred for one day at 80 ºC. The mother liquor was decanted and replaced with fresh MeCN and allowed to sit at 80 ºC for 3 h, after which time the mother liquor was decanted and replaced with fresh MeCN. This washing procedure was repeated three times, followed by drying under vacuum to afford **2-(DPA)$CuClr_2$-**

5%. The observed Cu/Mg ratio by ICP-OES of 0.03 confirms quantitative metalation of the bis(2-pyridylmethyl) sites.

6.2e Synthesis of 2-(DPA)Cu(OTf)$_2$-5%.

20.0 mg of MeCN solvated 2-DPA-5% was suspended in 1.5 mL of MeCN in a PTFE wrapped scintillation vial charged with a stir bar. Anhydrous Cu(OTf)$_2$ (0.06 mL of 0.10 M stock solution, 0.006 mmol, 3 equiv.) was added, and the inhomogeneous solution was stirred for one day at 80 ºC. The mother liquor was decanted and replaced with fresh MeCN and allowed to sit at 80 ºC for 3 h, after which time the mother liquor was decanted and replaced with fresh MeCN. This washing procedure was repeated three times, followed by drying under vacuum to afford **2-(DPA)Cu(OTf)$_2$-5%**. The observed Cu/Mg ratio by ICP-OES of 0.03 confirms quantitative metalation of the bis(2-pyridylmethyl) sites.

7. General procedure for metal content analysis via ICP-OES.

Roughly 5 mg of washed material was placed in a 10 mL microwave tube, along with 0.750 mL of concentrated nitric acid and 0.250 mL of 20 wt% H_2O_2. The sample was capped, then heated under microwave at 150 ºC for 5 minutes. The resulting clear solution was transferred to a 50 mL falcon tube and diluted with HPLC grade water and diluted to a final nitric acid concentration of 3% by volume. Standard solutions in 3% nitric acid with 0.5, 1, 2, 5, and 10 ppm of the metals of interest and 0.5, 2, 7, 10, 15, and 20 ppm of Mg were prepared for the calibration curve. All curves had correlation coefficients ≥ 0.9999.

8. Sample activation and gas sorption analysis.

8.1 Activation of 1-XL-R% and 2-XL-R% materials.

Due to the thermal sensitivity of the tertiary dicarbamate cross-linkers, activation was carried out at room temperature. MeOH-solvated cross-linked MOF samples were first immersed in DCM for

1 x 3h washes, followed by filtration. The samples were then transferred to a preweighed glass tube and subjected to drying under flowing N_2 at RT for 8 h. After the initial N_2 purge, samples were capped with a Transeal and transferred to a Micromeritics Smart VacPrep instrument and heated under dynamic vacuum at RT for overnight. The glass tube and Transeal were subsequently weighed to determine the final mass of the activated sample.

8.2 Activation of 1-NH_2-R%, 2-CH_2NH_2-R%, 1-IP-R%, 2-DPA-R% materials.

MeOH or MeCN solvated samples were first immersed in DCM for 1 x 3h washes, followed by filtration. The samples were then transferred to a preweighed glass tube and subjected to drying under flowing N2 at 85 ºC for 1 h, and 150 ºC for 1 h. After the initial N2 purge, samples were capped with a Transeal and transferred to a Micromeritics Smart VacPrep instrument and heated under dynamic vacuum at 150 ºC for overnight. The glass tube and Transeal were subsequently weighed to determine the final mass of the activated sample.

8.3 Activation of metalated materials.

In a nitrogen filled glovebox, samples were loaded into preweighed glass tubes and placed under vacuum at room temperature for 6 h. After, samples were capped with a Transeal and transferred to a Micromeritics Smart VacPrep instrument and placed under dynamic vacuum at room temperature overnight. The glass tube and Transeal were subsequently weighed to determine the final mass of the activated sample.

8.4 N_2 adsorption measurements.

For all gas adsorption measurements, ~50 mg of sample was transferred to a preweighed glass sample tube. Low-pressure N_2 adsorption experiments (up to 1 bar) were performed using a Micromeritics 3Flex Surface Characterization Analyzer. Ultrahigh purity N_2 (5.0 grade, 99.999%)

was used in all adsorption experiments. N_2 adsorption measurements were performed using a liquid N_2 bath (77K).

BET surface areas were calculated using data points between 0.02 and 0.08 P/P_0. In all cases, the following BET consistency criteria were followed: 1) the pressure range has values of $v(P_0–P)$ increasing with P/P_0 and 2) positive y intercept.[8] All correlation coefficients were ≥0.999.

9. Computational details.

9.1 Modeling cross-linker conformations.

Extended structures of Mg_2dotpdc were created using Mg_2dobdc (MOF-74-Mg) as a starting point, followed by geometry optimization using the Forcite module in Materials Studio. The relative energies of two different configurations of the **L1** and **L2** cross-linkers down the pore channels were probed by density functional theory (DFT) using the Gaussian 16 program. The periodic structure obtained in Materials Studio was truncated to just two neighboring ligands, and a bridging cross-linker was added. The oxygens of the peripheral phenyl groups on the two ligands were frozen, mimicking the geometric constraints of the MOF lattice. The geometries of the cross-linker and central phenyl ring were optimized at the B3LYP/6-31+G(d) level of theory with empirical dispersion correction (D3BJ) and solvent correction via a polarization continuum model using methanol as the solvent. Frequency calculations were performed at this same level of theory to confirm that the final geometry was at a stationary point. Free energy corrections were determined at the B3LYP/6-31+G(d) level of theory at 298.15 K. Single point energies were computed at the B3LYP/6-311+G(d, p) level of theory with empirical dispersion correction (D3BJ) and solvent correction via polarization continuum using methanol as the solvent. All molecular structures were rendered in Diamond.

9.2 Modeling 1-(IP)$NiCl_2$ and 2-(DPA)$CuBr_2$ sites.

Similarly to the cross-linker conformations, the periodic structure obtained in Materials Studio was truncated to between three and four neighboring ligands for the mononuclear and binuclear systems, respectively, and the chelating ligands and metals were then added. The oxygens of the peripheral phenyl groups on the two ligands were frozen, mimicking the geometric constraints of the MOF lattice. The geometries were optimized using a split basis set of B3LYP/6-31+G(d) for the C,N,O,H,X (X= Cl or Br) and B3LYP/LANL2DZ for Ni and Cu. Frequency calculations were performed at this same level of theory to confirm that the final geometry was at a stationary point. Free energy corrections were determined at the B3LYP/6-31+G(d) level of theory at 298.15 K. Single point energies were computed at the B3LYP/6-311+G(d, p) and B3LYP/LANL2DZ level of theory with empirical dispersion correction (D3BJ) and solvent correction via polarization continuum using methanol or acetonitrile as the solvent for **1-(IP)$NiCl_2$** and **2-(DPA)$CuBr_2$**, respectively. All molecular structures were rendered in Diamond.

10. X-ray absorption spectroscopy (XAS).

10.1 Data collection and normalization

XAS measurements were conducted using the mail-in program at the Advanced Photon Source. Powder samples were prepared as wafers without additional grinding, and sealed with Kapton tape.

Ni K-edge data were collected on the XAS beamline 12-BM (4.5 – 20 keV) using a Si(111) monochromator. Transmission and fluorescence data were collected simultaneously at room temperature (24 ºC). The data presented here are from transmission mode. Energy calibration was achieved by using metal foil as a reference and the first peak in the first derivative of the metal foil XAS spectrum was calibrated to 8331.6 eV. Calibration and data alignment were performed using

Larch through the XAS Viewer GUI.[9] After averaging, the spectra of the studied samples were normalized to a total absorption of unity and processed using the Larch data normalization and analysis package. For normalization, the spline r-background parameter was set to 1.0. The background subtraction was done using a pre-edge range of -200 to -50 eV and a post edge linear range of 60 to 830 eV. A spline range of $k = 0$ to $k = 15$ $Å^{-1}$ and k-weight of 2 was used to isolate the EXAFS (chi) function. The Ni K-edge EXAFS spectra were Fourier transformed over a k-range of 2-11$Å^{-1}$.[10]

Cu K-edge data were collected on the XAS beamline 12-BM (4.5 – 20 keV) using a Si(111) monochromator. Transmission and fluorescence data were collected simultaneously at room temperature (24 ºC). The data presented here are from fluorescence mode. Energy calibration was achieved by using metal foil as a reference and the first peak in the first derivative of the metal foil XAS spectrum was calibrated to 8980.48 eV. Calibration and data alignment were performed using Larch through the XAS Viewer GUI. After averaging the spectra of the studied samples were normalized to a total absorption of unity and processed using the Larch data normalization and analysis package. For normalization, the spline r-background parameter was set to 1.0. The background subtraction was done using a pre-edge range of -200 to -50 eV and a post edge linear range of 60 to 830 eV. A spline range of $k = 1.0$ to $k = 15$ $Å^{-1}$ and k-weight of 2 was used to isolate the EXAFS (chi) function. The Cu K-edge EXAFS spectra were Fourier transformed over a k-range of 2-11$Å^{-1}$.

10.2 EXAFS Fitting of 1-(IP)$NiCl_2$.

Fitting of the Ni K-edge EXAFS spectra was carried out by Larch software. The spectra of **1-(IP)$NiCl_2$** were fitted in R-space with a R range of 1 to 3.0 Å, and the fittings were done with a k-

weight of 3. The Fourier transform was performed using a Kaiser-bessel window with a Dk of 4.0. The inverse Fourier transform and DR of 0.50. From the reference fit we obtain the amplitude factor (S_0^2) of 0.999. Coordination numbers were fixed during fitting. Fits obtained by omitting the additional solvent O atom showed unreasonable fits based on the R-factor and much greater uncertainty in the Debye-Waller factor. The best fit parameters are outlined in **Table S3**.

10.3 EXAFS Fitting of 2-(DPA)CuBr$_2$.

Fitting of the Cu K-edge EXAFS spectra was carried out by Larch software. The spectra of **2-(DPA)CuBr$_2$** were fitted in *R*-space with a *R* range of 1 to 3.0 Å, and the fittings were done with a *k*-weight of 3. The Fourier transform was performed using a Kaiser-bessel window with a Dk of 4.0. The inverse Fourier transform and DR of 0.50. From the reference fit we obtain the amplitude factor (S_0^2) of 0.96. Coordination numbers were fixed during fitting. The best fit parameters are outlined in **Table S6**.

11. Electron paramagnetic resonance (EPR).

X-band EPR data were collected at 100K on a Bruker EMXnano spectrometer (microwave (mw) frequency, 9.64 GHz) equipped with a liquid nitrogen cooling system. A power-saturation sweep was performed between 50 and 0.15 mW. A microwave power of 1 mW, modulation amplitude of 8.23 G and a modulation frequency of 100 kHz were used. Samples were prepared in a nitrogen filled glovebox by gently mixing samples of **2-(DPA)Cu(OTf)$_2$-5%** and Mg$_2$dotpdc-(DPA)Cu(OTf)$_2$-5% with pre-ground KBr. Tubes were capped and sealed with electrical tape before removal from the glovebox and obtaining spectra. Adequate signal-to-noise was achieved after 10 scans. The allowed $\Delta m_s = 1$ transition of each spectrum was fit using EasySpin as a two-component system consisting of the organic radical and the Cu(II) center.

To compare the relative intensities of the forbidden $\Delta m_s = 2$ transitions, the X-band spectra were first background subtracted using a 5th order polynomial in Bruker's Xenon processing software. In order to account for any differences in the number of spins in **2-(DPA)Cu(OTf)$_2$-5%** and Mg$_2$dotpdc-(DPA)Cu(OTf)$_2$-5%, the allowed $\Delta m_s = 1$ transitions were doubly integrated to obtain the area under the absorption curve. These values were used to normalize the spectra, allowing us to compare the integrated areas of the forbidden $\Delta Dm_s = 2$ transition at g ~ 4 (**Table 3.S10**).

12. Tables and figures.

Table 3.S1 | Summary of relative equivalents of metal salt and ligand used to synthesize Mg$_2$dotpdc, **1-XL-R%** and **2-XL-R%** including the predicted and observed percentages of cross-linked dotpdc^{4-} to total dotpdc^{4-} in the framework (R%).

	Mg^{2+} salt[1] (equiv)	**Cross-linked ligand** (equiv)	**H_4dotpdc** (equiv)	**Predicted**[2] **R%** (%)	**Observed**[3] **R%** (%)
Mg$_2$dotpdc	2.50	0	1.00	0%	0%
1-XL-18%	2.75	0.100	0.900	18%	18%
1-XL-34%	3.13	0.250	0.750	40%	34%
2-XL-5%	2.56	0.025	0.975	5%	5%
2-XL-23%	2.75	0.100	0.900	18%	23%

[1] 2.5 equivalents of $Mg(NO3)_2 \cdot 6(H_2O)$ were added per dotpdc^{4-} unit. Note that each ligand dimer contains two dotpdc^{4-} units.
[2] The predicted percentage of cross-linked dotpdc^{4-} relative to the total amount of dotpdc^{4-} ligands in the framework.
[3] Observed percentages were determined by ^{1}H NMR characterization of frameworks digested in DCl/DMSO-d_6.

Table 3.S2 | Summary of electronic energies, free energy corrections, and final Gibbs free energies obtained from DFT calculations for the symmetric and offset cross-linker configurations. Calculations were performed at B3LYP/6-311+G(d,p)//B3LYP/6-31+G(d) with D3BJ dispersion correction and solvent correction (methanol).

	L1 Symmetric configuration	**L1 Offset configuration**	**L2 Symmetric configuration**	**L2 Offset configuration**
Electronic energy (Hartrees)	-3285.5376	-3285.534	-3324.8569	-3324.5735
Free energy correction at 298.15 K (Hartrees)	0.782349	0.783189	0.811621	0.806289
G^0 at 298.15 K (Hartrees)	-3284.7553	-3284.7508	-3324.0453	-3323.7672

G^0 at 298.15 K (kcal/mol)	-2059541.5	-2059538.8	-2084176.4	-2084002

Table 3.S3 | Summary of metalation results.

	Percent functionalization[a]	Expected M/Mg ratio	Found M/Mg Ratio[b]
1-(IP)$MnCl_2$[d]	18	0.09	0.09
1-(IP)$FeCl_2$[d]	18	0.09	0.09
1-(IP)CoI_2[d]	18	0.09	0.08
1-(IP)$NiCl_2$[c]	34	0.17	0.16
1-(IP)$NiCl_2$[d]	18	0.09	0.07
1-(IP)$NiBr_2$[d]	18	0.09	0.08
1-(IP)CuCl[c]	18	0.09	0.09
2-(DPA)$FeCl_2$	23	0.12	0.12
2-(DPA)CoI_2	23	0.12	0.12
2-(DPA)$NiBr_2$	23	0.12	0.10
2-(DPA)$CuBr_2$	23	0.12	0.12
2-(DPA)$CuCl_2$	5	0.03	0.03
2-(DPA)$Cu(OTf)_2$	5	0.03	0.03

[a] Determined by digestion ^{1}H NMR.
[b] Determined by ICP-OES.
[c] Synthesized using the one-pot method.
[d] Synthesized using the step-wise method.

Table 3.S4 | Fit results for Ni K-edge EXAFS 1-(IP)NiCl2

1-(IP)$NiCl_2$		**Fitting Range**	k: 3.0 - 11.0 Å R: 1.0 - 3.0 Å
Independent points	11	Variables	6
Reduced chi-squared	380	R-factor	0.079
DE_0 (eV)	0	S_0^2	1.000
CN (N/O)	3.0	CN (Cl)	2.0
R (Ni-N/O)	2.033 ± 0.060 Å	s^2 (Ni-N/O)	0.002
R (Ni-Cl)	2.291 ± 0.068 Å	s^2 (Ni-Cl)	0.011

Table 3.S5 | Tabulated distances for DFT optimized structure of 1-(IP)$NiCl_2$.

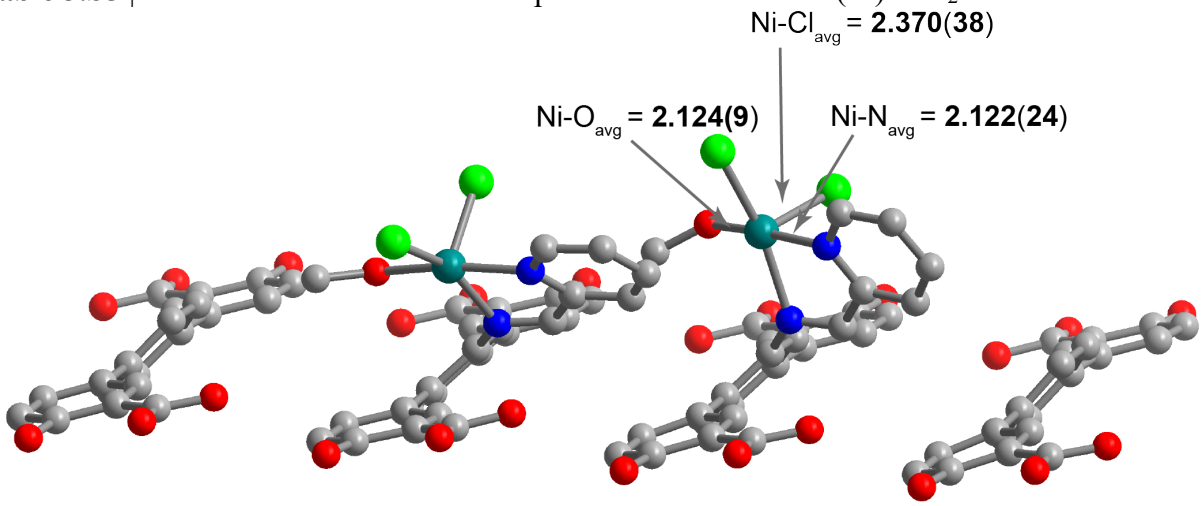

Metal center	Ni-N (Å)	Ni-O (Å)	Ni-Cl (Å)
Ni (1)	2.104	2.118	2.337
	2.145		2.397
Ni (2)	2.100	2.131	2.337
	2.141		2.341
Average	**2.122 (0.024)**	**2.124 (0.009)**	**2.370 (0.038)**

Table 3.S6 | Tabulation of reported five-coordinate nickel (II) iminopyridine complexes

CCDC Identifier	Ni–N (Å)	Ni–Cl (Å)	Ni–O (Å)
CUCDUC[11]	2.0642	2.318	2.043
	2.032	2.291	
ELEKIQ[12]	2.077	2.324	2.038
	2.055	2.278	
HAQLES[13]	2.058	2.321	2.155
	2.007	2.262	
HAQLIW[13]	2.111	2.313	2.077
	2.045	2.278	
LULYOI[14]	2.032	2.327	2.038
	2.075	2.299	2.048
	2.091	2.312	
	2.02	2.296	

MOTGIN[15]	2.037 2.083	2.305 2.282	2.099
PAJPIB[16]	2.021 2.077	2.3 2.286	2.069
YAPZIA[17]	2.032 2.073	2.304 2.315	2.089
YAPZOG[17]	2.025 2.072	2.313 2.3	2.097
Average	**2.054 (0.028)**	**2.301 (0.017)**	**2.075 (0.037)**

Table 3.S7 | Fit results for Cu K-edge EXAFS 2-(DPA)$CuBr_2$

2-(DPA)$CuBr_2$		**Fitting Range**	k: 2.0 - 11.0 Å R: 1.0 - 3.0 Å
Independent points	12	Variables	7
Reduced chi-squared	12	R-factor	0.013
DE_0 (eV)	11.5	S_0^2	0.96
$CN(N_{pyr})$	2.0	$CN(N_{alk})$	1.0
$CN(Br_{basal})$	1.0	$CN(Br_{apical})$	1.0
$R(Cu\text{-}N_{pyr})$	2.010 ± 0.012 Å	$s^2(Cu\text{-}N_{pyr})$	0.004
$R(Cu\text{-}N_{alk})$	2.143 ± 0.012 Å	$s^2(Cu\text{-}N_{alk})$	0.004
$R(Cu\text{-}Br_{basal})$	2.404 ± 0.015 Å	$s^2(Cu\text{-}Br_{basal})$	0.015
$R(Cu\text{-}Br_{apical})$	2.787 ± 0.023 Å	$s^2(Cu\text{-}Br_{apical})$	0.015

Table 3.S8 | Tabulation of reported distorted square pyramidal bis(2-pyridylmethyl)amine-ligated $CuBr_2$ complexes.

CCDC identifier	**Cu–N (pyridine) (Å)**	**Cu–N (amine) (Å)**	**Cu–Br (basal) (Å)**	**Cu–Br (apical) (Å)**
AJUFOC[18]	1.995 1.994	2.128	2.418	2.671
IRUWUN[19]	2.017 2.025	2.082	2.430	2.728
KAFDOO[20]	2.004 2.006	2.129	2.424	2.641

WESMIT[21]	2.017 2.015	2.081	2.407	2.639
XAKDAQ[22]	2.02 2.015	2.054	2.410	2.705
XIGQAF[23]	1.996 1.999	2.062	2.398	2.75
Average	**2.009 (0.011)**	**2.089 (0.032)**	**2.414 (0.012)**	**2.689 (0.046)**

Table 3.S9 | Tabulated distances for DFT-optimized structure of 2-(DPA)$CuBr_2$.

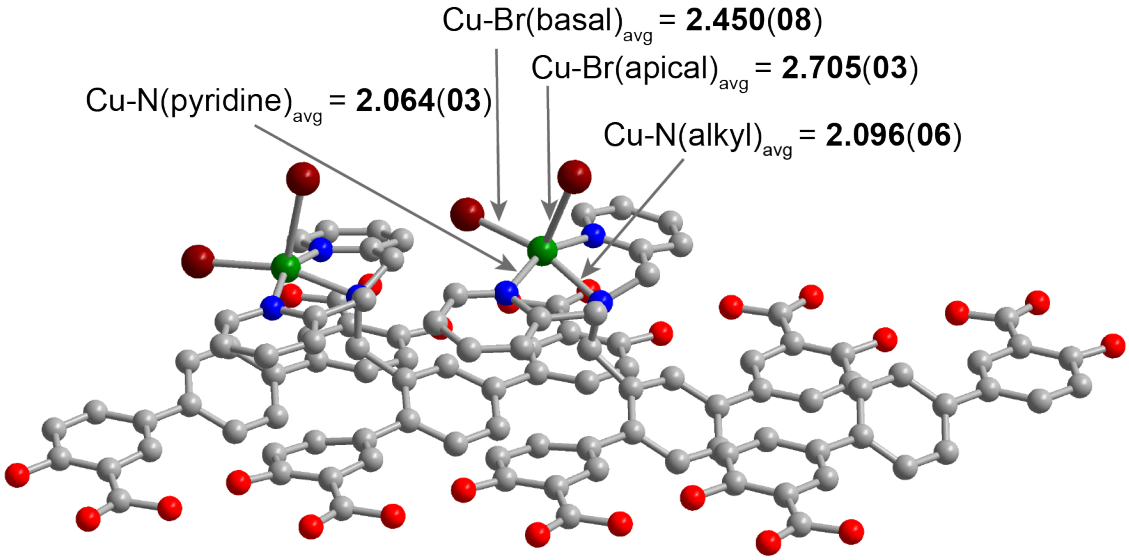

Metal center	Cu-N (pyridine) (Å)	Cu-N (alkyl) (Å)	Cu-Br (basal) (Å)	Cu-Br (apical) (Å)
Cu (1)	2.061 2.067	2.092	2.444	2.703
Cu (2)	2.063 2.065	2.1	2.455	2.708
Average	**2.064 (0.003)**	**2.096 (0.006)**	**2.450 (0.008)**	**2.705 (0.003)**

Table 3.S10 | Normalized double integrals for **2-(DPA)Cu(OTf)$_2$-5%** and Mg_2dotpdc-(DPA)Cu(OTf)$_2$-5%.

Material	$\Delta m_s = 1$ allowed	$\Delta m_s = 2$ forbidden	$\Delta m_s = 1$ allowed (Normalized)	$\Delta m_s = 1$ allowed (Normalized)
2-(DPA)Cu(OTf)$_2$-5%	276804.84	1669.58	100	0.613
Mg_2dotpdc-(DPA)Cu(OTf)$_2$-5%.	320404.81	1253.28	100	0.395

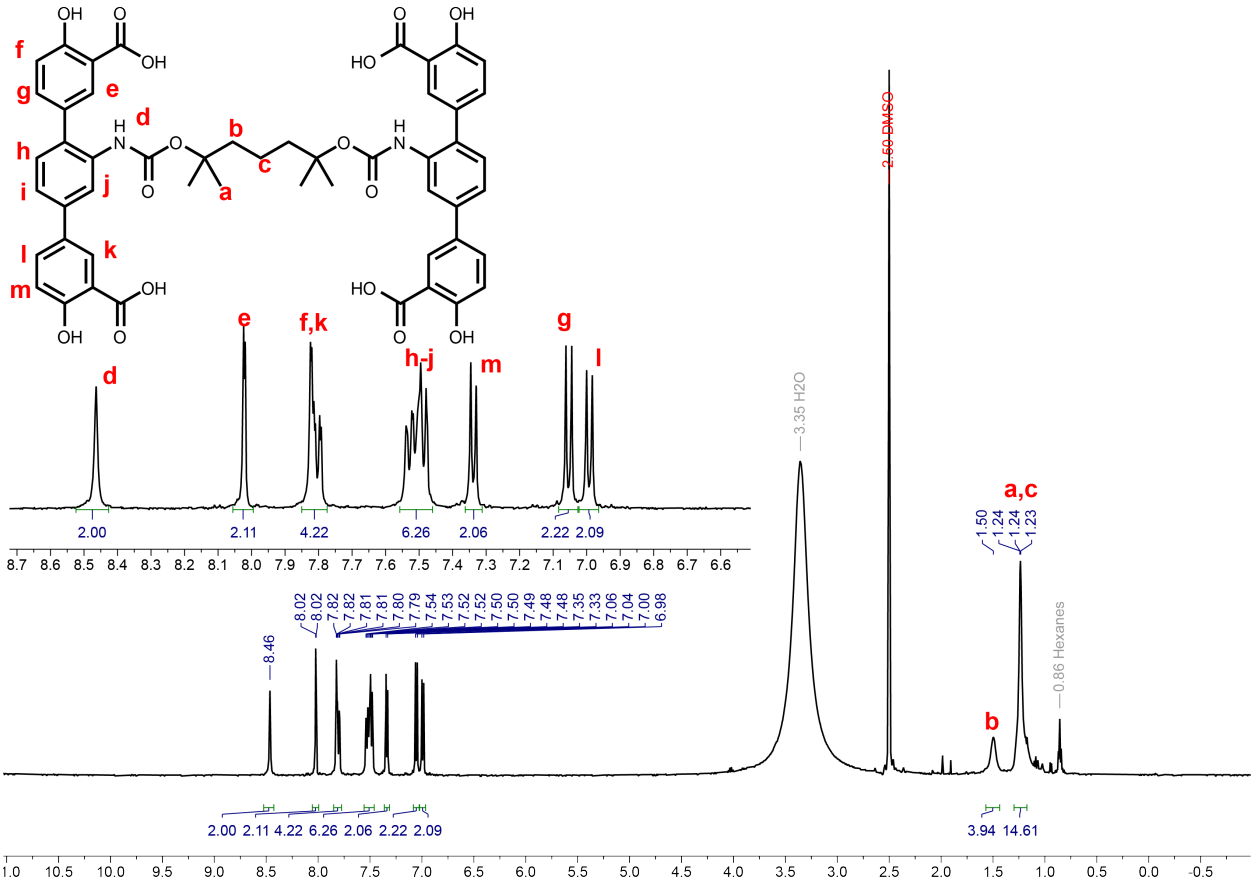

Figure 3.S1 | ^{1}H NMR spectrum of $\mathbf{L_1}$ with aromatic region (inset) taken in DMSO-d_6.

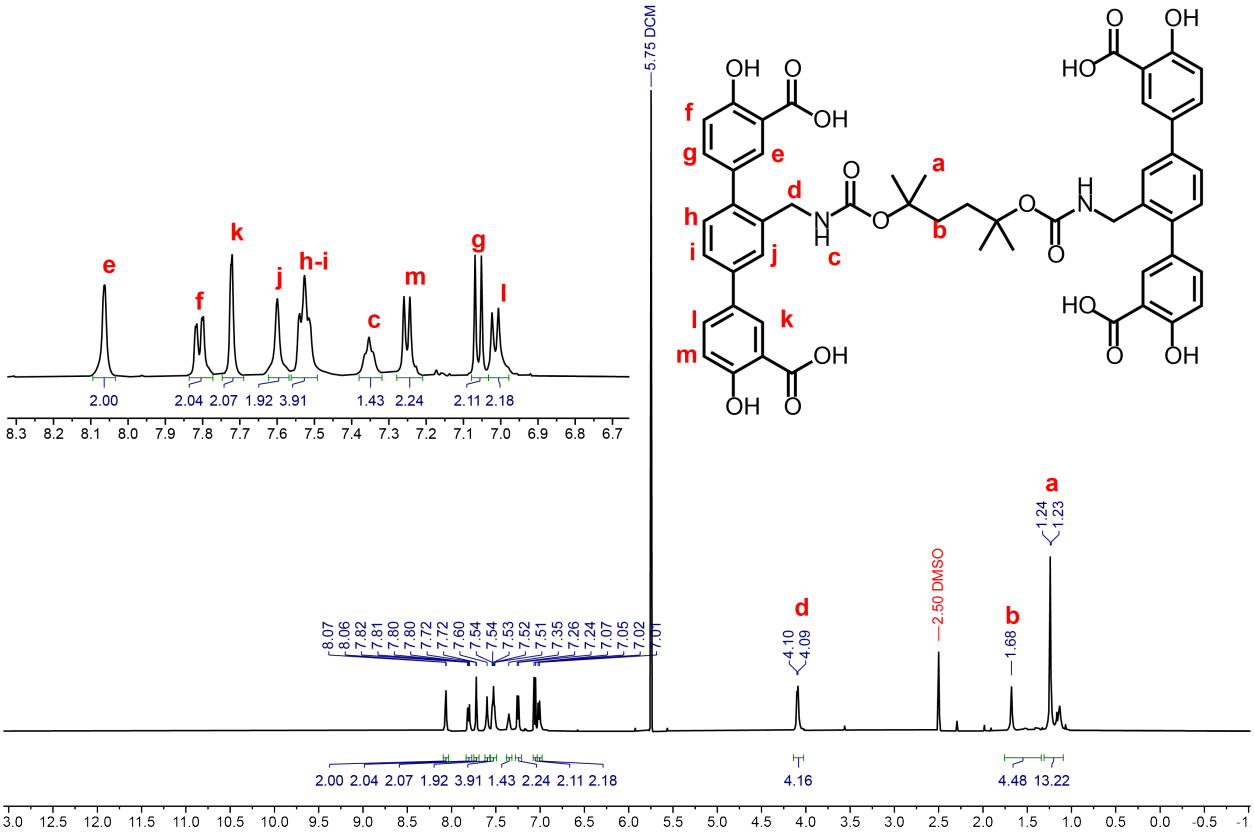

Figure 3.S2 | ^{1}H NMR spectrum of **L$_2$** with aromatic region (inset) taken in DMSO-d_6.

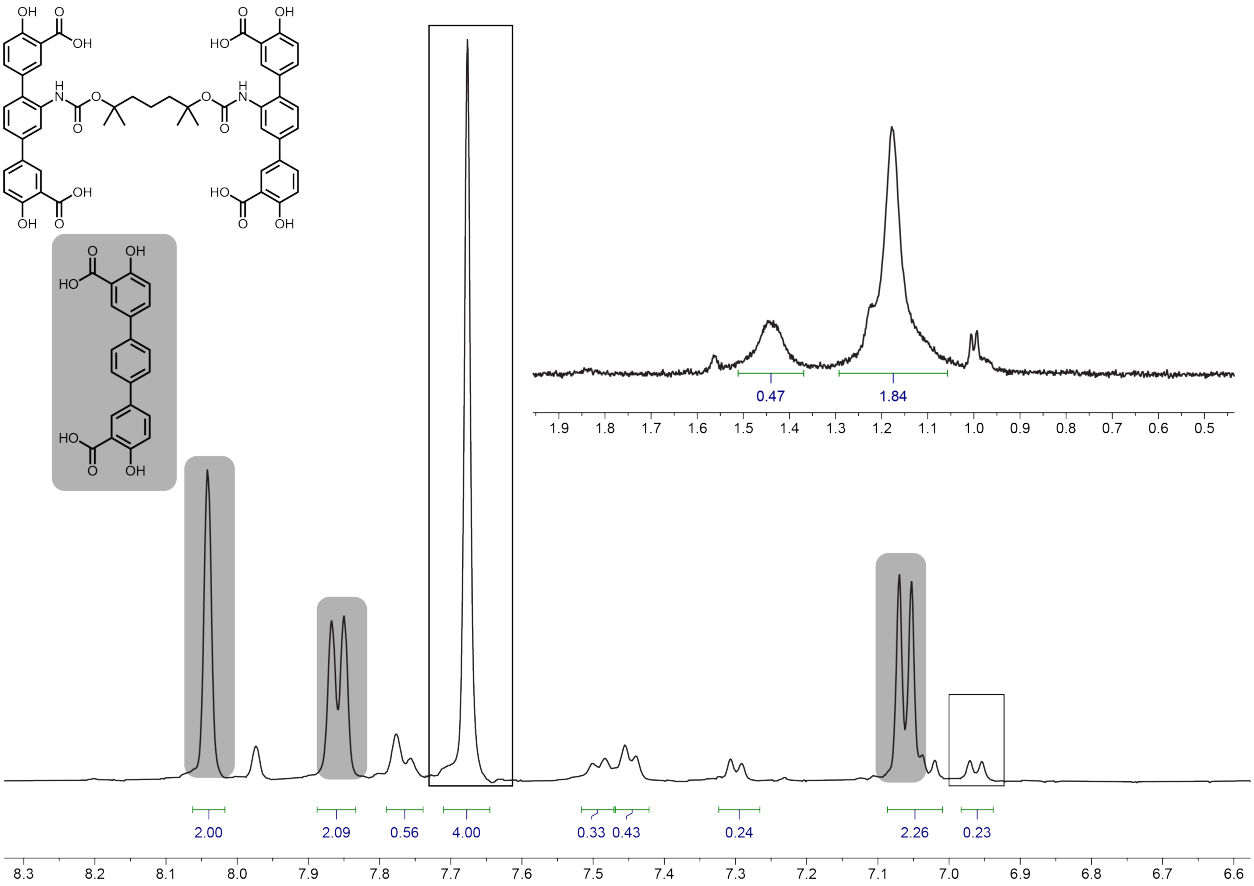

Figure 3.S3 | ^{1}H NMR spectrum of **1-XL-18%** with aromatic region (inset) taken in DMSO-d_6. The relative ratio of 0.23:4.00 observed between the cross-linked dotpdc^{4-} doublet at 6.95 ppm (1H per cross-linked dotpdc^{4-} unit) to H_4dotpdc singlet at 7.67 ppm (4H) corresponds to a percentage of 18%.

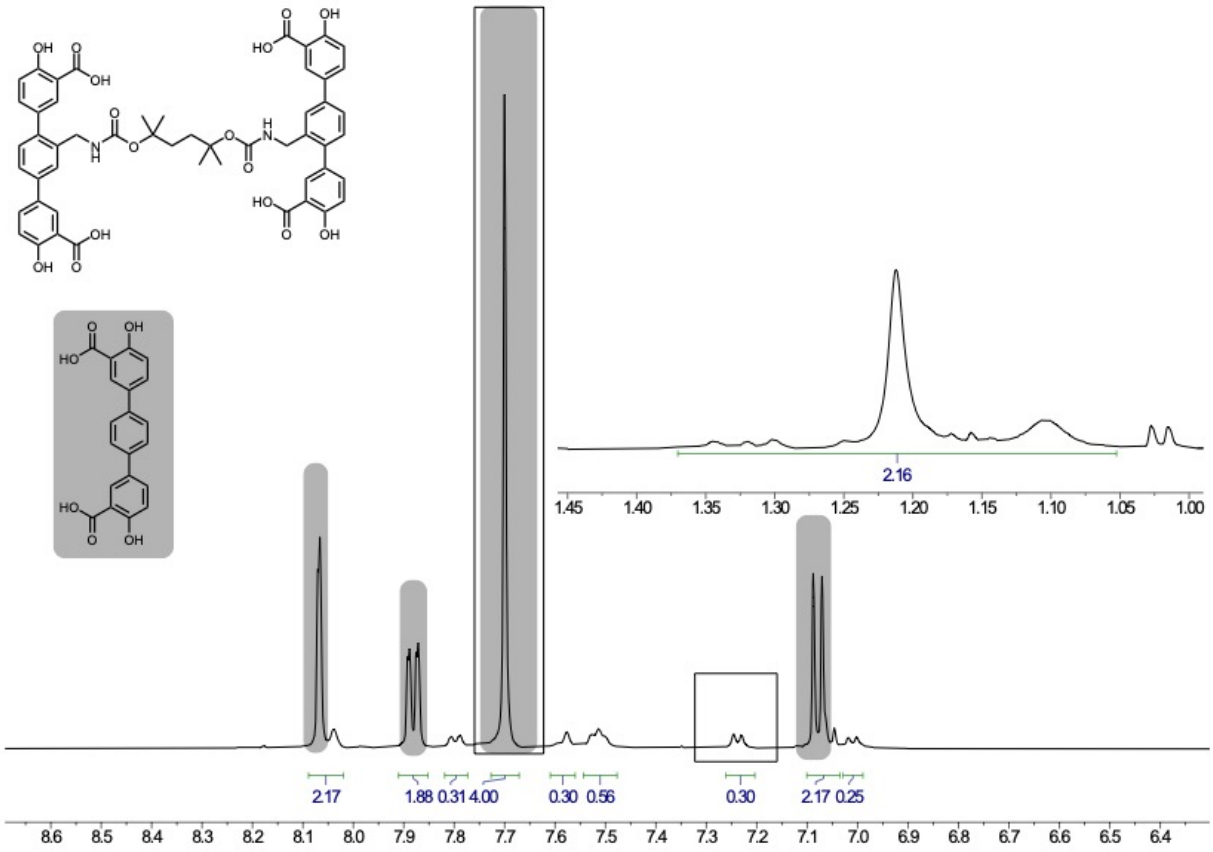

Figure 3.S4 | ^{1}H NMR spectrum of **2-XL-23%** with aromatic region (inset) taken in DMSO-d_6. The relative ratio of 0.30:4.00 observed between the cross-linked dotpdc^{4-} doublet at 6.23 ppm (1H per cross-linked dotpdc^{4-} unit) to H_4dotpdc singlet at 7.67 ppm (4H) corresponds to a percentage of 23%.

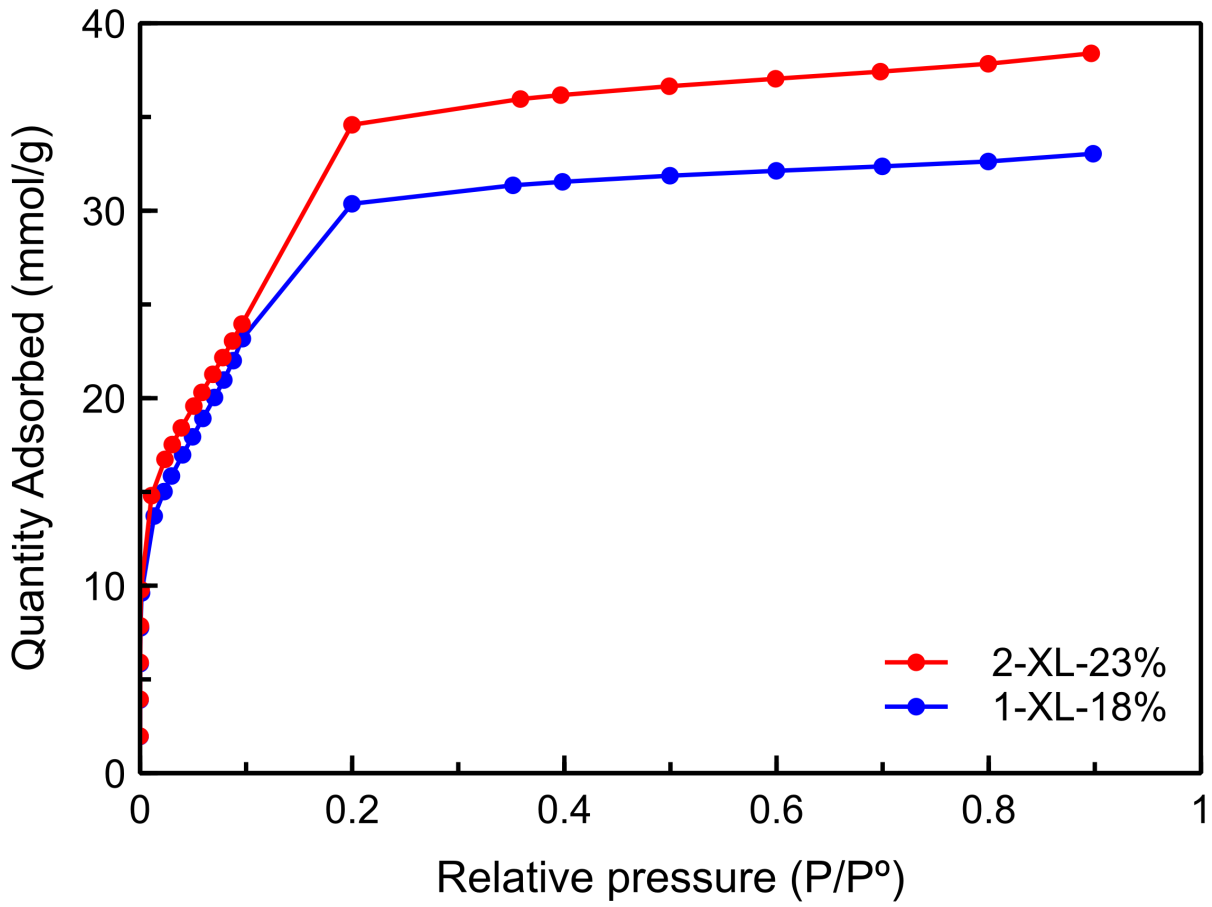

Figure 3.S5 | N_2 adsorption at 77K for **1-XL-18%** and **2-XL-23%.** Note that the slight differences in total uptake are likely due to the mild room temperature activation conditions required for the thermally sensitive cross-linked materials, leading to slight variations in the degree of activation.

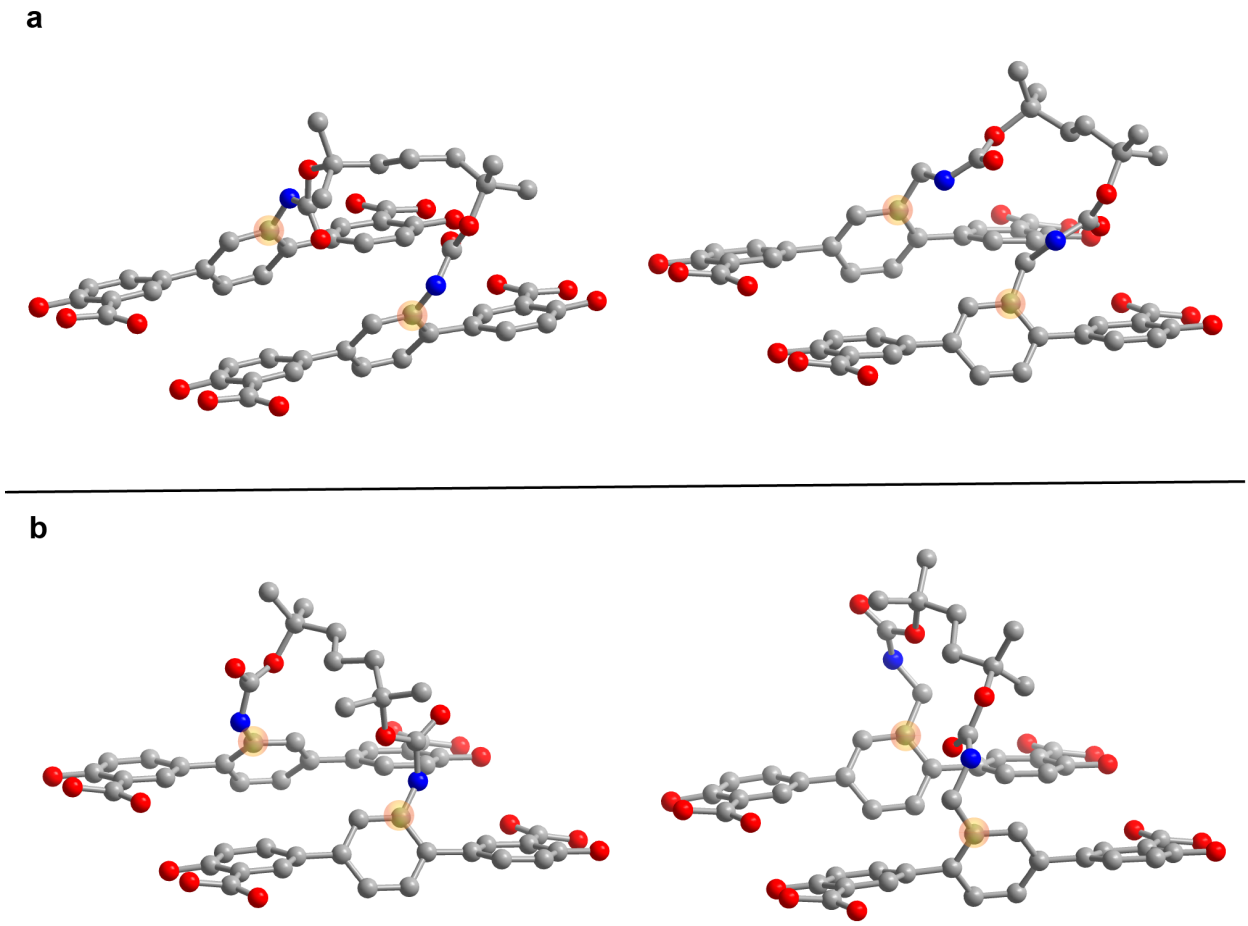

Figure 3.S6 | DFT optimized parallel (a) and offset (b) cross-linker apportionments for both $\mathbf{L_1}$ and $\mathbf{L_2}$. Structures were optimized at the B3LYP/6-31+G(d) level of theory with empirical dispersion correction (D3BJ) and solvent correction via a polarization continuum model using methanol as the solvent.

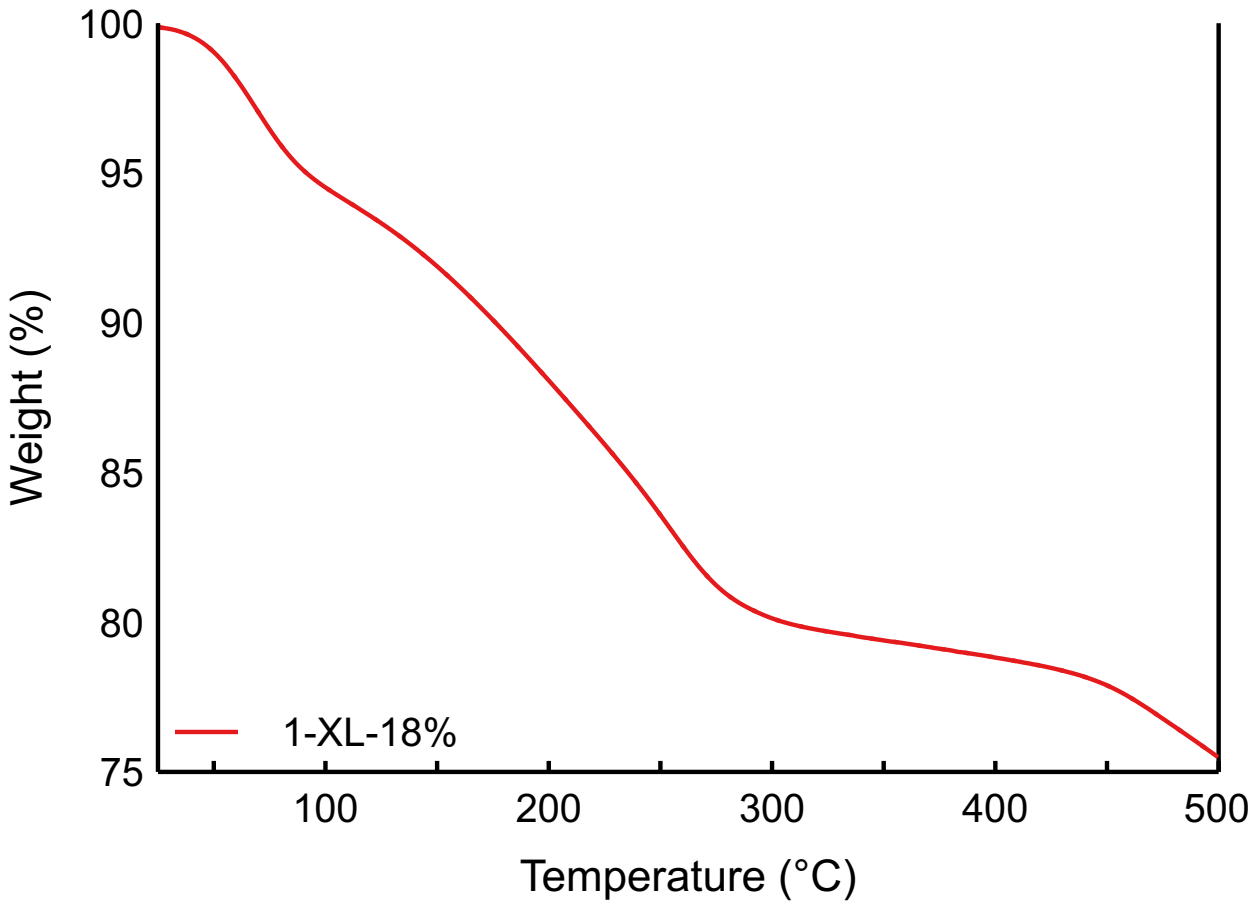

Figure 3.S7 | Thermogravimetric analysis of **1-XL-18%** under N_2.

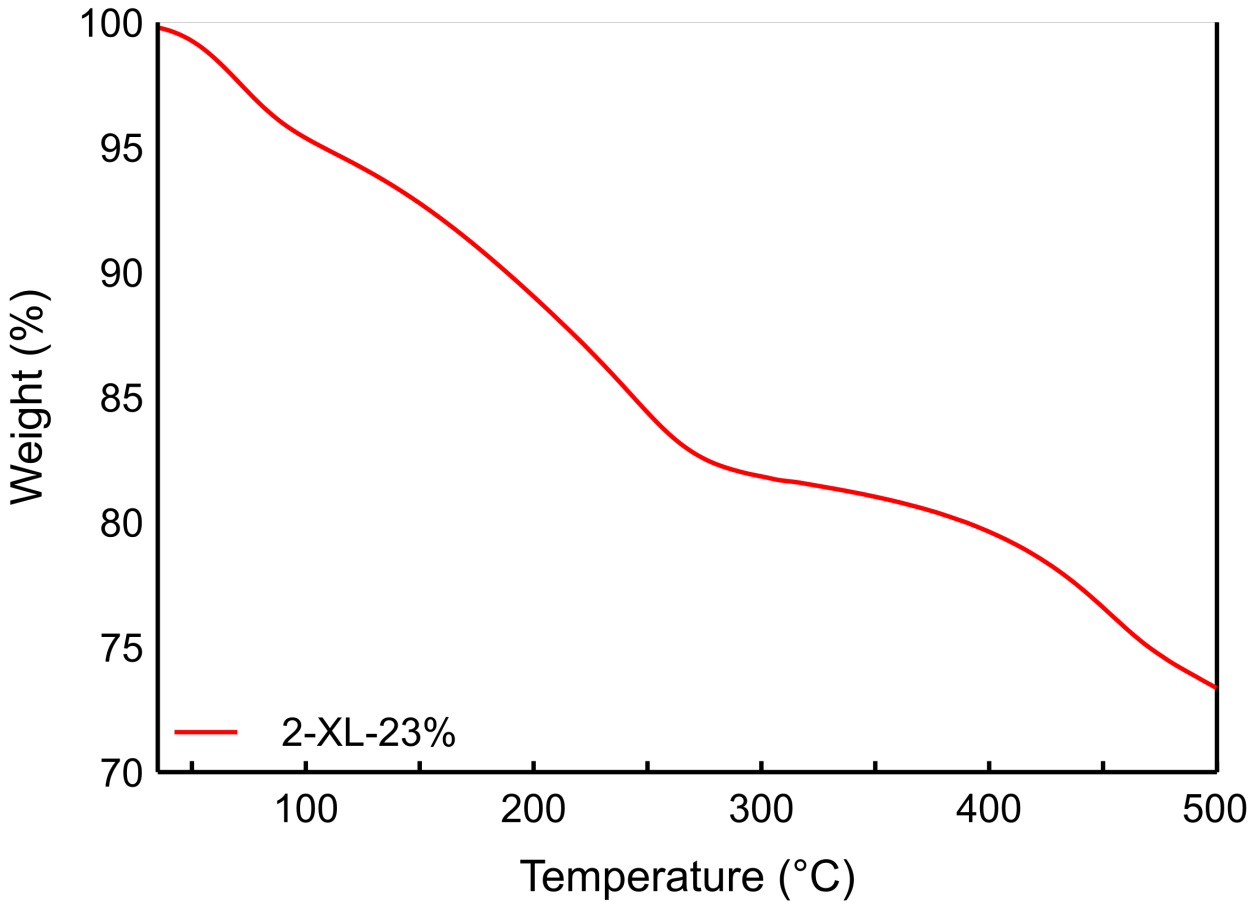

Figure 3.S8 | Thermogravimetric analysis of **2-XL-23%** under N_2.

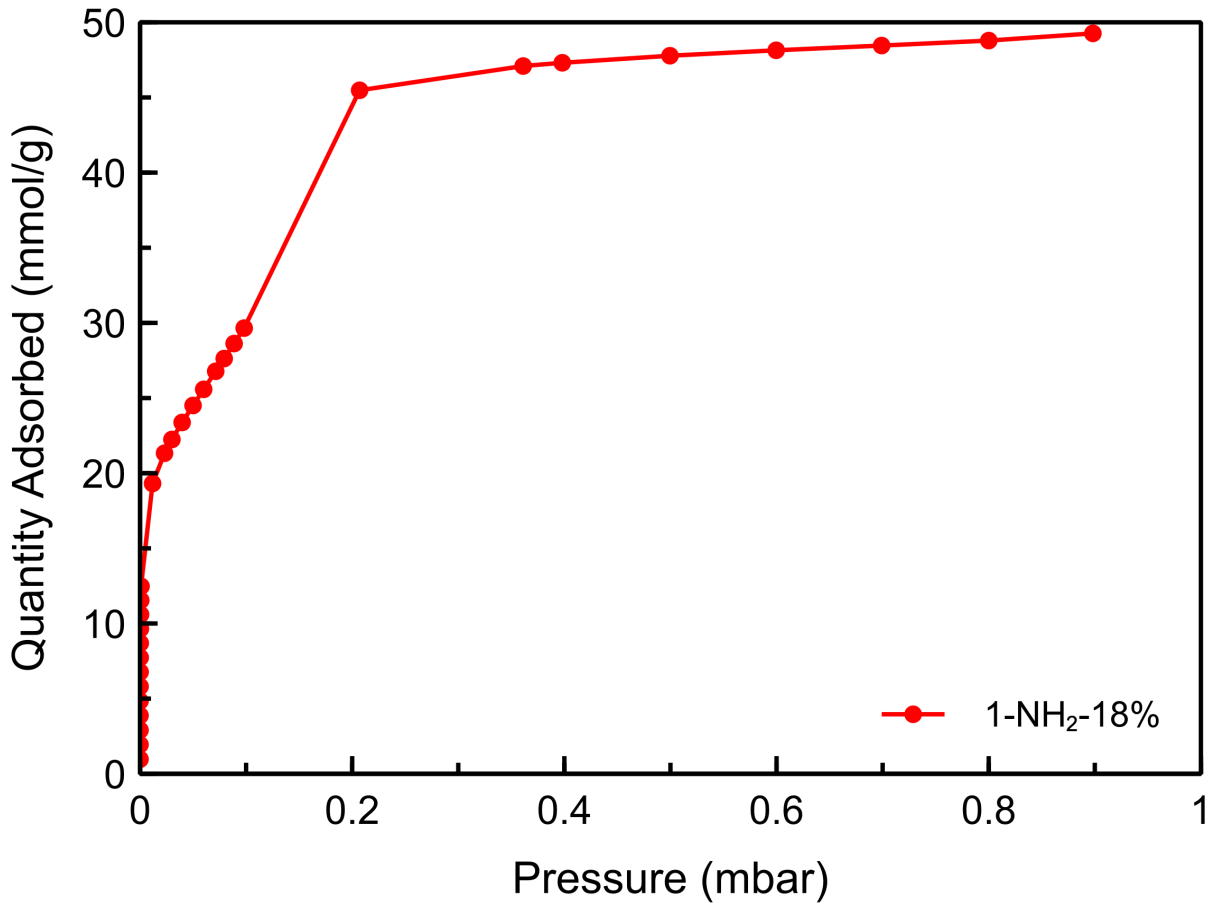

Figure 3.S9 | N_2 adsorption at 77K for **1-NH_2-18%.**

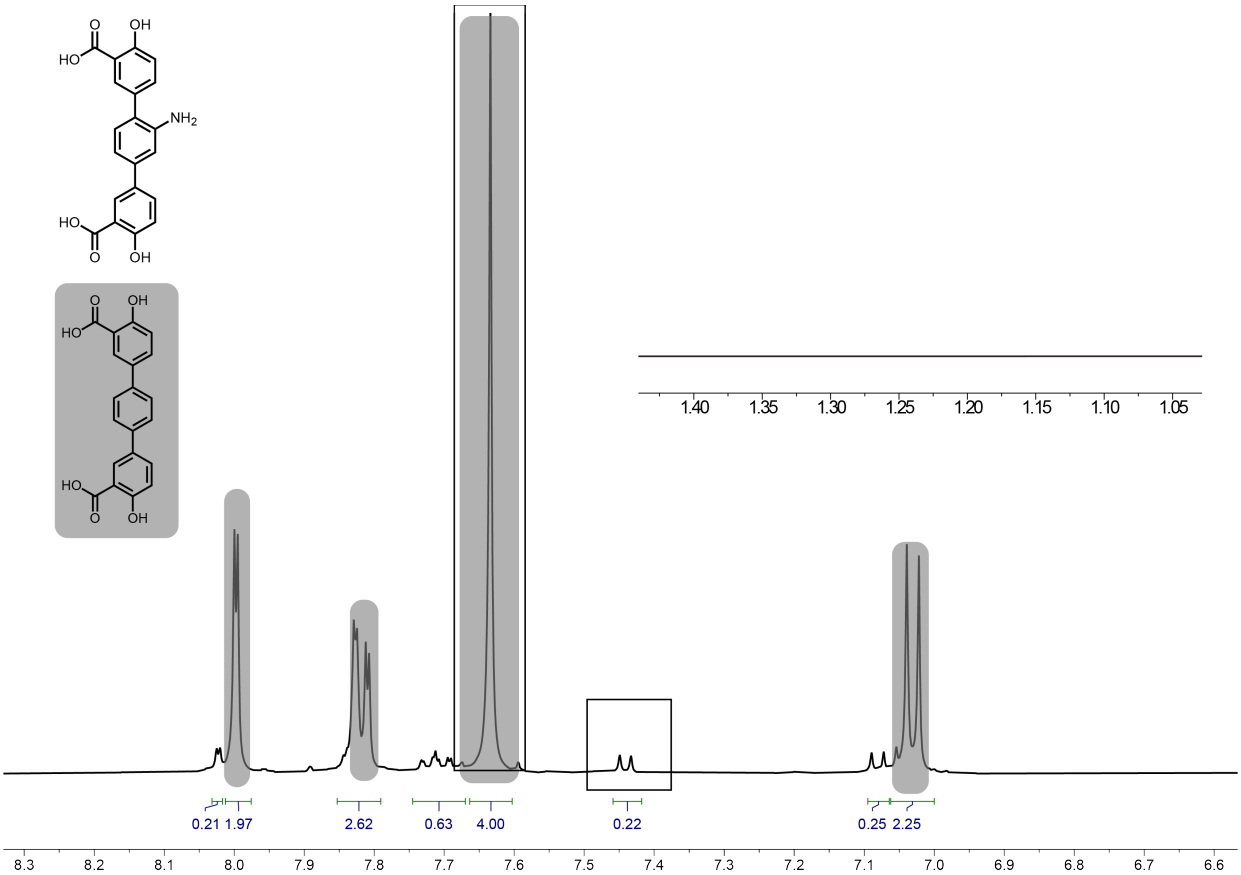

Figure 3.S10 | ^{1}H NMR spectrum of **1-NH_2-18%** with aromatic region (inset) taken in DMSO-d_6. The relative ratio of 0.22:4.00 observed between the -NH_2 functionalized dotpdc^{4-} doublet at 7.48 ppm (1H) to the H_4dotpdc singlet at 7.67 ppm (4H) corresponds to a percentage of 18%. Complete cross-linker cleavage is evidenced by the absence of alkyl signals between 1-1.4 ppm.

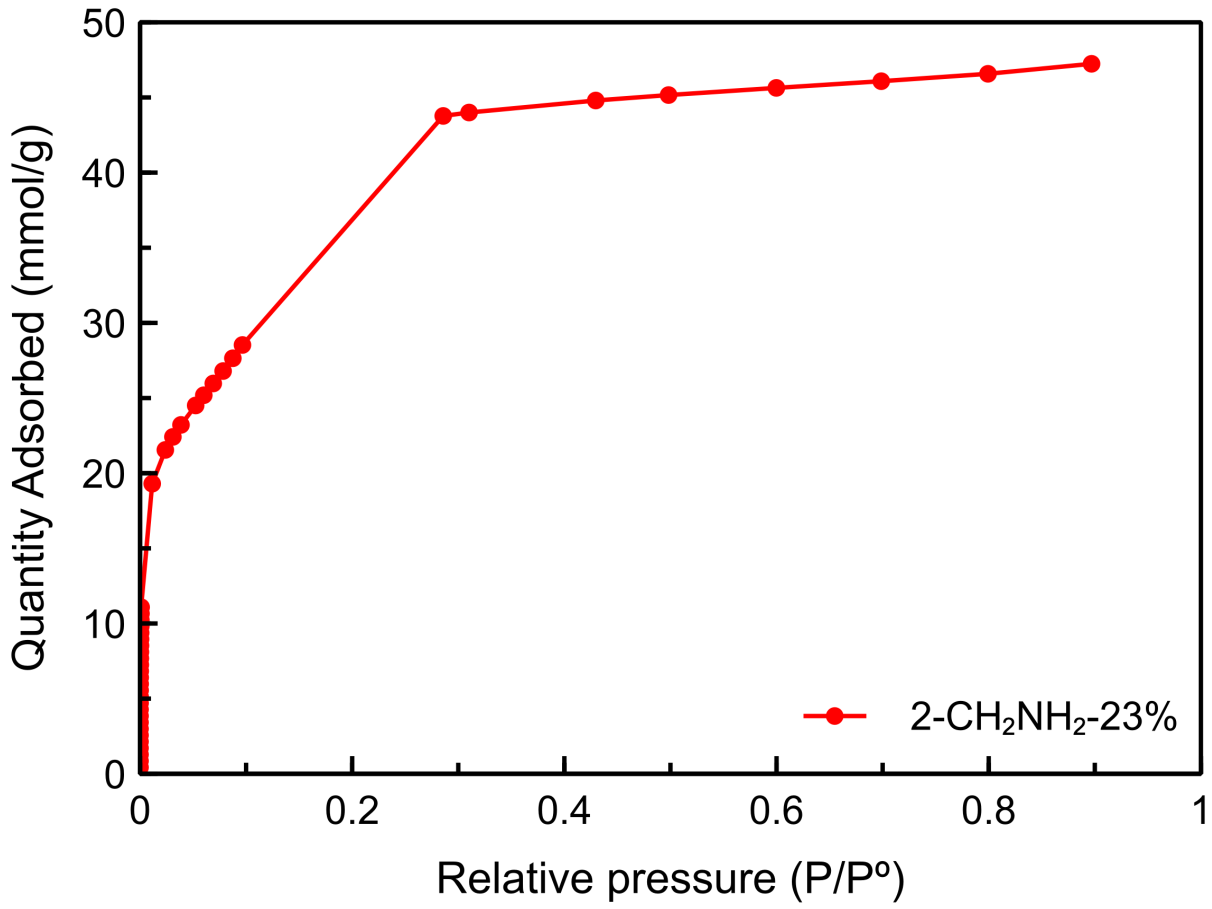

Figure 3.S11 | N_2 adsorption at 77K for **2-CH_2NH_2-23%.**

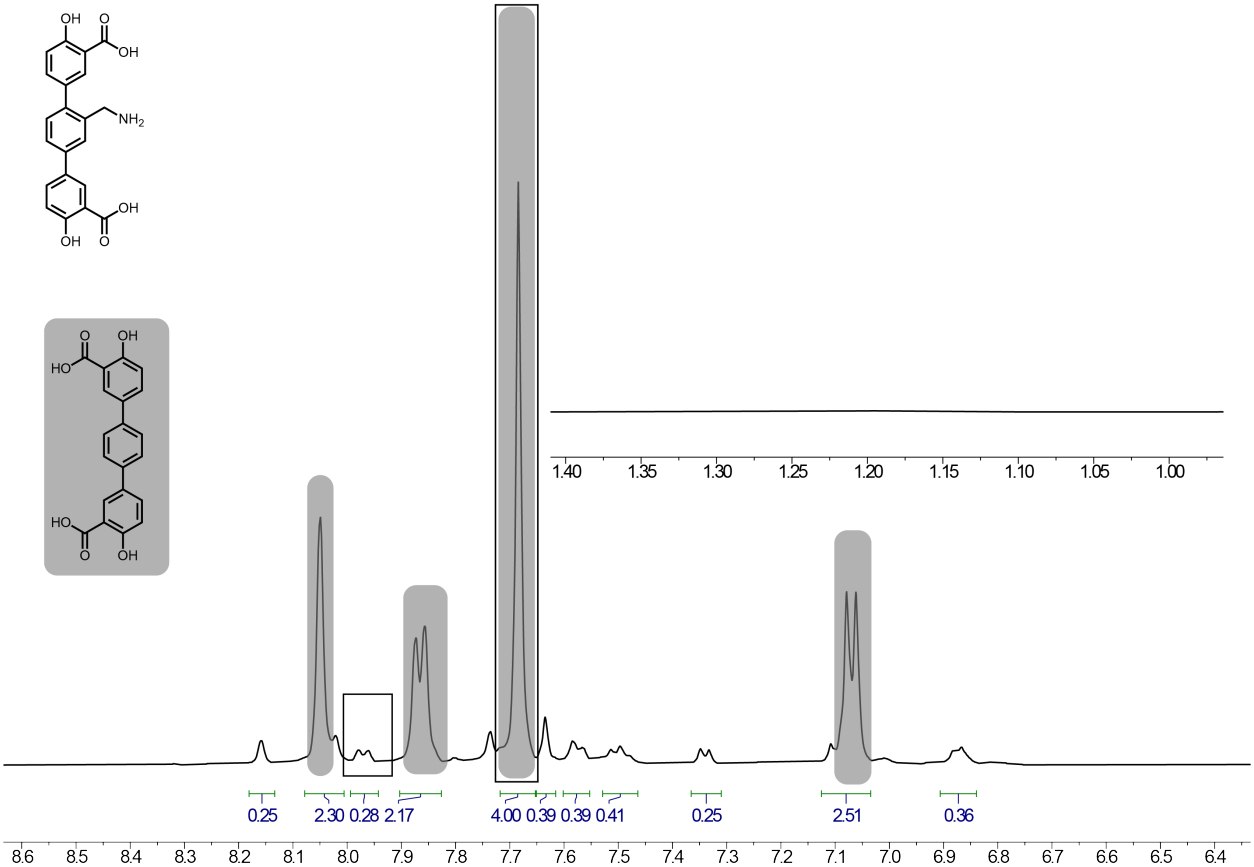

Figure 3.S12 | ^{1}H NMR spectrum of **2-CH_2NH_2-23%** with aromatic region (inset) taken in DMSO-d_6. The relative ratio of 0.28:4.00 observed between the -CH_2NH_2 functionalized dotpdc^{4-} doublet at 7.96 ppm (1H) to the H_4dotpdc singlet at 7.67 ppm (4H) corresponds to a percentage of 23%. Complete cross-linker cleavage is evidenced by the absence of alkyl signals between 1-1.4 ppm.

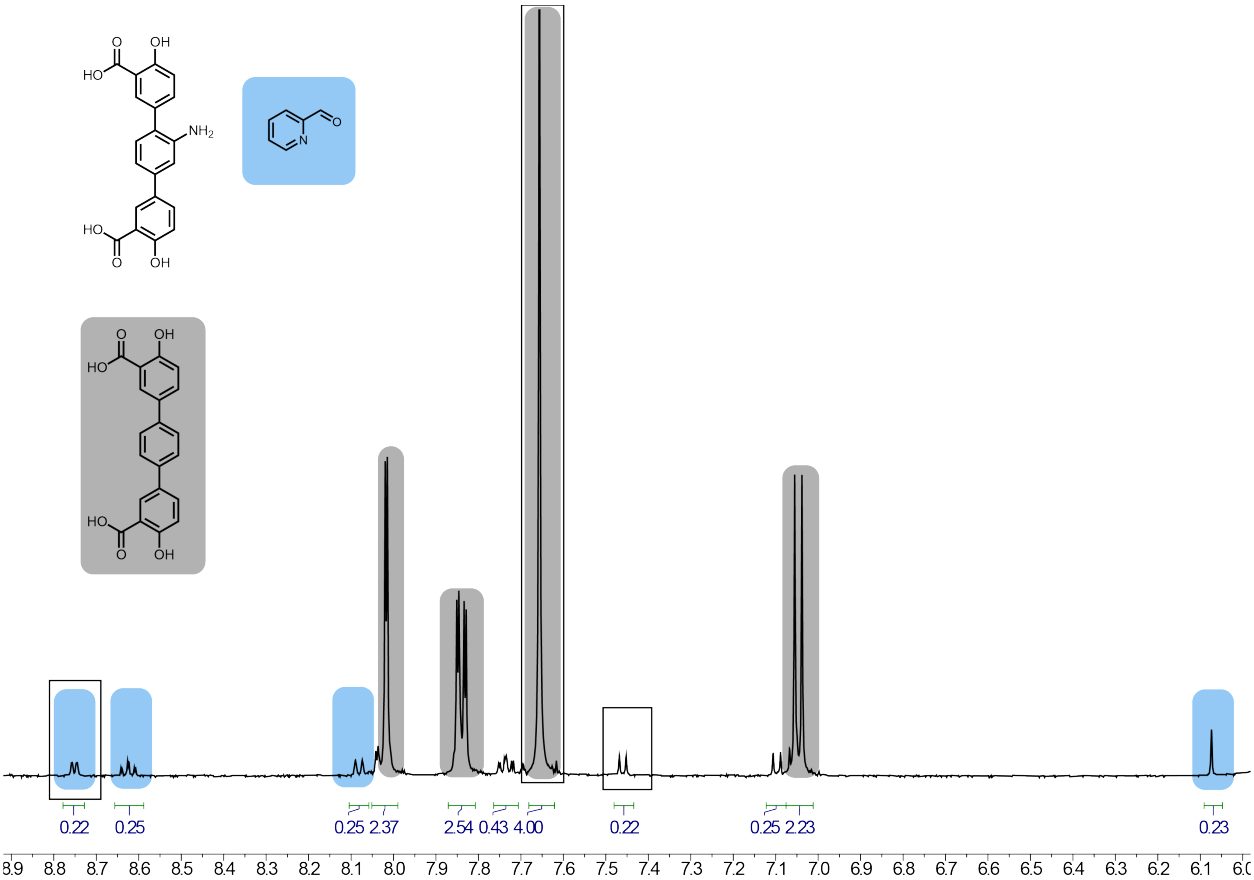

Figure 3.S13 | ^{1}H NMR spectrum of **1-IP-18%** taken in DMSO-d_6. The relative ratio of 0.22:4.00 observed between the -NH_2 functionalized dotpdc^{4-} doublet at 7.45 ppm (1H) to the H_4dotpdc singlet at 7.67 ppm (4H) corresponds to a percentage of 18%. Quantitative imine formation is evidenced by the 1:1 ratio of -NH_2 to 2-pyridinecarboxaldehyde.

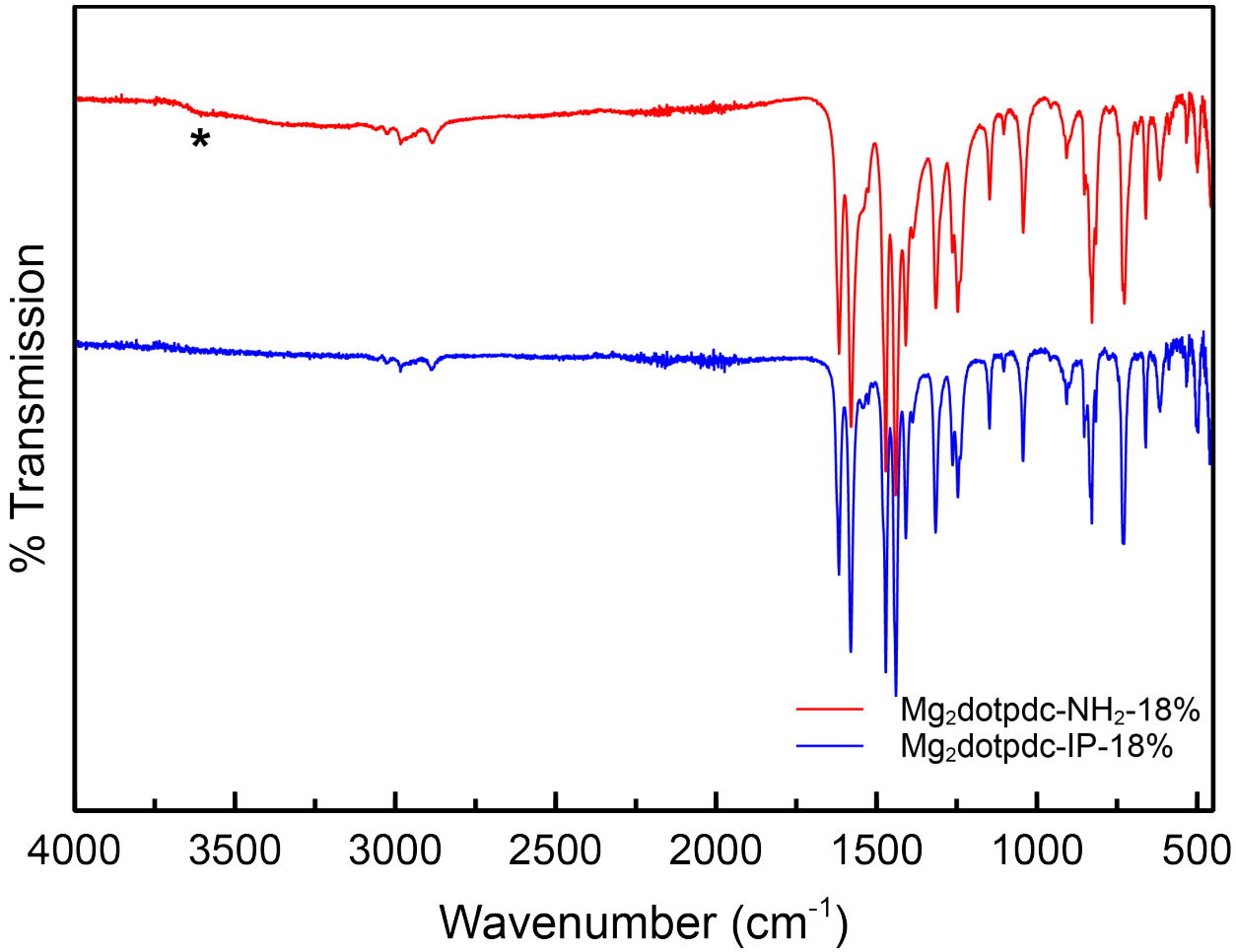

Figure 3.S14 | FT-IR ATR spectra of Mg_2dotpdc-NH_2-18% (red), and Mg_2dotpdc-IP-18% (blue) showing clear loss of the amine N-H stretch (marked with an *) upon reaction to form the iminopyridine moiety.

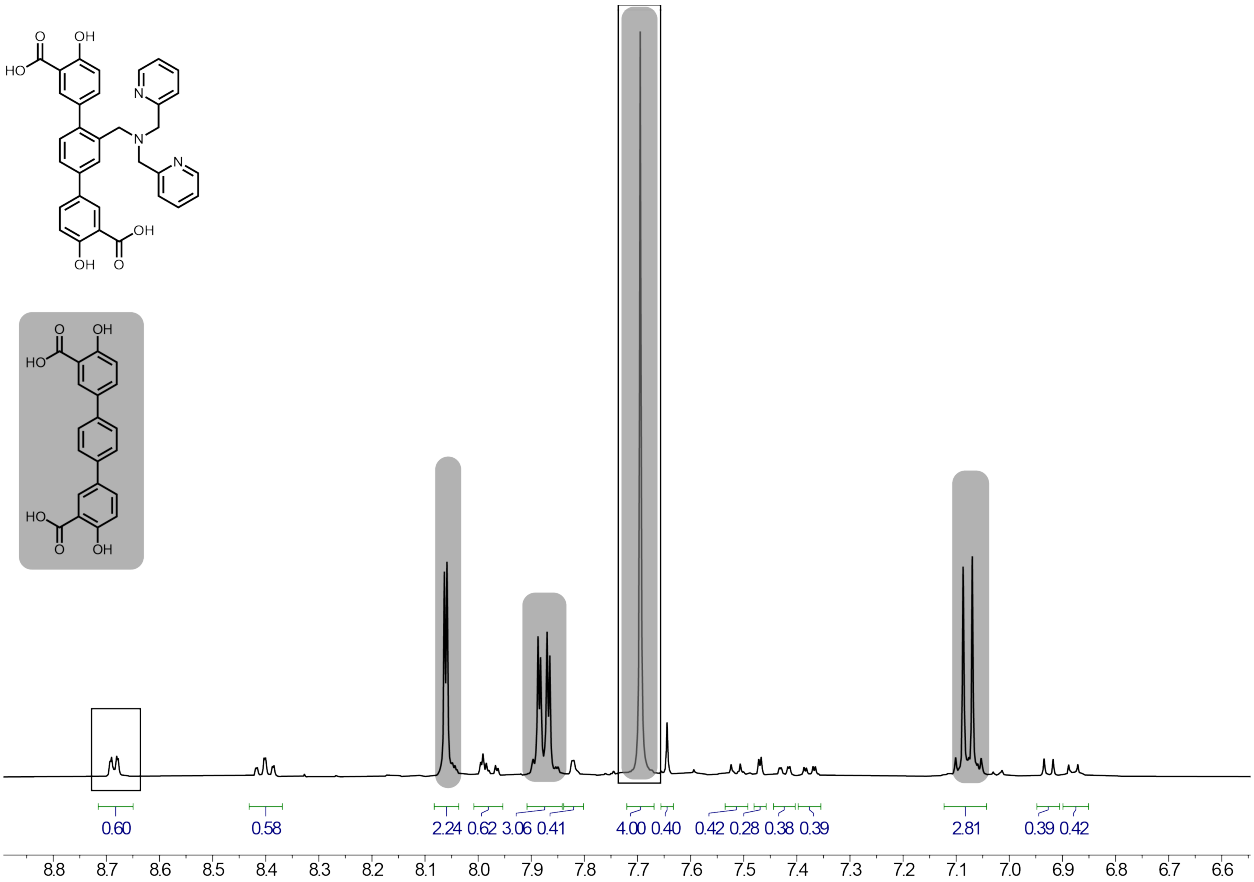

Figure 3.S15 | ^{1}H NMR spectrum of **2-DPA-23%** taken in DMSO-d_6. The relative ratio of 0.58:4.00 observed between the DPA functionalized dotpdc^{4-} triplet at 8.4 ppm (2H) to the H_4dotpdc singlet at 7.67 ppm (4H) corresponds to a percentage of 23%.

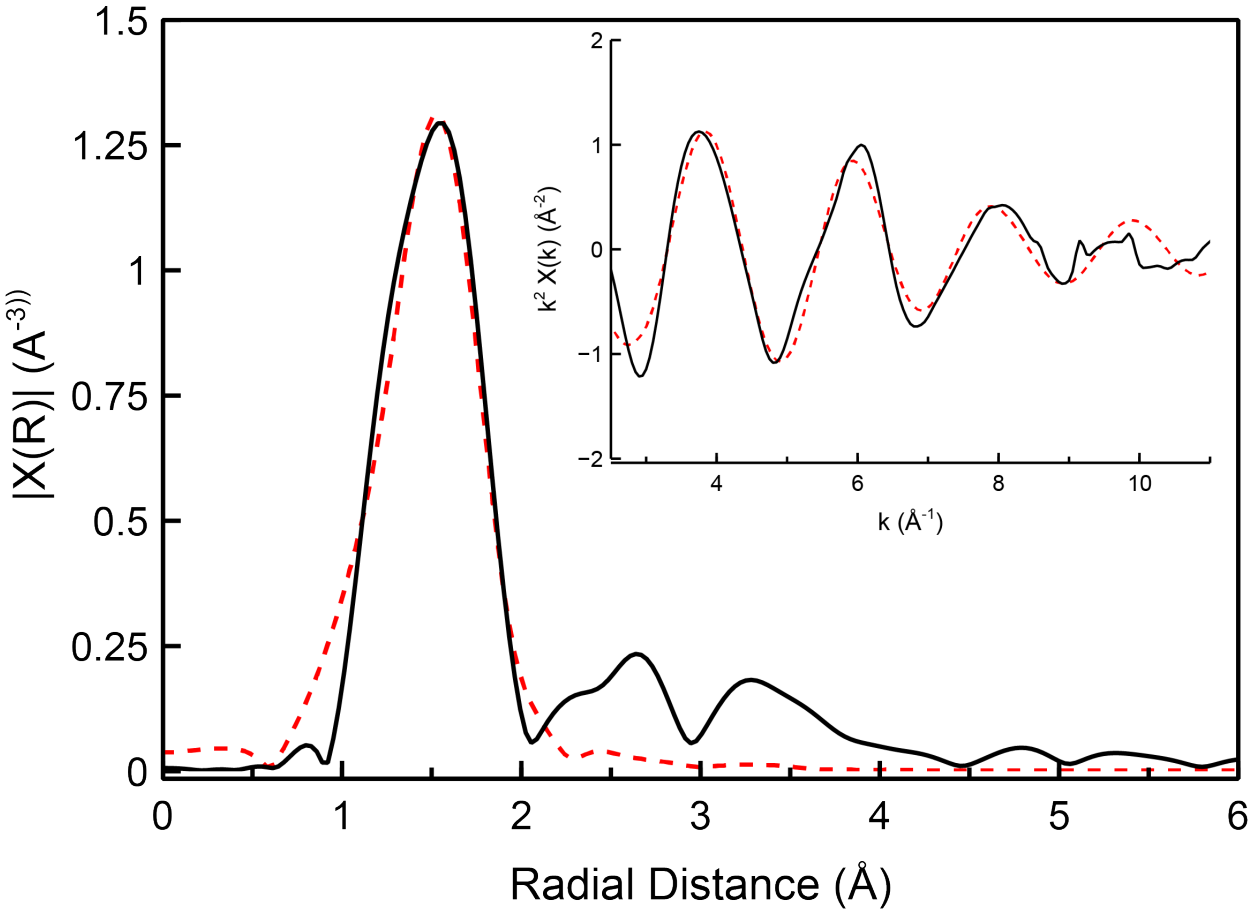

Figure 3.S16 | Fit (red dashed lines) to EXAFs spectrum of **1-(IP)NiCl2** (solid black line). (Inset) Corresponding k^2-weighted oscillations. See Table S3 for fitting parameters.

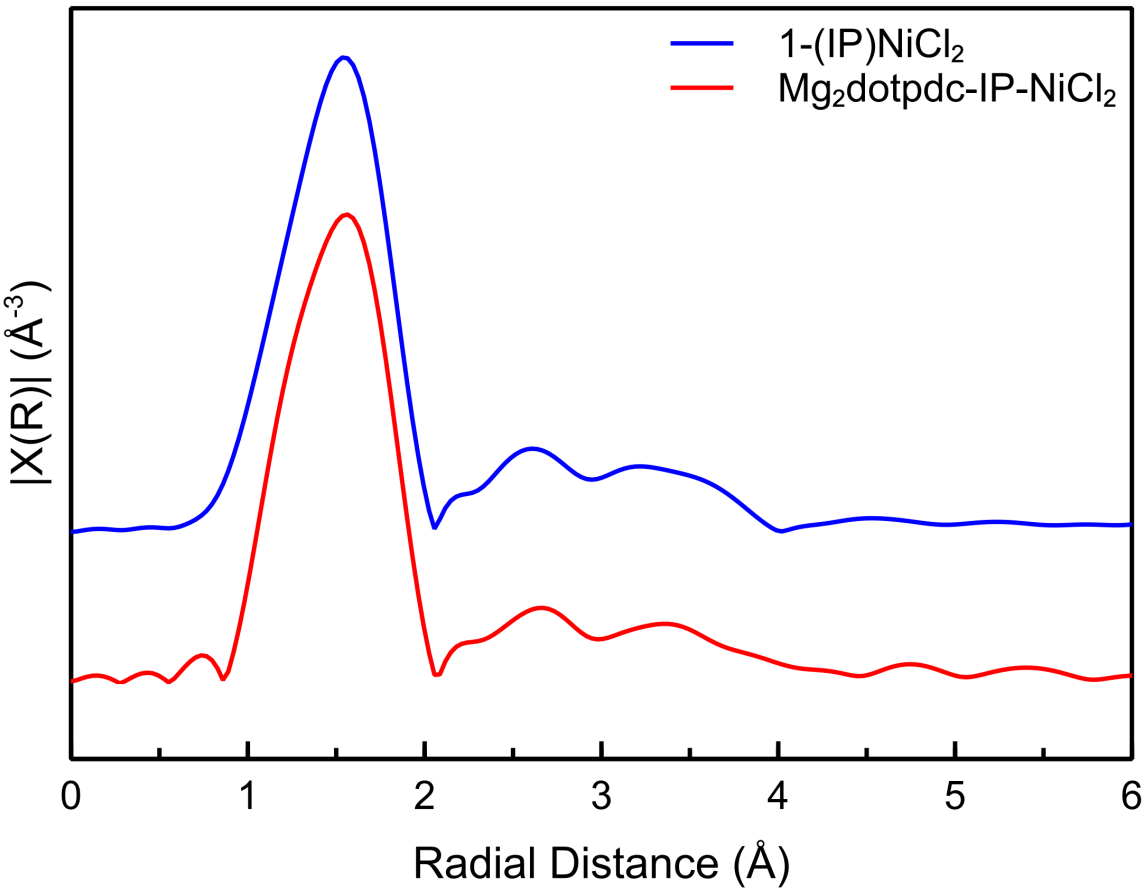

Figure 3.S17 | Comparison of EXAFs spectrum of templated **1-(IP)NiCl2** (blue line, top) to non-templated Mg_2dotpdc-IP-$NiCl_2$ (red line, bottom).

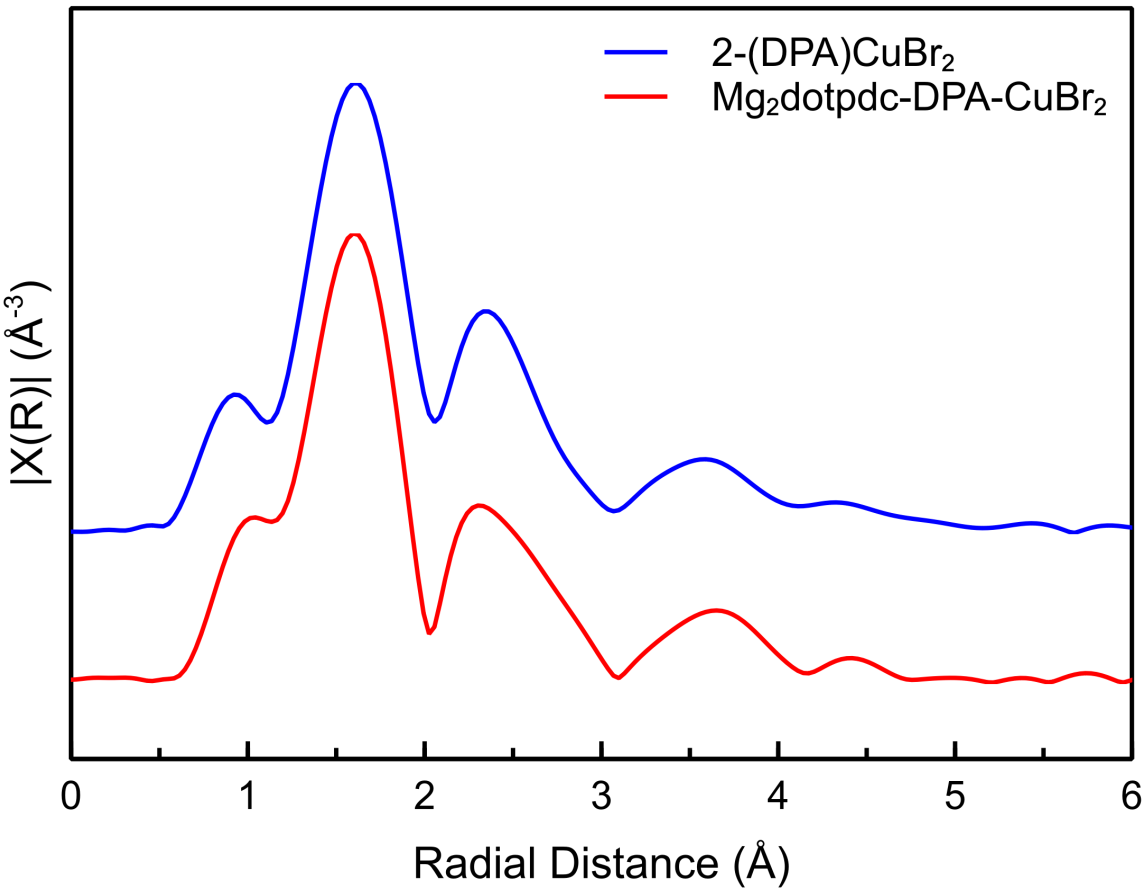

Figure 3.S18 | Comparison of EXAFs spectrum of templated **2-(DPA)CuBr$_2$** (blue line, top) to non-templated Mg$_2$dotpdc-DPA-CuBr$_2$ (red line, bottom).

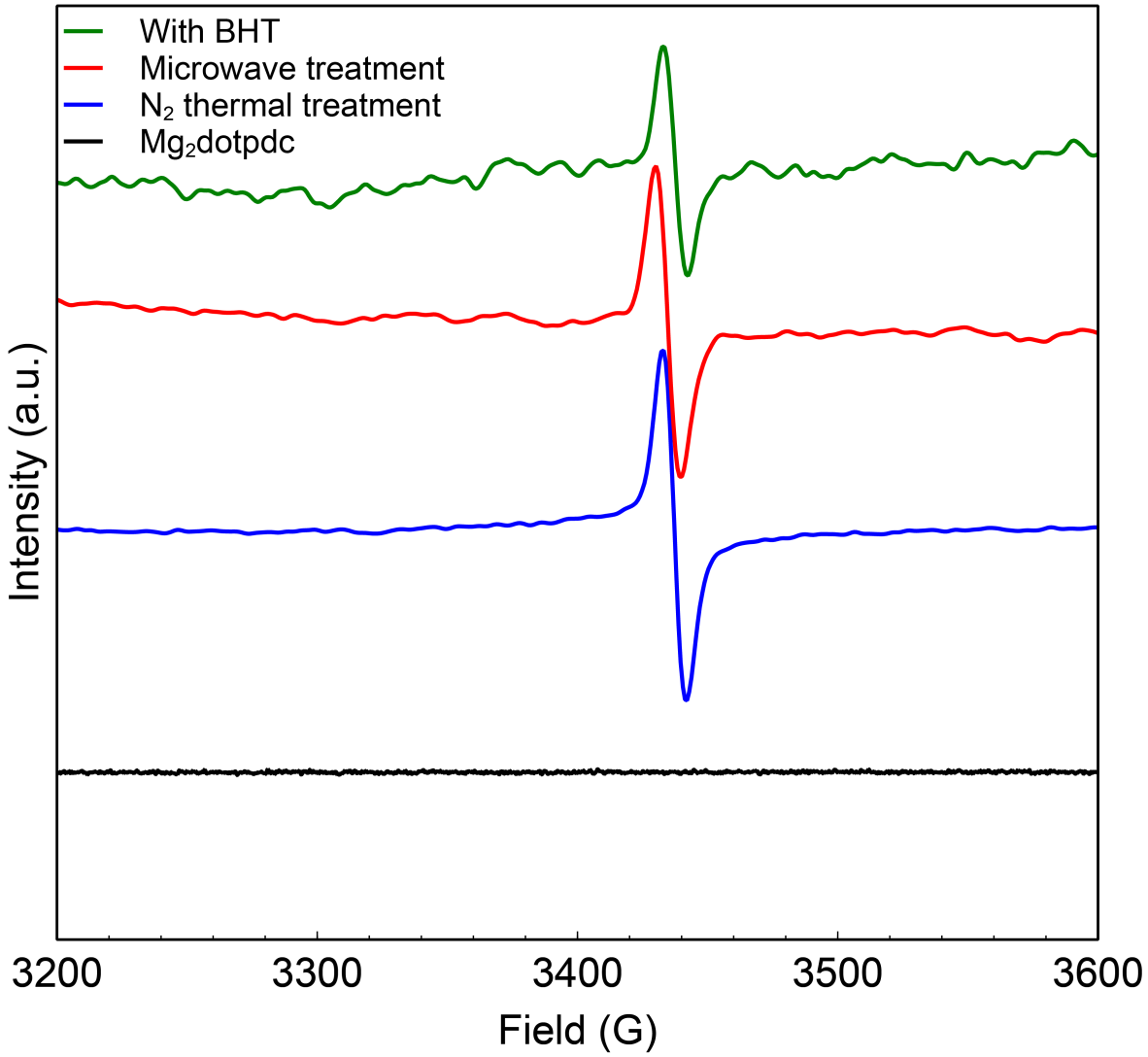

Figure 3.S19 | Room temperature X-band EPR spectra of Mg_2dotpdc (black line), Mg_2dotpdc subjected to 250 ºC N_2 thermolysis treatment (blue line), Mg_2dotpdc subjected to standard microwave thermolysis in 2-ethyl-1-hexanol (red line), and Mg_2dotpdc subjected to microwave heating in the presence of butylated hydroxytoluene (green line).

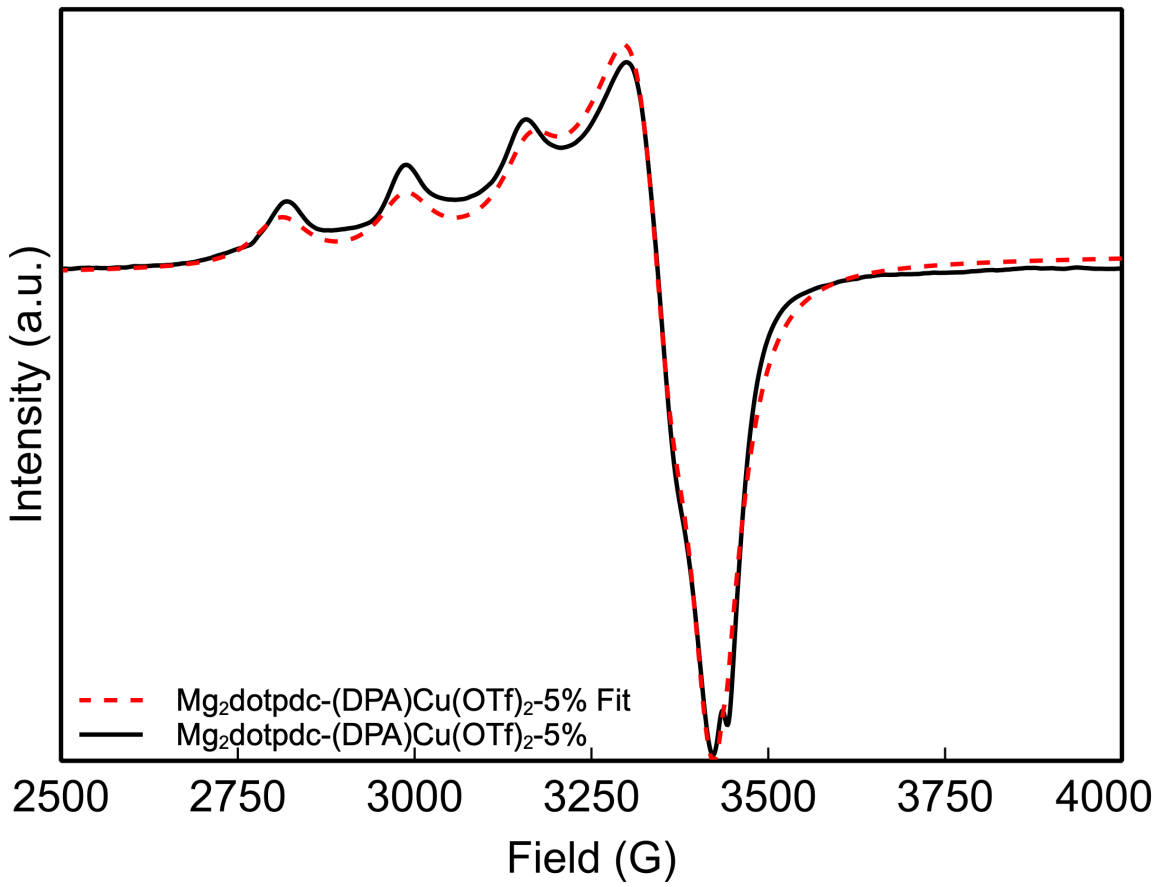

Figure 3.S20 | Fit (red dashed line) to X-band spectrum of non-templated Mg_2dotpdc-(DPA)Cu$(OTf)_2$ collected at 100K (solid black line). Fit parameters: g = 2.06, 2.24; A = 32, 540.

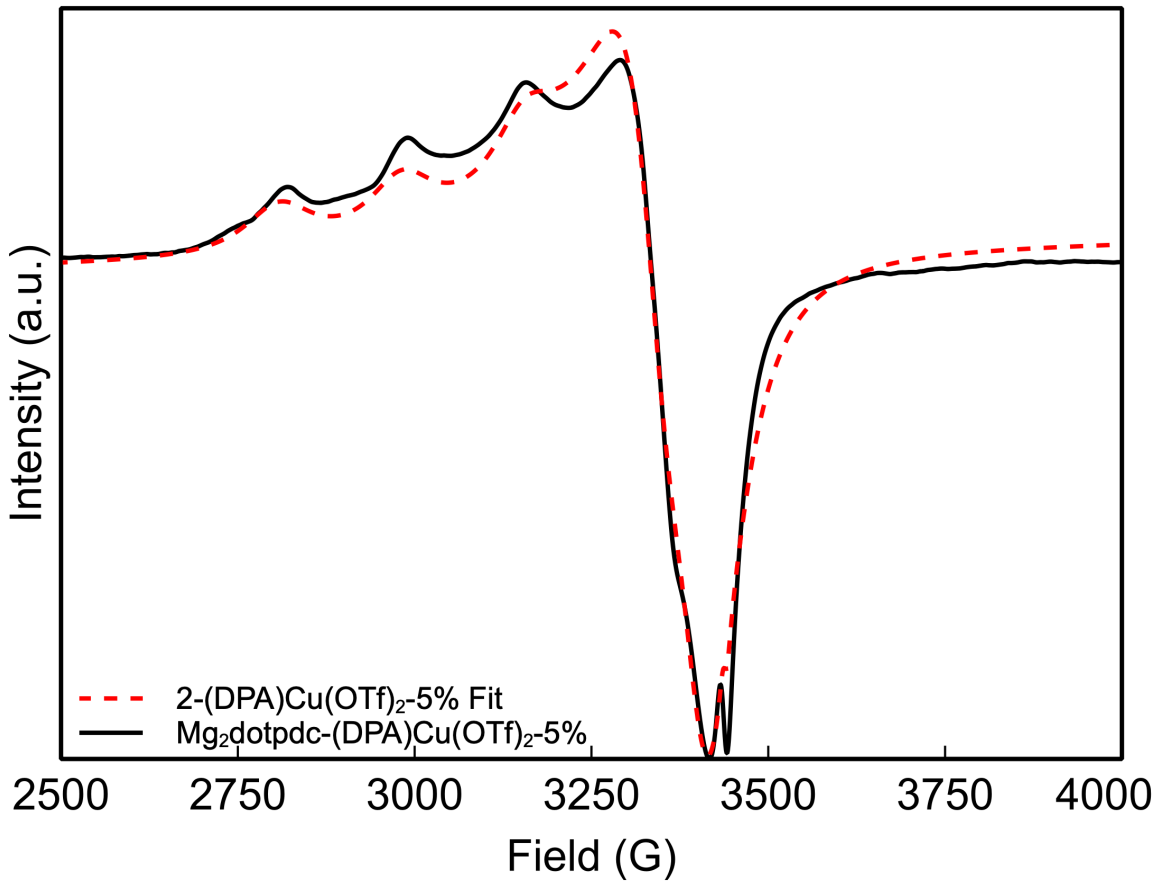

Figure 3.S21 | Fit (red dashed line) to X-band spectrum of templated **2-(DPA)Cu(OTf)$_2$** collected at 100K (solid black line). Fit parameters: g = 2.06, 2.24; A = 35, 533.

13. Supplementary DFT-optimized coordinates

Table 3.S11 | DFT-optimized structure of 1-(IP)$NiCl_2$ with a coordinated methanol, with turquoise, light green, blue, red and grey representing nickel, chlorine, nitrogen, oxygen,a nd carbon, respectively. Hydrogens omitted for clarity.

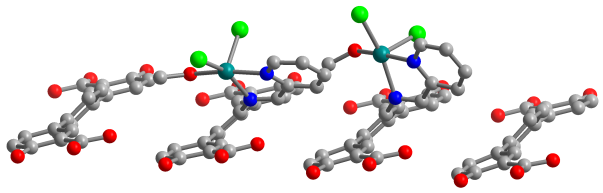

Symbol	X	Y	Z	O	5.4903	18.6104	2.474704
C	5.184952	18.413344	5.447583	C	13.137172	12.383728	6.920501
C	6.255206	17.748325	4.648063	C	11.105107	13.861837	6.790107
C	6.341212	17.879163	3.235776	C	10.691492	13.506079	5.494258
O	4.30989	19.15969	4.995703	C	9.7768	14.286875	4.788148

H	13.261127	12.482168	5.848794	O	13.920204	8.640119	13.55068
H	11.063236	12.591064	5.042045	O	14.840338	10.769783	9.801554
H	9.456213	13.960589	3.802937	C	5.151076	15.385693	11.541347
C	15.164429	10.955158	6.831373	C	6.15142	14.699058	10.851567
C	14.086838	11.606935	7.614642	C	6.135543	14.778818	9.444507
O	15.164739	11.213297	5.499567	C	5.181517	15.537572	8.788918
O	16.021411	10.221021	7.279697	C	7.162019	13.898288	11.584278
C	7.22466	16.94144	5.283408	C	7.562025	14.269316	12.874285
C	8.249706	16.283727	4.607221	C	8.461524	13.49723	13.616563
C	8.298352	16.437341	3.206096	H	5.155105	15.271904	12.61962
C	7.365248	17.215631	2.540709	H	6.884954	14.255441	8.859027
C	9.236716	15.458847	5.346547	H	5.151647	15.571648	7.705165
C	9.65653	15.817676	6.640292	H	7.218816	15.203989	13.304736
C	10.56671	15.035476	7.34713	H	10.888081	15.362297	8.33183
H	7.195695	16.786827	6.356432	C	0.995332	15.269727	17.991878
H	9.088371	15.957783	2.636442	C	2.090275	14.63362	17.191633
H	7.411147	17.339088	1.463415	C	2.126881	14.710802	15.771677
H	9.296018	16.737517	7.091542	O	3.065291	16.586623	13.046456
C	3.089426	16.839458	11.718458	O	0.107205	15.998089	17.537215
C	4.164246	16.177299	10.915169	O	1.287699	15.448791	15.016303
C	4.214732	16.272431	9.497126	C	9.008303	9.328669	19.487716
O	5.166611	18.167417	6.775694	C	9.977975	11.471049	13.841695
O	2.208608	17.578887	11.266434	C	9.830675	11.251831	15.224097
O	3.389003	17.029583	8.745517	C	10.763977	10.513052	15.9338
C	11.060873	10.850532	13.211772	C	7.039721	10.87259	19.370198
C	12.077636	13.040175	7.550592	C	6.674554	10.537862	18.051547
C	11.977045	12.900611	8.947176	C	5.750374	11.269733	17.311473
C	12.899036	12.149894	9.660536	H	9.15505	9.465441	18.424161
C	9.034985	12.321362	13.077623	H	8.976726	11.649216	15.758281
C	8.650647	11.979175	11.769352	H	10.635984	10.376115	17.001429
C	7.738869	12.737708	11.038142	H	7.088195	9.635718	17.612353
H	11.201439	10.985826	12.146614	H	5.484782	10.924864	16.317313
H	11.155942	13.367591	9.48281	C	10.977359	7.818176	19.388756
H	12.791618	12.048827	10.735502	C	9.926111	8.505218	20.168781
H	9.044851	11.068726	11.328589	C	11.864198	9.908033	15.307934
H	7.450524	12.398929	10.048169	O	10.962485	8.052222	18.040306
C	13.072835	9.390774	13.114836	O	11.818909	7.059321	19.821488
C	12.005635	10.060699	13.896572	O	12.739006	9.188962	16.072474
C	13.966743	11.490203	9.029766	C	3.101184	13.876859	17.82273
O	13.063871	9.633045	11.769552	C	4.100854	13.184386	17.134703

C	4.061688	13.234839	15.726107	C	4.563383	10.667199	26.140626
C	3.094803	13.973787	15.066877	H	1.118246	12.375685	25.203338
C	5.129049	12.402159	17.864797	H	2.799781	11.250126	21.447338
C	5.518756	12.771093	19.15621	H	0.995094	12.435858	20.277217
C	6.442341	12.035185	19.91572	H	3.248593	12.332967	25.879419
H	3.124625	13.802046	18.904127	N	6.763017	12.569801	21.198947
H	4.798461	12.69603	15.138492	C	7.916837	14.301344	15.743218
H	3.050736	13.983698	13.983121	C	8.290789	14.820723	17.054932
H	5.145123	13.695533	19.580563	N	9.620299	14.915417	17.291651
N	8.831168	13.955874	14.905745	C	10.041865	15.364854	18.473011
C	-1.092765	13.709261	24.264767	C	9.15057	15.726105	19.490912
C	0.034306	13.120728	23.475913	C	7.782236	15.629062	19.255773
C	0.058786	13.176768	22.054222	C	7.340248	15.179629	18.008258
O	0.963996	15.005817	19.317286	C	5.771042	12.990627	21.910636
O	-1.994093	14.417314	23.808018	C	5.977394	13.858243	23.063822
O	-0.813693	13.867977	21.287111	N	7.241565	14.293994	23.258068
C	7.02834	7.871883	25.760642	C	7.497883	15.12701	24.267467
C	7.951616	9.984824	20.124452	C	6.491029	15.57376	25.131456
C	7.786314	9.751722	21.499226	C	5.184181	15.132675	24.935152
C	8.678306	8.957255	22.198715	C	4.918375	14.260597	23.877019
C	5.101692	9.480891	25.610403	H	6.857008	14.190742	15.511467
C	4.679591	9.100825	24.323252	H	11.116808	15.42368	18.602766
C	3.735805	9.846347	23.619086	H	9.537831	16.050559	20.44884
H	7.142941	7.93731	24.686842	H	7.068704	15.898377	20.028004
H	6.966891	10.206099	22.041609	H	6.28522	15.108891	17.771889
H	8.550869	8.836164	23.266705	H	4.741367	12.753392	21.641726
H	5.053389	8.182324	23.880843	H	8.531593	15.435471	24.375071
H	3.404489	9.482715	22.651118	H	6.740384	16.255207	25.937219
C	8.895496	6.256929	25.66154	H	4.383098	15.460081	25.589775
C	7.899507	7.007816	26.452865	H	3.915408	13.898725	23.681075
C	9.770731	8.339358	21.577038	O	-1.137415	13.424994	25.58798
O	8.861162	6.471488	24.311068	C	6.04202	8.633651	26.388445
O	9.717516	5.478486	26.092334	C	5.951589	8.517895	27.788893
O	10.637662	7.608128	22.343352	C	6.789114	7.667853	28.502077
C	1.082455	12.422777	24.119809	H	5.192985	9.073298	28.331788
C	2.105021	11.756115	23.439392	H	6.670338	7.588418	29.57997
C	2.050079	11.776812	22.029685	C	7.767194	6.884064	27.86782
C	1.0509	12.462774	21.360305	O	8.536895	6.027745	28.613407
C	3.165874	11.010519	24.166658	H	4.89548	11.02575	27.110535
C	3.62009	11.41397	25.435612	H	4.830365	19.030253	3.071789

H	2.740868	17.464664	9.34449	Cl	8.893139	11.772423	23.993498
H	14.555427	10.856628	10.728589	Cl	10.462504	14.72496	22.602163
H	0.6378	15.883692	15.61364	O	9.897945	11.98494	21.063127
H	12.434563	9.23739	16.996629	C	10.677328	12.338914	19.907867
H	-1.473939	14.292649	21.87988	H	11.29294	11.486614	19.609893
H	10.31543	7.6415	23.262408	H	11.302157	13.210779	20.116661
H	-0.461532	12.783166	25.859548	H	9.965286	12.566613	19.114336
H	8.285952	6.11209	29.548787	Cl	10.50703	16.803423	14.859437
H	15.915533	10.716573	5.124434	O	11.852086	13.948273	13.853901
H	5.91513	17.629466	7.075924	C	11.736362	14.561714	12.553158
H	13.682102	8.98483	11.380873	H	10.72451	14.361189	12.203613
H	3.806999	16.038175	13.34549	H	12.460367	14.104471	11.874729
H	11.559933	7.383927	17.653078	H	11.896637	15.639638	12.62101
H	1.664143	14.399723	19.604857	H	10.464918	11.610534	21.759167
H	9.433472	5.782025	23.922617	H	12.7632	14.042491	14.187432
Ni	10.770518	14.558968	15.571844	Cl	12.874634	14.392662	16.675102
Ni	8.650989	13.251321	22.144071				

Table 3.S12 | DFT-optimized structure of **2-(DPA)CuBr$_2$**, with green, dark brown, blue, red and grey representing copper, bromine, nitrogen, oxygen, and carbon, respectively Hydrogens omitted for clarity.

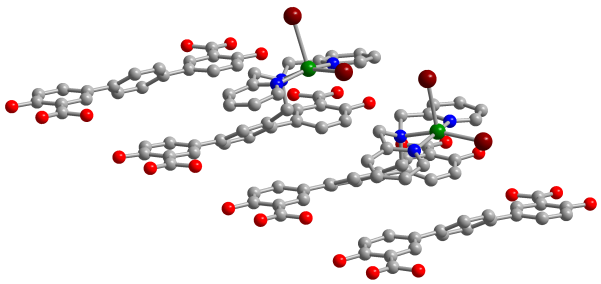

Symbol	**X**	**Y**	**Z**	H	7.895938	10.055383	5.024514
C	1.642519	15.391301	5.721591	H	5.828908	10.933803	4.059796
C	2.525822	14.617212	4.826939	C	12.533428	9.17543	5.644485
C	2.197022	14.365053	3.463896	C	11.650812	9.971419	6.567096
O	0.5935	15.9248	5.3838	O	12.1247	9.0566	4.3415
O	1.0739	14.804	2.8219	O	13.5783	8.6205	5.949
C	10.432958	10.504534	6.088974	C	3.719846	14.08444	5.350194
C	8.27215	11.767196	6.292659	C	4.604005	13.323386	4.586633
C	7.550874	11.039124	5.329896	C	4.254961	13.088937	3.23987
C	6.370759	11.538589	4.781166	C	3.083111	13.595797	2.694971
H	10.138314	10.35516	5.056318	C	5.856186	12.786789	5.173579

C	6.571946	13.50953	6.145187	H	5.90338	14.150763	13.456424
C	7.752376	13.011249	6.692786	H	8.293808	13.617056	7.413637
H	3.936371	14.268992	6.395311	C	1.647654	15.398929	19.317965
H	4.922072	12.516525	2.602377	C	2.546482	14.648792	18.409183
H	2.832708	13.412695	1.654752	C	2.222883	14.411003	17.04304
H	6.222707	14.490715	6.453297	O	2.0471	15.4886	13.7911
C	1.627702	15.365925	12.526914	O	0.5935	15.9248	18.9834
C	2.479586	14.537068	11.643389	O	1.0739	14.804	16.4215
C	2.161907	14.303432	10.274849	C	10.50886	10.615648	19.652627
O	2.0471	15.4886	6.9913	C	9.486312	11.148547	13.686338
O	0.5935	15.9248	12.1836	C	9.741203	11.165352	15.069545
O	1.0739	14.804	9.6217	C	10.951258	10.726967	15.570334
C	10.459922	10.554347	12.876525	C	8.300323	11.809	19.875471
C	9.540698	11.250575	6.862394	C	7.741156	11.264885	18.702974
C	9.906118	11.502346	8.196199	C	6.593903	11.784514	18.112293
C	11.096131	11.00898	8.704887	H	10.369463	10.684994	18.581016
C	8.222935	11.693586	13.118954	H	8.993858	11.526993	15.766147
C	7.577105	10.996466	12.078713	H	11.175819	10.875512	16.618572
C	6.381765	11.436354	11.512789	H	8.191966	10.381017	18.262279
H	10.267464	10.56772	11.809667	H	6.200833	11.299739	17.224632
H	9.252328	12.076341	8.845571	C	12.548884	9.190687	19.254266
H	11.380105	11.24557	9.725842	C	11.676366	9.995121	20.156206
H	8.009393	10.067315	11.719484	C	11.925891	10.128153	14.756099
H	5.933402	10.853358	10.714229	O	12.1247	9.0566	17.9411
C	12.540094	9.180348	12.455577	O	13.5783	8.6205	19.5486
C	11.654318	9.973707	13.36753	O	13.0979	9.7412	15.311
C	11.969908	10.222718	7.9323	C	3.75286	14.12731	18.912497
O	12.1247	9.0566	11.1413	C	4.660977	13.415999	18.12436
O	13.5783	8.6205	12.7488	C	4.326105	13.228104	16.767271
O	13.0979	9.7412	8.5112	C	3.133383	13.702678	16.2463
C	3.634523	13.935534	12.175672	C	5.915976	12.869596	18.694203
C	4.493402	13.137075	11.417073	C	6.46857	13.405735	19.863839
C	4.154091	12.928602	10.064343	C	7.647722	12.932156	20.447458
C	3.014284	13.493088	9.51096	H	3.953563	14.282154	19.964175
C	5.742434	12.588992	11.999423	H	5.008408	12.707179	16.103214
C	6.368502	13.258109	13.056597	H	2.877824	13.543319	15.206181
C	7.600152	12.875087	13.593079	H	5.964264	14.232504	20.347774
H	3.843186	14.108792	13.223203	C	1.659668	15.41194	26.107138
H	4.802774	12.335833	9.42682	C	2.581405	14.703605	25.191333
H	2.766373	13.336188	8.467304	C	2.247436	14.452723	23.829638

O	2.0471	15.4886	20.5909	H	8.370413	13.788164	27.802663
O	0.5935	15.9248	25.7832	H	0.549159	15.329312	3.467165
O	1.0739	14.804	23.2213	H	0.554865	15.333064	10.269247
C	10.565624	10.680931	26.401637	H	12.997241	9.749696	9.483737
C	9.512874	11.17509	20.458253	H	0.533157	15.29826	17.078549
C	9.707487	11.07321	21.848582	H	12.991238	9.676272	16.282377
C	10.908834	10.633826	22.365227	H	0.528722	15.288844	23.881136
C	8.457979	12.043244	26.529042	H	12.985921	9.664373	23.080969
C	7.810036	11.402052	25.457189	H	1.357221	15.983352	27.872256
C	6.634547	11.911593	24.910118	H	13.1219	10.009522	29.844622
H	10.350414	10.57678	25.347512	H	11.313099	9.550678	4.14761
H	8.922866	11.345387	22.542295	H	1.341346	15.888534	7.533992
H	11.090404	10.723629	23.426293	H	11.173925	9.228779	11.034286
H	8.195876	10.463393	25.071091	H	1.354505	15.921053	14.326003
H	6.149075	11.357241	24.112541	H	11.157264	9.120538	17.863879
C	12.549395	9.191126	26.056295	H	1.333342	15.871538	21.13635
C	11.710279	10.05091	26.937814	H	11.154923	9.061719	24.672089
C	11.922934	10.107648	21.552043	N	8.813674	15.016076	21.327488
O	12.1247	9.0566	24.7409	C	9.999489	14.860193	20.467325
O	13.5783	8.6205	26.3484	C	7.893243	16.094489	20.913152
O	13.0979	9.7412	22.1108	C	6.995859	16.418001	22.078364
C	3.825749	14.249741	25.67638	C	11.131478	14.259652	21.257383
C	4.750979	13.578397	24.873477	N	7.584396	16.331143	23.294025
C	4.393531	13.359426	23.527313	C	6.875817	16.60186	24.399699
C	3.172937	13.777508	23.022548	C	5.534065	16.970807	24.341229
C	6.039556	13.082081	25.416834	C	4.915552	17.057687	23.09514
C	6.697892	13.732788	26.474396	C	5.659415	16.781098	21.945923
C	7.879003	13.228489	27.014163	N	11.118067	14.489836	22.587187
H	4.048791	14.422393	26.722543	C	12.114591	14.018444	23.355994
H	5.085158	12.858472	22.857255	C	13.1843	13.310479	22.8197
H	2.911325	13.604044	21.986166	C	13.211094	13.074168	21.443991
H	6.298768	14.661504	26.870231	C	12.165794	13.548227	20.654572
O	2.0471	15.4886	27.3907	H	8.511609	16.966894	20.6847
C	9.685117	11.472174	27.139655	H	7.3301	15.84387	20.011135
C	10.003405	11.669398	28.496996	H	10.294527	15.856487	20.130251
C	11.135654	11.097493	29.05794	H	9.77848	14.263537	19.57569
H	9.350644	12.260931	29.130604	H	5.207172	16.83631	20.961265
H	11.354153	11.268008	30.109143	H	3.866936	17.325869	23.015926
C	12.003089	10.28282	28.311258	H	4.989555	17.167339	25.257587
O	13.0979	9.7412	28.9106	H	7.411699	16.505646	25.336375

H	12.032054	14.230828	24.415479	H	7.401936	14.270412	15.199663
H	13.969093	12.943165	23.471592	H	8.925592	13.414843	15.24911
H	12.139896	13.361397	19.586909	H	14.046827	12.73035	15.259007
Cu	9.539985	15.676361	23.183984				
Br	10.614448	17.956925	22.194771				
Br	10.063169	15.747869	25.581096				
C	8.156578	13.710473	21.645706				
H	7.33058	13.922505	22.326161				
H	8.892346	13.159567	22.214778				
H	14.024613	12.512642	20.996365				
N	8.906445	15.019063	13.936699				
C	10.204348	14.635484	13.34957				
C	8.072816	15.846808	13.040782				
C	7.025987	16.548542	13.865055				
C	11.200684	14.384534	14.453948				
N	7.410088	16.8868	15.11573				
C	6.544703	17.503896	15.935413				
C	5.248206	17.816111	15.535018				
C	4.843414	17.47712	14.243592				
C	5.746847	16.83406	13.39586				
N	10.984694	15.050822	15.608835				
C	11.836781	14.901212	16.63614				
C	12.954949	14.077544	16.548634				
C	13.1901	13.389338	15.357101				
C	12.298321	13.543557	14.296574				
H	8.735235	16.598376	12.60056				
H	7.627206	15.26198	12.231072				
H	10.555368	15.479382	12.748327				
H	10.110138	13.764055	12.693191				
H	5.461246	16.541492	12.390814				
H	3.835999	17.692922	13.904244				
H	4.57427	18.306587	16.228726				
H	6.919294	17.738956	16.924912				
H	11.599863	15.469513	17.528				
H	13.622968	13.981792	17.397599				
H	12.437171	13.007246	13.364121				
Cu	9.349211	16.302442	15.529283				
Br	10.58202	18.163425	14.004925				
Br	9.465101	17.206712	17.797443				
C	8.199205	13.858821	14.577898				

14. References

(1) Milner, P. J.; Martell, J. D.; Siegelman, R. L.; Gygi, D.; Weston, S. C.; Long, J. R. Overcoming Double-Step CO_2 Adsorption and Minimizing Water Co-Adsorption in Bulky Diamine-Appended Variants of Mg_2(Dobpdc). *Chem. Sci.* **2018**, *9* (1), 160–174. https://doi.org/10.1039/C7SC04266C.

(2) Fischer, R.; Görls, H.; Langer, J.; Enke, M.; Westerhausen, M. Magnesiacycloalkanes with Different Ring Sizes. *Organometallics* **2016**, *35* (4), 587–594. https://doi.org/10.1021/acs.organomet.5b01010.

(3) Brown, J. W.; Henderson, B. L.; Kiesz, M. D.; Whalley, A. C.; Morris, W.; Grunder, S.; Deng, H.; Furukawa, H.; Zink, J. I.; Stoddart, J. F.; Yaghi, O. M. Photophysical Pore Control in an Azobenzene-Containing Metal–Organic Framework. *Chem. Sci.* **2013**, *4* (7), 2858–2864. https://doi.org/10.1039/C3SC21659D.

(4) Ong, W. S. Y.; Smaldone, R. A.; Dodani, S. C. A Neutral Porous Organic Polymer Host for the Recognition of Anionic Dyes in Water. *Chem. Sci.* **2020**, *11* (29), 7716–7721. https://doi.org/10.1039/D0SC02941F.

(5) Akbulut, H.; Endo, T.; Yamada, S.; Yagci, Y. Synthesis and Characterization of Polyphenylenes with Polypeptide and Poly(Ethylene Glycol) Side Chains. *Journal of Polymer Science Part A: Polymer Chemistry* **2015**, *53* (15), 1785–1793. https://doi.org/10.1002/pola.27621.

(6) Fracaroli, A. M.; Furukawa, H.; Suzuki, M.; Dodd, M.; Okajima, S.; Gándara, F.; Reimer, J. A.; Yaghi, O. M. Metal-Organic Frameworks with Precisely Designed Interior for Carbon Dioxide Capture in the Presence of Water. *Journal of the American Chemical Society* **2014**, *136* (25), 8863–8866. https://doi.org/10.1021/ja503296c.

(7) Geary, J.; Wong, A. H.; Xiao, D. J. Thermolabile Cross-Linkers for Templating Precise Multicomponent Metal–Organic Framework Pores. *J. Am. Chem. Soc.* **2021**, *143* (27), 10317–10323. https://doi.org/10.1021/jacs.1c04030.

(8) Walton, K. S.; Snurr, R. Q. Applicability of the BET Method for Determining Surface Areas of Microporous Metal−Organic Frameworks. *J. Am. Chem. Soc.* **2007**, *129* (27), 8552–8556. https://doi.org/10.1021/ja071174k.

(9) Newville, M. Larch: An Analysis Package for XAFS and Related Spectroscopies. *J. Phys.: Conf. Ser.* **2013**, *430*, 012007. https://doi.org/10.1088/1742-6596/430/1/012007.

(10) Calvin, S. *XAFS for Everyone*; CRC Press: Boca Raton, 2013. https://doi.org/10.1201/b14843.

(11) Li, J.; Zhang, Q.; Hu, X.; Ma, Y.; Solan, G. A.; Sun, Y.; Sun, W.-H. 2-Acetyloxymethyl-Substituted 5,6,7-Trihydroquinolinyl-8-Ylideneamine-Ni(II) Chlorides and Their Application in Ethylene Dimerization/Trimerization. *Applied Organometallic Chemistry* **2020**, *34* (1), e5254. https://doi.org/10.1002/aoc.5254.

(12) Yu, J.; Hu, X.; Zeng, Y.; Zhang, L.; Ni, C.; Hao, X.; Sun, W.-H. Synthesis, Characterisation and Ethylene Oligomerization Behaviour of N-(2-Substituted-5,6,7-Trihydroquinolin-8-Ylidene)Arylaminonickel Dichlorides. *New J. Chem.* **2011**, *35* (1), 178–183. https://doi.org/10.1039/C0NJ00516A.

(13) Hou, X.; Liang, T.; Sun, W.-H.; Redshaw, C.; Chen, X. 2-Substituted 8-(2-Benzhydrylarylimino)-5,6,7-Trihydroquinoline-N,N′ Nickel Dichlorides: Synthesis, Characterization and Catalytic Behavior towards Ethylene. *Journal of Organometallic Chemistry* **2012**, *708–709*, 98–105. https://doi.org/10.1016/j.jorganchem.2012.02.031.

(14) Wang, S.; Zhang, W.; Du, S.; Asuha, S.; Flisak, Z.; Sun, W.-H. Propyl Substituted 4-Arylimino-1,2,3-Trihydroacridylnickel Complexes: Their Synthesis, Characterization and Catalytic Behavior toward Ethylene. *Journal of Organometallic Chemistry* **2015**, *798*, 408–413. https://doi.org/10.1016/j.jorganchem.2015.05.001.
(15) Wang, S.; Du, S.; Zhang, W.; Asuha, S.; Sun, W.-H. Nickel(II) Complexes Bearing 4-Arylimino-1,2,3-Trihydroacridines: Synthesis, Characterization, and Ethylene Oligomerization. *ChemistryOpen* **2015**, *4* (3), 328–334. https://doi.org/10.1002/open.201402113.
(16) Song, S.; Xiao, T.; Wang, L.; Redshaw, C.; Wang, F.; Sun, W.-H. 2-(1-Arylimino)Quinolylnickel Halides: Synthesis, Characterization and Catalytic Behavior towards Ethylene. *Journal of Organometallic Chemistry* **2012**, *699*, 18–25. https://doi.org/10.1016/j.jorganchem.2011.11.001.
(17) Chai, W.; Yu, J.; Wang, L.; Hu, X.; Redshaw, C.; Sun, W.-H. Synthesis, Characterization and Ethylene Oligomerization Behavior of N-(2-Alkyl-5,6,7-Trihydroquinolin-8-Ylidene)Arylaminonickel(II) Dichlorides. *Inorganica Chimica Acta* **2012**, *385*, 21–26. https://doi.org/10.1016/j.ica.2011.12.008.
(18) Fei, B.-L.; Huang, Z.-X.; Xu, W.-S.; Li, D.-D.; Lu, Y.; Gao, W.-L.; Zhao, Y.; Zhang, Y.; Liu, Q.-B. Chiral Copper(II) Complex Based on Natural Product Rosin Derivative as Promising Antitumour Agent. *Journal of Photochemistry and Photobiology B: Biology* **2016**, *160*, 43–52. https://doi.org/10.1016/j.jphotobiol.2016.03.044.
(19) Koval, I. A.; Huisman, M.; Stassen, A. F.; Gamez, P.; Lutz, M.; Spek, A. L.; Reedijk, J. Unusual CuII and MnII Complexes of Phenol-Based Ligands Containing Amine, Pyridine and Formyl Functions: Unexpected Structural Features and Solution Studies. *European Journal of Inorganic Chemistry* **2004**, *2004* (3), 591–600. https://doi.org/10.1002/ejic.200300567.
(20) Zhang, Y.-P.; Ma, Z.-Y.; Qiao, P.-P.; Gao, C.-Y.; Tian, J.-L.; Zhao, J.-Z.; Du, W.-J.; Xu, J.-Y.; Yan, S.-P. Design and Biological Evaluations of Mono- and Di-Nuclear Copper(II) Complexes: Nuclease Activity, Cytotoxicity and Apoptosis. *Polyhedron* **2021**, *193*, 114880. https://doi.org/10.1016/j.poly.2020.114880.
(21) Colomban, C.; Martin-Diaconescu, V.; Parella, T.; Goeb, S.; García-Simón, C.; Lloret-Fillol, J.; Costas, M.; Ribas, X. Design of Zn-, Cu-, and Fe-Coordination Complexes Confined in a Self-Assembled Nanocage. *Inorg. Chem.* **2018**, *57* (7), 3529–3539. https://doi.org/10.1021/acs.inorgchem.7b02852.
(22) Bartholomä, M.; Cheung, H.; Zubieta, J. [μ-N,N,N′,N′-Tetra-kis(2-Pyridyl-meth-yl)Butane-1,4-Diamine]-bis-[Dibromidocopper(II)]. *Acta Cryst E* **2010**, *66* (10), m1198–m1198. https://doi.org/10.1107/S1600536810034537.
(23) Evans, A. J.; Watkins, S. E.; Craig, D. C.; Colbran, S. B. Copper Complexes with Ferrocenyl Pendants: Evidence for an FeII∼ CuII⇌ FeIII∼ CuI Electron Transfer Equilibrium Leading to a Reaction with Dioxygen. *J. Chem. Soc., Dalton Trans.* **2002**, No. 6, 983–994. https://doi.org/10.1039/B105150B.

Chapter 4. Stabilizing Large Pores in a Flexible Metal–Organic Framework via Chemical Cross-linking

4.1 Introduction.

Isoreticular expansion is a simple yet powerful tool for the rational design of larger pore metal–organic frameworks (MOFs).[1,2] Broadening the number of chemically robust MOFs amenable to systematic pore expansion is critical for applications requiring the encapsulation or diffusion of large guests, such as catalysis, sensing, and drug delivery.[3,4] Despite its conceptual simplicity, isoreticular expansion is often challenging to implement in practice. In addition to reduced chemical and structural stability, frameworks with large pores are prone to interpenetration, which reduces the overall accessible pore volume and surface area.[1,3,4]

Frameworks composed of rod-like secondary building units are promising candidates for isoreticular expansion, as the pore walls are tightly framed by ligands and cannot be interpenetrated.[5,6] However, rod-packing frameworks face other barriers to pore expansion, including competing phase formation and complex breathing behavior. Phase purity challenges are best illustrated by considering the reaction of a simple linker, 1,4-benzenedicarboxylic acid (H_2bdc), with various metal cations. While it is possible to achieve rod-packing motifs, such as those found in MOF-69C ($Zn_3(OH)_2(bdc)_2$)[5] and MIL-140A (ZrO(bdc)),[7] alternative phases are often equally, if not more, synthetically accessible. In the case of Zn^{2+} and Zr^{4+}, competing phases include MOF-5 ($Zn_4O(bdc)_3$)[8] and UiO-66 ($Zr_6O_4(OH)_4(bdc)_6$),[9] two of the most well-known and highly-studied frameworks to date. Because the formula units of MOF-69C vs. MOF-5 and MIL-140A vs. UiO-66 differ only in their bridging oxide/hydroxide content, achieving phase purity is nontrivial and requires the laborious testing of various solvents, additives, and heating methods.[6,10]

Reprinted (adapted) with permission from:
1. J. Geary,* D. S. Rollins,* A. H. Wong and D. J. Xiao, *Chem. Commun.*, 2022, **58**, 12361 **DOI:** 10.1039/D2CC04829A

In contrast to the complex structural landscape observed with M^{2+} and M^{4+} salts, combining H_2bdc with a M^{3+} cation typically leads to phase-pure MIL-53(M) (M = Al, Sc, Cr, V, Fe, Ga, In) (**Fig. 4.1**).[11–17] However, many frameworks in the MIL-53 series display large breathing behavior, with pores opening and closing in response to environmental changes.[13] The flexibility of the MIL-53 structure type adds a new layer of difficulty to the construction of larger-pore variants, as the breathing behavior changes unpredictably as a function of linker length.[18,19] Due to these challenges, no rod-packing MOF architecture has replicated the success of the MOF-74 family (also known as M_2(dobdc), dobdc^{4-} = 2,5-dioxido-1,4-benzenedicarboxylate), which can be expanded to achieve permanently porous channels approaching 10 nm in diameter.[20] Broadening the number of rod-packing architectures that are robust to isoreticular expansion remains an important synthetic goal.

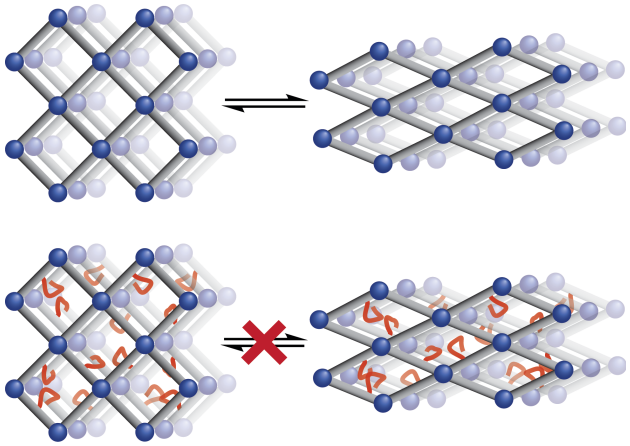

Fig. 4.1 | Overview of chemical cross-linking strategy to induce pore rigidification in flexible frameworks.

Here we show that chemical cross-linking can be used to enhance the structural rigidity of expanded MIL-53 analogues, providing access to large-pore variants. We report the synthesis of Al(OH)dmtpdc (dmtpdc^{2-} = 2',5'-dimethyl-[1,1':4',1"-terphenyl]-4,4"-dicarboxylate), a terphenyl-expanded variant of MIL-53(Al). While Al(OH)dmtpdc partially closes upon guest evacuation, the installation of simple cross-linkers between ligands effectively locks the pores in the open form. Gas sorption measurements show that the cross-linked material possesses ~17 Å diameter pores and a Brunauer–Emmett–Teller (BET) surface area of 1870 m^2/g.

4.2 Results and Discussion.

4.2.1 Synthesis and characterization of cross-linked frameworks.

We have been interested in developing pore-expanded analogues of MIL-53(Al) due to its resistance to interpenetration, good chemical stability, and tunable pores decorated with mildly Brønsted acidic and functionalizable hydroxyl groups.[21,22] The MIL-53(Al) structure is composed of infinite chains of corner-sharing Al^{3+} octahedra bridged by bdc^{2-} ligands to form one-dimensional, diamond-shaped channels (**Fig. 4.1**). Previous reports have shown that the central benzene ring of MIL-53(Al) can be readily replaced with naphthyl, biphenyl, and bipyridyl units.[18,19] These expanded analogues are all permanently porous, with BET surface areas of 1308, 1613, and 2160 m^2/g, respectively.[18,19]

Given the apparent amenability of MIL-53(Al) to isoreticular expansion, we sought to synthesize the terphenyl variant, Al(OH)dmtpdc (2',5'-dimethyl-[1,1':4',1"-terphenyl]-4,4"-dicarboxylate) (**Fig. 4.2**). Equimolar amounts of $AlCl_3 \cdot 6H_2O$ and H_2dmtpdc were heated in DMF to afford a microcrystalline white solid whose powder X-ray diffraction pattern (PXRD) largely matches the simulated pattern for fully open Al(OH)dmtpdc (**Fig. 4.3a**). However, in addition to the predicted peaks, additional features at ~6.5 and 10.5° 2θ were also observed. These peaks are inconsistent with the open form and are tentatively attributed to partially closed phase(s) (**Fig. 4.S5**).

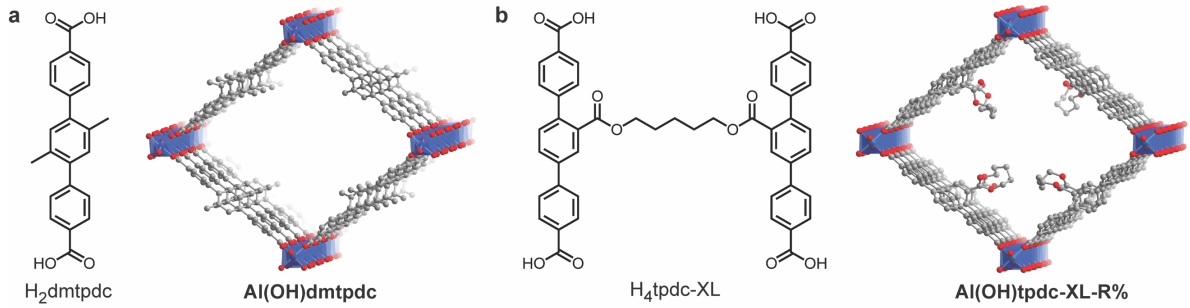

Fig. 4.2 | Modeled structures of the terphenyl expanded MIL-53(Al) frameworks (a) Al(OH)dmtpdc and (b) Al(OH)tpdc-XL-R%.

Like other members of the MIL-53 family, Al(OH)dmtpdc is flexible and undergoes structural changes in response to changes in solvation and pressure. While the PXRD patterns of DMF and MeCN-soaked samples are relatively similar, significant changes were observed under all other tested conditions (MeOH, THF, H_2O, vacuum activation) (**Fig. 4.S6**). Specifically, the appearance of new peaks and significant peak broadening were observed. Furthermore, these structural changes are not fully reversible, and the original PXRD pattern could not be recovered even after resolvation in DMF or MeCN (**Fig. 4.S7–4.S8**).

Gas sorption studies further confirmed that the flexible pores of Al(OH)dmtpdc are unstable to solvent exchange and activation. The theoretical surface area of fully open Al(OH)dmtpdc was calculated using the software Zeo++ and a predicted value of 3180 m^2/g was obtained.[23] In contrast, the experimentally measured BET surface area of Al(OH)dmtpdc was 645 m^2/g, significantly lower than the theoretical value, indicating substantial pore collapse upon solvent removal (**Fig. 4.3b**). To further probe the pore structure, density functional theory (DFT) methods were used to calculate the pore size distribution from 77 K N_2 adsorption data. A mixture of pore sizes was obtained, with large pores centered around 16–18 Å as well as smaller pores between 8–10 Å in diameter (**Fig. 4.S9**). The broad

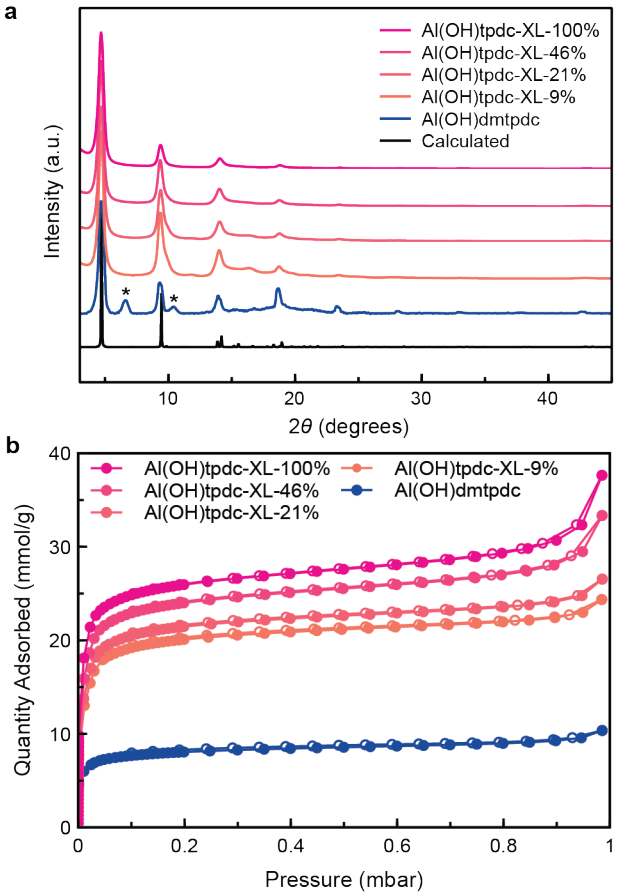

Fig. 4.3 | (a) PXRD patterns and (b) N_2 adsorption isotherms at 77 K for Al(OH)dmtpdc and cross-linked Al(OH)tpdc-XL-R% frameworks.

distribution of pore diameters suggests that the activated material is not a single phase but is likely a complex mixture of open, partially open, and closed phases.

Given the structural flexibility and low porosity of Al(OH)dmtpdc, we investigated various strategies to rigidify the framework. Previous reports have shown that the presence of bulky functional groups can modulate flexible behavior through a combination of steric hindrance and intraframework interactions.[24] We hypothesized that installing short cross-linkers between pairs of ligands would more effectively stabilize the open configuration (**Fig. 4.1**). Relative to simple functional groups, cross-linkers should provide stricter geometric constraints on the motion of the pores, similar to how rigid ligands have been previously used as "girders" to enhance the mechanical stability of MOFs.[25] Cross-linking MOF ligands is well-studied, and has been used to generate "poly-MOFs" with enhanced chemical stability.[26,27] Our group has previously used short diester bridges to cross-link terphenyl expanded MOF-74 analogues.[28] Given that the MIL-53 structure type possesses similar one-dimensional pore channels, we posited an analogous approach would be viable.

We synthesized the ligand H_4tpdc-XL, which contains two terphenyldicarboxylic acid units linked by a 5-carbon diester chain (**Fig. 4.2b**). Combining $AlCl_3 \cdot 6H_2O$ with various ratios of H_2dmtpdc and H_4tpdc-XL readily produces the cross-linked framework Al(OH)tpdc-XL-R%, where 'R%' refers to the percentage of cross-linked ligand struts in the framework (**Fig. 4.2b**, see SI for synthetic details).

The experimental powder pattern of the cross-linked Al(OH)tpdc-XL-R% closely matches the predicted structure of a fully open Al(OH)dmtpdc framework (**Fig. 4.3a**). In contrast to the PXRD of Al(OH)dmtpdc, no additional peaks indicating the presence of partially closed phases were observed. Pawley refinement of the fully cross-linked material, Al(OH)tpdc-XL-100%,

afforded a unit cell of a = 6.77(8) Å, b = 29.02(28) Å, and c = 24.71(22) Å in the *Pnma* space group, consistent with computational models of the fully open structure (**Fig. 4.S10, Table 4.S3**). ^{1}H NMR of digested samples confirmed the input ratio of H_2dmtpdc to H_4tpdc-XL was closely retained in the final material, with no indication of cross-linker decomposition (see SI). The incorporation of the cross-linker was further confirmed by FT-IR, with the growth of the ester carbonyl stretch at 1718 cm^{-1} (**Fig. 4.S11**) at higher cross-linker concentrations.

Gas sorption measurements confirm that chemically cross-linking successfully stabilizes the open configuration. A BET surface area of 1870 m^2/g was obtained for the fully cross-linked Al(OH)tpdc-XL-100%, nearly three-fold higher than Al(OH)dmtpdc. While this value is still lower than the predicted value for open Al(OH)dmtpdc, a decrease in surface area is expected as the pores are partially occupied by cross-linkers. In addition to an improved surface area, the DFT pore size distribution shows only large pores centered around 16–19 Å, rather than a complex mixture of small and large pore diameters. The slight variations in pore size between 16–19 Å may be due to subtle changes in the extent of pore opening. We found that the surface area of Al(OH)tpdc-XL-R% was directly correlated with the percentage of cross-linker incorporation. The BET surface areas increase from 1330 m^2/g to 1870 m^2/g between Al(OH)tpdc-XL-9% and Al(OH)tpdc-XL-100%, respectively (**Fig. 4.3b**).

In addition to a higher surface area, the fully cross-linked Al(OH)tpdc-XL-100% also exhibits markedly improved solvent stability compared to the parent framework. While samples immersed in protic solvents like methanol or boiling water initially lose diffraction peak intensity, the intensity is fully recovered upon re-immersion in an aprotic solvent such as acetonitrile (**Fig. 4.S12–4.S14**). Finally, thermogravimetric analysis of the parent and cross-linked materials reveals excellent thermal stability for the cross-linked materials (**Fig. 4.S15**).

To probe the necessity of the cross-linker, we synthesized a simple propyl ester analogue of H_2dmtpdc, mimicking the steric profile of the cross-linked ligand but with greater rotational freedom (**Fig. 4.S16**). The resultant propyl ester-functionalized framework shows poor crystallinity compared to both Al(OH)dmtpdc and Al(OH)tpdc-XL-100%, and a BET surface area of only 1275 m2/g (**Fig. 4.S17-4.S18**). Together, these results suggest that the rigidity engendered by cross-linkers plays a crucial role in stabilizing open pores.

Next, the configuration of the cross-linkers in the pores was probed via modeling studies. We investigated two possible configurations, which are illustrated in **Fig. 4.4**. In the "down-pore" configuration, the cross-linker bridges adjacent ligands down the pore channel, whereas in the "across-pore" configuration, the cross-linker bridges neighboring ligands in the *bc* plane. To carry out these calculations, the extended structure of Al(OH)dmtpdc was first optimized in Materials Studio (**Table 4.S3**) and then truncated to two neighboring ligands. The ligands were partially frozen such that only the central phenyl rings could freely move, mimicking the geometric restrictions of the framework lattice. For both configurations, a bridging cross-linker was added, and the geometries were optimized using DFT (see SI for computational details). Altogether, our modeling studies suggest the "down-pore" configuration is the dominant structure in the framework, with an energetic preference of over 14 kcal/mol (**Table 4.4S3**).

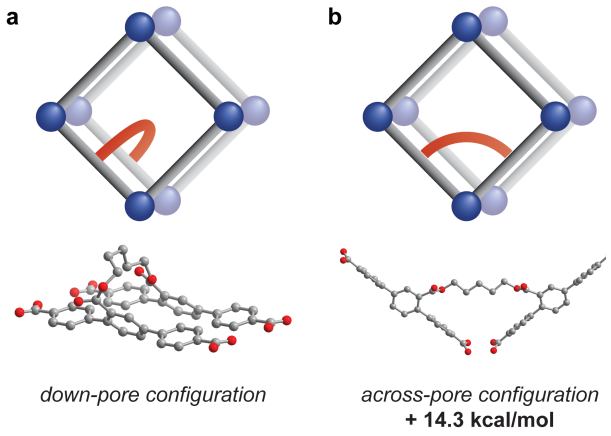

Fig. 4.4 | Truncated model structures showing the (a) "down-pore" and (b) "across-pore" cross-linker configurations.

4.2.2 Prins condensation catalysis.

Due to its increased pore size and structural stability, we hypothesized that the fully cross-linked Al(OH)tpdc-XL-100% would outperform Al(OH)dmtpdc in applications requiring the diffusion of guests through the pores, such as catalysis. The Prins condensation between β-pinene and paraformaldehyde to form nopol was investigated as a proof-of-concept reaction (see **Scheme 4.S3** for reaction overview). Previous reports have shown that the Prins reaction can be catalyzed by Lewis acidic metal centers in MOFs.[29] While the bulk of Al^{3+} centers in MIL-53(Al) are coordinatively saturated, the framework is known to contain a small amount of Lewis acidic defect sites that can be used to catalyze this reaction.[30] We found that cross-linked Al(OH)tpdc-Xl-100% outperformed the noncross-linked framework. Specifically, Al(OH)dmtpdc showed negligible catalytic activity at 80 °C in MeCN, while Al(OH)tpdc-XL-100% showed ca. 19 % conversion under the same conditions (**Table S7**). We note that the incomplete conversion may be due to the relatively low concentration of Lewis acidic defect sites as well as possible product adsorption and inhibition.

4.3 Conclusions.

In conclusion, we have shown how cross-linking stabilizes open pores in the terphenyl expanded analogues of MIL-53(Al), leading to improved mass transport and higher catalytic activity. While we have focused on the MIL-53 family, chemical cross-linking may serve as a generalizable route for accessing stable, large-pore variants of flexible metal–organic frameworks. More broadly, these results suggest that our crosslinking strategy may be a way to alter the thermodynamic landscape, making otherwise inaccessible framework motifs thermodynamically favorable products.

4.4 Acknowledgements

This work was supported by the National Science Foundation under grant No. 2142798. J.G. was supported by an NSF graduate research fellowship, and A.H.W. was supported by a Mary Gates research scholarship. This work was facilitated through the use of advanced computational, storage, and networking infrastructure provided by the Hyak supercomputer system at the University of Washington.

4.5 References

(1) Eddaoudi, M.; Kim, J.; Rosi, N.; Vodak, D.; Wachter, J.; O'Keeffe, M.; Yaghi, O. M. Systematic Design of Pore Size and Functionality in Isoreticular MOFs and Their Application in Methane Storage. *Science* **2002**, *295* (5554), 469–472. https://doi.org/10.1126/science.1067208.

(2) Yaghi, O. M.; O'Keeffe, M.; Ockwig, N. W.; Chae, H. K.; Eddaoudi, M.; Kim, J. Reticular Synthesis and the Design of New Materials. *Nature* **2003**, *423* (6941), 705–714. https://doi.org/10.1038/nature01650.

(3) Song, L.; Zhang, J.; Sun, L.; Xu, F.; Li, F.; Zhang, H.; Si, X.; Jiao, C.; Li, Z.; Liu, S.; Liu, Y.; Zhou, H.; Sun, D.; Du, Y.; Cao, Z.; Gabelica, Z. Mesoporous Metal–Organic Frameworks: Design and Applications. *Energy Environ. Sci.* **2012**, *5* (6), 7508. https://doi.org/10.1039/c2ee03517k.

(4) Xuan, W.; Zhu, C.; Liu, Y.; Cui, Y. Mesoporous Metal–Organic Framework Materials. *Chem. Soc. Rev.* **2012**, *41* (5), 1677–1695. https://doi.org/10.1039/C1CS15196G.

(5) Rosi, N. L.; Kim, J.; Eddaoudi, M.; Chen, B.; O'Keeffe, M.; Yaghi, O. M. Rod Packings and Metal−Organic Frameworks Constructed from Rod-Shaped Secondary Building Units. *J. Am. Chem. Soc.* **2005**, *127* (5), 1504–1518. https://doi.org/10.1021/ja045123o.

(6) Rosi, N. L.; Eddaoudi, M.; Kim, J.; O'Keeffe, M.; Yaghi, O. M. Infinite Secondary Building Units and Forbidden Catenation in Metal-Organic Frameworks The National Science Foundation Support to M.O'K. (DMR- 9804817) and O.M.Y. (DMR-9980469) Is Gratefully Acknowledged. *Angew. Chem. Int. Ed.* **2002**, *41* (2), 284. https://doi.org/10.1002/1521-3773(20020118)41:2<284::AID-ANIE284>3.0.CO;2-M.

(7) Guillerm, V.; Ragon, F.; Dan-Hardi, M.; Devic, T.; Vishnuvarthan, M.; Campo, B.; Vimont, A.; Clet, G.; Yang, Q.; Maurin, G.; Férey, G.; Vittadini, A.; Gross, S.; Serre, C. A Series of Isoreticular, Highly Stable, Porous Zirconium Oxide Based Metal-Organic Frameworks. *Angew. Chem. Int. Ed.* **2012**, *51* (37), 9267–9271. https://doi.org/10.1002/anie.201204806.

(8) Li, H.; Eddaoudi, M.; O'Keeffe, M.; Yaghi, O. M. Design and Synthesis of an Exceptionally Stable and Highly Porous Metal-Organic Framework. *Nature* **1999**, *402* (6759), 276–279. https://doi.org/10.1038/46248.

(9) Cavka, J. H.; Jakobsen, S.; Olsbye, U.; Guillou, N.; Lamberti, C.; Bordiga, S.; Lillerud, K. P. A New Zirconium Inorganic Building Brick Forming Metal Organic Frameworks with Exceptional Stability. *J. Am. Chem. Soc.* **2008**, *130* (42), 13850–13851. https://doi.org/10.1021/ja8057953.

(10) Liang, W.; Babarao, R.; D'Alessandro, D. M. Microwave-Assisted Solvothermal Synthesis and Optical Properties of Tagged MIL-140A Metal–Organic Frameworks. *Inorg. Chem.* **2013**, *52* (22), 12878–12880. https://doi.org/10.1021/ic4024234.
(11) Serre, C.; Millange, F.; Thouvenot, C.; Noguès, M.; Marsolier, G.; Louër, D.; Férey, G. Very Large Breathing Effect in the First Nanoporous Chromium(III)-Based Solids: MIL-53 or CrIII(OH)·{O2C−C6H4−CO2}·{HO2C−C6H4−CO2H}x·H2Oy. *J. Am. Chem. Soc.* **2002**, *124* (45), 13519–13526. https://doi.org/10.1021/ja0276974.
(12) Barthelet, K.; Marrot, J.; Riou, D.; Férey, G. A Breathing Hybrid Organic–Inorganic Solid with Very Large Pores and High Magnetic Characteristics. *Angewandte Chemie International Edition* **2002**, *41* (2), 281–284. https://doi.org/10.1002/1521-3773(20020118)41:2<281::AID-ANIE281>3.0.CO;2-Y.
(13) Loiseau, T.; Serre, C.; Huguenard, C.; Fink, G.; Taulelle, F.; Henry, M.; Bataille, T.; Férey, G. A Rationale for the Large Breathing of the Porous Aluminum Terephthalate (MIL-53) Upon Hydration. *Chemistry – A European Journal* **2004**, *10* (6), 1373–1382. https://doi.org/10.1002/chem.200305413.
(14) Whitfield, T. R.; Wang, X.; Liu, L.; Jacobson, A. J. Metal-Organic Frameworks Based on Iron Oxide Octahedral Chains Connected by Benzenedicarboxylate Dianions. *Solid State Sciences* **2005**, *7* (9), 1096–1103. https://doi.org/10.1016/j.solidstatesciences.2005.03.007.
(15) Anokhina, E. V.; Vougo-Zanda, M.; Wang, X.; Jacobson, A. J. In(OH)BDC·0.75BDCH2 (BDC = Benzenedicarboxylate), a Hybrid Inorganic−Organic Vernier Structure. *J. Am. Chem. Soc.* **2005**, *127* (43), 15000–15001. https://doi.org/10.1021/ja055757a.
(16) Vougo-Zanda, M.; Huang, J.; Anokhina, E.; Wang, X.; Jacobson, A. J. Tossing and Turning: Guests in the Flexible Frameworks of Metal(III) Dicarboxylates. *Inorg. Chem.* **2008**, *47* (24), 11535–11542. https://doi.org/10.1021/ic800008f.
(17) Mowat, J. P. S.; Miller, S. R.; Slawin, A. M. Z.; Seymour, V. R.; Ashbrook, S. E.; Wright, P. A. Synthesis, Characterisation and Adsorption Properties of Microporous Scandium Carboxylates with Rigid and Flexible Frameworks. *Microporous and Mesoporous Materials* **2011**, *142* (1), 322–333. https://doi.org/10.1016/j.micromeso.2010.12.016.
(18) Senkovska, I.; Hoffmann, F.; Fröba, M.; Getzschmann, J.; Böhlmann, W.; Kaskel, S. New Highly Porous Aluminium Based Metal-Organic Frameworks: Al(OH)(Ndc) (Ndc=2,6-Naphthalene Dicarboxylate) and Al(OH)(Bpdc) (Bpdc=4,4′-Biphenyl Dicarboxylate). *Microporous and Mesoporous Materials* **2009**, *122* (1–3), 93–98. https://doi.org/10.1016/j.micromeso.2009.02.020.
(19) Bloch, E. D.; Britt, D.; Lee, C.; Doonan, C. J.; Uribe-Romo, F. J.; Furukawa, H.; Long, J. R.; Yaghi, O. M. Metal Insertion in a Microporous Metal-Organic Framework Lined with 2,2′-Bipyridine. *Journal of the American Chemical Society* **2010**, *132* (41), 14382–14384. https://doi.org/10.1021/JA106935D/SUPPL_FILE/JA106935D_SI_001.PDF.
(20) Deng, H.; Grunder, S.; Cordova, K. E.; Valente, C.; Furukawa, H.; Hmadeh, M.; Gandara, F.; Whalley, A. C.; Liu, Z.; Asahina, S.; Kazumori, H.; O'Keeffe, M.; Terasaki, O.; Stoddart, J. F.; Yaghi, O. M. Large-Pore Apertures in a Series of Metal-Organic Frameworks. *Science* **2012**, *336* (6084), 1018–1023. https://doi.org/10.1126/science.1220131.
(21) Meilikhov, M.; Yusenko, K.; Fischer, R. A. Turning MIL-53(Al) Redox-Active by Functionalization of the Bridging OH-Group with 1,1′-Ferrocenediyl-Dimethylsilane. *J. Am. Chem. Soc.* **2009**, *131* (28), 9644–9645. https://doi.org/10.1021/ja903918s.
(22) Ravon, U.; Chaplais, G.; Chizallet, C.; Seyyedi, B.; Bonino, F.; Bordiga, S.; Bats, N.; Farrusseng, D. Investigation of Acid Centers in MIL-53(Al, Ga) for Brønsted-Type Catalysis:

In Situ FTIR and Ab Initio Molecular Modeling. *ChemCatChem* **2010**, *2* (10), 1235–1238. https://doi.org/10.1002/cctc.201000055.
(23) Willems, T. F.; Rycroft, C. H.; Kazi, M.; Meza, J. C.; Haranczyk, M. Algorithms and Tools for High-Throughput Geometry-Based Analysis of Crystalline Porous Materials. *Microporous and Mesoporous Materials* **2012**, *149* (1), 134–141. https://doi.org/10.1016/j.micromeso.2011.08.020.
(24) Henke, S.; Schneemann, A.; Wütscher, A.; Fischer, R. A. Directing the Breathing Behavior of Pillared-Layered Metal–Organic Frameworks via a Systematic Library of Functionalized Linkers Bearing Flexible Substituents. *J. Am. Chem. Soc.* **2012**, *134* (22), 9464–9474. https://doi.org/10.1021/ja302991b.
(25) Kapustin, E. A.; Lee, S.; Alshammari, A. S.; Yaghi, O. M. Molecular Retrofitting Adapts a Metal–Organic Framework to Extreme Pressure. *ACS Cent. Sci.* **2017**, *3* (6), 662–667. https://doi.org/10.1021/acscentsci.7b00169.
(26) Allen, C. A.; Boissonnault, J. A.; Cirera, J.; Gulland, R.; Paesani, F.; Cohen, S. M. Chemically Cross-linked Isoreticular Metal–Organic Frameworks. *Chemical Communications* **2013**, *49* (31), 3200. https://doi.org/10.1039/c3cc40635k.
(27) Zhang, Z.; Nguyen, H. T. H.; Miller, S. A.; Cohen, S. M. polyMOFs: A Class of Interconvertible Polymer-Metal-Organic-Framework Hybrid Materials. *Angewandte Chemie International Edition* **2015**, *54* (21), 6152–6157. https://doi.org/10.1002/anie.201502733.
(28) Geary, J.; Wong, A. H.; Xiao, D. J. Thermolabile Cross-Linkers for Templating Precise Multicomponent Metal–Organic Framework Pores. *J. Am. Chem. Soc.* **2021**, *143* (27), 10317–10323. https://doi.org/10.1021/jacs.1c04030.
(29) Opanasenko, M.; Dhakshinamoorthy, A.; Hwang, Y. K.; Chang, J.-S.; Garcia, H.; Čejka, J. Superior Performance of Metal–Organic Frameworks over Zeolites as Solid Acid Catalysts in the Prins Reaction: Green Synthesis of Nopol. *ChemSusChem* **2013**, *6* (5), 865–871. https://doi.org/10.1002/cssc.201300032.
(30) Wang, Z.; Babucci, M.; Zhang, Y.; Wen, Y.; Peng, L.; Yang, B.; Gates, B. C.; Yang, D. Dialing in Catalytic Sites on Metal Organic Framework Nodes: MIL-53(Al) and MIL-68(Al) Probed with Methanol Dehydration Catalysis. *ACS Appl. Mater. Interfaces* **2020**, *12* (47), 53537–53546. https://doi.org/10.1021/acsami.0c16559.

4.6 Supporting Information

1. General materials and methods.

Reagents and solvents were purchased from commercial vendors (Millipore Sigma, TCI America, Alfa Aesar, Fisher, Oakwood Chemical, Combi-Blocks) and used without purification unless otherwise noted. Deuterated solvents ($CDCl_3$, DMSO-d_6) were purchased from Cambridge Isotope Laboratories. NMR spectra were acquired on Bruker AV300, AV301, DRX499, or AV500 instruments. ^{1}H and ^{13}C NMR spectra were referenced to residual deuterated solvent peaks. High resolution mass spectrometry data of ligands and their intermediates were collected on a Thermo

Scientific LTQ Orbitrap XL instrument in positive ion mode. C, H, N combustion analysis was conducted by Atlantic Microlabs Inc.

Powder X-ray diffraction data were collected on either a Bruker D8 Discover powder X-ray diffractometer located in University of Washington's Molecular Analysis Facility, or a Bruker D2 PHASER benchtop diffractometer.

Gas Chromatography Mass Spectrometry data was collected on an Agilent 5973 GC-MS.

Infrared (IR) spectra were recorded on a FTIR Perkin Elmer Frontier (2 cm^{-1} resolution) instrument.

2. Ligand Syntheses.

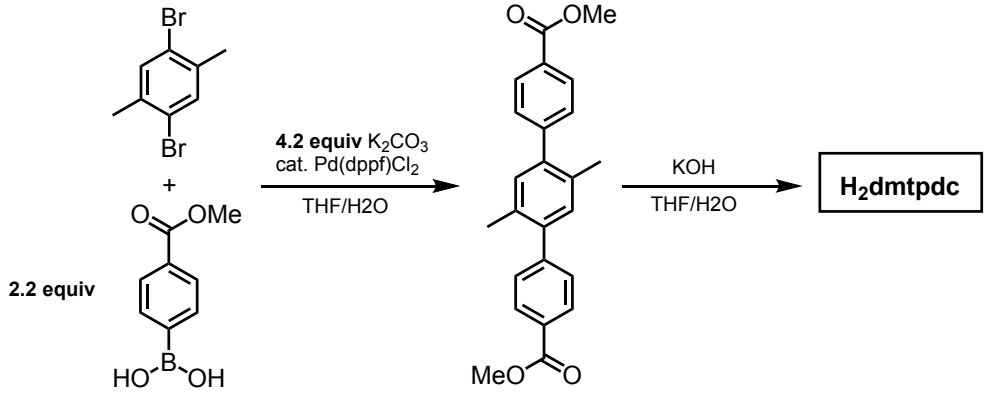

Scheme 4.S1. Overview of the synthesis of **H_2dmtpdc**.

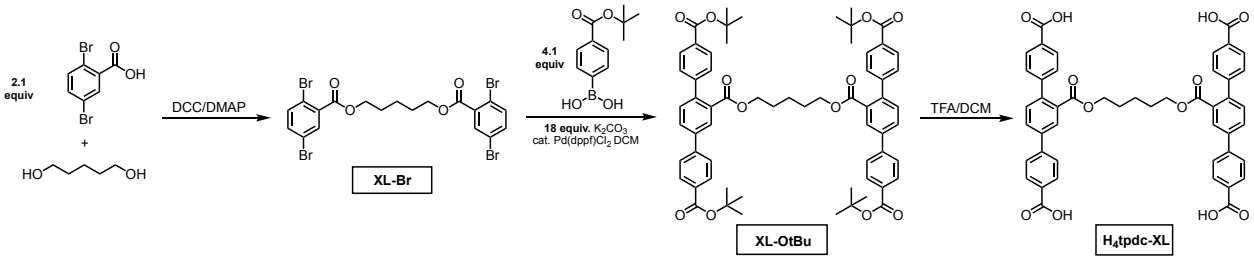

Scheme 4.S2. Overview of the synthesis of primary ester-based ligand dimer, **H_4tpdc-XL**.

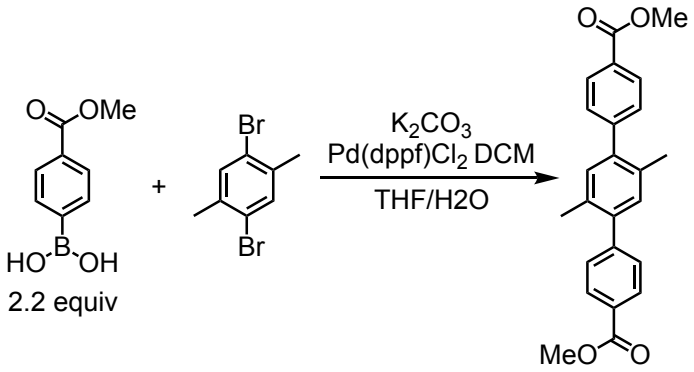

A 500 mL 2-neck round bottom flask equipped with a stir bar and reflux condenser was charged with 2,5-Dibromo-p-xylene (2.000 g, 7.58 mmol, 1 equiv.), 4-methoxycarbonylphenylboronic acid (2.976 g, 16.67 mmol, 2.20 equiv.), and K_2CO_3 (4.411 g, 31.84 mmol, 4.20 equiv.). Next, 200 mL THF followed by 50 mol deionized water were added. While stirring, the solution was purged with N_2 for 40 minutes. Subsequently, Pd(dppf)Cl_2 DCM (0.124 g, 0.15 mmol, 0.02 equiv.) was added under positive N_2 flow and the solution was stirred at 70 ºC for 18 h, during which time the solution

turned a dark brown. The reaction was cooled to room temperature and diluted with deionized water (50 mL) followed by 50 mL EtOAc. The organic layer was separated, and the aqueous layer extracted with EtOAc (2x50 mL). The combined organics were dried using $MgSO_4$, concentrated *in vacuo*, and the resultant brown residue subjected to filtration through a pad of silica gel (DCM). The pale yellow filtrate was concentrated *in vacuo* to give pale yellow solids. The solids were washed with n-hexanes to afford [1,1′:4′,1″-Terphenyl]-4,4″-dicarboxylic acid, 2′,5′-dimethyl-, 4,4″-dimethyl ester (2.280 g, 80 % yield) as an off-white solid, which was used without further purification. ^{1}H NMR (300 MHz, $CDCl_3$) δ 8.11 (d, J = 8.4 Hz, 4H), 7.45 (d, J = 8.4 Hz, 4H), 7.16 (s, 2H), 3.96 (s, 6H), 2.27 (s, 6H). This spectrum is consistent with what is reported in the literature.[1]

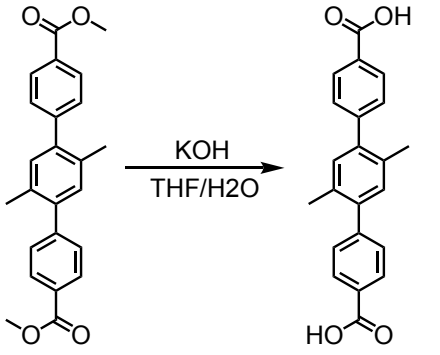

To a 500 mL round bottom flask charged with a stir bar, was added [1,1′:4′,1″-Terphenyl]-4,4″-dicarboxylic acid, 2′,5′-dimethyl-, 4,4″-dimethyl ester (1.965 g, 5.25 mmol, 1 equiv.) followed by 100 mL THF. Separately, KOH (5.834 g, 104.96 mmol, 20 equiv.) was dissolved in 100 mL deionized water. While stirring, the KOH solution was added to the round bottom flask. The reaction was then allowed to stir at 50 ºC overnight. The reaction was cooled to room temperature and acidified to pH= 1 using 1M HCl, resulting in white precipitate. The precipitate was then filtered, washed with water then n-hexanes, and allowed to dry in air, affording **H_2dmtpdc** (1.703

g, 95% yield) as a white solid which was used without further purification. ^{1}H NMR (500 MHz, DMSO-d_6): δ 12.99 (s, 2H), 8.02 (d, J = 8.3 Hz, 4H), 7.52 (d, J = 8.3 Hz, 4H), 7.20 (s, 2H), 2.24 (s, 6H). This spectrum is consistent with what is reported in the literature.[1]

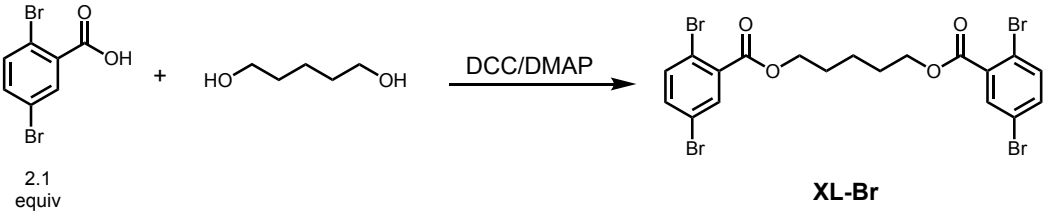

XL-Br

A 250 mL oven-dried Schlenk flask equipped with a stir bar was charged with 2,5-dibromobenzoic acid (2.849 g, 10.20 mmol, 2.10 equiv.), N,N'-dicyclohexylcarbodiimide (3.006 g, 14.57 mmol. 3.00 equiv.), 4-(dimethylamino)pyridine (1.246 g, 10.20 mmol, 2.10 equiv.) and anhydrous dichloromethane (150 mL), and the slurry was allowed to stir for 5 minutes. Next, 1,5-pentanediol (0.509 mL, 4.86 mmol, 1.00 equiv.) was added via syringe. The inhomogeneous solution was allowed to stir for 24 h, cooled to 0 °C, filtered over celite, and the organics washed with $NaHCO_3$ (1x100 mL) and HCl (1M, 1x120 mL). The organics were then dried over $MgSO_4$, filtered and concentrated *in vacuo* to afford a pale yellow oil. The oil was brought up in fresh hexanes and cooled to 0 °C overnight before filtration over celite and concentration to afford **XL-Br** as an oil which was used without further purification (2.33 g, 76% yield). ^{1}H NMR (300 MHz, $CDCl_3$): δ 7.89 (d, J = 2.4 Hz, 2H), 7.51 – 7.44 (m, 4H), 4.37 (t, J = 6.5 Hz, 4H), 1.86 (dt, J = 14.1, 6.8 Hz, 4H), 1.69 – 1.58 (m, 2H) ppm. This spectrum is consistent with what is reported in the literature.[2]

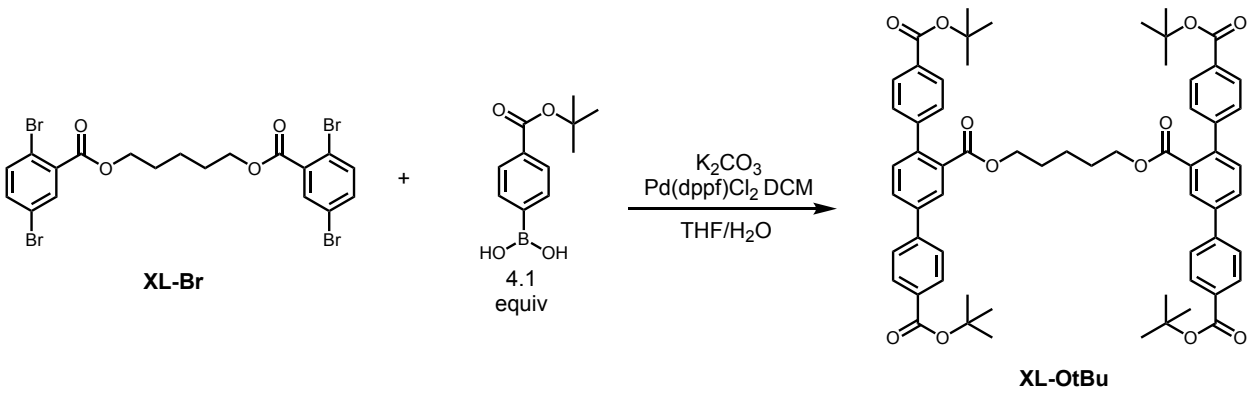

A 500 mL 2-neck round bottom flask equipped with a stir bar and reflux condenser under N_2 was charged with **XL-Br** (2.33 g, 3.71 mmol, 1.00 equiv.), tert-butyl 2-hydroxy-5-(4,4,5,5-tetramethyl-1,3,2-dioxaborolan-2-yl)benzoate (3.375 g, 15.21 mmol, 4.1 equiv.), K_2CO_3 (9.204 g, 66.6 mmol, 18.0 equiv.), THF (160 mL) and deionized water (40 mL). The solution was sparged with N_2 for 40 minutes, followed by addition of Pd(dppf)Cl_2 DCM (0.0906 g, 0.111 mmol, 0.0300 equiv.). The solution was heated to 60 °C for 16 h. The reaction mixture was cooled to room temperature, followed by addition of deionized water (250 mL) and EtOAc (250 mL). The organics were separated, and the aqueous layer extracted with EtOAc (2x100 mL). The combined organics were dried over $MgSO_4$, filtered, and concentrated in vacuo, and the resultant dark brown residue was subjected to filtration through a pad of silica gel (DCM), and the filtrate concentrated to afford **XL-OtBu** as an off white powder which was used without further purification (3.33 g, 88% yield). ^{1}H NMR (500 MHz, DMSO-d_6): δ 8.05 (s, 2H), 8.03 – 7.93 (m, 6H), 7.89 (d, J = 8.0 Hz, 4H), 7.84 (d, J = 8.0 Hz, 4H), 7.51 (d, J = 8.0 Hz, 2H), 7.37 (d, J = 8.0 Hz, 4H), 3.95 (t, J = 6.2 Hz, 4H), 1.56 (s, 18H), 1.51 (s, 18H), 1.23 – 1.14 (m, 4H), 0.65 (p, J = 8.0 Hz, 2H). ^{13}C NMR (75 MHz, DMSO-d_6) δ 167.40, 164.55, 144.51, 142.45, 139.92, 138.52, 131.55, 131.11, 130.70, 130.24, 129.68, 128.83, 128.24, 127.77, 126.75, 80.70, 80.58, 64.51, 27.70, 27.62, 27.26, 21.48. MS (ESI/ion trap) *m/*z: $[M+Na]^+$ $C_{63}H_{68}O_{12}Na$: 1039.5; found: 1039.5.

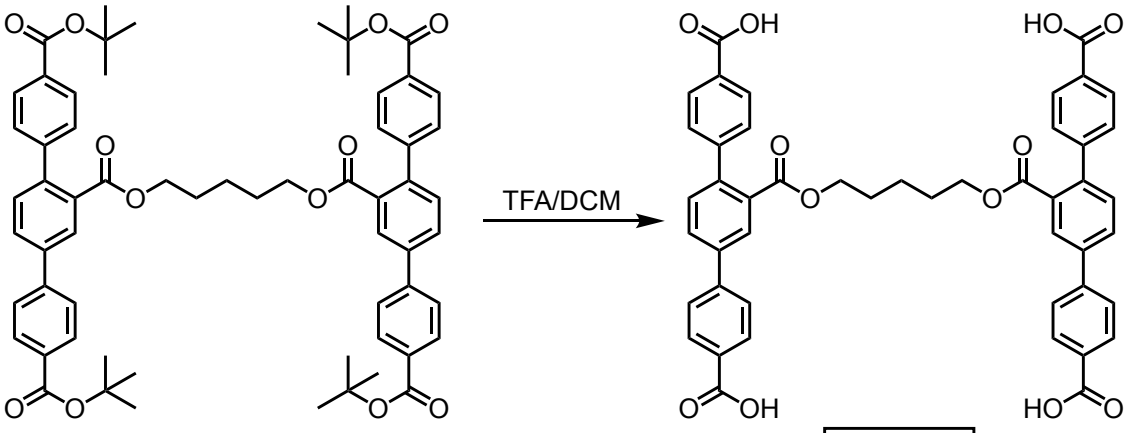

To a 100 mL round bottom flask equipped with a stir bar was added PE-L_5-O^{t}Bu (3.33 g, 3.28 mmol). The flask was cooled to 0 °C in an ice bath, followed by addition of DCM (30 mL) and concentrated trifluoroacetic acid (30 mL). The solution was removed from the ice bath and allowed to stir at room temperature for 2 h, during which time no solids precipitated out. After, the solution was diluted with hexanes (60 mL), the resultant inhomogeneous mix centrifuged, and the mother liquor decanted. The solids were washed with hexanes repeatedly to remove remaining acid and afford **H_4tpdc-XL** as an off-white solid (2.405 g, 93% yield). ^{1}H NMR (300 MHz, DMSO-*d_6*): δ 8.11 – 8.00 (m, 6H), 8.00 (d, *J* = 2.0 Hz, 1H), 7.95 (d, *J* = 8.4 Hz, 5H), 7.87 (d, *J* = 8.2 Hz, 4H), 7.54 (d, *J* = 8.0 Hz, 2H), 7.40 (d, *J* = 8.2 Hz, 0H), 3.95 (t, *J* = 6.1 Hz, 4H), 1.27 – 1.14 (m, 4H), 0.78 – 0.63 (m, 2H). ^{13}C NMR (75 MHz, DMSO) δ 167.62, 167.16, 167.10, 144.63, 142.60, 140.10, 138.67, 131.75, 131.24, 130.29, 130.13, 129.82, 129.30, 128.39, 127.93, 126.92, 64.71, 30.98, 27.39, 22.08, 21.73, 13.93. MS (ESI/ion trap) *m/*z: $[M+Na]^+$ $C47H_{36}O_{12}Na$: 815.8; found: 815.4.

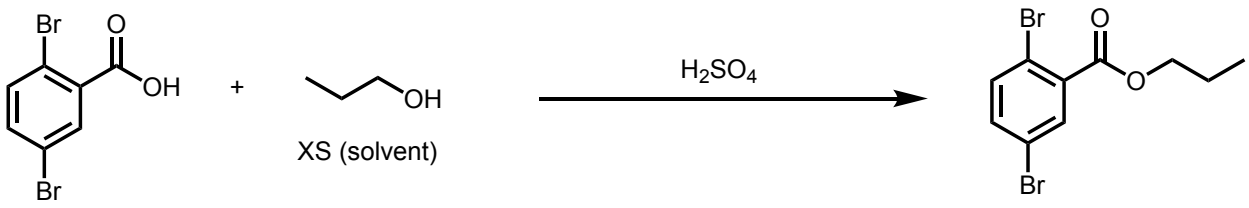

To a 50 mL 2-neck round bottom flask equipped with a stir bar and reflux condenser was added 2,5-dibromobenzoic acid (0.500 g, 1.79 mmol, 1.00 equiv.), 1-propanol (9.00 mL, 118.88 mmol, excess), and H_2SO_4 (0.125 mL, 2.33 mmol, 1.30 equiv.). The solution was refluxed at 100 ºC overnight. After evaporating off the majority of the 1-propanol (*ca*. 8 mL) and neutralizing with aqueous $NaHCO_3$, the product was extracted with EtOAc (2x 50 mL), dried over $MgSO_4$, filtered, and concentrated in vacuo to afford propyl 2,5-dibromobenzoate as a yellow oil which was used without further purification (0.54 g, 94%). The procedure was repeated once and the combined products carried forward in the next step. ^{1}H NMR (300 MHz, $CDCl_3$) δ 7.90 (d, *J* = 2.4 Hz, 1H), 7.52 (d, *J* = 8.5 Hz, 1H), 7.43 (dd, *J* = 8.5, 2.4 Hz, 1H), 4.30 (t, *J* = 6.7 Hz, 2H), 1.80 (h, *J* = 7.2 Hz, 2H), 1.04 (t, *J* = 7.4 Hz, 3H).

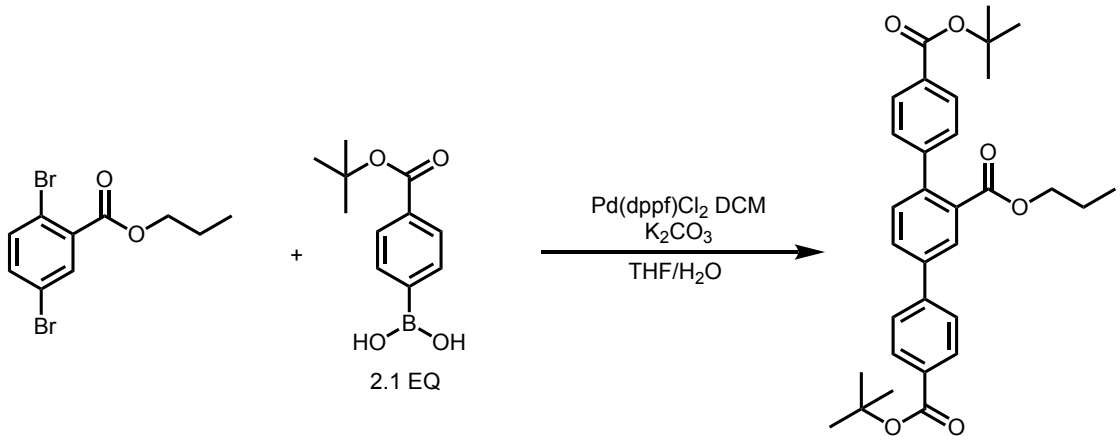

Propyl-OtBu

To a 250 mL 2-neck round bottom flask equipped with a stir bar and reflux condenser under N_2 was added propyl 2,5-dibromobenzoate (1.14 g, 3.54 mmol, 1.00 equiv.), (4-(*tert*-butoxycarbonyl)phenyl)boronic acid (1.65 g, 7.43 mmol, 2.10 equiv.), K_2CO_3 (1.96 g, 14.16

mmol, 4.00 equiv.), THF (120 mL) and H_2O (30 mL). The solution was sparged for 45 minutes with N_2, then Pd(dppf)Cl_2 DCM (0.058 g, 0.07 mmol, 2.00 mol%) was added and the solution was heated at 60 ºC for 18 h. The reaction mixture was cooled to room temperature, followed by addition of deionized water (250 mL) and EtOAc (250 mL). The organics were separated, and the aqueous layer extracted with EtOAc (2x100 mL). The combined organics were dried over $MgSO_4$, filtered, and concentrated in vacuo, and the resultant dark brown residue was subjected to filtration through a pad of silica gel (3:1 DCM/EtOAc), and the filtrate concentrated to afford **Propyl-OtBu** as a pale yellow oil which was used without further purification (1.82 g, quantitative). ^{1}H NMR (300 MHz, $CDCl_3$) δ 8.15 – 7.99 (m, 5H), 7.79 (dd, *J* = 8.0, 2.0 Hz, 1H), 7.70 (d, *J* = 8.4 Hz, 2H), 7.45 (d, *J* = 8.0 Hz, 1H), 7.40 (d, *J* = 8.4 Hz, 2H), 4.05 (t, *J* = 6.7 Hz, 2H), 1.46 (h, J=7.2 Hz, 2H), 0.74 (t, *J* = 7.4 Hz, 3H).

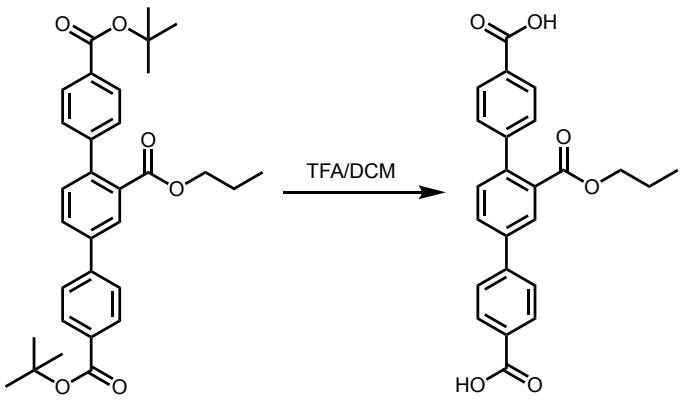

Propyl-OtBu **H_2tpdc-propyl**

To a 100 mL roundbottom flask equipped with a stir bar was added **Propyl-OtBu** (1.82 g, 3.54 mmol) The flask was cooled to 0 °C in an ice bath, followed by addition of DCM (15 mL) and concentrated trifluoroacetic acid (15 mL). The solution was removed from the ice bath and allowed to stir at room temperature for 2 h, during which time no solids precipitated out. After, the solution was diluted with hexanes (30 mL), the resultant inhomogeneous mix centrifuged, and the mother liquor decanted. The solids were washed with hexanes repeatedly to remove remaining acid and

afford **H_2tpdc-propyl** as an off-white solid (1.41 g, 98% yield). ^{1}H NMR (500 MHz, DMSO) δ 8.10 (d, *J* = 2.0 Hz, 1H), 8.07 (d, *J* = 8.3 Hz, 2H), 8.02 (dd, *J* = 9.3, 7.6 Hz, 3H), 7.91 (d, *J* = 8.3 Hz, 2H), 7.60 (d, *J* = 8.0 Hz, 1H), 7.47 (d, *J* = 8.2 Hz, 2H), 3.99 (t, *J* = 6.5 Hz, 2H), 1.46 – 1.31 (m, 2H), 0.62 (t, *J* = 7.4 Hz, 3H). ^{13}C NMR (75 MHz, DMSO) δ 167.77, 167.18, 167.09, 144.63, 142.62, 140.08, 138.71, 131.88, 131.27, 130.31, 130.15, 129.84, 129.33, 128.43, 127.84, 126.96, 66.57, 21.11, 10.05. MS (ESI/ion trap) *m/z*: $[M-H]^-$ $C_{24}H_{19}O_6$: 403.1. Found: 403.3.

3. Synthesis and characterization of frameworks

3.1 General procedure for Al(OH)tpdc-XL-R% frameworks

Al(OH)tpdc-XL-R% frameworks were synthesized using an adapted procedure from the literature.[3] A 20 mL scintillation vial was charged with 0.063*(100-**x**%) mmol H2dmtpdc and 0.063***x**% mmol **H_4-PE-L_5** to give a total of 0.063 mmol ligand. $AlCl_3 \cdot 6H_2O$ (1.00 equiv. per dmtpdc unit) was then added, followed by N,N-dimethylformamide (10.0 mL). The threads of the scintillation vial were wrapped with PTFE tape, capped, and taped with black electrical tape to prevent solvent evaporation. The vial was sonicated to dissolve all solids and afford a pale-yellow solution. The solution was then heated in a dry bath at 120 °C for 16 h, after which the vial was cooled to room temperature, the mother liquor was decanted, and the solids re-immersed in fresh DMF and heated to 120 °C. After 3 h the mother liquor was syringed off and replaced with fresh DMF. This process was repeated a total of three times, then the material was filtered and partially dried on filter paper, to afford DMF-solvated material. Powder X-ray diffraction measurements and digestion ^{1}H NMRs were taken of the DMF-solvated material. For full list of reaction conditions with metal salt and ligand ratios, as well as predicted and observed percentages of cross-linked dmtpdc, see Table S1. Reactions were scaled batch-wise. The parent framework was synthesized in a similar manner.

In a typical MOF digestion experiment to quantify ligand ratios, ~10–15 mg of DMF-solvated material was suspended in 0.50 mL of DMSO-d6, followed by addition of 30 drops of TFA using a 5 ¾" Pasteur pipette. The solution was sonicated briefly and allowed to sit overnight to fully dissolve. ^{1}H NMR spectra were taken of the dissolved solution.

3.2 Syntheses of parent and cross-linked frameworks.

Synthesis of Al(OH)dmtpdc

A 20 mL scintillation vial equipped with PTFE tape was charged with **H_2dmtpdc** (0.050 g, 0.144 mmol, 1.00 equiv.) and $AlCl_3 \cdot 6H_2O$ (0.035 g, 0.144 mmol, 1.00 equiv.). The general procedure shown above (see Section 3.1) was followed. Anal. Calc. for $Al(C_{22}H_{17}O_5)(H_2O)_{1.5}(C_3H_7NO)_{0.4}$: C, 62.67; H, 5.17; N, 1.26. Found: C, 62.24; H, 4.87; N, 1.10.

Synthesis of Al(OH)tpdc-XL-100%

A 20 mL scintillation vial equipped with PTFE tape was charged with **H_4-PE-L_5** (0.0499 g, 0.063 mmol, 1.00 equiv.) and $AlCl_3 \cdot 6H_2O$ (0.0304 g, 0.126 mmol, 2.00 equiv.). The general procedure shown above (see Section 3.1) was followed. The ratio of cross-linked tdc^{2-} to total tdc^{2-} was 100% as determined by ^{1}H NMR of digested samples. Anal. Calc. for $Al(C_{23.5}H_{17}O_7)(H_2O)_{0.8}$: C, 62.34; H, 4.14. Found: C, 62.02; H, 3.99.

Synthesis of Al(OH)tpdc-XL-46%

A 20 mL scintillation vial equipped with PTFE tape was charged with **H_4-PE-L_5** (0.0165 g, 0.021 mmol, 0.33 equiv.), H_2dmtpdc (0.0144 g, 0.042 mmol. 0.66 equiv.), and $AlCl_3 \cdot 6H_2O$ (0.020 g, 0.083 mmol, 1.32 equiv.). The general procedure shown above (see Section 3.1) was followed. The ratio of cross-linked tdc^{2-} to total tdc^{2-} was 47% as determined by ^{1}H NMR of digested

samples. Anal. Calc. for $Al(C_{22.95}H_{17}O_{6.28})(H_2O)_{1.0}(C_3H_7NO)_{0.05}$: C, 62.78; H, 4.41; N, 0.16. Found: C, 62.79; H, 4.30; N, 0.14.

Synthesis of Al(OH)tpdc-XL-21%

A 20 mL scintillation vial equipped with PTFE tape was charged with **H_4-PE-L_5** (0.007 g, 0.009 mmol, 0.143 equiv.), H_2dmtpdc (0.0187 g, 0.054 mmol. 0.857 equiv.), and $AlCl_3 \cdot 6H_2O$ (0.017 g, 0.072 mmol, 1.14 equiv.). The general procedure shown above (see Section 3.1) was followed. The ratio of cross-linked tdc^{2-} to total tdc^{2-} was 21% as determined by ^{1}H NMR of digested samples. Anal. Calc. for $Al(C_{22.52}H_{17}O_{5.69})(H_2O)_{1.0}(C_3H_7NO)_{0.1}$: C, 63.60; H, 4.61; N, 0.33. Found: C, 63.68; H, 4.55; N, 0.25.

Synthesis of Al(OH)tpdc-XL-9%

A 20 mL scintillation vial equipped with PTFE tape was charged with **H_4-PE-L_5** (0.003 g, 0.004 mmol, 0.067 equiv.), H_2dmtpdc (0.020 g, 0.059 mmol. 0.933 equiv.), and $AlCl_3 \cdot 6H_2O$ (0.015 g, 0.067 mmol, 1.07 equiv.). The general procedure shown above (see Section 3.1) was followed. The ratio of cross-linked tdc^{2-} to total tdc^{2-} was 9% as determined by ^{1}H NMR of digested samples. Anal. Calc. for $Al(C_{22.25}H_{17}O_{5.33})(H_2O)_{0.5}(C_3H_7NO)0_{.05}$: C, 65.73; H, 4.52; N, 0.17. Found: C, 65.35; H, 4.56; N, 0.17.

4. Sample activation and gas sorption analysis.

4.1 Activation of parent Al(OH)(dmtpdc) and cross-linked materials.

DMF-solvated samples were filtered to a powder. The samples were then transferred to a pre-massed glass tube and subjected to drying under flowing N_2 at 100 °C overnight. After the initial N_2 purge, samples were capped with a Transeal and transferred to a Micromeritics Smart VacPrep instrument and heated under vacuum at 100 °C overnight. Note that the initial N_2 purge step was

critical; framework collapse was occasionally observed if solvated samples were immediately placed under vacuum.

4.2 N_2 adsorption measurements.

For all gas adsorption measurements, ~100 mg of sample was transferred to a pre-massed glass sample tube. Low-pressure N_2 adsorption experiments (up to 1 bar) were performed using a Micromimetics 3Flex Surface Characterization Analyzer. Ultrahigh purity N2 (5.0 grade, 99.999%) was used in all adsorption experiments. N_2 adsorption measurements were performed using a liquid N_2 bath (77 K). BET surface areas were calculated using data points between 0.02 and 0.08 P/P0. In all cases, the following BET consistency criteria were followed: 1) the pressure range has values of $v(P_0 - P)$ increasing with P/P_0 , and 2) positive y intercept.[4] All correlation coefficients were ≥0.999.

5. Computational details.

Extended structures of Al(OH)dmtpdc were created using Al(OH)bpdc as a starting point, followed by geometry optimization using the Forcite module in Materials Studio. The relative energies of two different configurations of the cross-linker within the pore channels were probed by density functional theory (DFT) using the Gaussian 16 program. The periodic structure obtained in Materials Studio was truncated to just two ligand struts, and a bridging cross-linker was added. The oxygens of the peripheral phenyl groups on the two ligands were frozen and only the central phenyl ring and bridging cross-linker were allowed to freely remove, mimicking the geometric constraints of the MOF lattice. The geometries of the cross-linker and central phenyl ring were optimized at the B3LYP/6-31+G(d) level of theory with empirical dispersion correction (D3BJ) and solvent correction via a polarization continuum model using acetonitrile as the solvent. Frequency calculations were performed at this same level of theory to confirm that the final

geometry was at a stationary point. Free energy corrections were determined at the B3LYP/6-31+G(d) level of theory at 298.15 K. Single point energies were computed at the B3LYP/6-311+G(d, p) level of theory with empirical dispersion correction (D3BJ) and solvent correction via polarization continuum using methanol as the solvent. All molecular structures were rendered in Diamond.

6. Catalysis of the Prins reaction between β-(-)-pinene and formaldehyde

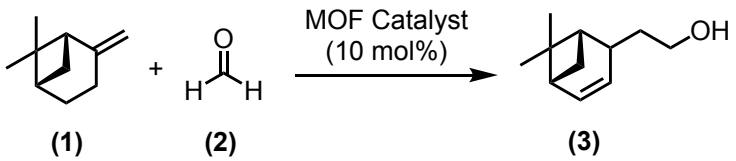

Scheme 4.S3. Prins reaction of β-(-)-pinene (1) and formaldehyde (2) to yield nopol (3).

6.1 General reaction procedure:

MOF catalysts were synthesized according to the general procedure described in section 3 and activated according to the procedure described in section 4.1. β-(-)-pinene (0.4 mmol, 63.0 μL), paraformaldehyde (0.8 mmol, 24.0 mg), MOF catalyst (10 mol% ca. based on bridging hydroxy groups), dodecane (75.0 μL) as an internal standard, and acetonitrile (unless indicated otherwise) (3.0 mL) as a solvent were combined. The solution was sonicated for 2-3 min before stirring at 80°C (unless indicated otherwise) for 5h. The reaction mixture was then filtered to separate the catalyst.

7. Supplementary tables.

Table 4.S1 | Summary of relative equivalents of metal salt and ligand used to synthesize parent Al(OH)dmtpdc and cross-linked Al(OH)tpdc-XL-R% frameworks, including the predicted and observed percentages of cross-linked $tpdc^{2-}$ to total $tpdc^{2-}$ in the framework (R%).

	Al^{3+} salt[1] (equiv)	**Cross-linked ligand** (equiv)	**H_2dmtpdc** (equiv)	**Predicted**[2] **R%** (%)	**Observed**[3] **R%** (%)

Al(OH)dmtpdc	1.00	0	1.00	0%	0%
Al(OH)tpdc-XL-R%	1.07	0.067	0.933	12.5%	9%
	1.14	0.143	0.857	25%	21%
	1.32	0.33	0.67	50%	47%
	2.00	1.00	0	100%	100%

[1] 2.5 equivalents of $AlCl_3 \cdot 6(H_2O)$ were added per $tpdc^{2-}$ unit. Note that each ligand dimer contains two $tpdc^{2-}$ units.
[2] The predicted percentage of cross-linked $tpdc^{2-}$ relative to the total amount of $tpdc^{2-}$ ligands in the framework.
[3] Observed percentages were determined by ^{1}H NMR characterization of frameworks digested in TFA/DMSO-d_6.

Table 4.S2 | Summary of BET and Langmuir surface areas of parent Al(OH)dmtpdc and cross-linked Al(OH)tpdc-XL-R% frameworks reported in this work. BET surface areas were calculated using data points between 0.02 and 0.08 P/P_0. In all cases, the following BET consistency criteria were followed: 1) the pressure range has values of $v(P_0–P)$ increasing with P/P_0, and 2) positive y intercept.[4] All correlation coefficients were ≥0.999.

	Langmuir SA (m^2/g)	**BET SA** (m^2/g)	**BET *y* intercept**	**BET Correlation Coefficient (R^2)**
Al(OH)dmtpdc	920 ± 7	645 ± 18	0.00009	0.9994
Al(OH)tpdc-XL-9%	2230 ± 12	1330 ± 20	0.00005	0.9994
Al(OH)tpdc-XL-21%	2400 ± 15	1420 ± 20	0.00005	0.9997
Al(OH)tpdc-XL-46%	2780 ± 27	1640 ± 26	0.00005	0.9993
Al(OH)tpdc-XL-100%	3080 ± 44	1870 ± 24	0.00004	0.9996

Table 4.S3 | Summary of optimized 'open-pore' structure unit cell parameters compared with Pawley refined parameters

Cell parameter	**Forcite optimized structure**	**Pawley refined**
a	6.61[a]	6.77 ± 0.08
b	28.94	29.02 ± 0.28
c	24.56	24.71 ± 0.22

[a] This value is fixed to 6.61 Å, consistent with the structure of MIL-53(Al).[5]

Table 4.S4 | Summary of electronic energies, free energy corrections, and final Gibbs free energies obtained from DFT calculations for the symmetric and offset cross-linker configurations. Calculations were performed at B3LYP/6-311+G(d,p)//B3LYP/6-31+G(d) with D3BJ dispersion correction and solvent correction (methanol).

	Down-pore configuration	**Cross-pore configuration**
Electronic energy (Hartrees)	-2716.4737	-2716.4485
Free energy correction at 298.15 K (Hartrees)	0.4914	0.4890
G^0 at 298.15 K (Hartrees)	-2175.9820	-2175.9595

G^0 at 298.15 K (kcal/mol)	-1702920.9	-1702906.6

Table 4.S5 | DFT optimized structure of the "down-pore" cross-linker configuration.

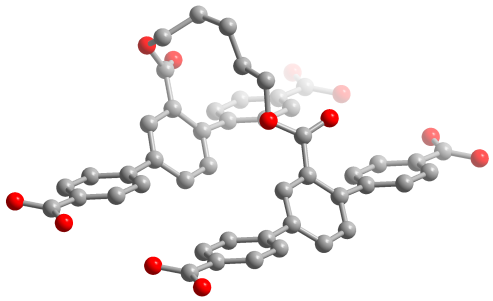

Symbol	X	Y	Z	H	5.423683	-5.018779	-1.708831
C	-5.031199	-3.638185	-1.557277	C	1.425658	-2.775231	-0.961964
H	-5.623729	-4.465378	-1.931444	C	0.720206	-3.721382	-0.211251
C	-3.638046	-3.728526	-1.516852	H	1.272687	-4.476612	0.337907
H	-3.149254	-4.633464	-1.852243	C	-0.678164	-3.713872	-0.141826
C	-2.872834	-2.656053	-1.035422	C	-1.355453	-4.740323	0.72169
C	-3.517464	-1.482579	-0.618393	O	7.719108	-4.381353	-0.951071
H	-2.933896	-0.661182	-0.214838	C	5.706863	-3.02785	-0.919225
C	-4.908627	-1.385539	-0.669643	C	7.178175	-3.143425	-0.834184
H	-5.358113	-0.476122	-0.281589	O	-7.795035	-3.36864	-1.405281
C	-1.395233	-2.748349	-0.908341	C	-4.548051	2.895616	-0.702261
C	-0.66822	-1.766166	-1.595081	H	-5.14093	2.072124	-1.082541
H	-1.214271	-1.010677	-2.151484	C	-3.154908	2.805286	-0.661819
C	0.720315	-1.762813	-1.617188	H	-2.664191	1.897555	-0.997646
O	-7.69362	-1.109467	-1.107039	C	-2.38972	3.877752	-0.180357
C	-5.681365	-2.462995	-1.138888	C	-3.034309	5.051216	0.236636
C	-7.152708	-2.34741	-1.223903	H	-2.450334	5.874712	0.635312
O	7.820497	-2.122189	-0.652803	C	-4.425467	5.148285	0.185363
C	5.05668	-1.852632	-0.500844	H	-4.874837	6.060443	0.567204
H	5.647216	-1.02757	-0.118245	C	-0.912994	3.763873	-0.102123
C	3.663513	-1.762299	-0.541254	C	-0.182944	4.786623	-0.718553
H	3.170121	-0.864749	-0.180804	H	-0.723072	5.588958	-1.211422
C	2.898305	-2.834845	-1.022683	C	1.206549	4.788122	-0.727376
C	3.542954	-4.008263	-1.439695	O	-7.210474	5.424335	-0.252019
H	2.953455	-4.844543	-1.80361	C	-5.198219	4.070818	-0.283871
C	4.934079	-4.105264	-1.388441	C	-6.669557	4.186396	-0.368885

O	8.303658	4.411609	0.202217	O	-2.465087	-5.162224	0.462236
C	5.539833	4.681223	0.354178	O	-0.671343	-5.281161	1.795629
H	6.130021	5.507749	0.734056	C	-0.170665	-4.392449	2.829404
C	4.146662	4.771522	0.31378	C	-1.326499	-3.788982	3.64204
H	3.654274	5.670878	0.671163	C	-1.070304	-2.321685	4.003172
C	3.381444	3.698917	-0.167643	C	-1.093961	-1.422029	2.761686
C	4.026105	2.525539	-0.584672	H	1.256476	-1.002181	-2.176958
H	3.439434	1.692379	-0.959096	H	1.748164	5.597909	-1.207175
C	5.41723	2.428544	-0.533425	H	-1.341417	0.580642	3.589669
H	5.907944	1.517225	-0.858331	H	0.323018	-0.058623	3.65893
C	1.906358	3.72641	-0.150541	H	0.454223	-3.620666	2.37461
C	1.190594	2.687266	0.466129	H	0.471649	-5.029342	3.438752
H	1.731409	1.890863	0.965819	H	-1.495121	-4.384425	4.545738
C	-0.206493	2.699158	0.531789	H	-2.249274	-3.853495	3.052506
C	-0.910152	1.763407	1.477686	H	-0.096622	-2.231641	4.505649
O	8.202259	2.152452	-0.096051	H	-1.824529	-1.984573	4.724603
C	6.190015	3.505956	-0.064207	H	-2.105724	-1.382562	2.339271
C	7.661326	3.39038	0.020835	H	-0.44416	-1.832185	1.981538
O	-7.311884	3.165164	-0.550261	H	9.172533	2.246381	-0.037858
O	-2.000719	2.060769	1.936448	H	8.689404	-4.287025	-0.892662
O	-0.217014	0.639277	1.836216	H	-6.522379	6.109755	-0.254155
C	-0.597765	-0.024218	3.068948	H	-7.005876	-0.424033	-1.099047

Table 4.S6 | DFT optimized structure of the "cross-pore" configuration.

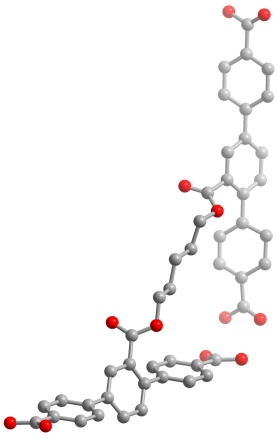

Symbol	**X**	**Y**	**Z**	H	-11.097103	-3.733883	2.048246
O	-13.218471	-4.637513	-1.246948	C	-9.8384	-2.257333	1.182431
C	-11.658277	-3.324863	-0.029231	H	-9.255794	-2.144723	2.091546
C	-12.792041	-4.32263	-0.148127	C	-9.508115	-1.506362	0.044677
C	-10.911687	-3.150279	1.150262	C	-10.249333	-1.678402	-1.133185

H	-9.98363	-1.114763	-2.022345	C	4.579618	-0.913053	0.242137
C	-11.314245	-2.579308	-1.171174	O	-1.278666	5.165536	1.219324
H	-11.880296	-2.723756	-2.084767	C	-2.812321	3.872427	0.06997
C	-8.33528	-0.595558	0.02689	C	-1.705086	4.85059	0.120518
C	-7.041937	-1.101481	0.194767	C	-3.558904	3.69788	-1.109524
H	-6.896334	-2.164667	0.357556	H	-3.29664	4.263792	-1.997185
O	-13.212606	-4.780586	1.05692	C	-4.632212	2.804893	-1.141685
C	-8.503158	0.774547	-0.218685	H	-5.205048	2.674737	-2.054984
C	3.570389	3.640698	-1.113293	C	-4.962603	2.053922	-0.003894
H	3.260156	4.241109	-1.960794	C	-4.221277	2.225999	1.173928
C	4.687843	2.725365	-1.198425	H	-4.477514	1.654407	2.061377
H	5.290026	2.557283	-2.080129	C	-3.156347	3.12684	1.211907
C	4.920167	2.034744	0.081241	H	-2.588123	3.264866	2.125052
C	4.148007	2.206283	1.290956	C	-6.103688	1.119561	-0.064113
H	4.427289	1.622662	2.161652	C	-7.399927	1.621616	-0.24295
C	3.073572	3.103039	1.328419	H	-7.537301	2.690697	-0.375043
C	6.087438	1.119444	0.064149	O	13.213284	-4.63589	-1.296161
C	7.385751	1.641124	-0.039421	C	11.657375	-3.323431	-0.072642
H	7.520673	2.71799	-0.078746	C	12.790828	-4.321068	-0.195789
C	8.494645	0.799246	-0.073972	O	1.283589	5.295357	-0.941339
O	-1.242346	5.344762	-1.054387	O	3.675114	-0.613056	-0.714029
C	-5.924286	-0.259818	0.109375	C	2.441389	-1.3649	-0.733924
C	-4.581455	-0.907125	0.262653	C	1.28318	-0.534994	-0.215754
O	1.234367	5.200786	1.337191	C	-0.001527	-1.336418	-0.415339
C	2.790042	3.811484	0.154657	C	-1.285814	-0.535679	-0.211421
C	1.703907	4.8508	0.114171	C	-2.446833	-1.36697	-0.721551
O	13.21591	-4.778957	1.007697	O	4.383622	-1.689108	1.159133
C	10.91526	-3.148939	1.109623	O	-3.678693	-0.613804	-0.700375
H	11.103871	-3.733114	2.006609	O	-4.380488	-1.689357	1.17563
C	9.841892	-2.256124	1.145789	H	2.573102	-2.282389	-0.157368
H	9.262498	-2.143575	2.056832	H	2.294985	-1.616464	-1.787354
C	9.507279	-1.505195	0.009275	H	1.235422	0.407449	-0.775708
C	10.244126	-1.677144	-1.171342	H	1.435382	-0.28378	0.840855
H	9.97689	-1.11058	-2.058333	H	-0.000048	-2.210508	0.249521
C	11.3091	-2.57792	-1.213296	H	-0.003247	-1.732006	-1.441521
H	11.872401	-2.721116	-2.12875	H	-1.24138	0.405379	-0.773984
C	8.332801	-0.590373	0.026709	H	-1.43282	-0.281728	0.845296
C	7.039899	-1.112393	0.12881	H	-2.576895	-2.281968	-0.140683
H	6.896056	-2.186053	0.19861	H	-2.304134	-1.623255	-1.77445
C	5.921158	-0.268222	0.108726	H	2.485329	3.180947	2.236424

H	-0.328301	5.702038	-0.915003	H	12.833347	-4.254386	1.728841
H	1.831722	4.884366	2.033537	H	9.492667	1.220278	-0.154298
H	-12.82772	-4.255676	1.776573	H	-9.501902	1.177908	-0.358162

Table 4.S7 | Summary of reaction conditions and conversion values of Nopol over Al(OH)dmtpdc and Al(OH)tpdc-XL-100% as catalysts.

Catalyst	Solvent	Temperature (°C)	Conversion (%)[1]
Al(OH)dmtpdc	Acetonitrile	80	< 1
Al(OH)tpdc-XL-100%	Acetonitrile	80	18.84
Al(OH)dmtpdc	Toluene	80	< 1
Al(OH)tpdc-XL-100%	Toluene	80	8.53
Al(OH)dmtpdc	*p*-xylene	120	1.05
Al(OH)tpdc-XL-100%	*p*-xylene	120	5.17

All reactions were run with β-(-)-pinene (0.4 mmol, 63.0 μL), paraformaldehyde (0.8 mmol, 24.0 mg), MOF catalyst (10 mol% ca. based on bridging hydroxy groups), dodecane (75.0 μL) as an internal standard, and 3.0 mL of solvent for 5h.
[1] The observed conversion values were determined by GCMS.

8. Supplementary figures.

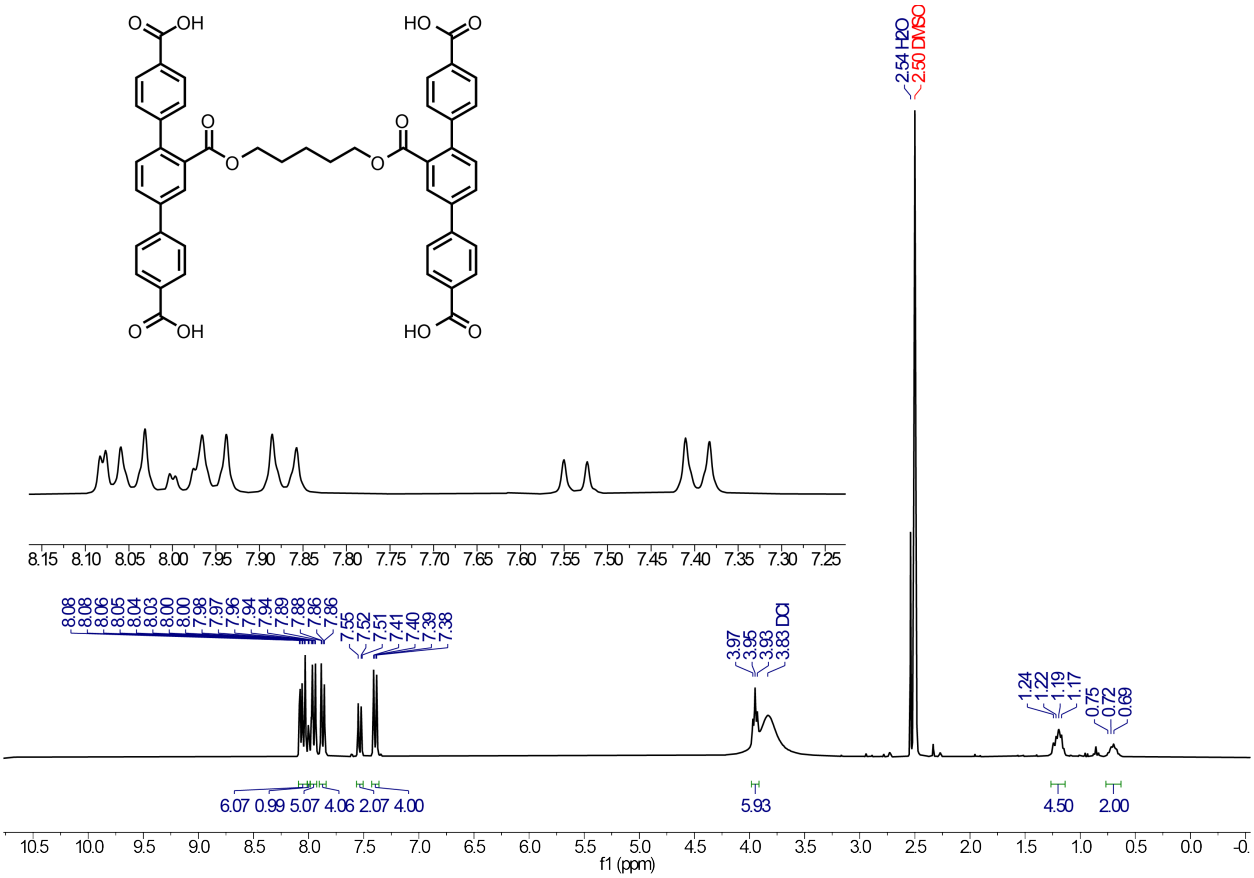

Fig. 4.S1 | Proton NMR of final ligand, **H_4tpdc-XL**.

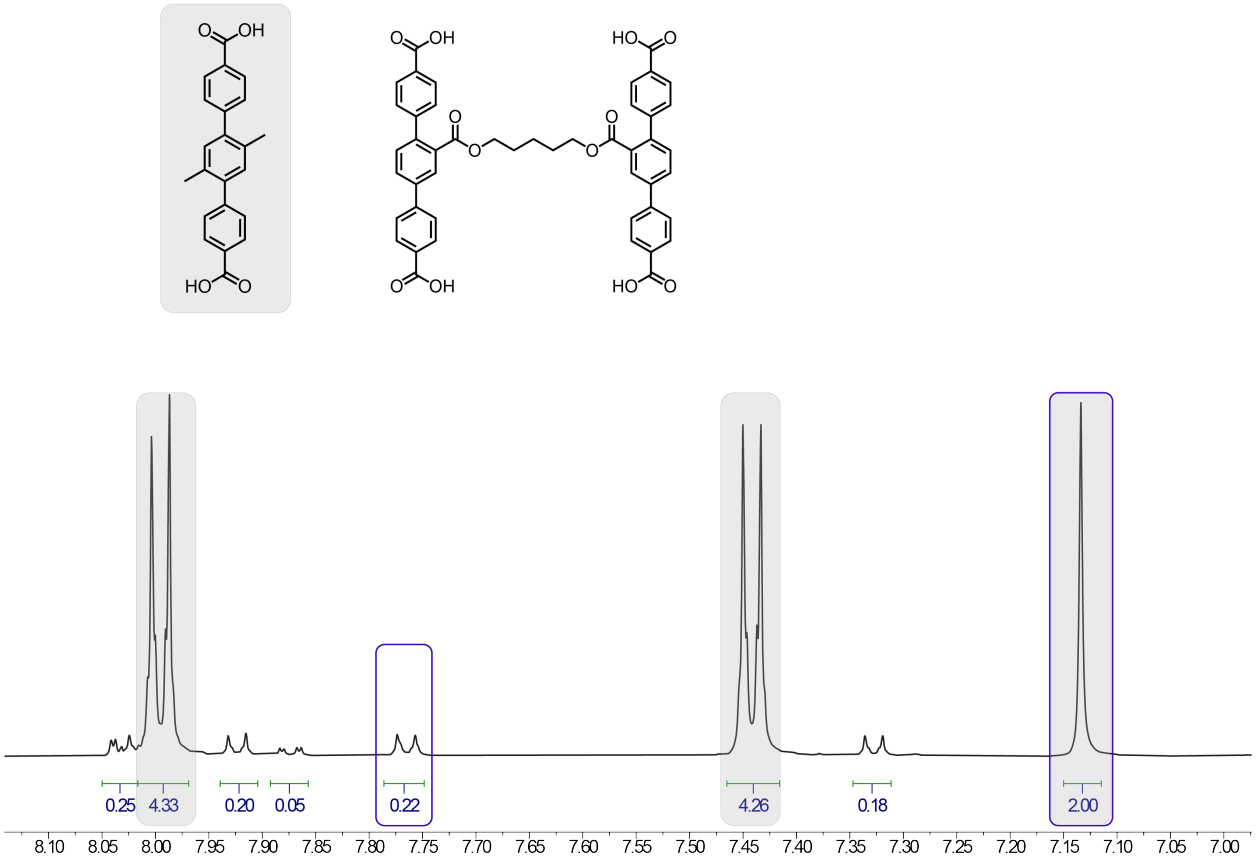

Fig. 4.S2 | Digestion ^{1}H NMR of **Al(OH)tpdc-XL-9%** in DMSO-d_6/DCl. The relative ratio of 0.22/2.00 observed between cross-linked tpdc^{2-} doublet at 7.76 ppm (2H per cross-linked tpdc^{2-} unit) and H_2dmtpdc singlet at 7.12 ppm (2H) corresponds to a percentage of 9%.

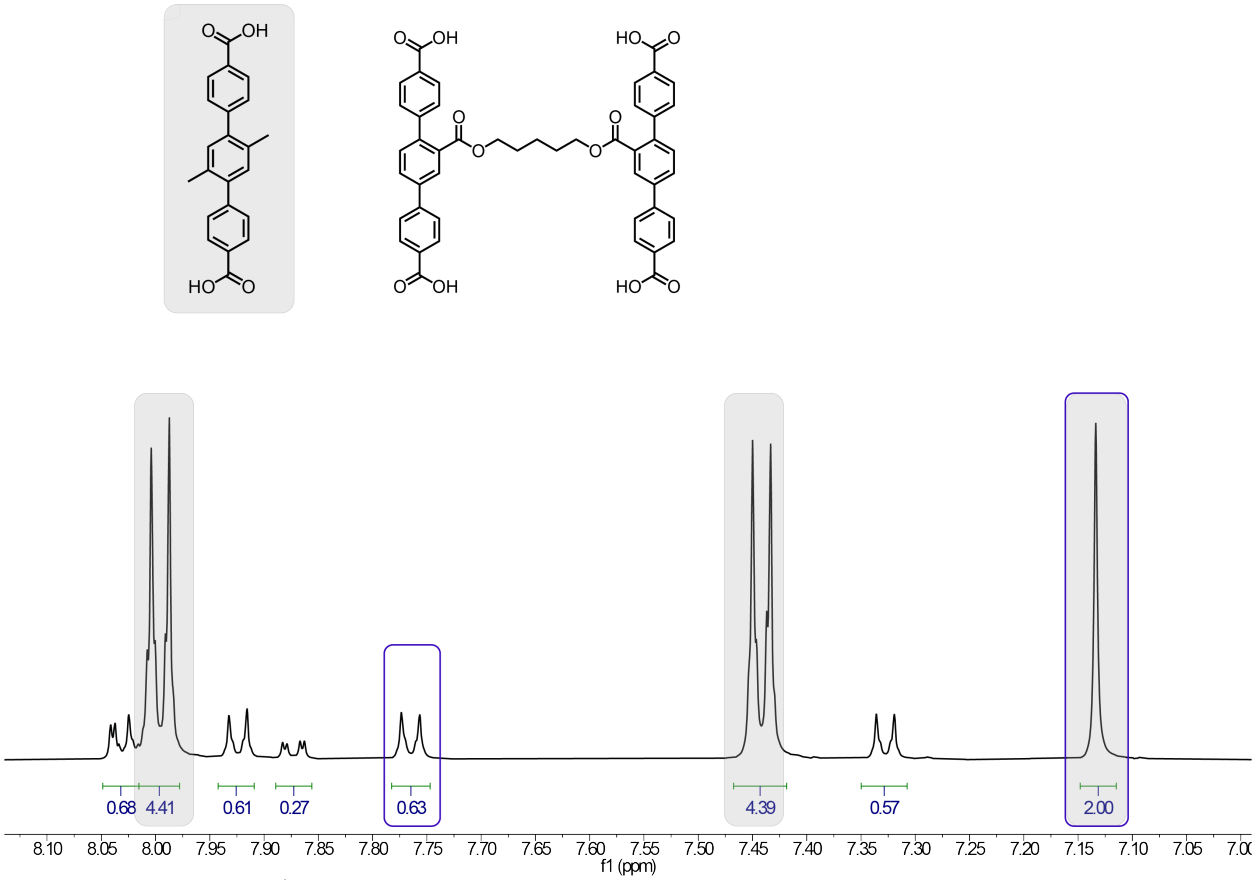

Fig. 4.S3 | Digestion ^{1}H NMR of **Al(OH)tpdc-XL-21%** in DMSO-d_6/DCl. The relative ratio of 0.63/2.00 observed between cross-linked $tpdc^{2-}$ doublet at 7.76 ppm (2H per cross-linked $tpdc^{2-}$ unit) and H_2dmtpdc singlet at 7.12 ppm (2H) corresponds to a percentage of 21%.

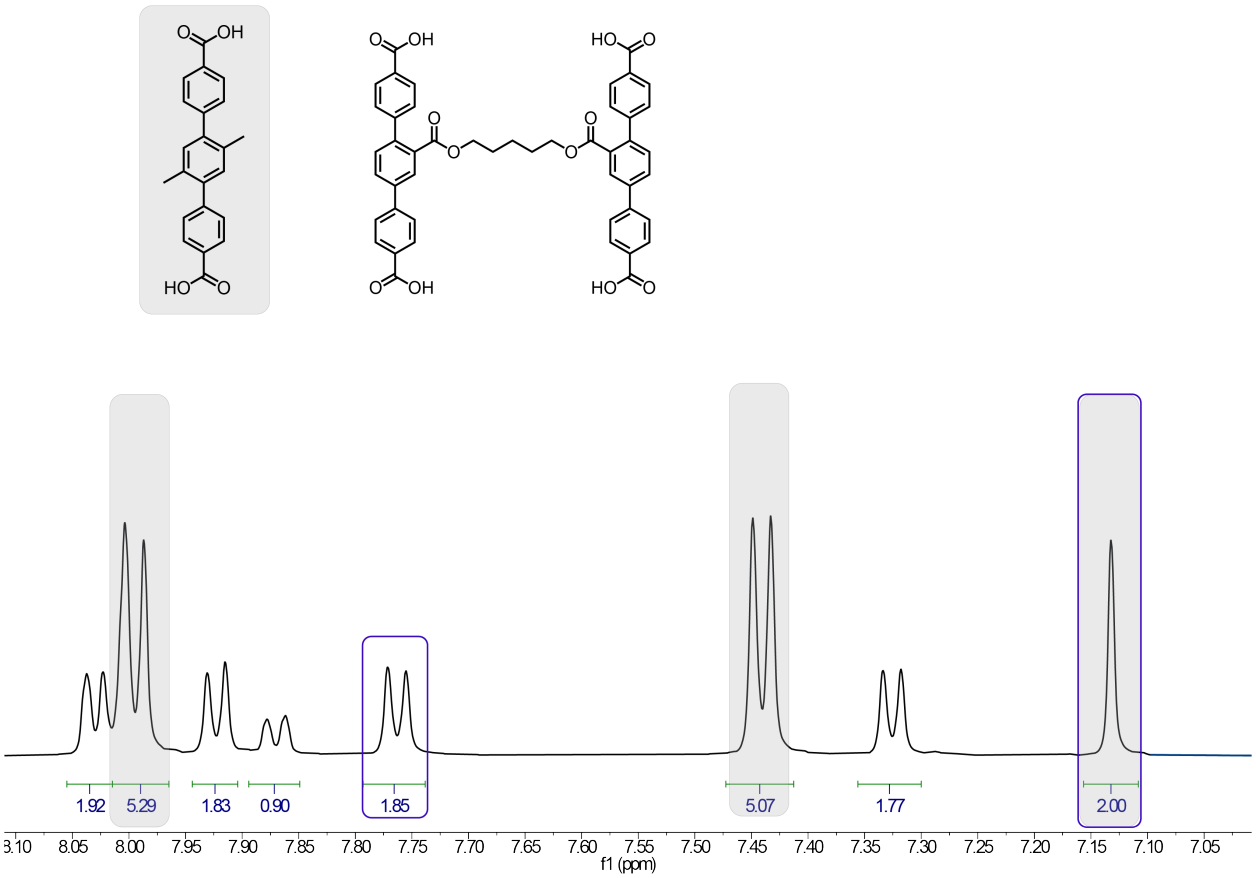

Fig. 4.S4 | Digestion ^{1}H NMR of **Al(OH)tpdc-XL-46%** in DMSO-d_6/DCl. The relative ratio of 1.85/2.00 observed between cross-linked $tpdc^{2-}$ doublet at 7.76 ppm (2H per cross-linked $tpdc^{2-}$ unit) and H_2dmtpdc singlet at 7.12 ppm (2H) corresponds to a percentage of 46%.

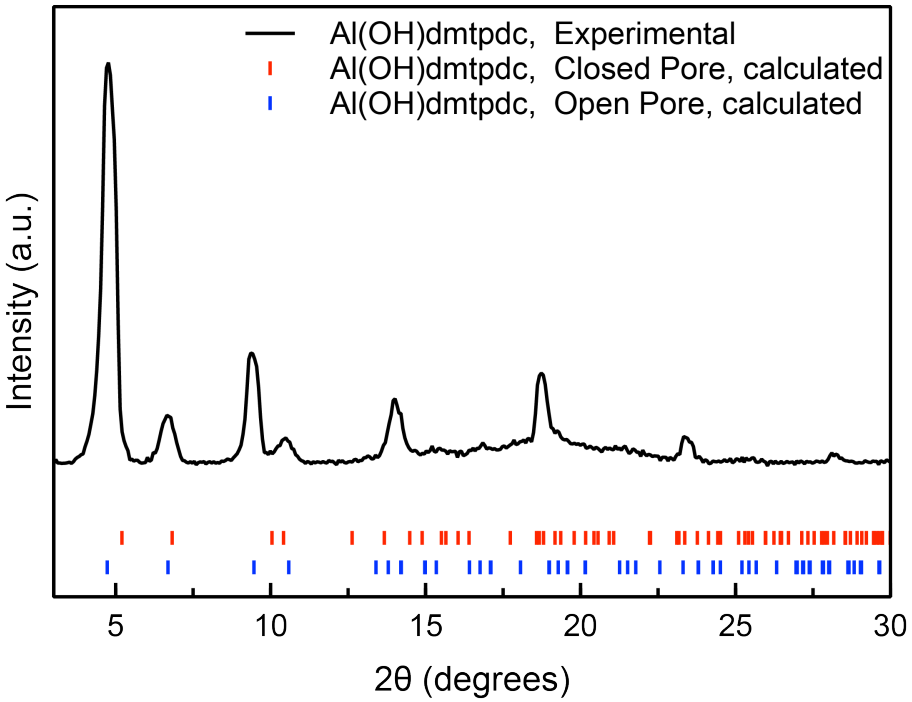

Fig. 4.S5 | Powder X-ray diffraction patterns for parent **Al(OH)dmtpdc** framework stacked with the calculated patterns for both the open and closed pore structures. The unit cell parameters for the closed form of Al(OH)dmtpdc were estimated based off of the closed form of MIL-53, and lengthening it to accommodate the larger terphenyl ligand.

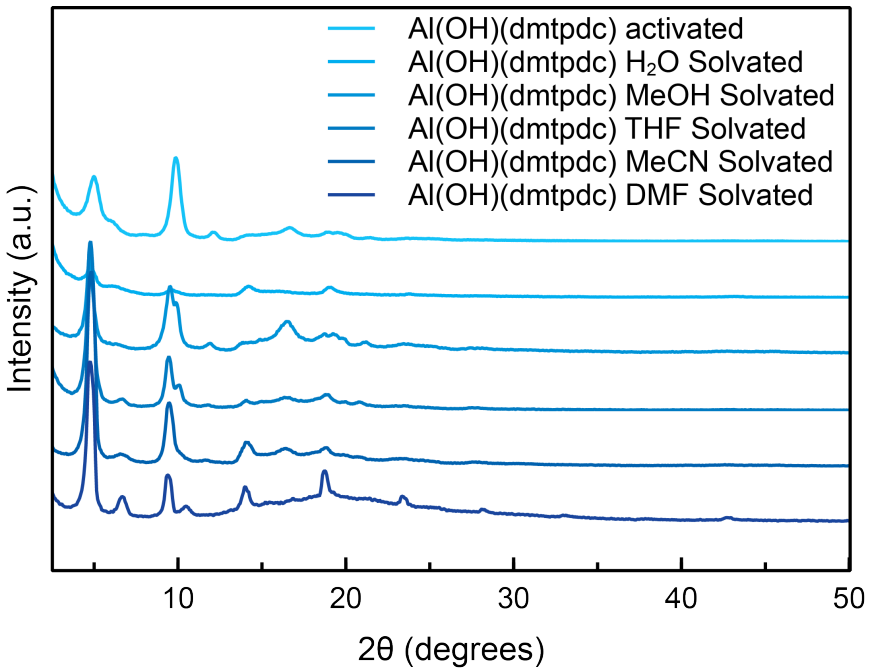

Fig. 4.S6 | Powder X-ray diffraction patterns for parent **Al(OH)dmtpdc** framework under different solvent conditions. Solvent exchanges were performed by doing 3x 3h soaks in specified solvents.

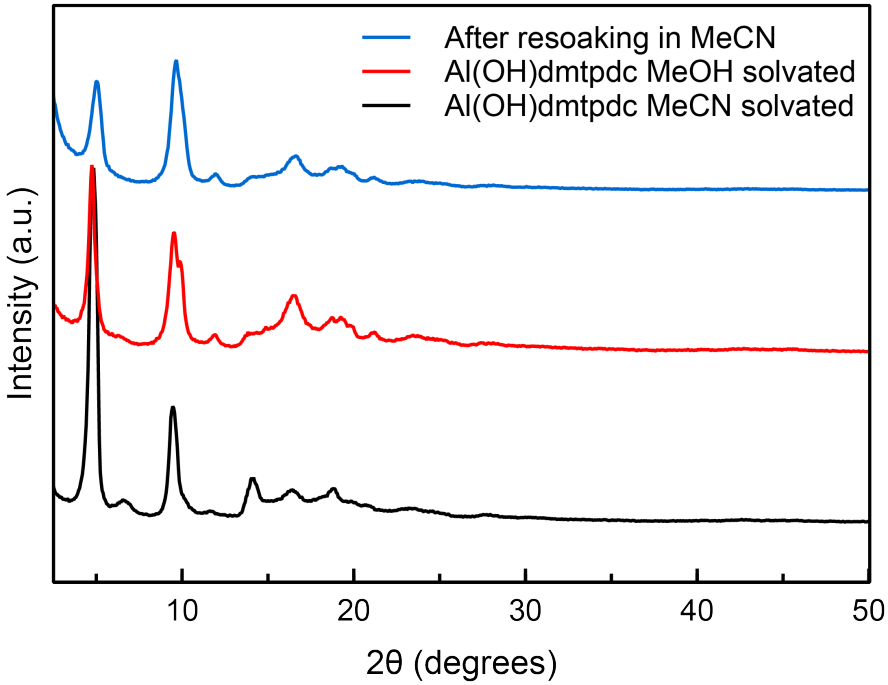

Fig. 4.S7 | Powder X-ray diffraction patterns for parent **Al(OH)dmtpdc** solvated first with MeOH then resolvated in MeCN.

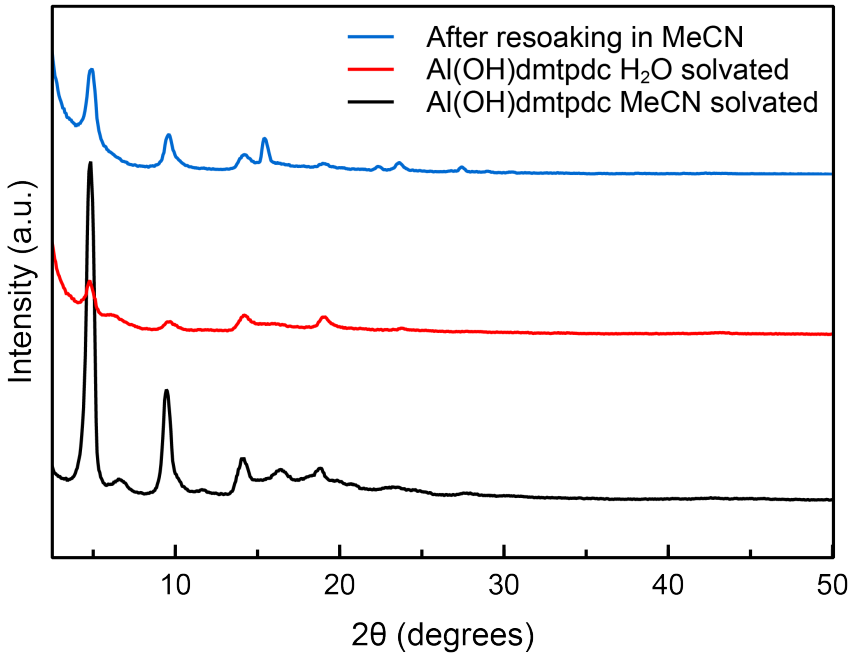

Fig. 4.S8 | Powder x-ray diffraction patterns for parent **Al(OH)dmtpdc** solvated first with H_2O then resolvated in MeCN.

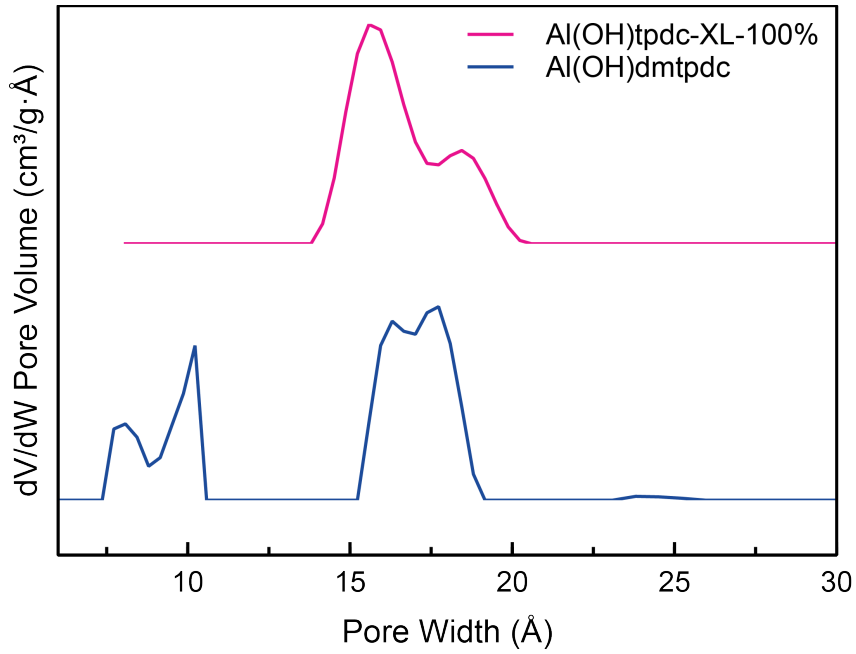

Fig. 4.S9 | DFT Pore size distribution for **Al(OH)dmptdc** (bottom trace) and **Al(OH)tpdc-XL-100%** (top trace)

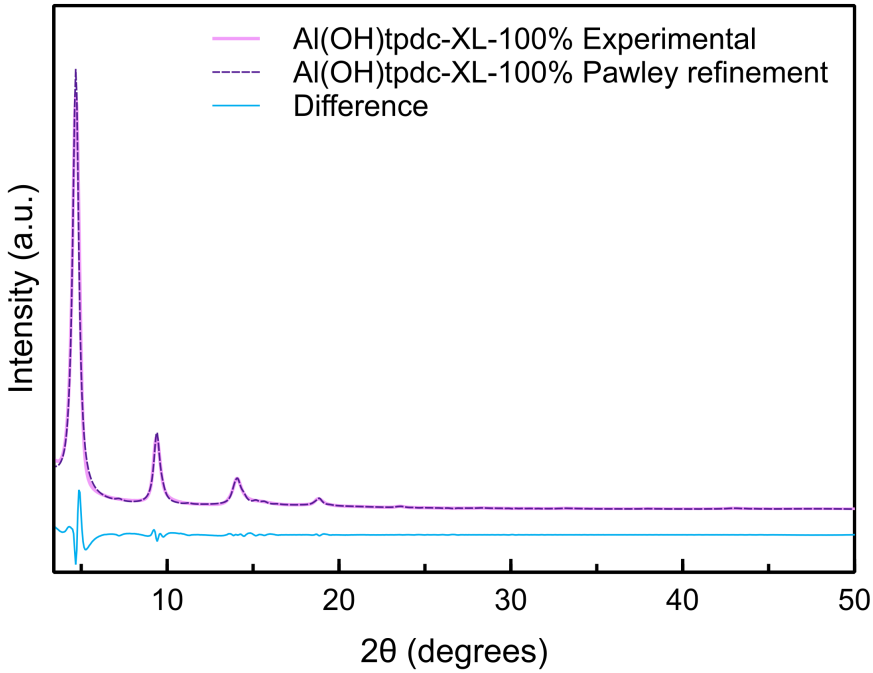

Fig. 4.S10 | Pawley refinement for **Al(OH)tpdc-XL-100%**. Experimental data is shown in purple, while the fit is shown in black. The difference is shown in light blue.

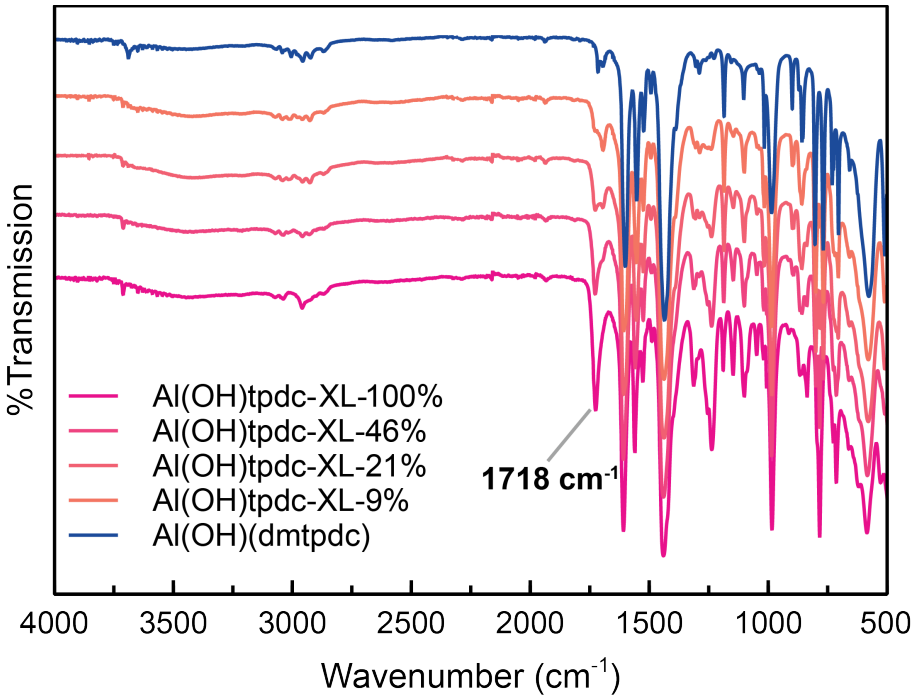

Fig 4.S11 | FT-IR data for parent **Al(OH)dmtpdc** and cross-linked **Al(OH)tpdc-XL-R%** series. The growth in of the carbonyl feature at 1718 cm^{-1} corresponds to increasing incorporation of the cross-linker.

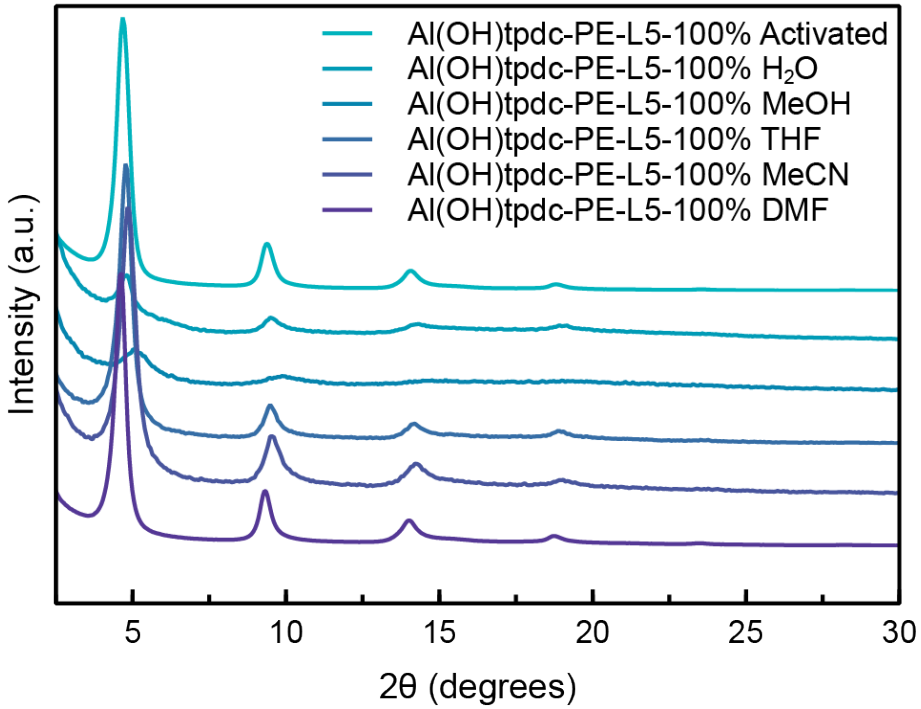

Fig. 4.S12 | Powder X-ray diffraction patterns for **Al(OH)tpdc-XL-100%** framework under different solvent conditions. Solvent exchanges were performed by doing 3x 3h soaks in specified solvents.

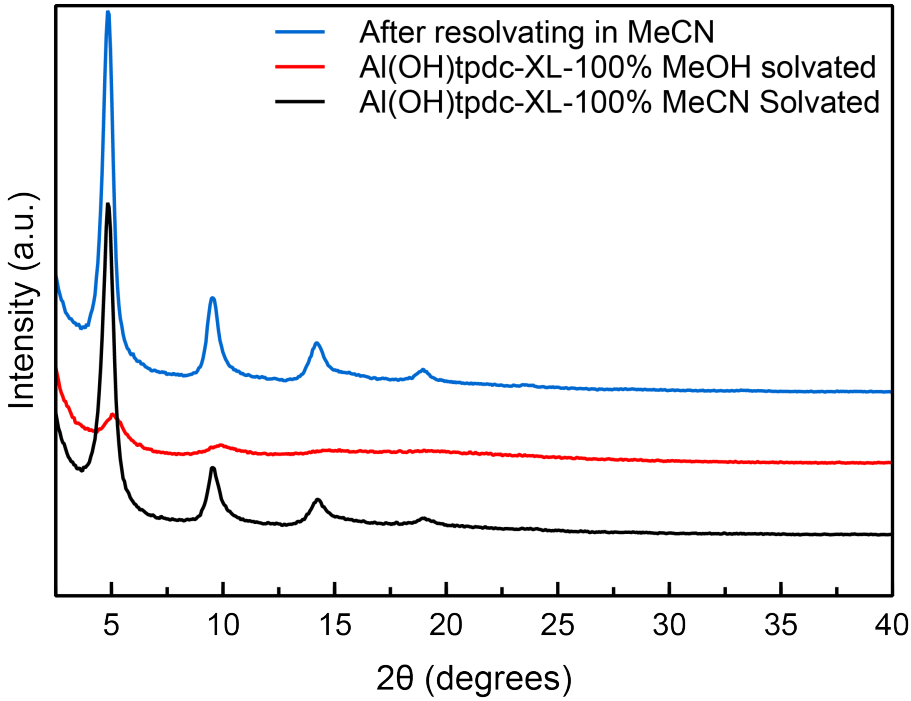

Fig. 4.S13 | Powder X-ray diffraction patterns for **Al(OH)tpdc-XL-100%** solvated first in MeOH (red) then resolvated in MeCN (blue).

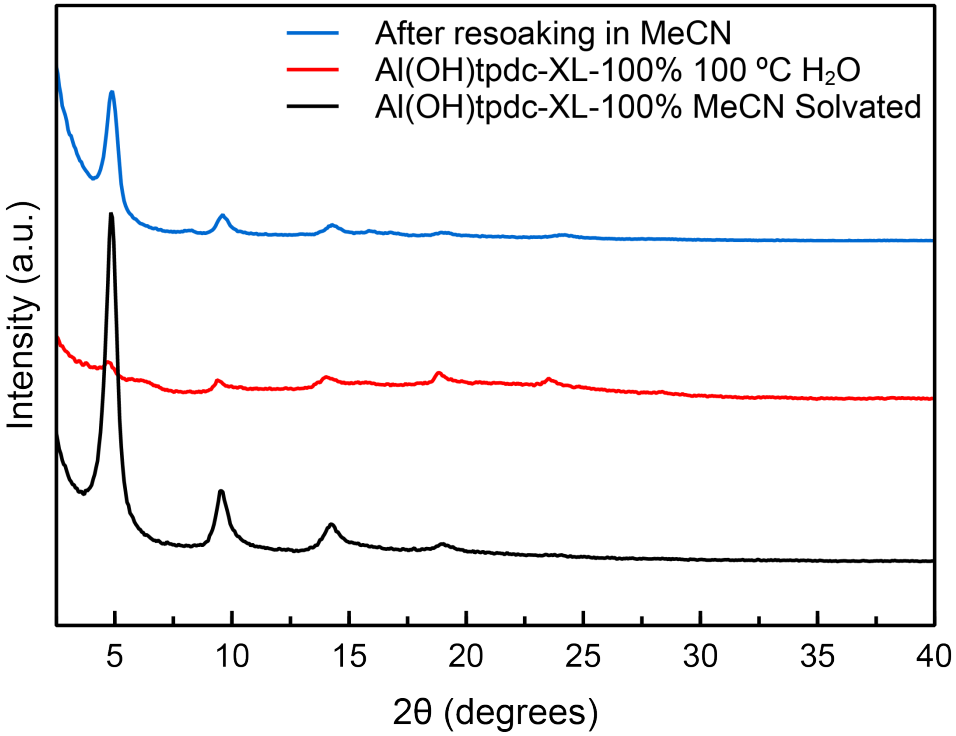

Fig 4.S14 | Powder X-ray diffraction patterns for **Al(OH)tpdc-XL-100%** solvated first in 100 ºC H_2O (red) then resolvated in MeCN (blue).

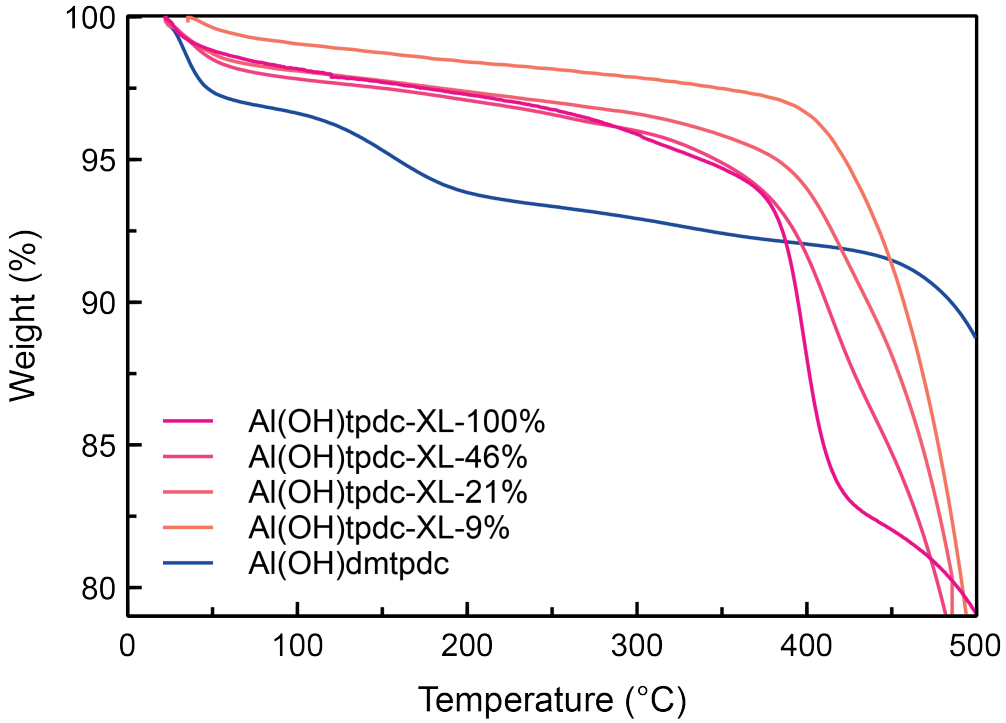

Fig. 4.S15 | Thermogravimetric analysis of parent **Al(OH)dmtpdc** and cross-linked **Al(OH)tpdc-XL-R%** series. The mass losses between 50 ºC and 150 ºC for the parent framework are attributed to solvent loss in the pores due to incomplete activation.

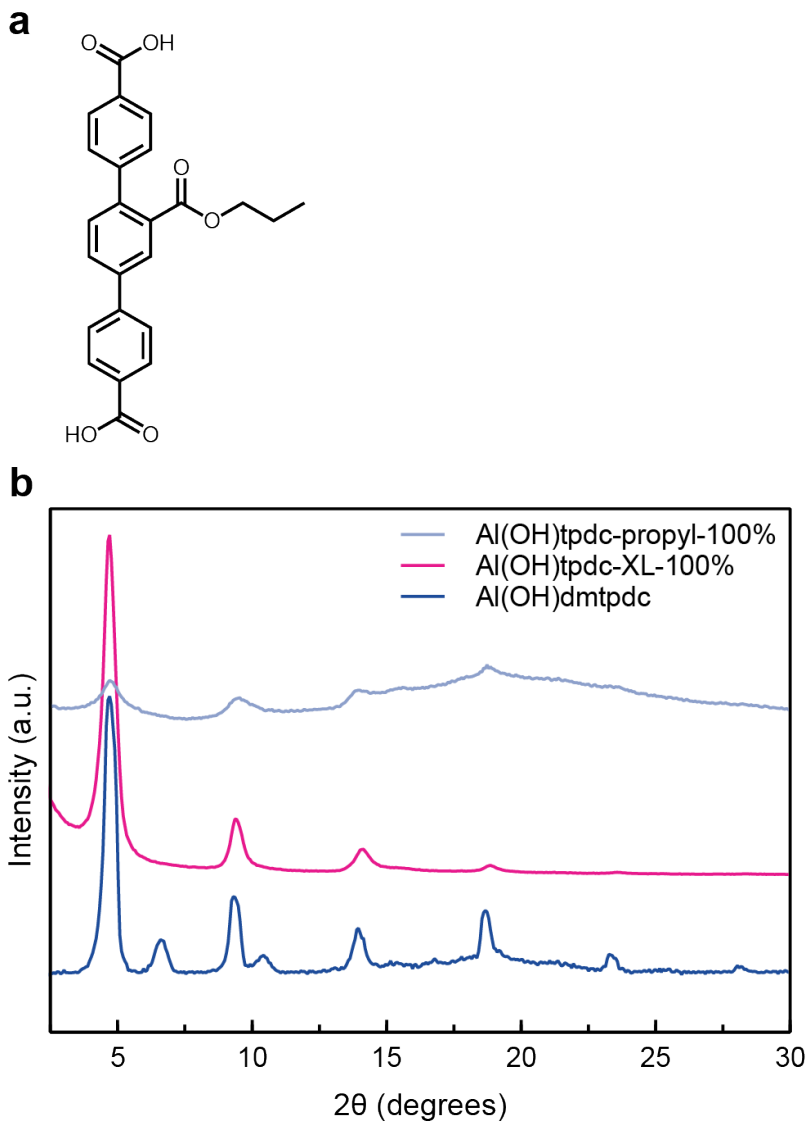

Fig. 4.S16 | (a) Structure of propyl control ligand, **H_2tpdc-propyl** and (b) powder X-ray diffraction patterns for **Al(OH)tpdc-propyl-100%** (top trace) compared to **Al(OH)tpdc-XL-100%** and **Al(OH)dmtpdc** (middle and bottom traces, respectively).

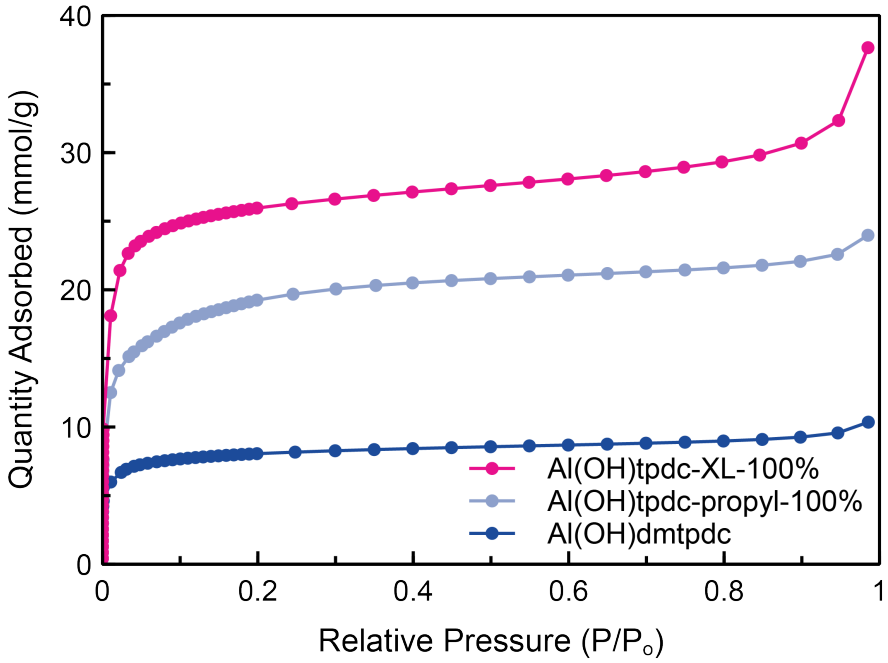

Fig. 4.S17 | N_2 adsorption data at 77K for **Al(OH)tpdc-propyl-100%** compared to **Al(OH)tpdc-XL-100%** and **Al(OH)dmtpdc**.

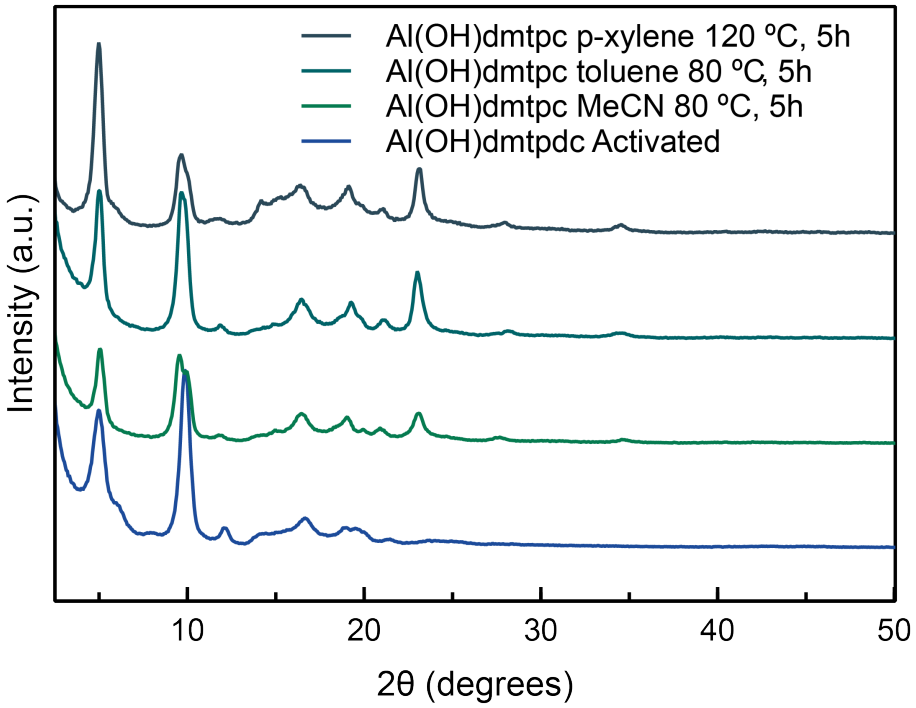

Fig. 4.S18 | Powder X-ray diffraction patterns for **Al(OH)dmtpdc** after catalysis.

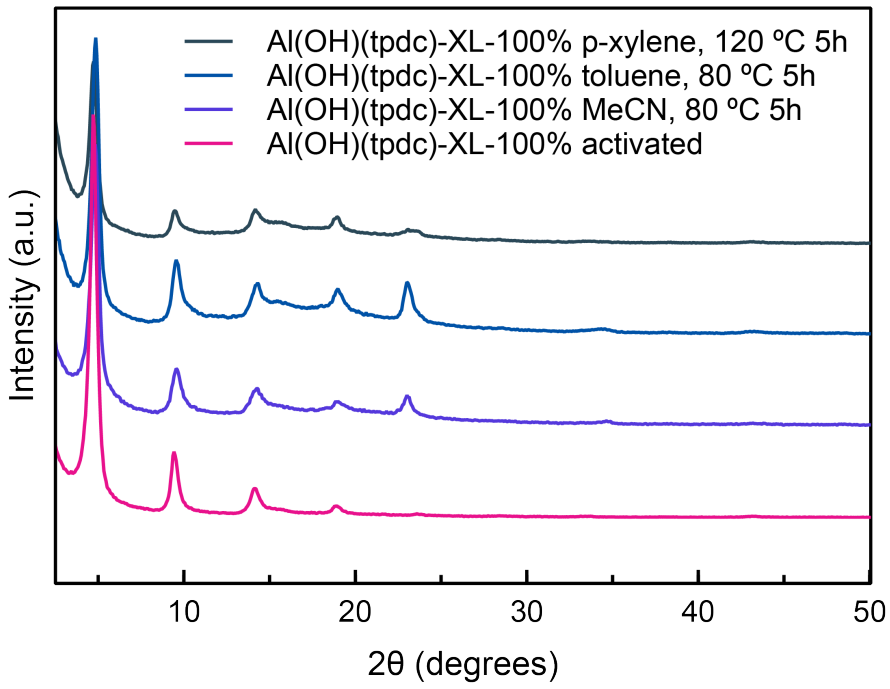

Fig. 4.S19 | Powder X-ray diffraction patterns for **Al(OH)tpdc-XL-100%** after catalysis.

9. References.

(1) Zhang, W.-Q.; Li, Q.-Y.; Zhang, Q.; Lu, Y.; Lu, H.; Wang, W.; Zhao, X.; Wang, X.-J. Robust Metal–Organic Framework Containing Benzoselenadiazole for Highly Efficient Aerobic Cross-Dehydrogenative Coupling Reactions under Visible Light. *Inorg. Chem.* **2016**, *55* (3), 1005–1007. https://doi.org/10.1021/acs.inorgchem.5b02626.

(2) Geary, J.; Wong, A. H.; Xiao, D. J. Thermolabile Cross-Linkers for Templating Precise Multicomponent Metal–Organic Framework Pores. *J. Am. Chem. Soc.* **2021**, *143* (27), 10317–10323. https://doi.org/10.1021/jacs.1c04030.

(3) Bloch, E. D.; Britt, D.; Lee, C.; Doonan, C. J.; Uribe-Romo, F. J.; Furukawa, H.; Long, J. R.; Yaghi, O. M. Metal Insertion in a Microporous Metal-Organic Framework Lined with 2,2′-Bipyridine. *Journal of the American Chemical Society* **2010**, *132* (41), 14382–14384. https://doi.org/10.1021/JA106935D/SUPPL_FILE/JA106935D_SI_001.PDF.

(4) Walton, K. S.; Snurr, R. Q. Applicability of the BET Method for Determining Surface Areas of Microporous Metal−Organic Frameworks. *J. Am. Chem. Soc.* **2007**, *129* (27), 8552–8556. https://doi.org/10.1021/ja071174k.

(5) Senkovska, I.; Hoffmann, F.; Fröba, M.; Getzschmann, J.; Böhlmann, W.; Kaskel, S. New Highly Porous Aluminium Based Metal-Organic Frameworks: Al(OH)(Ndc) (Ndc=2,6-Naphthalene Dicarboxylate) and Al(OH)(Bpdc) (Bpdc=4,4′-Biphenyl Dicarboxylate). *Microporous and Mesoporous Materials* **2009**, *122* (1–3), 93–98. https://doi.org/10.1016/j.micromeso.2009.02.020.

Appendix A: Synthesis and Metalation of New N-donor Ligands in Mg_2dotpdc

The post-synthetic chemistry described in this section is applicable to both templated and non-templated frameworks, but is described using non-templated examples for simplicity.

A1. Post-synthetic Ligand Syntheses.

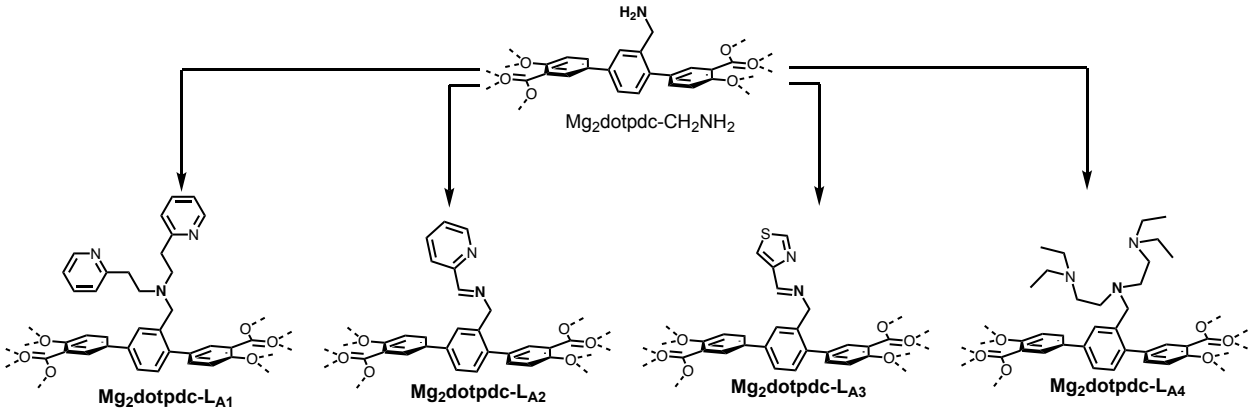

Scheme A1 | Overview of post-synthetic covalent modifications.

A1.1 Synthesis of Mg_2dotpdc-L_{A1}-18%.

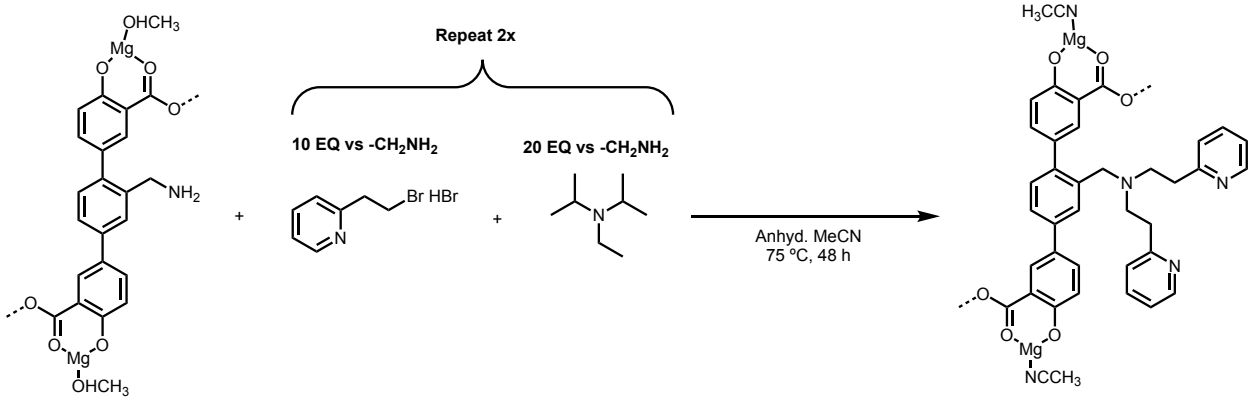

In a nitrogen filled glovebox, 75.0 mg of Mg_2dotpdc-CH_2NH_2-18% was suspended in 10 mL MeCN in a scintillation vial. Diisopropylethylamine (0.582 mmol, 20.0 equiv. versus -CH_2NH_2 groups, 0.101 mL) was added neat, followed by 2-(bromoethyl)pyridine hydrobromide (0.291 mmol, 10.0 equiv. versus -CH_2NH_2 groups, 2.910 mL of 0.100 M stock solution in MeCN). The

inhomogeneous solution was stirred at 75 ºC for 24 h. After, the reaction was cooled, and the mother liquor was removed, and replaced with fresh MeCN, diisopropylethylamine and 2-(bromoethyl)pyridine hydrobromide, and allowed to stir at 75 ºC for an additional 24 h. After, the reaction was cooled to room temperature, the mother liquor removed, replaced with fresh MeCN, and allowed to sit at room temperature for 3 h, after which time the mother liquor was replaced with fresh MeCN again. This washing procedure was repeated three times, followed by filtering to obtain Mg_2dotpdc-L_{A1}-18%. A portion was removed and analyzed by PXRD, **Figure A1**, and digestion ^{1}H NMR. The average observed H_4dotpdc-L_{A1}/H_4dotpdc ratio by digestion ^{1}H NMR of 0.22:1.00 corresponds to overall functionalization of 18%, **Figure A2**.

A1.2 Synthesis of Mg_2dotpdc-L_{A2}-17%.

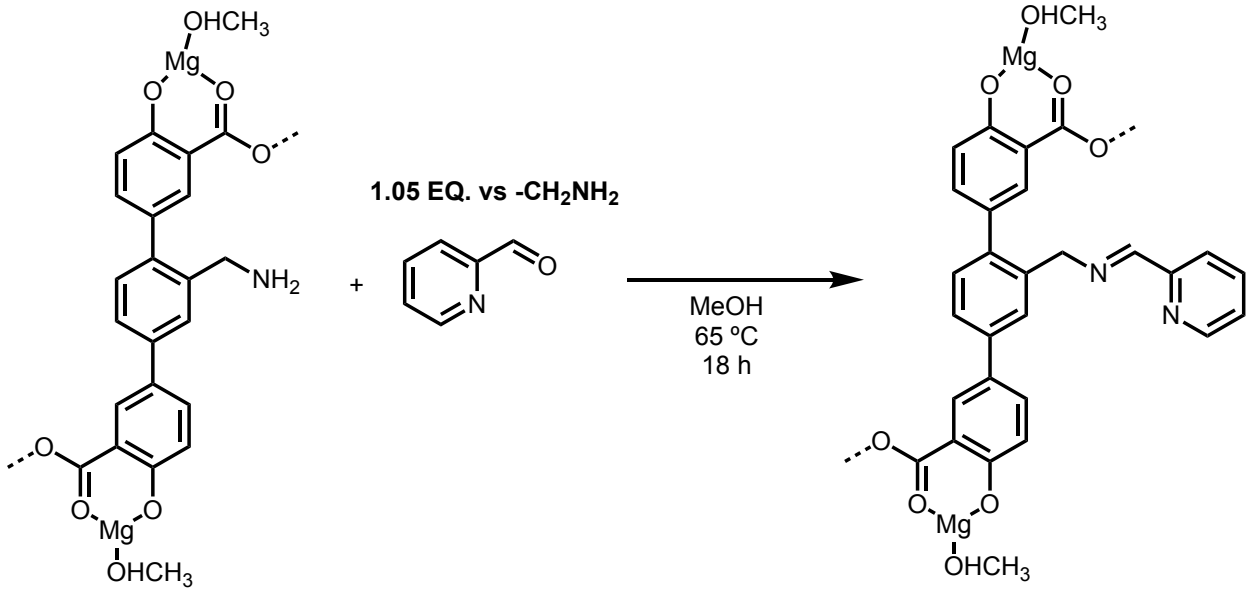

In a nitrogen filled glovebox, 100.0 mg of Mg_2dotpdc-CH_2NH_2-18% was suspended in 6.5 mL of MeOH in a scintillation vial equipped with a stir bar and wrapped with PTFE tape. 2-pyridine carboxaldehyde (0.040 mmol, 1.05 equiv. versus -CH_2NH_2 groups, 0.200 mL of 0.200 M stock in MeOH) was added. The inhomogeneous solution was allowed to stir at 65 ºC for 18 h. After, the reaction was cooled, the mother liquor was removed, replaced with fresh MeOH, and allowed to

sit at 65 ºC for 3 h, after which time the mother liquor was replaced with fresh MeOH again. This washing procedure was repeated for a total of three MeOH washes. After the third wash, the mother liquor was replaced with fresh THF, and allowed to sit at room temperature for 3 h. In preparation for $Ni(COD)_2$ metalation, after three THF solvent exchanges, the framework was filtered and dried on the filter paper. A portion was removed and analyzed by PXRD, **Figure A1**, and digestion ^1H NMR. While digestion conditions hydrolyze the imine bond, the observed H_4dotpdc-CH_2NH_2/ 2-pyridine carboxaldehyde confirms the quantitative conversion to the imine moiety in the framework, **Figure A3**.

A1.3 Synthesis of Mg_2dotpdc-L_{A3}-18%.

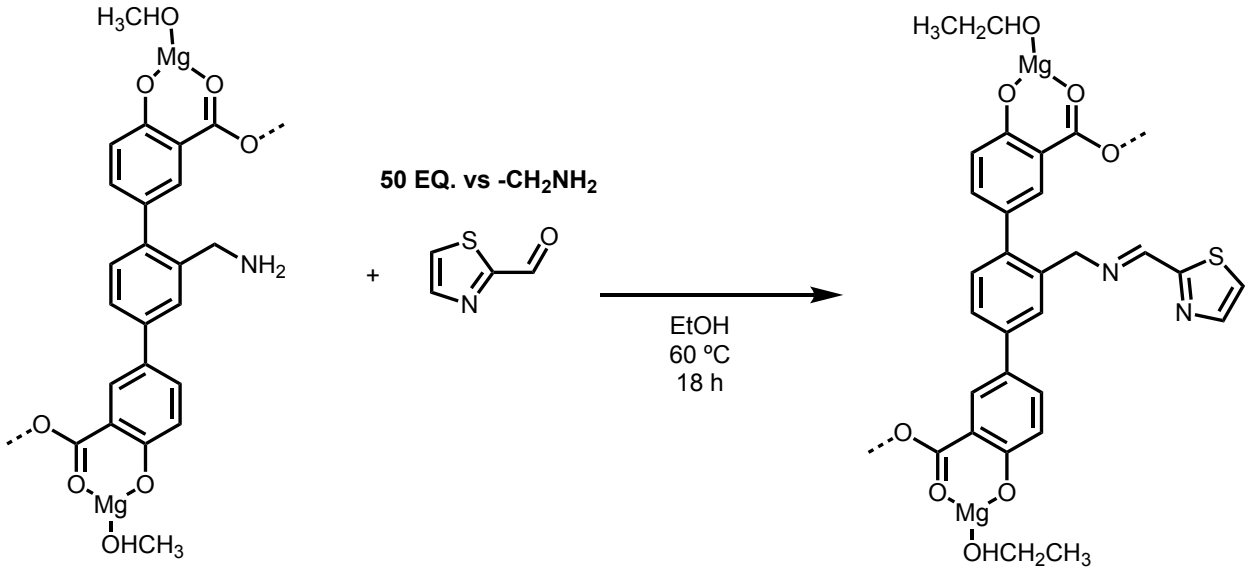

In air, 75.0 mg of Mg_2dotpdc-CH_2NH_2-18% was suspended in 10 mL EtOH in a scintillation vial equipped with a stir bar and wrapped with PTFE tape. 2-pyridine carboxaldehyde (1.45 mmol, 50 equiv. versus -CH_2NH_2 groups, 0.127 mL) was added neat. The inhomogeneous solution was stirred at 60 ºC for 18 h. After, the reaction was cooled, and the mother liquor was removed, replaced with fresh EtOH, and allowed to sit at 60 ºC for 3 h, after which time the mother liquor was replaced with fresh EtOH again. This washing procedure was repeated two times for a total

of three washes, followed by filtering to obtain Mg_2dotpdc-L_{A3}-18%. A portion was analyzed by PXRD and digestion ^{1}H NMR. A portion was removed and analyzed by PXRD, **Figure A1**, and digestion ^{1}H NMR. While digestion conditions hydrolyze the imine bond, the observed H_4dotpdc-CH_2NH_2/ 2-thiazole carboxaldehyde ratio by digestion ^{1}H NMR of 1.00:1.00 confirms the quantitative conversion to the imine moiety in the framework, **Figure A4**. Note that under the acidic digestion conditions, 2-thiazole carboxaldehyde exists in equilibrium as a combination of the aldehyde and corresponding gem diol.

A1.4 Synthesis of Mg_2dotpdc-L_{A4}-18%.

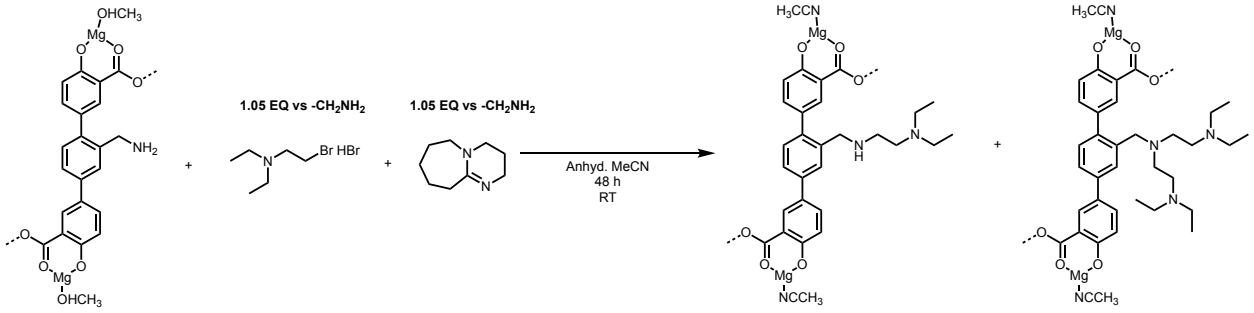

Attempts to cleanly synthesize the di-alkylated framework, Mg_2dotpdc-L_{A3}-18% were largely unsuccessful, likely due to the reactive nature of the alkyl bromide resulting in the formation of oligomeric side products which could not be removed from the framework. However, partial conversion to a mixture of mono- and di-alkylated sites could be achieved with minimal side-product formation using the following procedure:

In a nitrogen filled glovebox, 10.0 mg of Mg_2dotpdc-CH_2NH_2-18% was suspended in 2 mL MeCN in a 4 mL scintillation vial equipped with a stir bar. Separately, 1,8-diazabicyclo[5.4.0]undec-7-ene (0.004 mmol, 1.05 equiv. versus -CH_2NH_2 groups, 0.041 mL of 0.100 M stock in MeCN) and 2-bromo-N,N-diethylethylamine hydrobromide (0.004 mmol, 1.05 equiv. versus -CH_2NH_2 groups, 0.041 mL of 0.100 M stock in MeCN) were combined and shaken briefly. The combined solution was then added to the vial containing the framework, and the mixture was allowed to stir for 48 h

at room temperature. After, the mother liquor removed, replaced with fresh MeCN, and allowed to sit at room temperature for 3 h, after which time the mother liquor was replaced with fresh MeCN again. This washing procedure was repeated two times for three total washes with MeCN, then repeated three more times using MeOH. After, the framework was filtered, and a portion was removed to be analyzed by PXRD, **Figure A1**, and digestion ^{1}H NMR. The ratio of methylene peaks for the di-alkylated product (4.44 ppm, 2H), mono-alkylated product (4.18 ppm, 2H) and the benzylamine starting material (3.97 ppm, 2H) of 0.12:0.17:0.11 corresponds to a distribution of 30% of benzylamine sites being di-alkylated, 42 % being mono-alkylated, and 28% being un-alkylated, **Figure A5**. Small features likely corresponding to oligomeric side-products are observed at ~3.42 ppm and ~1.26 ppm.

A2. Post-synthetic Metalations.

A2.1 Metalation of Mg_2dotpdc-L_{A1}-18% with $FeCl_2$.

In a nitrogen filled glovebox, 25.0 mg of Mg_2dotpdc-L_{A1}-18% was added to a PTFE wrapped 4 mL vial equipped with a stir bar and suspended in 2 mL of MeCN. $FeCl_2$ (0.087 mmol, 10.0 equiv. versus L_{A1} via 0.87 mL of 0.1 M stock in MeCN) was added, and the mixture was stirred at 80 ºC for 36 h. After, the reaction was cooled to room temperature, and the mother liquor was removed via pipette, replaced with fresh MeCN, and allowed to sit at 80 ºC for 3 h. This was repeated twice more for a total of three washes. The framework was then filtered out inside the glovebox, and a portion removed for PXRD and ICP-OES digestion. The observed Fe/Mg ratio by ICP-OES of 0.09 confirms quantitative metalation of the pyridyl sites.

A2.2 Metalation of Mg_2dotpdc-L_{A1}-18% with $NiBr_2$.

In a nitrogen filled glovebox, 25.0 mg of Mg_2dotpdc-L_{A1}-18% was added to a PTFE wrapped 4 mL vial equipped with a stir bar and suspended in 2 mL of MeCN. $NiBr_2$ (0.087 mmol, 10.0 equiv.

versus L_{A1} via 0.87 mL of 0.1 M stock in MeCN) was added, and the mixture was stirred at 80 ºC for 36 h. After, the reaction was cooled to room temperature, and the mother liquor was removed via pipette, replaced with fresh MeCN, and allowed to sit at 80 ºC for 3 h. This was repeated twice more for a total of three washes. The framework was then filtered out inside the glovebox, and a portion removed for PXRD and ICP-OES digestion. The observed Ni/Mg ratio by ICP-OES of 0.082 confirms metalation of 91% of the pyridyl sites.

A2.3 Metalation of Mg_2dotpdc-L_{A1}-18% with $Cu(OTf)_2$.

In a nitrogen filled glovebox, 25.0 mg of Mg_2dotpdc-L_{A1}-18% was added to a PTFE wrapped 4 mL vial equipped with a stir bar and suspended in 2 mL THF. $Cu(OTf)_2$ (0.087 mmol, 10.0 equiv. versus L_{A1} via 0.87 mL of 0.1 M stock in THF) was added, and the mixture was stirred at 65 ºC for 36 h. After, the reaction was cooled to room temperature, the mother liquor was removed via pipette, replaced with fresh THF, and allowed to sit at 65 ºC for 3 h. This process was repeated twice for a total of three washes. After the third wash, the mother liquor was removed, replaced with MeCN, and allowed to sit at 3 h. This washing procedure was repeated once for a total of two room temperature MeCN washes. After, the framework was filtered and dried on the filter paper. A portion was removed from the box for PXRD and ICP-OES. Over multiple attempts, observed Cu/Mg ratios from 0.02 to 0.06 were observed, suggesting that L_{A1} poorly binds copper (II).

A2.4 Metalation of Mg_2dotpdc-L_{A2}-18% with $Ni(COD)_2$.

In a nitrogen filled glovebox, 100.0 mg of Mg_2dotpdc-L_{A2}-17% was suspended in 3.5 mL of THF. $Ni(COD)_2$ (0.045 mmol, 1.1 equiv versus L_{A2} via 0.45 mL of 0.1 M stock in THF) was added, and the mixture was stirred at room temperature overnight. During this time, the material turned a deep purple color, consistent with Ni(0) iminopyridine complexes. After, the mother liquor was removed by pipette, replaced with fresh THF, and allowed to sit at room temperature for 3 h. This

process was repeated twice for a total of three washes. Then the framework was filtered, rinsed with additional THF, and retained in the box. A portion was removed from the box for PXRD and ICP-OES. The observed Ni/Mg ratio by ICP-OES of 0.09 confirms quantitative metalation of the iminopyridine sites.

A2.5 Metalation of Mg_2dotpdc-L_{A3}-18% with $Cu(OTf)_2$.

In a nitrogen filled glovebox, 10.0 mg of Mg_2dotpdc-L_{A3}-18% was added to a PTFE wrapped 4 mL vial equipped with a stir bar and suspended in 2 mL THF. $Cu(OTf)_2$ (0.029 mmol, 10.0 equiv. versus L_{A3} via 0.580 mL of 0.05 M stock in THF) was added, and the mixture was stirred at 65 ºC for one day. After, the reaction was cooled to room temperature, the mother liquor was removed via pipette, replaced with fresh THF, and allowed to sit at 65 ºC for 3 h. This process was repeated twice for a total of three washes. After the third wash, the mother liquor was removed, replaced with MeCN, and allowed to sit at 3 h. This washing procedure was repeated once for a total of two room temperature MeCN washes. After, the framework was filtered and dried on the filter paper. A portion was removed from the box for PXRD and ICP-OES. The observed Cu/Mg ratio by ICP-OES of 0.09 confirms quantitative metalation of the iminothiazole sites.

A3. Tables and Figures.

Table A1. | Summary of Successful Metalation Results by ICP-OES.

	Percent functionalization[a]	Expected M/Mg ratio	Found M/Mg Ratio[b]
Mg_2dotpdc-L_{A1}-$FeCl_2$-18%	18	0.09	0.09
Mg_2dotpdc-L_{A1}-NiBr-18%	18	0.09	0.08
Mg_2dotpdc-L_{A2}-Ni(COD)-17%	17	0.085	0.083
Mg_2dotpdc-L_{A3}-$Cu(OTf)_2$-18%	18	0.09	0.09

[a] Determined by digestion ^{1}H NMR.
[b] Determined by ICP-OES.

Table A2. | Summary of Unsuccessful Metalation Results by ICP-OES.

Framework	Metal source	Solvent	Expected M/Mg ratio[a]	Found M/Mg ratio[b]
Mg_2dotpdc-IP-18%[c]	$CuCl_2$	MeOH	0.09	0.29
Mg_2dotpdc-DPA-18%[c]	$MnCl_2$	MeOH	0.09	0.27

Mg_2dotpdc-DPA-18%[c]	$FeCl_3$	MeOH	0.09	0.39
Mg_2dotpdc-DPA-14%[c]	$CuCl_2$	MeOH	0.07	0.12
Mg_2dotpdc-L_{A1}-18%	$Cu(OTf)_2$	THF	0.09	0.14
Mg_2dotpdc-L_{A1}-18%	$Cu(OTf)_2$	MeCN	0.09	0.02-0.06
Mg_2dotpdc-L_{A2}-18%	$Cu(MeCN)_4PF_6$	MeCN	0.09	0.01
Mg_2dotpdc-L_{A2}-28%	$Cu(OTf)_2$	MeOH	0.14	0.37
Mg_2dotpdc-L_{A3}-18%	$Cu(OAc)_2$	EtOH	0.09	0.24
Mg_2dotpdc-L_{A3}-18%	$CuCl_2$	MeCN	0.09	0.00

[a] Based on digestion ^{1}H NMR.
[b] Determined by ICP-OES.
[c] Post-synthetic ligand synthesis discussed in Chapter 3.

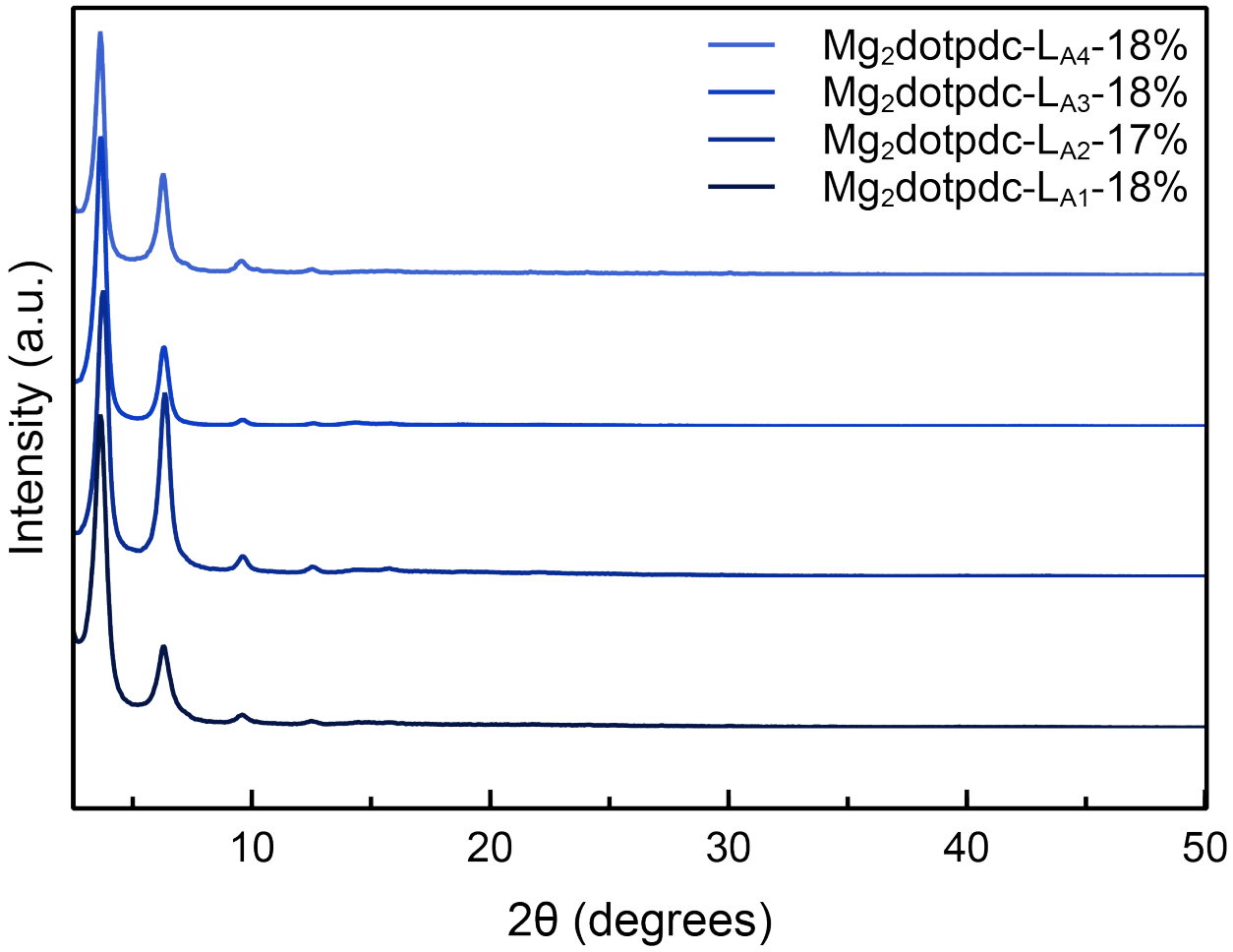

Figure A1 | PXRD patterns of the ligated frameworks.

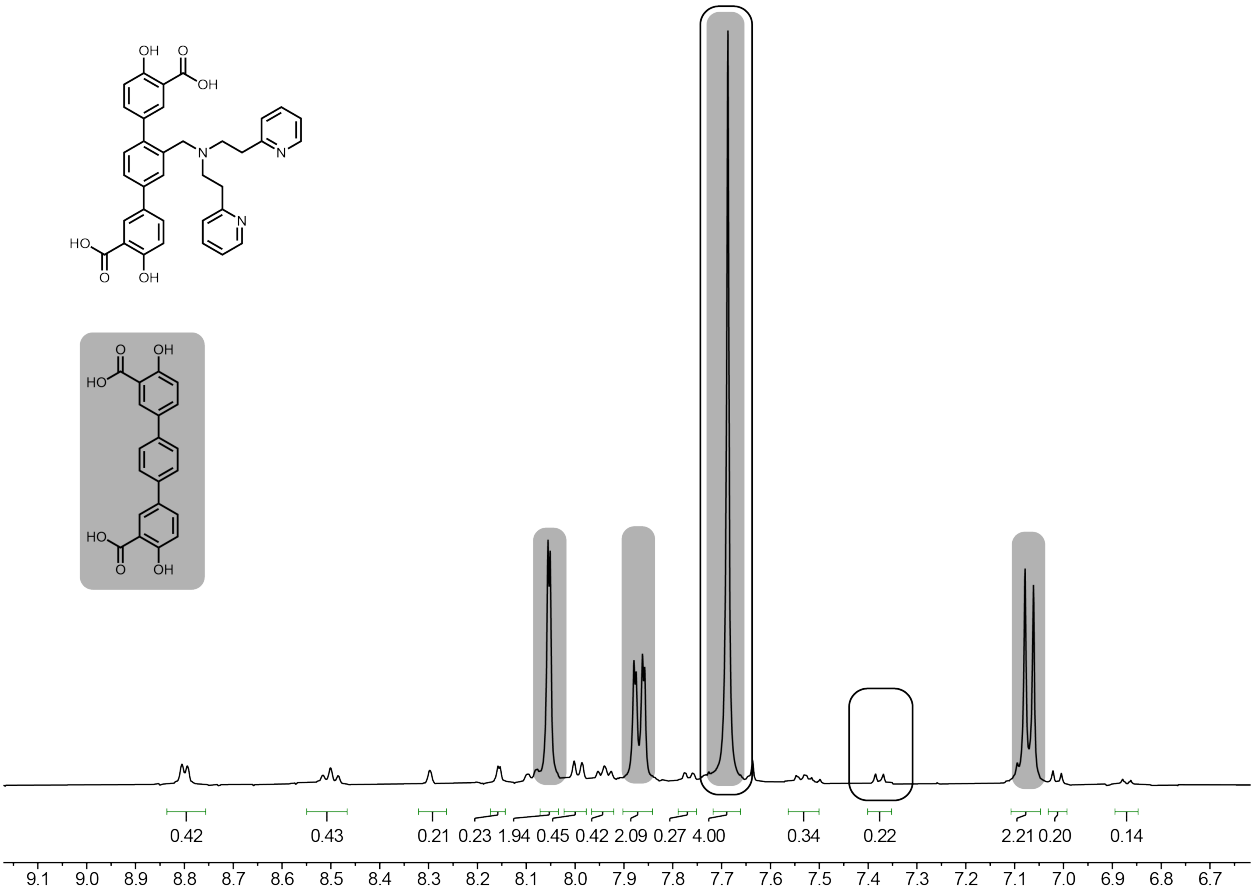

Figure A2 | Aromatic region of the digestion ^{1}H NMR spectrum of Mg_2dotpdc-L_{A1}-18% taken in DMSO-*d*$_6$. The relative ratio of 0.22:4.00 observed between the functionalized dotpdc^{4-} doublet at 7.35 ppm (1H) to the H_4dotpdc singlet at 7.67 ppm (4H) corresponds to a percentage of 18%.

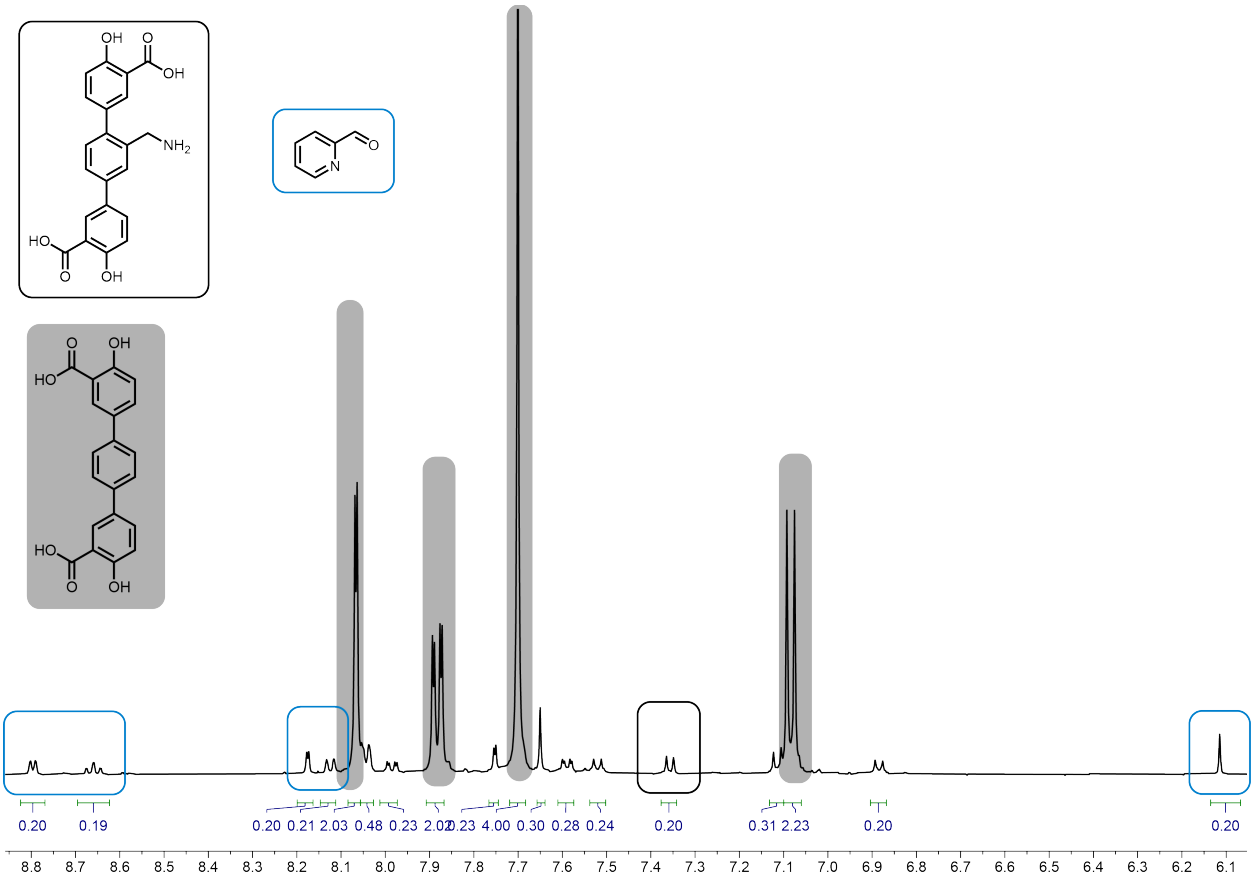

Figure A3 | Aromatic region of the digestion ^{1}H NMR spectrum of Mg_2dotpdc-L_{A2}-17% taken in DMSO-d_6. The relative ratio of 0.2:4.00 observed between the -CH_2NH_2 functionalized dotpdc^{4-} doublet at 7.35 ppm (1H) to the H_4dotpdc singlet at 7.67 ppm (4H) corresponds to a percentage of 17%. Quantitative imine bond formation is confirmed by the 1:1 ratio between the -NH_2 functionalized dotpdc^{4-} and the 2-pyradine carboxaldehyde peaks.

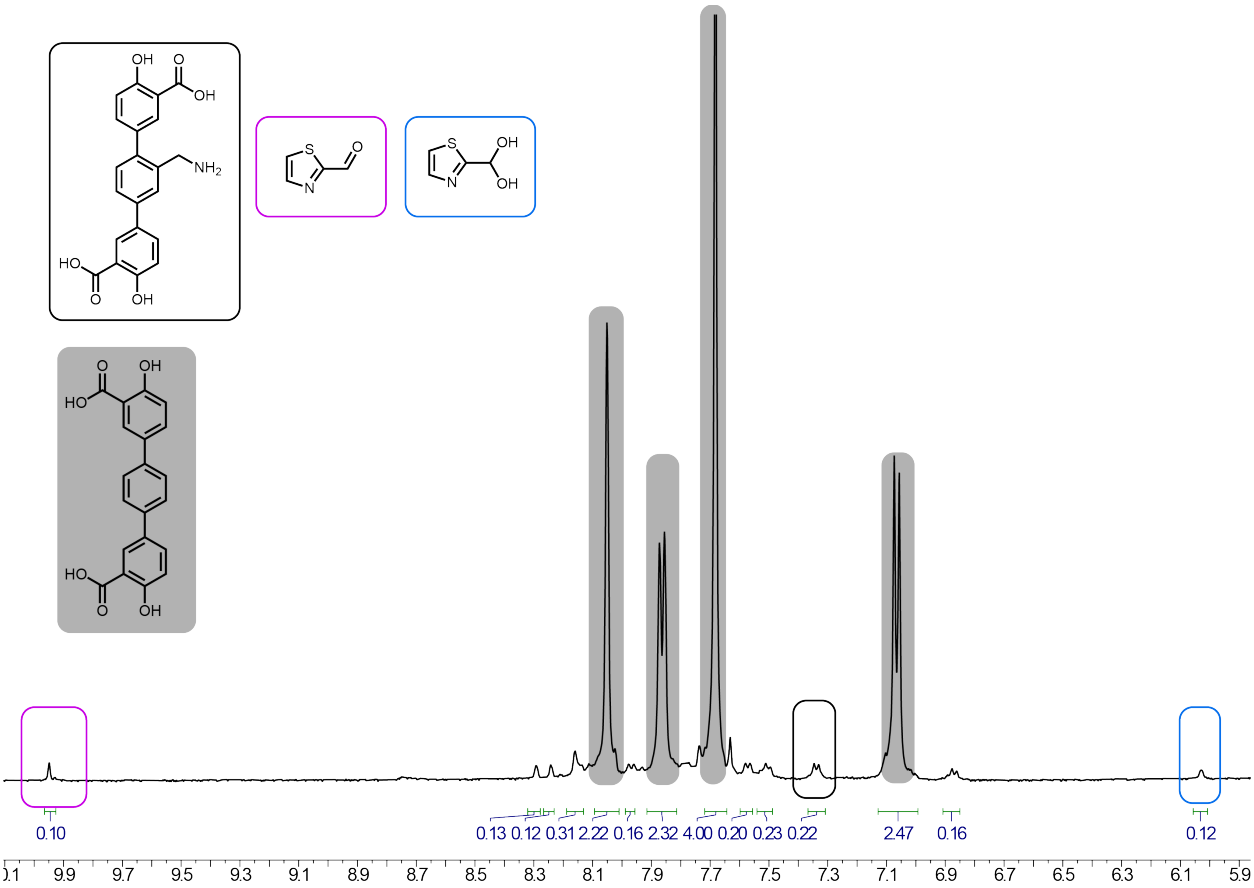

Figure A4 | Aromatic region of the digestion ^{1}H NMR spectrum of Mg_2dotpdc-L_{A2}-18% taken in DMSO-*d*$_6$. The relative ratio of 0.22:4.00 observed between the -CH_2NH_2 functionalized dotpdc^{4-} doublet at 7.3 ppm (1H) to the H_4dotpdc singlet at 7.67 ppm (4H) corresponds to a percentage of 18%. Quantitative imine bond formation is confirmed by the 1:1 ratio between the -NH_2 functionalized dotpdc^{4-} and the sum of the thiazole-2-carbaldehyde (9.9 ppm, 1H) and thiazol-2-ylmethanediol (6.0 ppm, 1H) peaks.

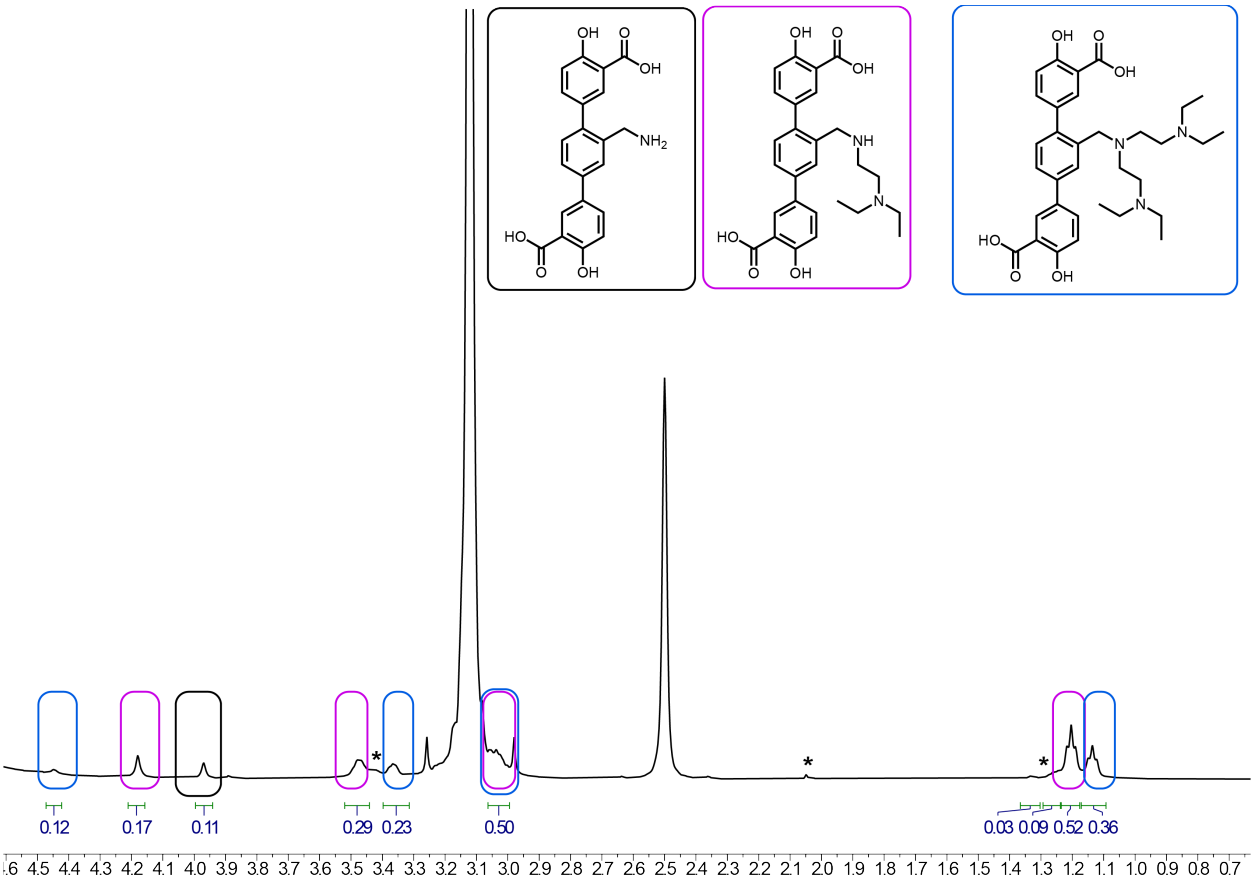

Figure A5 | Alkyl region of the ^{1}H NMR spectrum of Mg_2dotpdc-L_{A3}-18% taken in DMSO-d_6. of methylene peaks for the di-alkylated product (4.44 ppm, 2H), mono-alkylated product (4.18 ppm, 2H) and the benzylamine starting material (3.97 ppm, 2H) of 0.12:0.17:0.11 corresponds to a distribution of 30% of benzylamine sites being di-alkylated, 42 % being mono-alkylated, and 28% being un-alkylated. Small features likely corresponding to oligomeric off-products from the alkyl halide starting material are marked with a '*'.

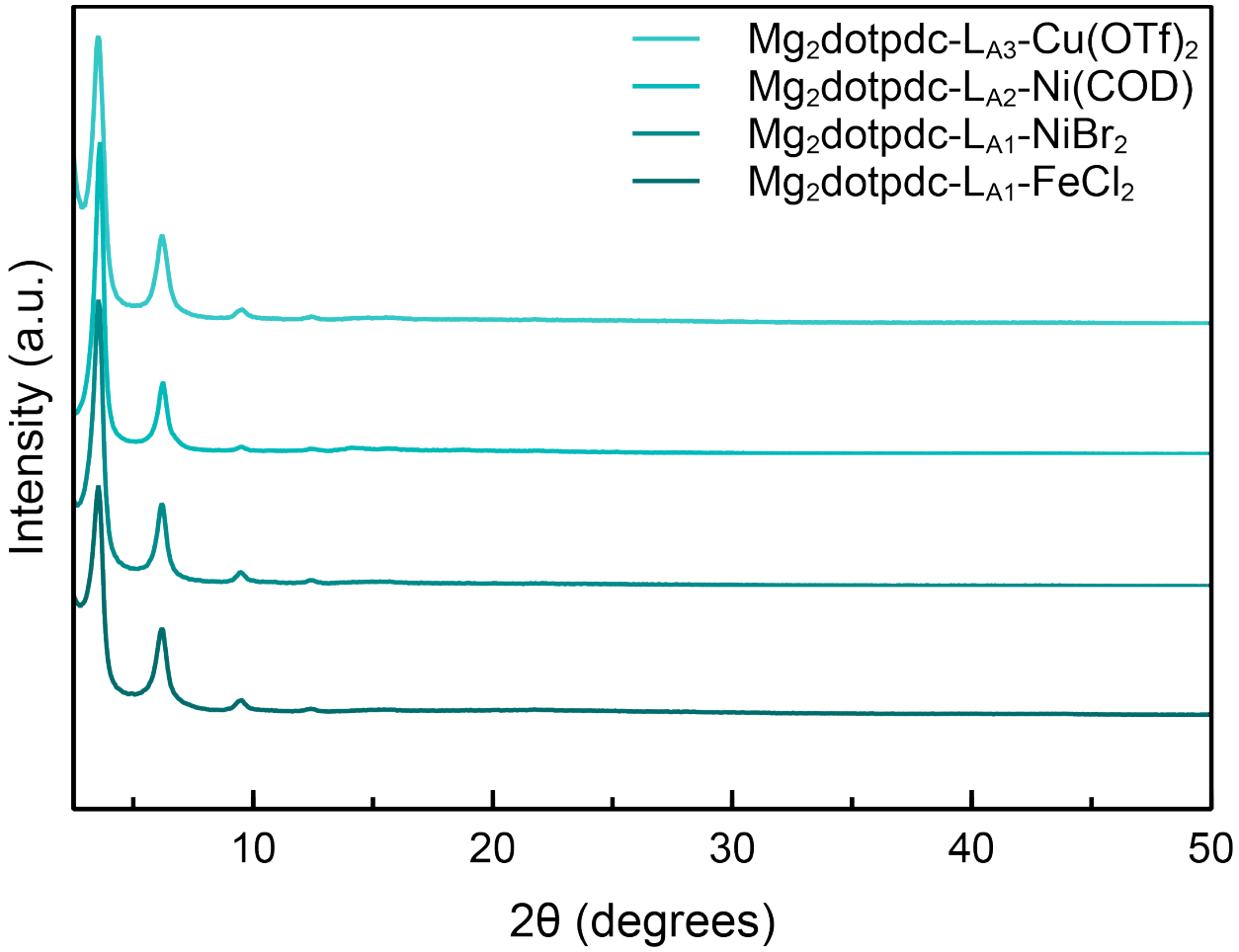

Figure A6 | PXRD patterns of the metalated frameworks.

Appendix B: Catalytic Catechol Oxidation using $Cu(OTf)_2$ Metalated Frameworks

B1. Design of Experiments Screening 3,5-Di-tert-butyl Catechol Oxidation using di-(2-picolyl)amine (DPA) Frameworks.

B1.1 General Catalytic Procedure for DoE Experiments with DPA frameworks.

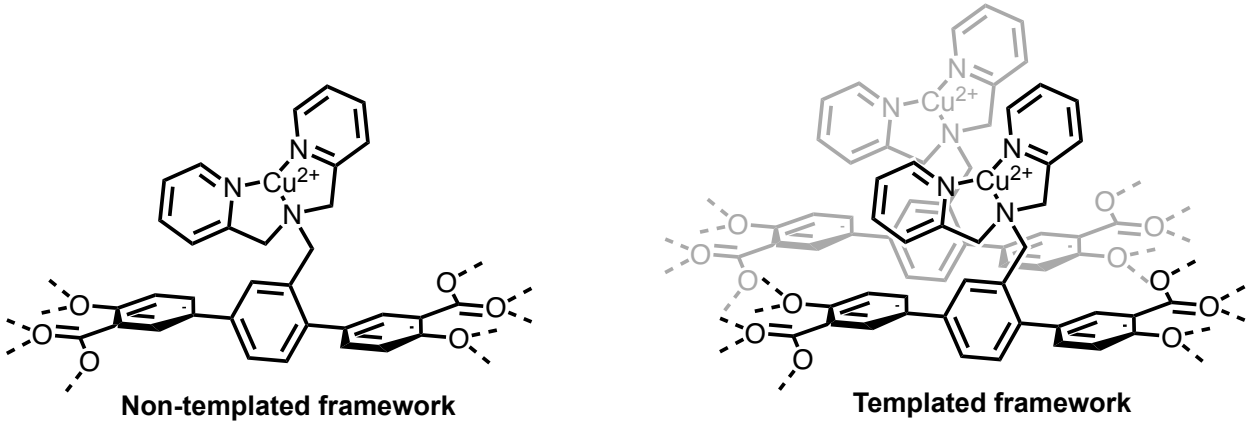

Scheme B2.1 | Depiction of the non-templated and templated $Cu(OTf)_2$ metalated DPA frameworks used in the design of experiments study. Frameworks were functionalized between 16-18%.

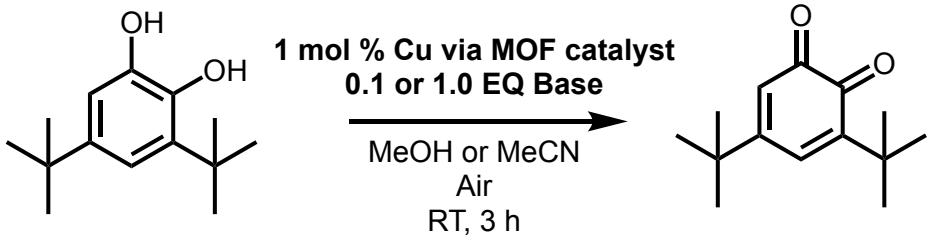

Scheme B1.2 | Catechol oxidation conditions for screening with Cu(II) metalated DPA frameworks using design of experiments methods.

In a nitrogen filled glovebox, framework (0.001 mmol Cu, 0.01 Equiv. versus 3,5-DTBC) was loaded into a 20 mL vial equipped with a stir bar and removed from the glovebox. Solvent (MeCN or MeOH) followed by 0.1 M base stock solution (pyridine, 4-dimethylaminopyridine (DMAP), imidazole, or morpholine) were then added, according to the volumes in **Table B1**. Finally, 1.0 mL of 0.1 M 3,5-di-tert-butyl catechol (3,5-DTBC) solution was added, and the vial was capped and stirred at room temperature for 3 hours. After, 1 mL of the solution was pipetted off, diluted

to 5.0 mL in MeOH, filtered through a syringe filter, and analyzed by UV-Vis. The absorbance at 400 nm, corresponding to 3,5-di-tert-butyl quinone (3,5-DTBQ) was used to quantify the conversion to the quinone. Background activity in the absence of copper under the same conditions was subtracted to assess the influence of the copper metalated framework.

B1.2 Oxidation Results and DoE Analysis with DPA materials.

In order to explore the potential impact of not only the templated nature of our copper sites, but also the influence of base identity and equivalents, as well as potential solvent effects, we turned to design of experiments (DoE) methods. Using templating, solvent identity, base identity, and base equivalents as factors, we built a screening factorial set of catalysis experiments using the JMP software.[1] The results of those experiments are summarized in **Table B2**-**B3**.

Briefly, the results suggest there is virtually no impact from templating under these conditions, with both templated and non-templated materials achieving comparable corrected conversions and turnover numbers of ~35. The only significant factors determined by the model are the identity and equivalents of base used, with 1.0 equiv. of the strongest base, DMAP (pKaH ~ 9.2) being predicted to give the highest corrected conversion. Conversely, the weakest base, pyridine (pKaH ~ 5.2) is predicted to have a negative impact on the corrected conversion, which bears out in the negative values obtained in experiments run using pyridine and morpholine.

B2. 3,5-DTBC Oxidation with Cu(II)-Iminothiazole Frameworks.

To confirm whether or not the lack of a templating effect observed with the DPA frameworks was unique to that ligand scaffold, we also investigated the oxidation of 3,5-DTBC using templated and non-templated $Cu(OTf)_2$-iminothiazole frameworks.

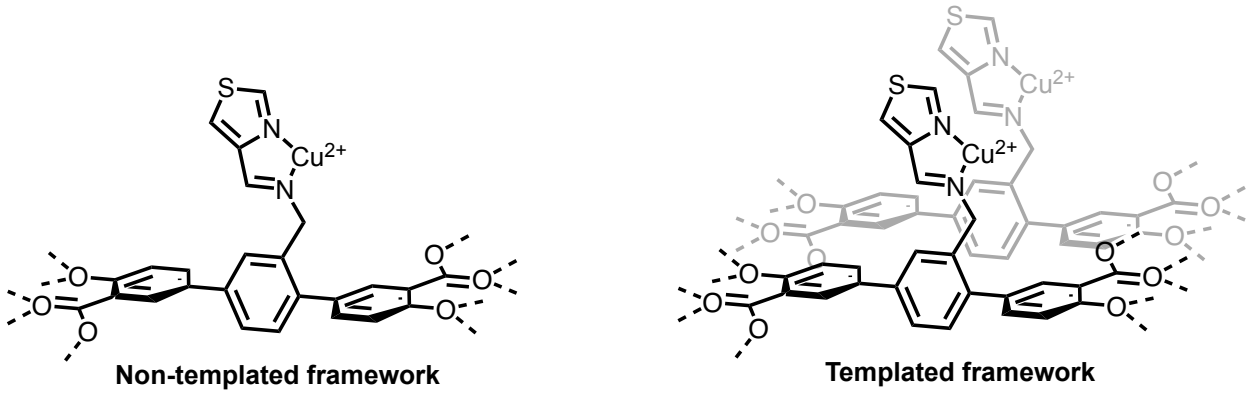

Scheme B2.1 | Depiction of the non-templated and templated $Cu(OTf)_2$ metalated iminothiazole frameworks used in the 3,5-DTBC oxidation studies. Frameworks were functionalized between 18-25%.

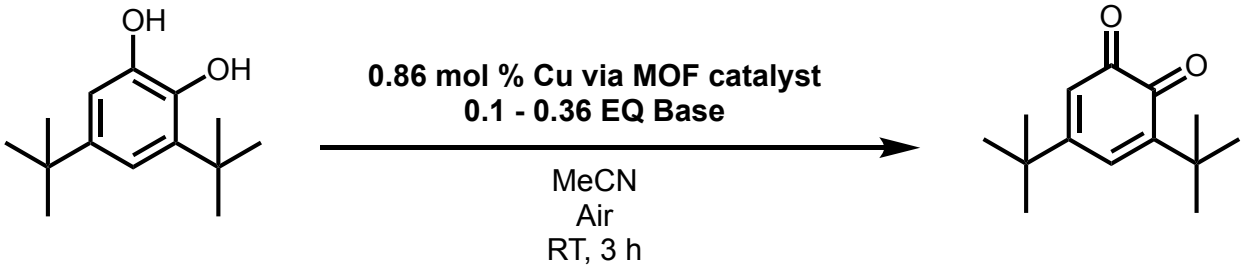

Scheme B2.2 | Catechol oxidation conditions for base screening with Cu(II) metalated iminothiazole frameworks.

B2.1 General Catalytic Procedure for 3 h base screening reactions.

Conditions were adapted from the literature.[2] In a nitrogen filled glovebox, framework (0.0016 mmol Cu, 0.0086 Equiv. versus 3,5-DTBC) was loaded into a 4 mL vial equipped with a stir bar and removed from the glovebox. 2.0 mL of 0.1 M 3,5-DTBC stock in MeCN, followed immediately by 0.2 M base stock in MeCN (NEt_3, DMAP, or 1:1 $NaCH_3COO/NEt_3$) were then added, according to the volumes in **Table B4**. The vial was loosely capped and allowed to stir at room temperature for 3 hours. After, 0.200 mL of the solution was pipetted off, diluted to 5.0 mL in MeOH, filtered through a syringe filter, and analyzed by UV-Vis. The absorbance at 400 nm, corresponding to 3,5-di-tert-butyl quinone (3,5-DTBQ) was used to quantify the conversion to the quinone. For each run, a control sample without framework was run, and its background activity was subtracted to assess the influence of the copper metalated framework.

B2.2 Base Screening Results.

The results of an initial set of screening reactions are summarized in **Table B5** and **Figure B1**, and suggest that, for the iminothiazole copper sites, the identity of the base greatly impacts the reactivity of the templated materials, while the non-templated material's activity was relatively consistent across the three different bases tested. This suggests that the two systems may go through different mechanisms. Consistent with the DPA study, increasing the equivalents of base led to greater conversion over the background. Based on this initial screen, we sought to further examine the activity of the templated and non-templated materials using 36 mol % NEt_3.

B2.3 General Procedure for Timepoint Reactions.

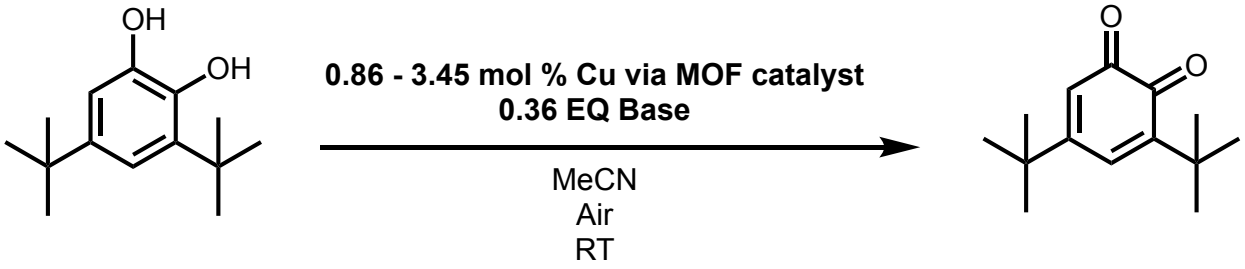

Scheme B2.3 | Catechol oxidation conditions for timepoints with Cu(II) metalated iminothiazole frameworks.

In a nitrogen filled glovebox, framework (0.0016 mmol Cu for 0.86 mol % or 0.0069 mmol Cu for 3.45 mol %) was loaded into a 4 mL vial equipped with a stir bar and removed from the glovebox. 2.0 mL of 0.1 M 3,5-DTBC stock in MeCN, followed immediately by NEt_3 (0.010 mL, 0.072 mmol, 0.36 equiv.) added neat. The vial was loosely capped and allowed to stir at room temperature for 5 hours. For each timepoint, the vial was centrifuged, 50.0 uL was removed and diluted with 5.0 mL of MeOH, then analyzed by UV-Vis. The absorbance at 400 nm, corresponding to 3,5-di-tert-butyl quinone (3,5-DTBQ) was used to quantify the conversion to the quinone. For each run, a control sample without framework was run, and its background activity was subtracted to assess the influence of the copper metalated framework. After 5 h, the

supernatant was analyzed by ^{1}H NMR. The framework was filtered off and ICP-OES was used to confirm the retention of copper in the framework.

B2.4 Iminothiazole Timepoint Study Results.

Consistent with our study using the DPA scaffold, the templated and non-templated frameworks exhibited essentially identical activity for the oxidation of 3,5-DTBC to 3,5-DTBQ at both 0.86 mol % and 3.45 mol % copper, **Figure B2**, **Table B2.3**. The final conversions and selectivity were confirmed by the UV-Vis and ^{1}H NMR spectra of the solutions after catalysis, **Figure B3-B4**. After 5 h, reactions with and without metalated framework have fully consumed the starting catechol. However, by ^{1}H NMR and UV-vis, the frameworks achieved ca. 86 % conversion to 3,5-DTBQ, while the background reaction achieved only ca. 35 % conversion, highlighting the markedly better selectivity for the quinone using the metalated frameworks.

Notably, the method by which the materials were thermolyzed to obtain free CH_2NH_2 sites prior to post-synthetic covalent modification and metalation appears to impact the overall activity. Materials thermolyzed under flowing N_2 at 250 ºC exhibited nearly 20 % higher conversion to 3,5-DTBQ compared to material thermolyzed using microwave heating at 250 ºC in a 2-ethyl-1-hexanol/ethylene glycol/ water mixture. This may be due to the presence of a higher number of backbone radicals in the N_2 thermolyzed materials (see Chapter 3 for additional discussion on the radical).

Minimal leaching was observed by ICP-OES, suggesting it is not due to free copper in solution. Further supporting this, controls run using just $Cu(OTf)_2$, or $Cu(OTf)_2$ plus bare Mg_2dotpdc as the catalyst exhibited lower conversion versus the copper-free background reactions, **Figure B5**. The large error in the non-templated replicates should be mitigatable by performing the reactions using greater masses of framework.

Overall, these results demonstrate that the metalated materials may be effective catalysts for the selective oxidation of 3,5-DTBC to 3,5-DTBQ. However, there is not strong evidence for this reaction benefiting from the metal centers being templated ~7Å from each other. It may be that a shorter Cu–Cu distance would facilitate higher activity.

B3. Tables and Figures.

Table B1. Solvent and Substrate Volumes for DoE Catalysis.

Base Equiv.	Base stock volume (mL)	Solvent volume (mL)	3,5-DTBC stock volume (mL)	Final total volume (mL)
0.1	0.1	9.0	1.0	10.1
1.0	1.0	8.0	1.0	10.0

Table B2. DoE Analysis Results.

Templating	Solvent	Base	Base Equiv.	Corrected Conversion (mmol)	TON
Non-templated	Wet MeCN	DMAP	1	0.03311	33.11
Templated	MeOH	Morpholine	1	0.00395	3.95
Non-templated	Wet MeCN	Imidazole	1	0.00286	2.86
Templated	Wet MeCN	Imidazole	0.1	0.00013	0.13
Non-templated	Wet MeCN	Pyridine	1	-0.00036	-0.36
Non-templated	Wet MeCN	Morpholine	1	0.01556	15.56
Non-templated	MeOH	Imidazole	0.1	-0.00518	-5.18
Templated	Wet MeCN	DMAP	0.1	0.01344	13.44
Templated	MeOH	Imidazole	1	-0.00170	-1.70
Templated	MeOH	Pyridine	1	-0.00493	-4.93
Templated	MeOH	DMAP	1	0.03630	36.30
Non-templated	MeOH	DMAP	0.1	0.01628	16.28
Non-templated	MeOH	Pyridine	0.1	-0.00280	-2.80
Templated	Wet MeCN	Morpholine	0.1	0.00644	6.44
Non-templated	MeOH	Morpholine	0.1	-0.00104	-1.04
Non-templated	MeOH	Imidazole	1	0.00194	1.94
Non-templated	MeOH	Morpholine	1	0.00918	9.18
Non-templated	Wet MeCN	Pyridine	1	-0.00036	-0.36
Non-templated	MeOH	DMAP	0.1	0.01628	16.28
Non-templated	Wet MeCN	Morpholine	1	0.01556	15.56
Templated	Wet MeCN	Morpholine	1	0.02020	20.20
Templated	MeOH	Pyridine	0.1	-0.00219	-2.19
Templated	Wet MeCN	Imidazole	0.1	0.00013	0.13

Table B3. Effects Test Summary.

Factor	Number of Parameters	Degrees of Freedom	Sum of Squares	F Ratio	*p*-value
Templating	1	1	4.50E-06	0.167	0.689
Solvent Identity	1	1	7.52E-05	2.780	0.115
Base Equiv.	1	1	3.03E-04	11.199	0.004
Base Identity	3	3	2.24E-03	27.607	<0.0001

Table B4. Solvent and Substrate Volumes for Catalysis using Iminothiazole Frameworks.

Base Equiv.	Base stock volume (mL)	3,5-DTBC stock volume (mL)	Final total volume (mL)
0.1	0.1	2.0	2.1
0.36	0.36	2.0	2.36

Table B5. Iminothiazole Frameworks Base Screening Results.

Base	Equiv.	Framework	Conversion (mmol)
NEt_3	0.1	Templated	0.0937
		Non-templated	0.0703
		Control	0.0595
	0.36	Templated	0.1062
		Non-templated	0.0712
		Control	0.0616
DMAP	0.1	Templated	0.0508
		Non-templated	0.0821
		Control	0.0298
1:1 NEt_3/CH_3COO^-	0.36	Templated	0.0564
		Non-templated	0.0830
		Control	0.0285

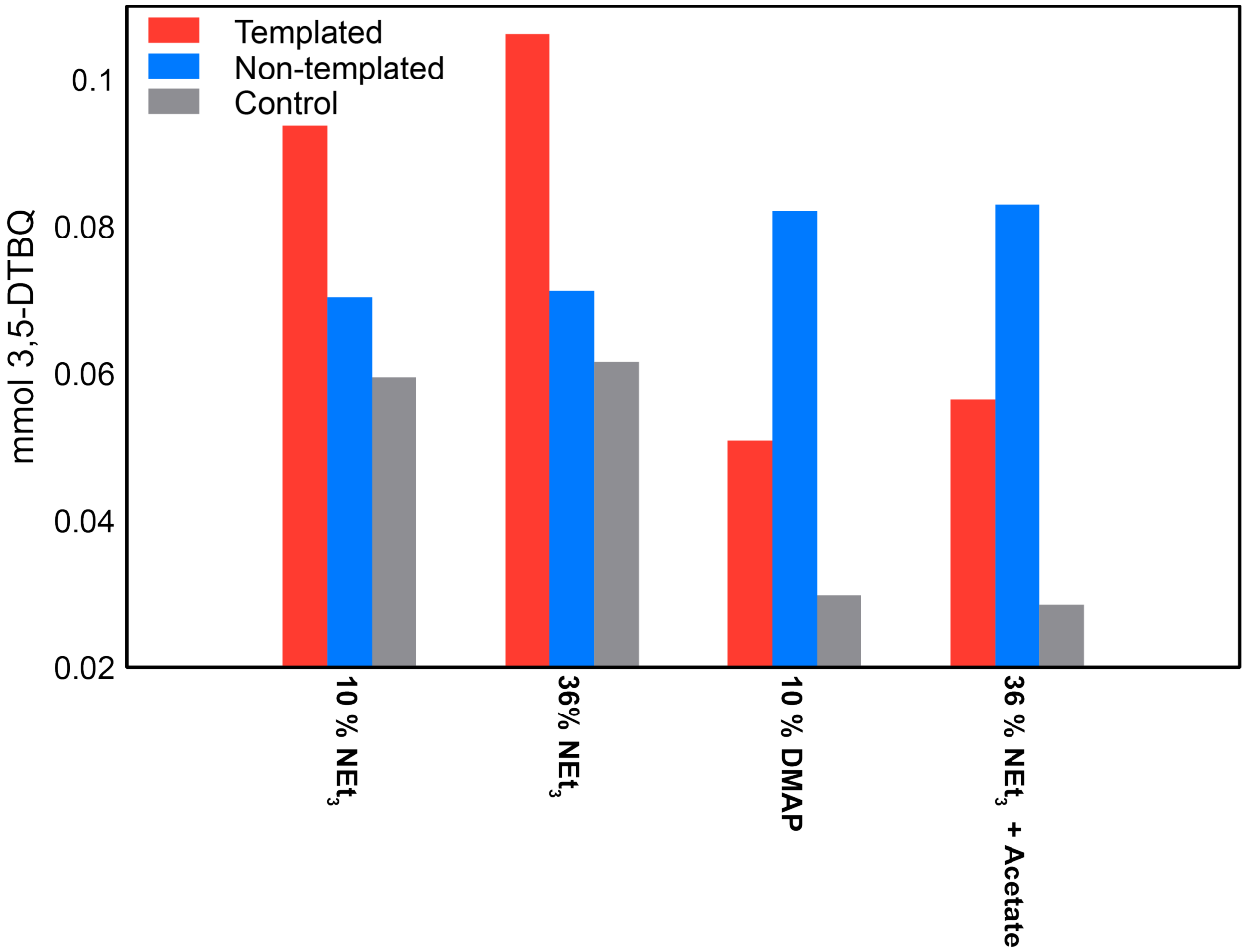

Figure B1 | Iminothiazole framework base screening catalysis bar chart.

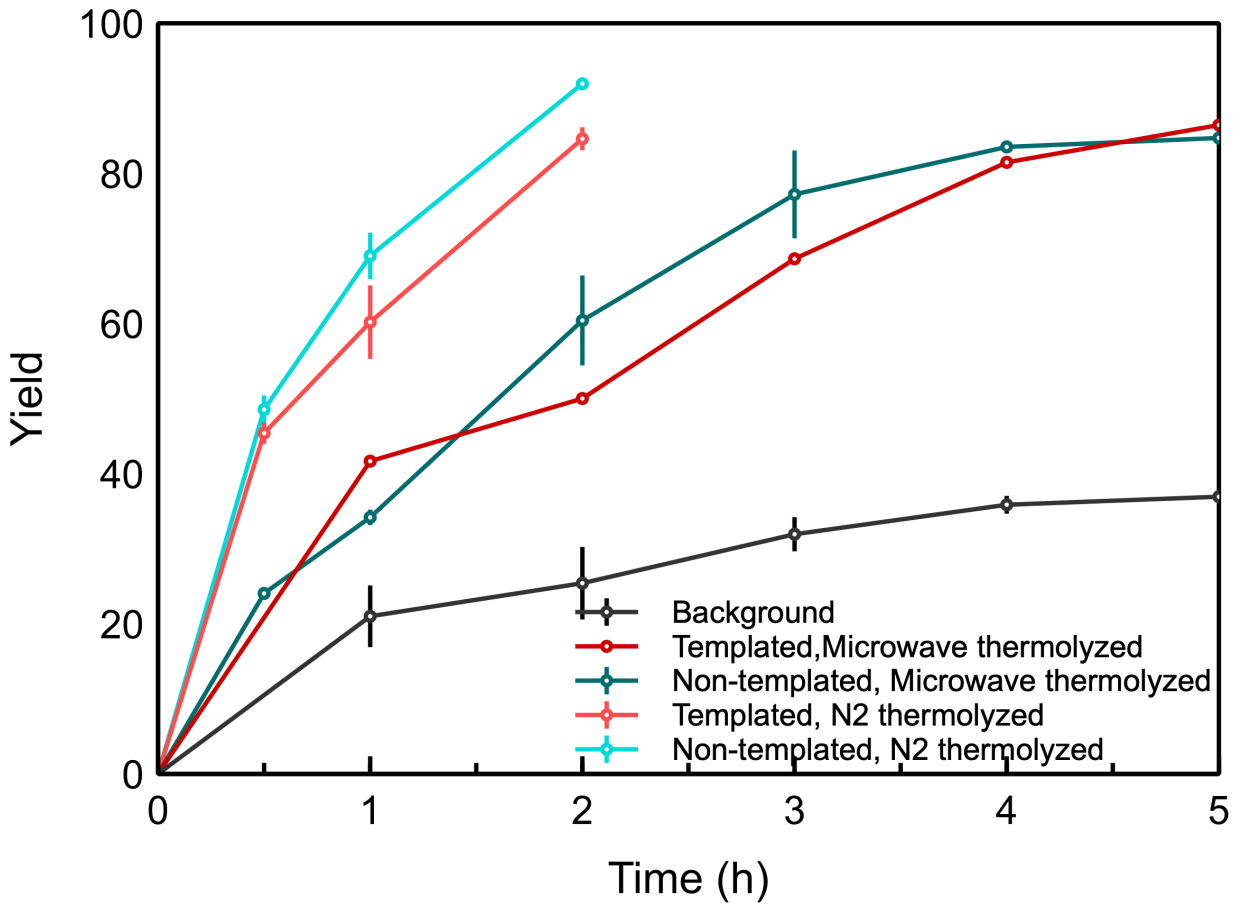

Figure B2 | 3,5-DTBC oxidation to 3,5-DTBQ yield timepoints with $Cu(OTf)_2$-iminothiazole frameworks using 36 mol % NEt_3, as determined by UV-Vis.

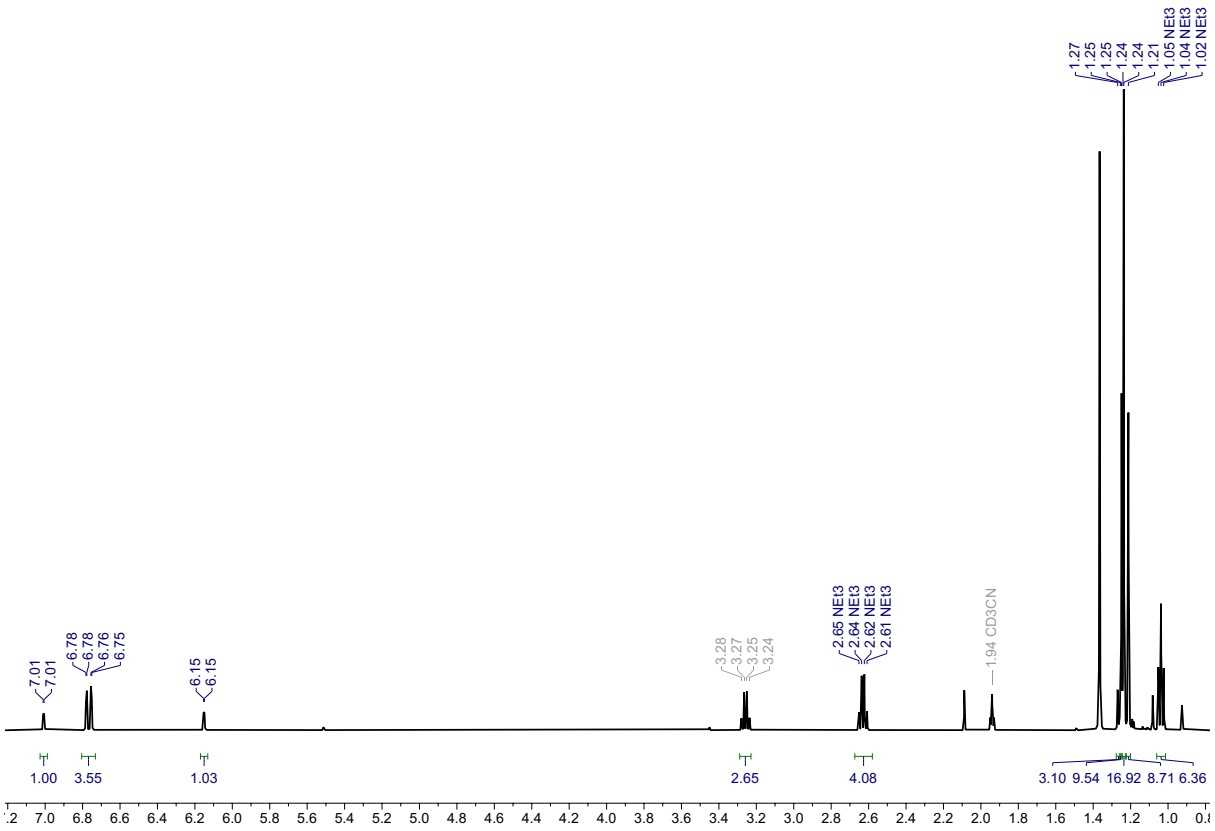

Figure B3 | ^{1}H NMR of 3,5-DTBC oxidation background reaction in CD_3CN after 5 hours. The peaks at 7.01, 6.15, and 1.21 ppm correspond to the quinone product, 3,5-DTBQ. The peaks at 6.78 and 1.25 ppm correspond to the side product, likely 4,6-di-tert-butyl-2H-pyran-2-one. The relative ratio of 1.00:3.55 observed between the 3,5-DTBQ aromatic peak (7.01 ppm, 1H), and 4,6-di-tert-butyl-2H-pyran-2-one (6.78 ppm, 2H) corresponds to 36 % conversion to the quinone, consistent with the UV-Vis results.

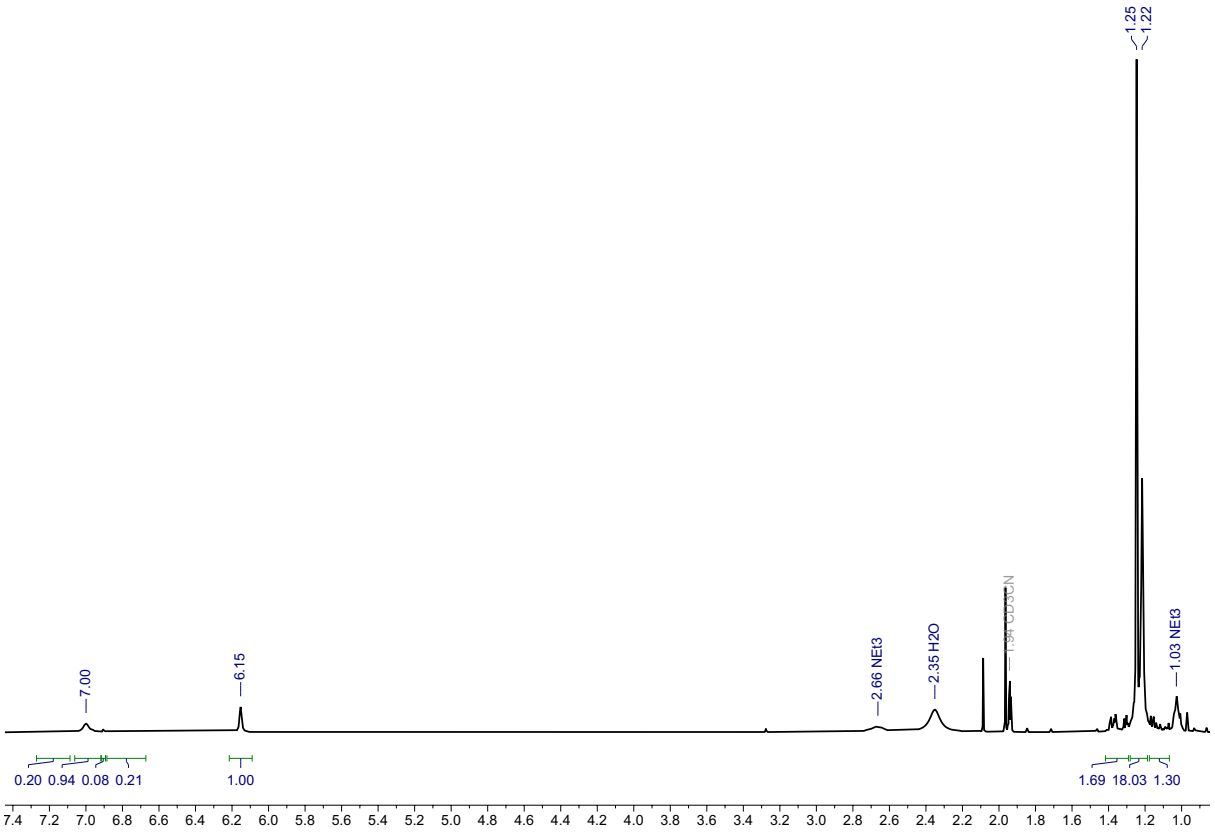

Figure B4 | ^{1}H NMR of 3,5-DTBC oxidation reaction using the templated framework in CD_3CN after 5 hours. The peaks at 7.01, 6.15, and 1.21 ppm correspond to the quinone product, 3,5-DTBQ. Small peaks are noticeable in the alkyl region, assigned to the *tert*-butyl peaks of side-products. The relative ratio of 18.03:3.99 observed between the 3,5-DTBQ *tert*-butyl peaks (18H), and the side product *tert*-butyl peaks (18H) corresponds to 87 % conversion to the quinone, consistent with the UV-Vis results.

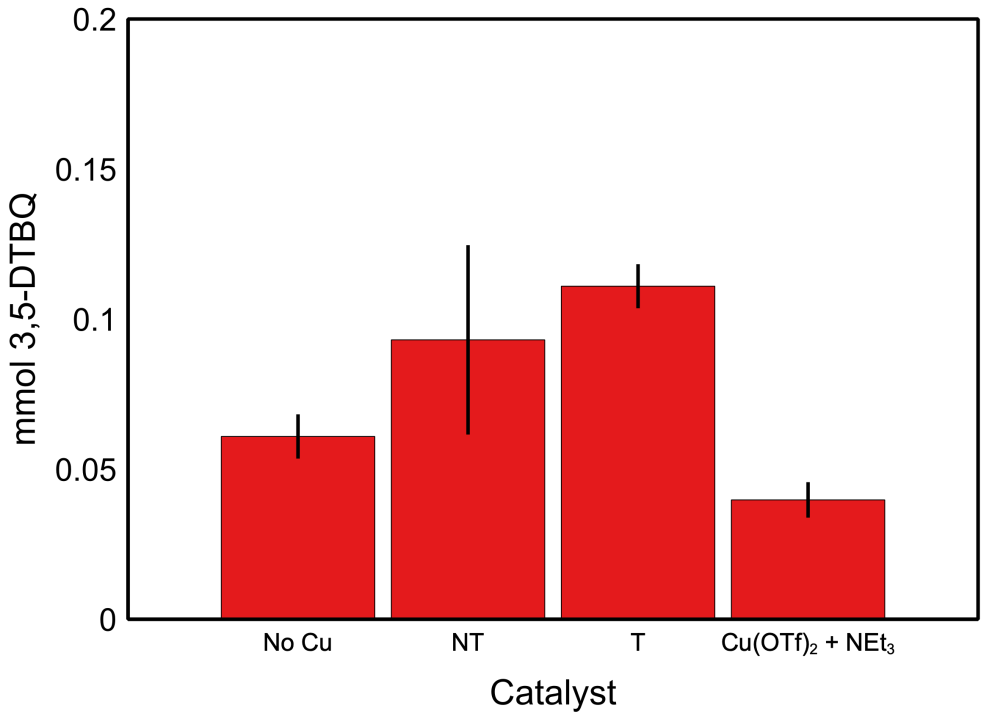

Figure B5 | Conversion of 3,5-DTBC to 3,5-DTBQ after 3 hours.

Appendix C: Templated Bimetallic Metal–Organic Frameworks in the Broader Context of Bimetallic Catalysts

C1. Introduction

As discussed in Chapter 1, binuclear active sites exist across the span of the catalysis landscape, including metalloenzymes, cooperative molecular catalysts, and heterogeneous platforms such as mesoporous silicas and zeolites. Several example systems are highlighted in **Figure C1**. While an emphasis has been placed on the metal–metal distance, additional factors such as the flexibility of the active site and its coordination environment work to dictate activity. For example, in the case of soluble methane monooxygenase (sMMO), the short Fe-Fe distance of 3.4 Å coupled with flexible carboxylate ligands, capable of adopting different coordination modes, facilitates substrate binding.[1–3] In contrast, a rigid ligand backbone can enforce much longer ≥ 6 Å distances between group IV metal centers in molecular olefin polymerization catalysts. The resultant constrained geometries facilitate multinuclear interactions between both metal centers and monomer substrates, leading to much higher activity for both homo- and copolymerization over mononuclear counterparts.[4,5] These types of ligand (or support) interactions can be observed in heterogeneous contexts as well. Through changes in functional group loading, the average distance between installed copper thiazole complexes on the surface of silica can be tuned, with shorter distances, and thus more bimetallic-in-nature sites, promoting the catalytic oxidation of 3,5-di-*tert*-butyl catechol to the corresponding quinone.[6] In zeolites, the ~7.5 Å Fe-Fe distance in iron-functionalized zeolites, a relatively rigid lattice, primes the iron centers to bind and split nitrous oxide across their span.[7,8]

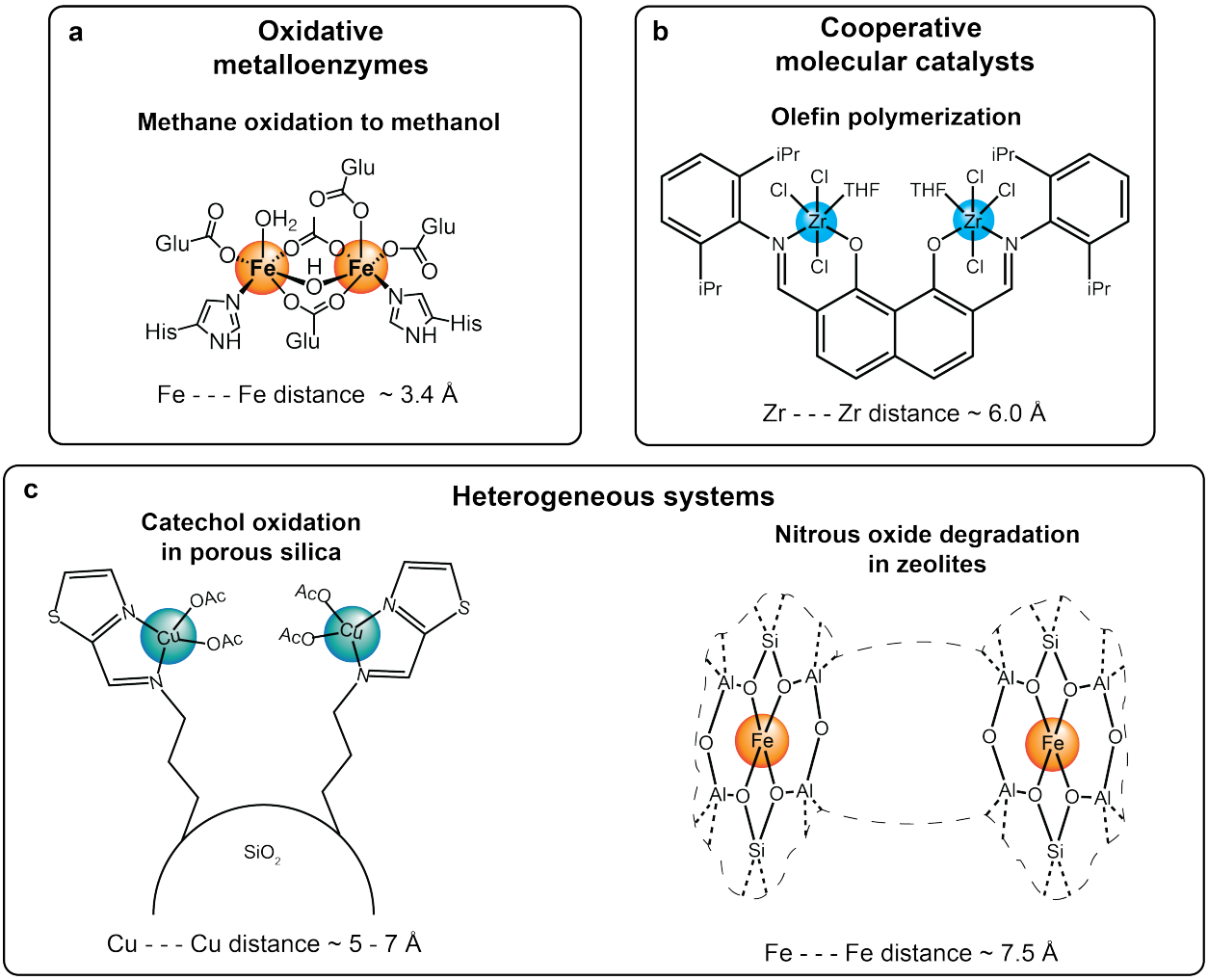

Figure C1 | Example bimetallic systems across subfields highlighting the variable metal–metal distances, including a) oxidative metalloenzymes, b) molecular catalysts and c) porous silica and zeolite materials. Figure redrawn from references 3, 4, 6, and 7.

Judicious control over these interplaying active site parameters- metal–metal distance, active site geometry, ligand/support rigidity- is critical for developing next generation catalysts. Chapter 1 describes the current landscape of building bimetallic sites within metal–organic frameworks (MOFs). Here, I will briefly outline how our design strategy for installing templated bimetallic sites within metal–organic framework pores compares to two other common heterogeneous scaffolds, functionalized silicas and zeolites, highlighting how our strategy and choice of scaffold are an excellent compromise between the two. Compared to functionalized silicas, our strategy draws parallels to the use of protecting group chemistry to install well-spaced

functional groups such as amines on the surface of mesoporous silica. However, the crystalline nature of our MOF scaffold begets a level of structural precision inaccessible to the silica platform. On the other hand, while zeolites are crystalline, our choice of scaffold outshines in its high degree of tunability.

C2. Comparison with Functionalized silica

There are numerous reports on the immobilization of mononuclear and binuclear sites on silica surfaces and within the pores of mesoporous silica.[6,9–12] In both cases, this is traditionally achieved first by hydrolytically grafting organosilanes at the surface hydroxyl groups on the silica surface. If the organosilane precursors possess orthogonally reactive functional groups, subsequent post-synthetic chemistry can be performed to access reactive sites for metal binding. While tunable with regards to functional group identity, this strategy suffers from issues in controlling active site nuclearity; often, clustering of functional groups on the surface is observed, especially as loadings increase.[13,14]

Direct synthesis of silicas via condensation of tetraalkoxysilanes with functionalized organosilanes, such as trityl group protected 3-aminopropylsilane, can help mitigate this issue, resulting in better dispersion of functional groups across the bulk surface.[15–17] The issue of nuclearity parallels the issue of nuclearity in installing bimetallic sites in MOFs discussed in Chapters 1 and 3. However, the exceptionally high level of spatial precision required to adjust active site parameters on the order of a few angstroms is virtually impossible with a platform like mesoporous silica, which is fundamentally limited by the amorphous nature of the bulk material. The morphology of the nanoparticles can be controlled,[18] and efforts to correlate the distribution of active sites on the surface have been made.[6] Yet here, our templating strategy in MOFs shines because we can leverage the structural fidelity of the crystalline framework scaffold and

molecular-level control of the organic building blocks to accurately position active sites relative to one another.

C3. Comparison with Zeolites

Zeolites have been functionalized with amines using grafting and impregnation methods.[19–21] The grafting method is akin to what is done in mesoporous silica, wherein organosilanes such as 3-aminopropylsilane react with surface hydroxyls. These functional groups could in principle serve as building blocks for post-synthetic modification and metalation. While the zeolite scaffolds are crystalline, there is no easy way to control the spacing of the functional groups across the surface, beyond constraints due to the pore structure.

Zeolites, by nature of their negative lattice charge, possess charge-balancing cations in their pores. These cations can be exchanged for transition metals such as copper and iron.[22] A variety of factors are known to impact the nuclearity of the resultant active sites, including pH,[23] counterion identity,[24] and the degree of Al substitutions in the zeolite.[25] Not only is the exchange process quite complex, but the resultant materials are not readily tuned. Our templating approach is both conceptually simpler, and provides much greater tunability with respect to the ligand environment around the metal centers. A key appeal of zeolites as a scaffold is that the constraints imposed by the lattice can stabilize otherwise thermodynamically inaccessible active site geometries.[8] However, similar effects can be observed in binuclear sites installed inside of MOFs as well.[26] Indeed, the work described in Chapter 4 highlights the ability of our crosslinking strategy to tune the rigidity of the host framework. While rigid and stable, zeolites lack the spatial capacity to build large or complex active sites, due to their small pores (typically less than 1 nm). This, coupled with the limited chemical versatility hinders zeolites as a chemical platform for the types of precise chemistry presented in the above chapters.

C5. References

(1) Jones, J. C.; Banerjee, R.; Shi, K.; Semonis, M. M.; Aihara, H.; Pomerantz, W. C. K.; Lipscomb, J. D. Soluble Methane Monooxygenase Component Interactions Monitored by 19F NMR. *Biochemistry* **2021**, *60* (25), 1995–2010. https://doi.org/10.1021/acs.biochem.1c00293.

(2) Tshuva, E. Y.; Lippard, S. J. Synthetic Models for Non-Heme Carboxylate-Bridged Diiron Metalloproteins: Strategies and Tactics. *Chem. Rev.* **2004**, *104* (2), 987–1012. https://doi.org/10.1021/cr020622y.

(3) Jasniewski, A. J.; Que, L. Dioxygen Activation by Nonheme Diiron Enzymes: Diverse Dioxygen Adducts, High-Valent Intermediates, and Related Model Complexes. *Chem. Rev.* **2018**, *118* (5), 2554–2592. https://doi.org/10.1021/acs.chemrev.7b00457.

(4) Salata, M. R.; Marks, T. J. Synthesis, Characterization, and Marked Polymerization Selectivity Characteristics of Binuclear Phenoxyiminato Organozirconium Catalysts. *J. Am. Chem. Soc.* **2008**, *130* (1), 12–13. https://doi.org/10.1021/ja076857e.

(5) Li, L.; Metz, M. V.; Li, H.; Chen, M.-C.; Marks, T. J.; Liable-Sands, L.; Rheingold, A. L. Catalyst/Cocatalyst Nuclearity Effects in Single-Site Polymerization. Enhanced Polyethylene Branching and α-Olefin Comonomer Enchainment in Polymerizations Mediated by Binuclear Catalysts and Cocatalysts via a New Enchainment Pathway. *J. Am. Chem. Soc.* **2002**, *124* (43), 12725–12741. https://doi.org/10.1021/ja0201698.

(6) Grigoropoulou, G.; Christoforidis, K. C.; Louloudi, M.; Deligiannakis, Y. Structure-Catalytic Function Relationship of SiO2-Immobilized Mononuclear Cu Complexes: An EPR Study. *Langmuir* **2007**, *23* (20), 10407–10418. https://doi.org/10.1021/la700815d.

(7) Sklenak, S.; Andrikopoulos, P. C.; Boekfa, B.; Jansang, B.; Nováková, J.; Benco, L.; Bucko, T.; Hafner, J.; Dědeček, J.; Sobalík, Z. N2O Decomposition over Fe-Zeolites: Structure of the Active Sites and the Origin of the Distinct Reactivity of Fe-Ferrierite, Fe-ZSM-5, and Fe-Beta. A Combined Periodic DFT and Multispectral Study. *Journal of Catalysis* **2010**, *272* (2), 262–274. https://doi.org/10.1016/j.jcat.2010.04.008.

(8) Rhoda, H. M.; Heyer, A. J.; Snyder, B. E. R.; Plessers, D.; Bols, M. L.; Schoonheydt, R. A.; Sels, B. F.; Solomon, E. I. Second-Sphere Lattice Effects in Copper and Iron Zeolite Catalysis. *Chem. Rev.* **2022**, *122* (14), 12207–12243. https://doi.org/10.1021/acs.chemrev.1c00915.

(9) Piovezan, C.; Jovito, R.; Bortoluzzi, A. J.; Terenzi, H.; Fischer, F. L.; Severino, P. C.; Pich, C. T.; Azzolini, G. G.; Peralta, R. A.; Rossi, L. M.; Neves, A. Heterodinuclear FeIIIZnII-Bioinspired Complex Supported on 3-Aminopropyl Silica. Efficient Hydrolysis of Phosphate Diester Bonds. *Inorg. Chem.* **2010**, *49* (6), 2580–2582. https://doi.org/10.1021/ic902489j.

(10) Louloudi, M.; Deligiannakis, Y.; Hadjiliadis, N. Design and Synthesis of New Biomimetic Materials by Sol−Gel: A CuII(Histidine)2 Complex Covalently Bonded on a Silica Matrix. *Inorg. Chem.* **1998**, *37* (26), 6847–6851. https://doi.org/10.1021/ic980665q.

(11) Zois, D.; Vartzouma, C.; Deligiannakis, Y.; Hadjiliadis, N.; Casella, L.; Monzani, E.; Louloudi, M. Active Catalytic Centers in Silica-Supported Cu(II) and Mn(II) Biomimetic Complexes: Correlation between Catalytic and EPR Data. *Journal of Molecular Catalysis A: Chemical* **2007**, *261* (2), 306–317. https://doi.org/10.1016/j.molcata.2006.11.023.

(12) Nakazawa, J.; Hori, T.; Stack, T. D. P.; Hikichi, S. Alkane Oxidation by an Immobilized Nickel Complex Catalyst: Structural and Reactivity Differences Induced by Surface-Ligand

Density on Mesoporous Silica. *Chemistry – An Asian Journal* **2013**, *8* (6), 1191–1199. https://doi.org/10.1002/asia.201300165.
(13) Kickelbick, G. Hybrid Inorganic–Organic Mesoporous Materials. *Angewandte Chemie International Edition* **2004**, *43* (24), 3102–3104. https://doi.org/10.1002/anie.200301751.
(14) Hoffmann, F.; Cornelius, M.; Morell, J.; Fröba, M. Silica-Based Mesoporous Organic–Inorganic Hybrid Materials. *Angewandte Chemie International Edition* **2006**, *45* (20), 3216–3251. https://doi.org/10.1002/anie.200503075.
(15) Lim, M. H.; Stein, A. Comparative Studies of Grafting and Direct Syntheses of Inorganic−Organic Hybrid Mesoporous Materials. *Chem. Mater.* **1999**, *11* (11), 3285–3295. https://doi.org/10.1021/cm990369r.
(16) Maria Chong, A. S.; Zhao, X. S.; Kustedjo, A. T.; Qiao, S. Z. Functionalization of Large-Pore Mesoporous Silicas with Organosilanes by Direct Synthesis. *Microporous and Mesoporous Materials* **2004**, *72* (1), 33–42. https://doi.org/10.1016/j.micromeso.2004.04.015.
(17) Hicks, J. C.; Dabestani, R.; Buchanan, A. C.; Jones, C. W. Spacing and Site Isolation of Amine Groups in 3-Aminopropyl-Grafted Silica Materials: The Role of Protecting Groups. *Chem. Mater.* **2006**, *18* (21), 5022–5032. https://doi.org/10.1021/cm061382w.
(18) Pal, N.; Lee, J.-H.; Cho, E.-B. Recent Trends in Morphology-Controlled Synthesis and Application of Mesoporous Silica Nanoparticles. *Nanomaterials* **2020**, *10* (11), 2122. https://doi.org/10.3390/nano10112122.
(19) Ahmad, K.; Mowla, O.; Kennedy, E. M.; Dlugogorski, B. Z.; Mackie, J. C.; Stockenhuber, M. A Melamine-Modified β-Zeolite with Enhanced CO2 Capture Properties. *Energy Technology* **2013**, *1* (5–6), 345–349. https://doi.org/10.1002/ente.201300027.
(20) Nik, O. G.; Chen, X. Y.; Kaliaguine, S. Amine-Functionalized Zeolite FAU/EMT-Polyimide Mixed Matrix Membranes for CO2/CH4 Separation. *Journal of Membrane Science* **2011**, *379* (1), 468–478. https://doi.org/10.1016/j.memsci.2011.06.019.
(21) Bahmanzadegan, F.; Ghaemi, A. Modification and Functionalization of Zeolites to Improve the Efficiency of CO2 Adsorption: A Review. *Case Studies in Chemical and Environmental Engineering* **2024**, *9*, 100564. https://doi.org/10.1016/j.cscee.2023.100564.
(22) Snyder, B. E. R.; Bols, M. L.; Schoonheydt, R. A.; Sels, B. F.; Solomon, E. I. Iron and Copper Active Sites in Zeolites and Their Correlation to Metalloenzymes. *Chem. Rev.* **2018**, *118* (5), 2718–2768. https://doi.org/10.1021/acs.chemrev.7b00344.
(23) Groothaert, M. H.; Smeets, P. J.; Sels, B. F.; Jacobs, P. A.; Schoonheydt, R. A. Selective Oxidation of Methane by the Bis(μ-Oxo)Dicopper Core Stabilized on ZSM-5 and Mordenite Zeolites. *J. Am. Chem. Soc.* **2005**, *127* (5), 1394–1395. https://doi.org/10.1021/ja047158u.
(24) Grundner, S.; Markovits, M. A. C.; Li, G.; Tromp, M.; Pidko, E. A.; Hensen, E. J. M.; Jentys, A.; Sanchez-Sanchez, M.; Lercher, J. A. Single-Site Trinuclear Copper Oxygen Clusters in Mordenite for Selective Conversion of Methane to Methanol. *Nat Commun* **2015**, *6* (1), 7546. https://doi.org/10.1038/ncomms8546.
(25) Markovits, M. A. C.; Jentys, A.; Tromp, M.; Sanchez-Sanchez, M.; Lercher, J. A. Effect of Location and Distribution of Al Sites in ZSM-5 on the Formation of Cu-Oxo Clusters Active for Direct Conversion of Methane to Methanol. *Top Catal* **2016**, *59* (17), 1554–1563. https://doi.org/10.1007/s11244-016-0676-x.
(26) Gimeno-Fonquernie, P.; Albalad, J.; Evans, J. D.; Price, J.; Doonan, C. J.; Sumby, C. J. Atomic-Scale Elucidation of Unusually Distorted Dimeric Complexes Confined in a Zr-

Based Metal–Organic Framework. *Inorg. Chem.* **2023**, *62* (47), 19208–19217. https://doi.org/10.1021/acs.inorgchem.3c02337.